MECHANICAL BEHAVIOR OF FIBROUS ROOT-INSPIRED ANCHORAGE SYSTEMS

A Dissertation
Presented to
The Academic Faculty

by

Seth D. Mallett

In Partial Fulfillment
of the Requirements for the Degree
Doctor of Philosophy in the
School of Civil and Environmental Engineering

Georgia Institute of Technology
December 2019

MECHANICAL BEHAVIOR OF FIBROUS ROOT-INSPIRED ANCHORAGE SYSTEMS

Approved by:

Dr. J. David Frost, Advisor
School of Civil and Environmental
Engineering
Georgia Institute of Technology

Dr. Arun M. Gokhale
School of Materials Science and
Engineering
Georgia Institute of Technology

Dr. Paul W. Mayne
School of Civil and Environmental
Engineering
Georgia Institute of Technology

Dr. Susan E. Burns
School of Civil and Environmental
Engineering
Georgia Institute of Technology

Dr. Michael E. Helms
CEISMC, Office of the Provost
Georgia Institute of Technology

Date Approved: 10/10/2019

ACKNOWLEDGMENTS

There are many people who are responsible for the generation of this work and recognition is due:

To my advisor, Dr. Frost, his support and guidance as both mentor and friend have been immeasurable. He is always available for discussion and a coffee, and more than anything, he is the ultimate champion of students, going out of his way to ensure our successes in all aspects of student life. As well, his creation of such a positive, dynamic, and supportive research group and environment has been inspiring and thoroughly enjoyable.

To my committee members, Dr. Susan Burns, Dr. Arun Gokhale, Dr. Michael Helms, and Dr. Paul Mayne, their instruction and guidance during my doctoral process is greatly appreciated, especially all of their helpful feedback for the improvement of this work.

To Dr. Satoshi Matsumura, his support and care was relentless during my time in Japan in terms of both life and research activities, ensuring I was enjoying the experience, and in research, bringing his much needed inquisitiveness, guidance, and dedication to the project.

To Dr. Jean-Michel Pereira, his supervision over the numerical modelling, his research philosophy, and his ensuring a productive and enjoyable stay in France is much appreciated.

TABLE OF CONTENTS

LIST OF TABLES

xiv

(P=Positive, N=Negative, I=indeterminate, a particular value is the optimal value).

LIST OF FIGURES

SUMMARY

Plant root-inspired geotechnics seeks to harness the principles of one of Earth's most ubiquitous foundation elements to redesign or enhance conventional geotechnical infrastructure. In particular, the anchorage and material efficiency attributes of fibrous root systems are encapsulated in a novel root-inspired anchor that has the capability of surpassing conventional anchorage systems (e.g. tiebacks, tiedowns, plate and pile anchors) particularly in areas with weak soil or spatial constraints. The scope of this research fully exposes the application of the bio-inspired design process to the realization of root-inspired anchorage systems from 1) the reasoning behind the selection of fibrous root systems as a prime source of inspiration for sustainable, resilient anchor elements (e.g. plastic and thigmotropic adaptability properties, multifunctionality), to 2) the identification of the critical attributes of fibrous root systems to pullout behavior through testing of leek (*Allium porrum*) and spider (*Chlorophytum comosum*) plants, to 3) the design and fabrication of root-inspired anchor models, to 4) an extensive performance evaluation. More specifically, the root-inspired anchors are assessed in terms of their pullout behavior through a combination of analytical, experimental, and numerical analyses. The slip line method from plasticity theory is used as the basis to derive a solution for the prediction of plate anchor pullout capacity that was further modified to account for the more complex geometry of root-inspired anchors through mechanics-informed insights. Experimentally, a series of 1g pullout tests are performed to parametrically study the role of root-inspired anchor features (i.e. morphology, topology, material properties, and interface roughness) as well as soil properties (i.e. relative density, particle angularity, and particle size) on

pullout behavior. Additionally, through a combination of x-ray CT imaging and digital image correlation (DIC), the formation and evolution of the soil failure surface during the uplift of a root-inspired anchor model is visualized and analyzed to connect the local soil kinematics to the global pullout response. With the finite volume method, the uplift process is simulated to validate experimental results and to extend the parametric study to a wider range of anchor and soil conditions. Finally a few considerations are highlighted concerning the upscale design, installation, and testing of these next generation anchor elements.

CHAPTER 1.   INTRODUCTION

1.1   Motivation

The political, economic, and environmental atmosphere of today is increasingly subjected to both natural and anthropogenic threats (e.g. cyclones, earthquakes, climate change, terrorist attacks), and justly, the demand for adaptive, sustainable, and resilient facilities is becoming more significant. At the same time, most infrastructure components and systems are constructed upon static, single-in-function, and conservatively, over-designed foundations that fail to meet the emerging demand. Consequently, the evolved qualities of nature's ubiquitous foundation, plant root systems, can perhaps inspire a new paradigm with regards to the design and construction of geotechnical infrastructure, termed root-inspired geotechnics.

Root-inspired geotechnics offers an alternative perspective to classic geotechnical design that not only promotes the application of bio-inspired engineering, but also more generally, a more open and broader mindset for the development of novel resilient and sustainable geotechnical solutions, and plant root systems possess a multitude of attractive attributes feasible for the potential translation into infrastructure design. First of all, root systems are capable of adapting to change. They contain both endogenous traits and exogenous responses that allow the plant to sense and respond to environmental conditions and stimuli. Plant roots are a prime example of a biological system that incorporates a multitude of functions into a single organism without diminished efficacy. Root systems are responsible for several vital tasks including, 1) locating, acquiring and transporting resources (i.e. minerals, water), 2) anchorage, 3) storing energy, and 4) reproduction. In

addition, root systems are efficient in resource allocation, where their survival and reproduction are dependent upon this, and through evolutionary adaptations, though not equal for all plant species, root systems regulate their growth and development based upon the nutrients available. As an example, in a mineral limited environment, plants might dedicate a more substantial amount of resources towards greater exploration of soil.

The incorporation of plant root system features into an adaptable, multifunctional, and sustainable geotechnical infrastructure stands as a grand challenge, and this research seeks to contribute a piece to the puzzle. This research is not intended to serve as a nucleation point of root-inspired geotechnics, for previous examples of root-inspired piles and subsurface exploring robots are documented, but rather as a catalyst for future innovation. Accordingly, an auxiliary aim of this research is to provide a glimpse into the infinite amount of information root systems seemingly possess for geotechnical design. Furthermore, to narrow the focus of the potential aspects of root system-inspired geotechnics and to provide a much needed building block for future development, this dissertation will focus on investigating the attributes of fibrous root systems for the structural enhancement of geotechnical anchor elements.

1.2 Organization

The research to accomplish this goal is structured in the following manner:

<u>Chapter 2: Fundamental Knowledge Base</u>

Within this chapter, previous concepts on the topics of biologically-inspired engineering as well as plant root systems and their traits and functions are mentioned to

form a basis of understanding. The review is presented from the viewpoint of a geotechnical engineer and highlights the material deemed relevant to this project. As well, conventional geotechnical anchorage systems are documented, and the concept of plant root-inspired geotechnics is introduced.

Chapter 3: X-ray CT for Bio-Geotechnics

This chapter first documents the physics of x-radiation and the concept of computed tomography (CT). Following, the design of an economical laboratory x-ray CT system for the purpose of studying internal soil processes is documented. Additionally, sample x-ray CT images are provided as well as a review of basic image processing for the quantitative analysis of x-ray images is discussed. X-ray CT is a core experimental technique used in the current bio-inspired root study.

Chapter 4: Materials and Methods

All of the experimental materials utilized within the various experimental endeavors of this research are presented, which details the various geomaterials, fibrous root-inspired anchors, 3D printed plastic filaments, and plant species. Additionally, both the experimental and numerical methods of analysis are discussed. Details of the experimental equipment, soil preparation methods, and finite volume model are thoroughly documented.

Chapter 5: The Design of a Root-Inspired Anchor

The complete bio-inspired design process of a root-inspired anchor is revealed, and the reasoning for the incorporation of specific root properties is highlighted. Fibrous root

features are selected based upon their correlations with pullout behavior, where pullout data from both the literature and from a small scale experiment is utilized. As well, select properties of the developed root-inspired anchor models are documented.

Chapter 6: Pullout Behavior of Root-Inspired Anchor Models: Experimental Endeavor

A multitude of experimental tests are performed to clarify the effect of root-inspired anchor geometry and soil properties on pullout behavior. The morphology and topology of the root-inspired anchorage systems are systemically varied, as well the relative density, particle roundness, and particle size of the geomaterial to identify the dominant factors affecting global pullout behavior.

Chapter 7: Visualization and Analysis of Breakout-Type Failure Surface during Root-Inspired Anchor Model Pullout

Within this chapter, the local soil behavior (e.g. soil deformation and kinematics) is revealed during the uplift of a root-inspired anchor model via x-ray CT imaging and associated image manipulation (i.e. Digital Image Correlation and strain mapping). Maps of displacement and maximum shear strain in both two and three dimensions are produced, and the results are associated to the global pullout response. Following, an analysis of the morphology of the failure surfaces provides insight into the underlying soil-anchor uplift resistance mechanisms.

Chapter 8: Pullout Capacity of Root-Inspired Anchor Models: An Analytical Study

The goal of this chapter is to formulate a method to predict pullout capacity of a root-inspired anchor. Previous analytical models concerning the pullout of fibrous root

systems and plate anchors are discussed, followed by the derivation of a new equation to predict pullout capacity of a plate anchor utilizing an axisymmetric slip line analysis. Finally, the Slip Line method is applied to root-inspired anchor models through various mechanistic and machine learning models.

Chapter 9: Numerical Investigation of Root-Inspired Anchor Uplift

The purpose of this research is to expand upon the previous chapters and to investigate to a greater extent the role of anchor and soil properties on uplift behavior. A calibrated numerical model allows for the reliable extension of the experimental study through simulations.

Chapter 10: Additional Factors Involved in the Pullout of Root-Inspired Anchor Models

Supplementary investigations are provided into additional factors, beyond model morphology and coarse-grained geomaterial properties and conditions, affecting anchor pullout behavior. Factors investigated include model material stiffness, surface roughness, topology, and model geometric scaling.

Chapter 11: Application

Within this chapter, preliminary thoughts concerning the design, installation, and testing of a root-inspired anchor are detailed. Additionally, a synthesis of the salient results of this research are noted to serve as constraints and guidelines for the upscaling of root-inspired anchors to field scale prototypes.

Chapter 12: Conclusions and Recommendations

A summary of the conclusions discovered in this work is presented, and the potential broader impacts are discussed. Additionally, recommendations and ideas for supplemental and further studies are mentioned.

CHAPTER 2.   FUNDAMENTAL KNOWLEDGE BASE

Within this chapter, overviews of the three primary disciplines (i.e. biologically inspired engineering, plant biology, and geotechnical anchorage systems) defining this research are presented. The purpose of this chapter is to provide the fundamental knowledge base for enhanced comprehension of latter chapters as well as a source of inspiration for future plant root-inspired designs.

2.1   Biologically Inspired Engineering

Biologically inspired design, also known as biomimetics and biomimicry, seeks to integrate an element of nature that has undergone modification and augmentation by means of evolutionary adaptation into a human designed creation. It is a design process with a four billion year old research database at its disposal. The concept of bio-inspired design involves the rigorous analysis of the principles (i.e. the functions, forms, behaviors, or phenomena) of biota, full knowledge of the problem or application space, and the translation of the biological principle into the design space.

Bio-inspired design utilizes the design concept of mimicry, which means that the final design will, in some form, replicate the biological inspiration. Perhaps, the most well-known example of bio-inspired design is that of the hook and loop fastener, commonly known by its commercial name of Velcro. When the inventor, George de Mestral, was removing burdock burrs from the fur of his dog, he noticed, upon closer inspection, that the tip of the burr spines were hooked, and purposefully, they mated well with the tangled, looped mass of his dog's hair. Correspondingly, de Mestral's hook and loop fastener functions in the same manner as the burdock burr, mimicking both its form and function. Another renowned bio-inspired solution, the Honey Bee Algorithm, mimics purely the behavior of an organism. The Honey Bee Algorithm, designed by a team of Georgia Tech

researchers, gains inspiration from how honey bee colonies most efficiently allocate their bees to obtain honey, and they use this behavioral solution to optimize the allocation of network servers (Nakrani and Tovey 2004). Furthermore, the pathways of Central Park, which were designed by the landscape architect and architect, Frederick Law Olmsted and Calvert Vaux, respectively, represent form or shape mimicry, where the pathways are visually reminiscent of the circulation system of the human body.
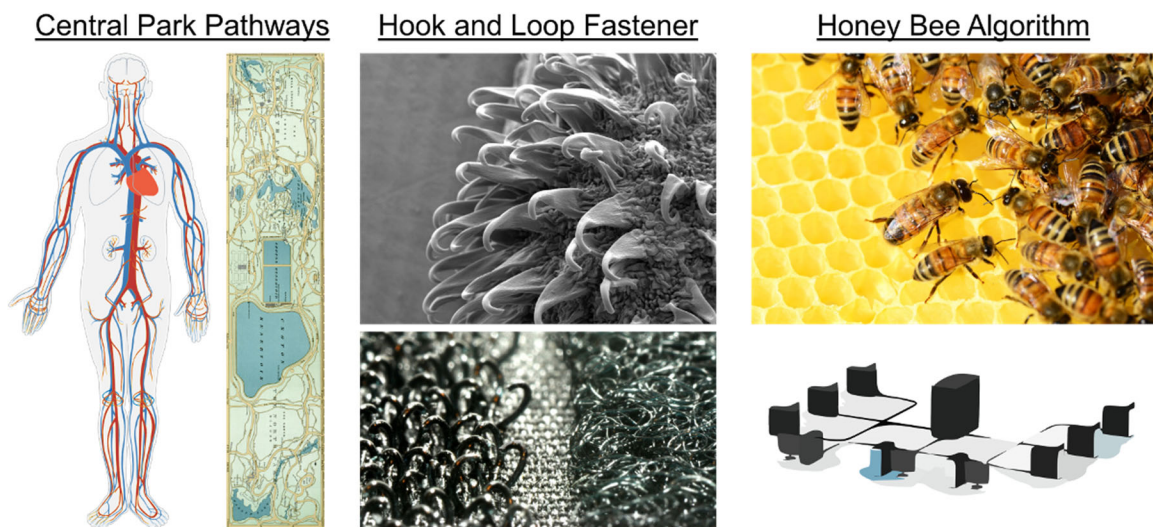
Figure 2-1. Notable examples of bio-inspired design (Sources: all Public Domain, with exception of Hook and Look Fastener (bottom) H. Garland 2009).

Various methodologies and tools, such as TRIZ, SAPPhIRE, AskNature, DANE, and function or problem decomposition, have been developed to aid users in all stages of the design process (Vincent and Mann 2002, Chakrabarti et al. 2005, Helms et al. 2009, Deldin and Schuknecht 2014). Cognitive scientists, who liken biomimicry to the design-by-analogy process, have extensively investigated the cognitive mechanisms involved in the bio-inspired design (Vincent et al. 2006, Helms et al. 2009, Fu et al. 2014). Furthermore, bio-inspired design can be approached from two main perspectives, the problem-driven approach, where designers identify a problem first and then search for biological principles to solve the problem, and the solution-based approach, where

designers first identify biological principles of interest and then target problems that could be solved from the inspiration (Helms et al. 2008, Helms et al. 2009). In general, the practice of bio-inspired design is abstract, does not follow a sequential set of operations, and demands critique and multiple iterations.

The beauty of bio-inspired design is found in its far-reaching versatility; capable of being applied in almost any discipline ranging from art to engineering to health care. To successfully utilize this concept, however, the user must be aware of a few details regarding the premise of this method (i.e. the mimicry of an extant organism). First of all, organisms and their functions and behaviors are not optimal solutions for all situations. In fact, they are not optimal at all in the true sense of the word (i.e. the best or most efficient solution); rather, they are simply sufficient, meaning they have evolved sufficiently as to reproduce and exist (though extant organisms are generally superior to their extinct ancestors) (R. Full, presentation, 2015). As a consequence, the resulting bio-inspired solution is not optimal either, though it might be an optimized solution. In addition, an organism has evolved under specific constraints and is not necessarily adaptable to new extremes and conditions. Furthermore, organisms must be viewed from a systems approach; the structures, the individual functions, the behaviors, and the phenomena that contribute to the survivability of an organism are all interrelated and are affected through competition among the various principles. In conclusion, since the extracted biological features are linked to a particular environment, time, and system, the practitioner needs to acknowledge that certain repercussions and artifacts can transpire in the incorporation of a biological feature into a designed product.

2.2   Biologically Inspired Geotechnics

Bio-inspired geotechnics refers to a new branch of geotechnical engineering that seeks to incorporate the knowledge of billions of years of evolution to create or enhance traditional geotechnical structures or implementation techniques. This division of geotechnics is quite distinct from biologically mediated geotechnics, where the latter relies on the direct incorporation or utilization of biological organisms in a design. Numerous examples of bio-mediated geotechnics exist, including soil stabilization through cultivation of plants or through microbial induced calcite precipitation (MICP) as well as groundwater and soil bioremediation. On the other hand, far fewer bio-inspired designs are as technically advanced. One of the earliest bio-inspired geotechnical designs, thought to be inspired by geocarpy (e.g. porcupine grass seed), is a pile that propagates into the soil due to external agitation (e.g. wind or water) and was developed by Henry Mitchell, a member of the U.S. Coastal Survey (Thoreau 1859, Vincent et al. 2006). Perhaps the first root-inspired geotechnics solution was invented in 1950 by Fernando Lizzi, an Italian engineer who designed and implemented underpinning and retention systems for the stabilization of foundations and slopes (Lizzi 1993). Additionally, numerous examples of bio-inspired robotics have been invented for the exploration of the subsurface, including designs inspired by plant roots, razor clams, locusts, and wood wasps (Menon et al. 2006, Winter and Hosoi 2011, Lucarotti et al. 2015).

2.3   Plant Root Systems

A brief overview of the principles of plant roots is provided as well as specific details of root systems that are particularly applicable to root geotechnics. Simply stated, root systems are the sub-terrain, leafless appendage of most vascular plants. From a more anatomically rigorous standpoint, roots are differentiated from other extant plant organs,

specifically from the stem, by the presence of a root cap, a protective mass of cells found at the tip of roots (Gregory 2006, Stern et al. 2006). First evidence of root structures found in fossils dates back approximately 400 million years ago to the Upper Silurian or Lower Devonian periods, and biologists theorize that roots first developed to extract nutrients from the subsurface (Raven and Edwards 2001). The majority of root biomass is found in the top 30cm of soil (Jackson et al. 1996). The deepest penetrating roots recorded were found in South Africa belonging to a wild fig tree (*Ficus natalensis*) and measured 120m deep. On average, the deepest roots are found in desert and grassland biomes, and the shallowest in tundra (Canadell et al. 1996, Schenk and Jackson 2002). Material efficiency in terms of transport capacity and mineral acquisition per volume of material increases with decreasing root diameter; however, a physical lower limitation on the size of roots (i.e. 50μm in diameter) is imparted due to the formation of a central stele (Nye and Tinker 1977, Fitter 1987).

2.3.1 Functions

Since their origination, plant roots have acquired two primary functions: 1) locate, capture, and transport vital water and mineral nutrients, and 2) anchorage, and two secondary functions: 1) storage of energy, and 2) vegetative reproduction. The ability to exploit the vast subsurface for nutrients allows plants to sustain growth. Anchorage exists so that plants are not uprooted, to provide support and rigidity to the above-ground portion of the plant, where upon uprooting and desiccation, roots perish. While most plants are capable of the two mentioned secondary functions to some extent, these functions are more prominently and naturally expressed in select species. For example, sweet potato plants

utilize their root system to both store food energy and as a means to facilitate vegetative propagation.

2.3.2 Types

A review of relevant plant root terminology is provided. A root refers to an individual axis of growth while root system refers to the complete collection of the root axes of a plant. Primary root refers to the dominant, first formed root of a root system, and lateral root refers to all roots that branch off from a previously formed root. Lateral roots are described in a hierarchical nature, where a second order lateral references a root axis that has bifurcated from a first order lateral. Additionally, root hairs are fine, typically unbranching structures that extend from a root surface and are thought to contribute substantially to water and nutrient absorption.

In plant biology, several types of specialty roots have been classified for roots that provide specific roles or functions. Examples include tuberous and storage roots (e.g. carrots, sweet potatoes), which store nutrients, adventitious roots (e.g. strawberry plants, maize), which originate from non-root organs such as the stem or branches of a plant, contractile roots (e.g. water lilies, hyacinth), which assist bulbous plants in attaining greater depths, and aerial roots (e.g. orchids, mangroves, strangler fig), which exist above ground for water or air absorption or for plant support.

A more recent division among roots has been in the classification of fine and coarse roots, and while the threshold for root diameter is still disputed, the distinction exists due to functionality differences (Reubens et al. 2007, Danjon et al. 2013). Coarse roots, which are typically described as those roots with a diameter greater than 2mm, are, in general, the

result of secondary thickening, which most monocotyledons are incapable of developing. Secondary thickening, which is radial growth that occurs from the generation of cork cambium on the outside of a root, reduces a roots absorptive capacity and consequently, distinguishes fine roots as roots responsible for absorption and coarse roots for anchorage and structure.

2.3.3   Root System Architecture

The architecture of a plant root system refers to the overall geometrical structure of the root system, but not the inner, anatomical nature of roots. The architecture encompasses various root system descriptors including morphology (i.e. the shape and arrangement) and topology (i.e. the spatial connectivity of the roots of a system) (Lynch 1995). While the inner cellular organization is fundamental to a root system, the architecture of a root system, which is the resultant of the development of the root system within the soil, is highly variable (Malamy 2005). Furthermore, the root system architecture is the convoluted result of the plants genetic predisposition to a form and the plant's responses to environmental conditions, and as *Barthélémy and Caraglio 2007* state, it is "the expression of an equilibrium between endogenous growth processes and exogenous constraints exerted by the environment" (Pagès 1999, Barthélémy and Caraglio 2007). Parenthetically, the intrinsic root system architecture is only theorized since plants cannot survive without some external influence. Therefore, root system architecture is a reflection of the competition between the various genetic and environmental constraints at specific points in time. As such, the classification of root systems into logical architectural sets is a complicated task; however, notable attempts have been made (Cannon 1949, Weaver 1958,

Köstler 1968 (in German, reproduced in Stokes and Mattheck 1996), Ennos and Fitter 1992).

For the purpose of this manuscript, the generalized classification system of *Ennos and Fitter 1992* is utilized (Figure 2-2). For root-bearing vascular plants, a clear distinction is apparent between the roots systems of monocotyledonous angiosperms (e.g. grasses, grains, orchids) and those of dicotyledonous angiosperms (e.g. sunflowers, oaks, maple) along with gymnosperms (e.g. conifers, ginkgo). While monocotyledons develop fibrous root systems, which consist of multiple root axes extending from a single point, dicotyledonous and polycotyledonous plants have taproot systems, which consist of a central primary root with minor lateral roots. With maturation, taproots develop into plate root systems as resources are gradually allocated to the lateral branches. Classification systems serve multiple purposes, such as aiding in the grouping of endogenous architectural traits (Barthélémy and Caraglio 2007) or associating root architecture attributes to various root functions (Fitter 1987, Fitter and Ennos 1989). In conclusion, the root system architecture of a plant is the temporal, integrated representation of both the natural growth of plant and the response of the plant to the environmental conditions.
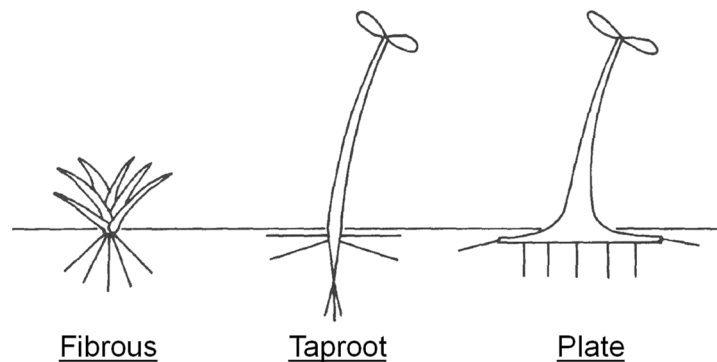
Figure 2-2. Simplistic representations of fibrous root, taproot, and plate root systems (adapted from *Ennos and Fitter 1992*).

2.3.3.1 Topology

Root system topology refers to the connections among the various root axes and provides no morphological information. The quantitative means by which they were first assessed comes from Strahler's stream classification method (Fitter 1987). Within this mathematical system, structures are comprised of segments and nodes (i.e. points of bifurcation), and various topological indices (e.g. altitude, maximum/total external pathlength, Strahler branching ratio) have been generated for the comparison of root systems (Fitter 1987, Berntson 1995, Berntson 1997). The topology of root systems exist on a spectrum between the symmetric, dichotomous topology and the asymmetric, herringbone topology (Figure 2-3). As well, a topological analysis can provide powerful insight into developmental constraints (Fitter et al. 1991, Bernston 1997). Root systems with greater total external pathlength, closer to the herringbone topology, are theorized to be more resource acquisition efficient and less resource transport efficient (Fitter 1987, Fitter et al. 1991). In connection with root developmental strategies, more exploratory species adopt herringbone topologies, while dichotomous topologies are favored for safer, more static species that thoroughly mine local resources (Oppelt et al. 2001).
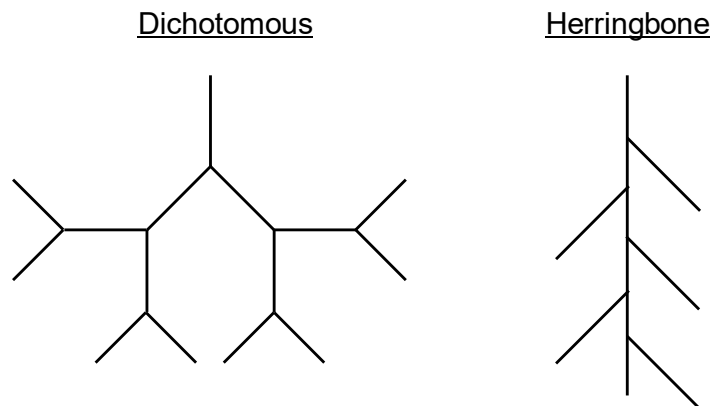
Figure 2-3. Schematic representations of dichotomous and herringbone topologies.

2.3.4   Root System Development

Root members grow through a combination of axial elongation, branching, and radial expansion actions, which occur as the result of a coordinated development of undifferentiated cells in the apical meristem, and root members mature through secondary thickening or lignification and eventual senescence (Gregory 2006, Hodge et al. 2009). Root growth is inherently dependent upon the acquisition of nutrients. Functional equilibrium refers to the balanced plant growth that occurs as a result of the efficiency by which resources are obtained, and a characteristic of this behavior is that resources are allocated to the plant organ that is limiting the growth of the plant (Brouwer 1963). As a result, the root system of the plant grows in accordance with the resource acquisition capabilities of both the above- and below-ground portions, and root growth is naturally dependent upon the atmospheric and edaphic constraints (van Noordwijk and de Willigen 1987). Furthermore, the functional growth equilibrium concept is dependent upon a species genotype and evolutionary-influenced growth strategies; for example, competitors, stress tolerators, or ruderals vary in their resource allocation based on their evolved growth-risk strategy (Grime 1977).

2.3.4.1   <u>Plasticity</u>

In botany, plasticity refers to the ability of the plant to perceive and respond to environmental conditions, and the plant root system implores various techniques to survive changes in environment, including tropic responses and developmental growth patterns. In general, plants have evolved multiple plasticity strategies due to their sessile nature, where plants that possess the ability to respond effectively to changes in external stimuli are most

able to survive and continue propagating. Plastic responses can be subdivided into morphological and physiological responses, where the former requires large resources and results in cellular growth and the latter is resource conscious and results in subcellular changes; the type of induced plasticity is theorized to be dependent upon the environmental conditions (Bradshaw 1965, Grime and Mackey 2002). One of the extensively studied physiological mechanisms behind some root plasticity is explained through the distribution and transportation of auxins, a plant hormone. Auxins are responsible for root organogenesis, including the formation of lateral roots and root hairs and multiple tropic responses (Went 1974, Pitts et al. 1998, Casimiro et al. 2001, Friml 2003). In particular, the axisymmetric distribution of auxins promotes differential cell elongation, which leads to the bending of the plant in the direction of the acting stimuli (Friml 2003, Petrášek and Friml 2009). Furthermore, auxin acts as a growth promoter in plant stems and inhibitor in plant roots (Gregory 2006).

2.3.4.1.1 Tropic Responses

Tropic response refers to the growth or movement of the root system in response to an external factor and is usually expressed as a positive or negative response depending on the direction of the action in relation to the direction of the environmental stimulus. As a general example, root systems grow in the direction of gravity (i.e. gravitropism), whereas lateral roots often grow perpendicular to gravity (i.e. diagravitropism). Various other tropisms that affect root system growth and development include chemotropism, response to chemicals, electrotropism, response to an electric field, halotropism, response to salt concentrations, hydrotropism, response to water, phototropism, response to light, thermotropism, response to temperature, and thigmotropism, response to mechanical force.

Often, tropic responses are in direct competition; for example, root systems grow against the direction of gravity when exposed to a beneficial nutrient or water concentrations or when the root becomes in contact with a particularly dense, immobile, or impenetrable object or soil layer.

2.3.4.1.1.1 Thigmotropism

Of particular interest to this research is thigmotropism, which provides evidence that root systems not only perceive mechanical forces but also respond to them as well. This concept, as described further in Chapter 5, is one of the critical concepts utilized for the reasoning and selection of root systems as the choice of biological inspiration. Numerous examples and experiments have been performed to realize the powerful effect of thigmotropism on the architecture of plant root systems, and jointly, thigmomorphogenesis is the change in shape of the plant in response to a mechanical stimulus (Jaffe 1973). The effect of thigmotropism on plant root systems has been primarily investigated for dicotyledonous species with taproot or plate root system architectures, particularly mature specimens with significant woody root members. Theories suggest that plants can sense larger stress concentrations and dedicate extensive resources to the strengthening the stressed region, with visual evidence found in the formation and distribution of buttress roots and the formation of T-beam and I-beam shaped root cross-sections (Mattheck 1991, Nicoll and Ray 1996, Mattheck 1998). More so, a greater number of roots and roots of greater cross-sectional area were found for root members parallel to a repeated unilateral force (Coutts 1983, Stokes 1994, Stokes et al. 1997, Coutts et al. 1999, Mickovoski and Ennos 2003, Cucchi et al. 2004), with evidence of even greater cross-sectional area on the leeward side than the windward side (Nicoll and Ray 1996).

Particularly for root members parallel to a prevailing wind direction, roots develop I-beam or T-beam shaped cross-sections, which is thought to be for those roots subjected to pure bending for I-beam shaped roots or combined tensile or compressive loading and bending for T-beam shaped roots (Nicoll and Ray 1996, Mattheck 1998). In particular, an I-beam shaped cross-section has a greater second moment of area than a circular cross-section, which augments a member's flexural rigidity; additionally, when normalized by the cross-sectional area, the material efficiency attributes of an I-beam shape root are perceived.

2.3.5   Soil-Root Interactions

The rhizosphere refers to the soil surrounding a root system that affects and is affected by the growth and development of the root system. The complex interactions that occur between the root system and rhizosphere can be broadly categorized into five main categories: 1) biological, 2) thermal, 3) hydraulic, 4) chemical, and 5) mechanical. Within each category, the interactions are subdivided into, 1) plastic responses (i.e. the response of the organism to an environmental stimulus) and behavioral changes of the plant, and 2) soil alterations (i.e. the changes the soil undergoes through the development of the root system). As a preface, the categorization of soil-root interactions into the five groups is not absolute; various phenomena exist in multiple categories due to their integrated nature. Furthermore, soil-root interactions vary temporally and spatially, where processes are dynamic, spatially heterogeneous, and occur at various scales.

2.3.5.1   <u>Biological</u>

The rhizosphere is one of the most biodiverse ecological systems on Earth (Hinsinger et al. 2009). A plethora of interactions occurs between roots and other biological

lifeforms within the soil, including bacteria, fungi, nematodes, protozoa and viruses, and the relationships between roots and other biota can be both positive and negative in nature. For example, various fungi inhabit root systems, and while the root provides a substrate and energy in the form of carbohydrates, the fungi increase the root system's water and nutrient absorptive capacity, forming a symbiotic relationship. The augmented absorptive capacity is due in parts to the increased surface area from fungal hyphae, which are on average longer and smaller in diameter than root hairs, and through chemical secretions. The general term for root-fungi associations is mycorrhizae. However, not all mycorrhizae are symbiotic; some interactions are parasitic, meaning the fungal colonies only extract resources from the plant and offer no value in return (Johnson et al. 1997). Some bacteria also form symbiotic associations with roots; nitrogen-fixing bacteria are able to convert nitrogen gas into ammonium, which the plant requires, in exchange for carbon sources. Additionally, various fauna, such as protozoa and nematodes, consume bacteria and fungi; however, their association with roots can range from mutualistic (e.g. biomass cycling) to predation (e.g. removing absorption enhancing fungi).

Plant root-induced biological activity significantly alters the soil behavioral state, and this process exists as a feedback loop, where increasing biological development in the rhizosphere amplifies the modifications to the system. Rhizospheric organisms influence physical transport phenomena (e.g. heat transfer, fluid flow, nutrient conduction and diffusion), alter the mechanical behavior of the soil, and contribute to pedogenesis. For example, various bacteria are known to form pathogen resistive biofilms (i.e. conglomeration of microorganisms and polymeric materials). While biofilms are often beneficial to the root system, they also contribute to bioclogging, which is the reduction in

hydraulic flow due to the growth of microorganisms in the soil pores. As well, through bio-cementation, many species of bacteria can influence transport processes in the soil as well as the mechanical behavior of the soil through assistance in the precipitation of minerals on particle surfaces and contacts. Additionally, the senescence of roots generates organic matter which affects various soil state properties including the water retention capacity and mechanical strength. Soil dwelling or tunneling invertebrates, such as annelids or arthropods, aerate the soil and enhance the porosity of the soil, which improves root growth.

2.3.5.2 <u>Thermal</u>

Plant root systems are impacted by temperatures of both the atmosphere and the soil. Soil temperature variations decrease exponentially with depth, and the degree of variation and the depth to which the variations extend depends on the time scale. Most root systems exist in soil depths subjected to both diurnal and seasonal temperature fluctuations, where temperatures changes can be experienced to approximately 1m and 10m for daily and annual periods, respectively (Hillel 2000, Schenk and Jackson 2002). The response of the root system to thermal stimulations is referred to as thermotropism. Root growth has inherent thermal limits, and the elongation and overall development of the root system can be severely restricted or halted if the ground temperature surpasses the optimum temperature bounds, which negatively impacts the ability of the root system to locate and absorb nutrients (Burholt and Van't Hof 1971, Gregory 1986, Kaspar and Bland 1992, Drennan and Nobel 1998). In addition, the thermotropic response of the root system is gradient dependent, and the direction and magnitude of the temperature change within the soil can dictate the root system architecture.

Due to the thermal properties of the soil, temperature change within the rhizosphere is more gradual as compared to the atmosphere. With regards to the effect of a root system on the thermal properties of soil, changes in the effective thermal conductivity and specific heat capacity are dependent on whether the root system replaces air or water filled voids, as demonstrated in Table 2-1. Additionally, decomposition of organic matter (e.g. decaying roots), particularly the oxidation of carbon, releases heat into the system.

Table 2-1. Compilation of material thermal properties located in the soil-root system.

Constituent	k_T [W m^{-1} K^{-1}]	c_p [J kg^{-1} K^{-1}]	ρ [kg m^{-3}]
Air	0.026[a]	1007[a]	1.16[a]
Water	0.56[a]	4217[a]	999.9[a]
Ice	2.14[a]	2110[a]	917[a]
Quartz	8.4[b]	730[b]	2650[b]
Dry clay	0.1-0.2[c]	800[b]	1200
Organic matter	0.25[d]	1950[d]	1300[d]
Moist wood	0.2-0.5[e]	3100[e]	500-700[e]

a) Lide et al. 2009, b) Farouki 1981, c) Cortes et al. 2009, d) Hillel 1980, e) Steinhagen 1977

2.3.5.3   Hydraulic

The role of water on the soil-root system is dramatic. Firstly, the availability of water is critical to the overall development of the plant and greatly affects many of the life sustaining processes of the plant (e.g. photosynthesis, respiration, transpiration, cell growth) (Passioura 1982, Gregory 2006). In addition, research confirms that plant root systems exhibit positive hydrotropic behavior; assuming other environmental stresses do not greatly dominate the growth response, roots can concentrate growth in the direction of a moisture gradient (Takano et al. 1995, Takahashi 1997, Eapen et al. 2005). Furthermore, water is responsible for the transportation of nutrients to the root surface; either through

diffusion from chemical gradients or advection from hydraulic gradients, roots rely on water for the mobilization of nutrients to the root absorbing surface.

The pore water pressure is a critical parameter to many processes within the soil; examples include effective stress, which is dependent upon the pressure head, and fluid flow, which is dependent on the pressure gradient. Roots alter the pore water pressure through a variety of processes. First of all, plant root systems that respire inherently exist in unsaturated conditions, due to their oxygen requirement. As such, the soil experiences capillary suction, which is the pressure difference between air and water and is a function of the surface tension of the water and the size of the pore throat. For plants in the vadose zone, capillary rise assists root systems in fulfilling water requirements. As the plant transpires, a suction is generated at the surface of the root, which allows water to be transported from the roots throughout the plant. As a result, water connected to the root surface experiences the transpiration suction, which is transmitted to the soil. Additionally, due to the absorption of nutrients from the water, an osmotic suction is generated due to solute concentration gradients between the pore water and the water within the root. However, osmotic suction component is quite complex and transient due to the nutritional requirements of the plant at various stages of the plants development. The effective stress state of the soil in the rhizosphere is enhanced through the contributions of the various root-induced suction forces; however, only water that is in continuous contact with the root surface experiences pressure alterations from the root system. Additionally, plant root systems significantly reduce the erodability of soils, especially sloped topographies.

2.3.5.4   Chemical

23

In addition to water, plants require various nutrients to sustain life, for both growth and metabolism; this includes elements such as calcium, carbon, hydrogen, magnesium, nitrogen, oxygen, phosphorous, potassium, and sulfur (Gregory 2006). For most required nutrients with the exception of carbon and oxygen, water is responsible for the transportation to the root surface, by either conduction, convection, or diffusion. For the diffusion case, the local solute concentration gradient in the soil determines the element mobility, and feedback loops occur as the concentration at the root surface is diminished due to absorption by the root, continuing the transportation and extraction of nutrients from the soil. Osmosis, which is a chemical process fundamental to the absorption of nutrients and water, occurs when a solvent, in this case water, permeates a semi-permeable wall, in this case the outer cell layers of the root surface, in the direction of the highest solute concentration; the plant adjusts the local concentrations within the root to promote the absorption of water or nutrients. Plant roots demonstrate both positive and negative chemotropic responses. For example, plant roots often grow in the direction of high nutrient concentrations; yet, chemically toxic conditions, such as high acidity, salinity, or metal concentrations, often stunt root growth (Bernstein 1975, Drew 1975, Ryan et al. 1992, Robinson 1994, Munns 2002). Furthermore, roots exude various compounds, referred to as exudates or mucilage, for a multitude of purposes, including water retention, protection from pathogens, root growth elongation easement, bacteria and fungi attraction for increased nutrient absorption, nutrient transport facilitation, and metal fixation (Oades 1978, McCully 1999, Gregory 2006). Mucilage is a polysaccharide viscous fluid that is released from the tip of the root usually in a layer 0.5μm to 50μm thick.

The presence of roots in the subsurface has profound effects on the chemical composition of the soil. Most importantly, plant roots are a primary culprit for the genesis of fine-grained sediments ($d_{particle}<75\mu m$); the transportation and absorption of minerals, the exudation of chemicals, and the decomposition of aging roots in the rhizosphere induces various chemical reactions (i.e. dissolution, hydration, hydrolysis, oxidation) that generates fine particles. Furthermore, the accumulation of bacteria in the presence of acid solutions assist in the formation of various precipitates, such as calcium carbonate and gypsum when calcium and sulfur are present. As well, the absorption of nutrients and water from the soil, as well as the production of mucilage lead to changes in the ionic concentration and pH of the pore fluid (Hinsinger et al. 2009). For fine-grained soils in particular, which are more susceptible to electrical forces, DLVO theory suggests that the diffuse double layer thickness is inversely related to the ionic concentration; consequently, a decrease in the ionic concentration results in a greater repulsive force and a more dispersed soil fabric (Hillel 1980, Santamarina 2001).

2.3.5.5 Mechanical

Plant root systems rely on their mechanical interactions with the soil to obtain their anchorage functionality, and proper anchorage is limited by the weakest component of the system, be that of individual roots, the soil, or the soil-root interface. Possible failure modes include soil shear failure, root tensile rupture, root shear failure, soil-root interface failure, and root buckling, where the most probable anchorage failure involves multiple mechanisms. Additionally, properties of the soil affect the elongation and radial growth of roots, ultimately affecting the overall architecture of the root system. For example, the rate of elongation significantly decreases as the resistance to penetration, measured via

penetrometer or actual root resistance, increases (Bengough and Mullins 1991). Penetration resistance is governed by the compressibility of the soil fabric, which is a function of the void ratio and confining pressure, and is affected by the soil particle properties (e.g. shape, mineral composition), in-situ stress state, and friction angle. For particularly low compressibility soils, roots expand radially by temporarily increasing the turgor pressure (i.e. the pressure within each cell), which increases the porosity at the tip of the root, allowing for easier root elongation; this propagation method is more broadly known as opening-mode fracturing (Bengough and Mullins 1990, Shin and Santamarina 2011). Furthermore, for optimal growing conditions an optimal soil density exists, where dense soil restricts elongation and exploitation of resources and loose soils is suggested to minimize nutrient absorption (Passioura and Leeper 1963). On an aside, a preferred soil particle size range exists for plants based on the water retention and mechanical resistance properties of the particulate medium (Donald et al. 1987). To further reduce penetration resistance, root caps have adapted a sloughing functionality, where external cells detach from root cap effectively reducing the interfacial friction at the root-soil interface (Bengough and McKenzie 1997). As well, roots preferentially grow in more penetrable areas (e.g. decaying organic matter, animal burrows, cracks) (Stirzaker et al. 1996).

The development of root systems alter the mechanical properties of the rhizosphere. For example, the radial and axial growth of roots lead to soil densification and altered and reoriented stress states (Dexter 1987). In addition, particles at the root surface tend to align with the direction of root extension. The primary surface of plate-like particles, in particular, are often reoriented parallel to root elongation (Dorioz et al. 1993). Furthermore, exuded mucilage forms a rhizosheath upon drying; the mucilage acts to assemble and bind

soil particles to the root surface, effectively contributing a cohesive strength (Watt et al. 1993, Czarnes et al. 2000). However, when wet, some mucilage has a lower surface tension than water (Read and Gregory 1997), which would lead to a decrease in capillary pressure and effective stress (i.e. Young-Laplace equation).

2.3.6   Root System Anchorage Mechanics
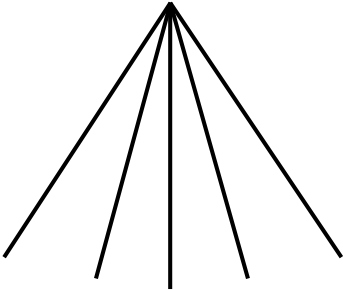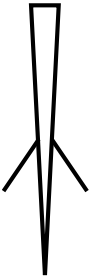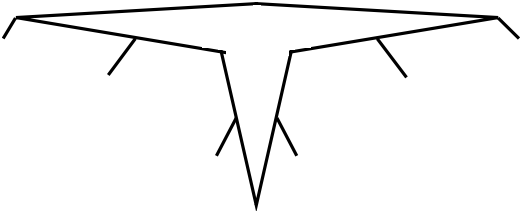
The anchorage mechanics of plant root systems have chiefly been studied for two primary reasons, from a biological standpoint, to identify the causes of tree overturn or crop lodging, and from an engineering standpoint, to utilize plant roots for slope stabilization. Root system overturn and lodging occurs when the anchorage functionality of root systems fails due to some irrevocable displacement and typically is the result of large bending moments from lateral forces (i.e. wind forces). Biologists, agronomists, and soil scientists seek to combat this economic concern through the identification of plant genes that promote greater anchorage capacity, through augmented agricultural techniques, and through soil modification (Coutts 1983, Stokes et al. 2009). Furthermore, geotechnical engineers and soil scientists have researched root anchorage mechanics from various scales, from individual roots and their contribution to the effective shear strength of the soil to the root system and their contribution to the stabilization of slopes (Waldron and Dakessian 1981, Gray and Ohashi 1983, Wu et al. 1988, Pollen and Simon 2005, Mickovski et al. 2010, Schwarz et al. 2010).

Additionally, the architecture of a root system significantly contributes to the root system's ability to anchor a plant (Coutts 1983, Ennos 1993, Ennos 2000, Reubens et al. 2007). Given a plant in the same environment, differences in architecture can lead to

dramatic differences in plant stability (Danjon et al. 2005). Architectural indices, both topological and morphological, are often correlated to specific traits of pullout behavior, namely ultimate pullout resistance and failure displacement (Reubens et al. 2007). From an additional perspective, the characteristic root architecture systems experience different loads regimes primarily due to the above-ground attributes of the plant (Ennos 2000). A summary of root system architectures with their associated external loading conditions is documented in Table 2-2. A brief introduction into the mechanics of root stabilized slopes and overturn is provided, followed by a more comprehensive review of root pullout.

Table 2-2. Association of root system architectures and loading conditions.

Architecture Classification	Representative Architecture	Plant Types	Loading Conditions*
Fibrous		Monocotyledons	**Herbivores (E)**, Self-weight (C), Trampling (C)
Taproot		Dicotyledons (juvenile), Dicotyledons (mature), Conifers (juvenile)	Wind (L), Self-weight (C)
Plate		Dicotyledons (mature), Conifers (mature), Ginkos (mature)	**Wind (L)**, Self-weight (C), Rain/Ice/Snow (C),

*Compression: (C), Extension (E), Lateral-induced Moment (L)

2.3.6.1   Slope Stabilization

The principal idea behind plant root-stabilized slopes is that root systems can improve the resistance to sliding by growing through potential slope failure surfaces and thereby enhancing the effective shear strength along the failure surface. Root systems enhance the soil shearing resistance through the tensile resistance of the root and the normal component of the induced confinement imparted by the loaded root axis (Waldron 1977, Waldron and Dakessian 1981, Gray and Ohashi 1983, Wu et al. 1988). The shear strength augmentation is manifested as long as the root system, 1) crosses the shearing plane, 2) is sufficiently anchored to distal soil layers through soil-root cohesion or interface shear resistance, and 3) is not loaded beyond the root tensile strength. The effective shear strength of the soil increases with increasing density distribution of roots (Waldron 1977, Operstein and Frydman 2000, Dumlao et al. 2015). Furthermore, an optimal angle between the failure surface plane and root axis exists to maximize the increase in shear strength (Gray and Ohashi 1983, Jewell and Wroth 1987). Due to the inherent progressive failure associated with vegetated slopes, fiber bundle models were applied to slope stability models to account for the distribution of root tensile strengths (Pollen and Simon 2005, Schwarz et al. 2010).

The utilization of a living entity for slope stabilization brings forth multiple concomitant processes, and their effect on the strengthening of the design is complex and is the result of the cumulated processes (Gary and Sotir 1995, Gray and Barker 2004, Stokes et al. 2009). One issue surrounding the use of plants is plant-induced water effects. Plants absorb water from the soil and transpire water from their leaves, which both act to stabilize the slope through increased effective stress and decreased slope weight. However,

plants generate organic matter, which enhances the available water capacity of the soil; this naturally diminishes the slopes resistance to sliding. Furthermore, plants add both dead and live loads to the stability analysis, and depending on the severity of the slope and the direction of the live loads (e.g. wind, rain, snow) relative to the orientation of the slope, they can act to strengthen or weaken the slope. Furthermore, plant root systems that do not significantly intersect the failure surface can act to destabilize the slope depending on the dip. As well, while plants aid in preventing erosion and slope degradation, conversely, plant life also provides habitation for burrowing animals, whose tunnels can lead to internal erosion and slope failure. Additionally, when stabilizing a slope with vegetation, potential risks, such as fire, extreme weather (e.g. high winds, severe rain, drought), clear cutting, grazing, must be assessed (Wu et al. 1979, Coppin et al. 1990).

2.3.6.2   Overturning

Plant failure due to excessive wind forces occurs by two main methods, lodging, where the plant stem fails in bending near the ground surface, and windthrow, where the entire plant including root system is overturned. Typically, lodging occurs in fibrous and tap root systems, whereas windthrow is more common for plate root systems. Overturning is the mechanical process by which root systems are progressively loaded and uprooted, and windthrow is a specific form of overturning failure due to lateral wind forces. For plants with plate root architectures, the general failure pattern for windthrow is that the plate-like root structure and surrounding soil mass is rotated about a hinge located on the leeward side. During loading, a variety of mechanisms occur, and individual root axes can be loaded in various manners (e.g. shear, tension, compression, bending, and torsion) depending on the root axis orientation in relation to the acting force and other root axes.

More specifically, the primary mechanisms involved in windthrow of a plate root system as identified by plant biologists include, 1) the mass of the overturning soil-root plate, 2) bending resistance of the leeward roots, 3) tensile resistance of windward roots, 4) "tensile" resistance of soil (Coutts 1983, Ennos 2000). However, many more mechanisms are involved including, 1) tensile and shear resistance of roots on the bottom and sides of the soil-root plate, 2) torsional resistance of roots on the side of the plate, 3) shear and bearing resistance of soil, and 4) shear resistance of soil-root interface. Overall, the resistance to overturning is dependent upon the properties of the root system (e.g. material properties including strength and rigidity, architecture including topology and geometry), the soil (e.g. strength and state properties), and soil-root interface properties (e.g. strength including friction angle and cohesion) as well as the direction of loading.

The overturning of plate root systems has been studied with various methods for the primary purpose of identifying the mechanisms involved in and factors affecting overturning so that methods of improving root anchorage can be devised. Initial experimental investigations into the overturning of trees were performed by applying a lateral force to the stem or trunk of the tree via a winch. From these studies, factors that affected roots system anchorage included root plate depth, soil type, soil conditions (e.g. drainage, oxygen levels, suction), and planting methods (e.g. ripping) (Fraser 1962, Armstrong et al. 1976, Somerville 1979, Deans and Ford 1983). Detailed analysis of static winch pullover tests revealed precise mechanisms involved in the root system overturn, particularly the role of architecture on the resistance to overturning (Coutts 1983, Coutts 1986). This was followed by the works of many (Ennos et al. 1993, Crook and Ennos 1996, Nicoll and Ray 1996, Crook and Ennos 1998, Ray and Nicoll 1998, Stokes 1999, Peltola

et al. 2000, Stokes et al. 2000, Goodman et al. 2001, Mickovski and Ennos 2003a/b, Cucchi et al. 2004, Nicoll et al. 2006, Khuder et al. 2007). Further studies included the comparison of overturned and stable root systems after severe weather with strong winds (Mason 1985, Cucchi and Bert 2003, Fourcaud et al. 2003, Danjon et al. 2005). Two- and three-dimensional finite element simulations of both analogs and scanned root systems have been performed (Dupuy et al. 1995a/b, Fourcaud et al. 2003, Dupuy et al. 2007, Fourcaud et al. 2007). Finally, various models for predicting windthrow have been developed which incorporate wind, soil, and plant characteristics (Deans and Ford 1983, Blackwell et al. 1990, Peltola and Kellomaki 1993, Peltola et al. 1999, Gardiner et al. 2000); most models utilize overturning resistance correlations with soil and above-ground plant characteristics based upon static winch tests.

2.3.6.3   Pullout Behavior

Pullout or uplift is the mechanical process of extracting embedded elements from soil, wherein a tensile force is the main loading component. The primary culprit of root pullout is performed by herbivores; however, during shearing of root permeated soil and during the overturning of a plate root system, some root axes are loaded in pullout. One of the clearest rationales for deciphering the mechanical behavior of an object under load is to consider all of the possible failure mechanisms. For the pullout of single root axis, the possible failure modes include, 1) root tensile failure, 2) soil-root interface failure, and 3) soil shear failure, and before complete global failure, all of the failure modes can occur. During pullout, resistance to uplift is provided by the tensile resistance of the root (i.e. elastic modulus), shear resistance of soil-root interface (i.e. both interface friction and cohesion), and shear resistance of soil (i.e. soil shear strength) (Gray and Barker 2004).

The resulting pullout behavior is dependent upon the various soil, root, and soil-root interface properties as well as the relative differences among them. Depending on the ratio between the tensile stiffness of the root member and the effective shear stiffness of the soil-root interface, dramatic differences in the transfer of tensile load to the soil occurs. For example, for a relatively rigid root element, the full strength of the soil-root interface is mobilized upon initial loading or displacement, whereas for an elastic root member, the shear strength is progressively mobilized upon loading. For pullout of most root systems, the latter case is expected (Hamza et al. 2007, Mickovski et al. 2007). For the pullout of an entire plant root system, resistance can be provided by the three aforementioned resistances as well as additional factors including, bearing resistance of the soil and the force component of the soil-root mass. An attempt to model the pullout of an entire root system was modeled analytical using beam theory for both small and large displacements, where a lateral resistance is provided from the bearing capacity equation and a shearing resistance is provided from a shear spring (Wu et al. 1988). Additional attempts to model the pullout response of a root system consider purely the shearing resistance, and these models range in complexity and input parameters (Ennos 1990, Pollen and Simon 2005, Schwarz et al. 2010).

Experimentally, numerous pullout tests have been performed on individual root axes as well as root systems, particularly those of fibrous and taproot systems. A compilation of select pullout were analyzed, and the various characteristics of the root system architecture, the soil, and soil-root interface and their effect on pullout capacity, or the peak pullout resistance, were extracted from the data set (Table 2-3)

Table 2-3. Compilation of key factors affecting pullout resistance (P = Positive, N = Negative).

System	Parameter	Pullout Resistance Correlation	Reference
Plant	Root Segment Length	P	Anderson et al. 1989; Nilaweera and Nutalaya 1999; Ennos 1989; Ennos 1990; Mickovski et al. 2010
	Total root system length	P	Edmaier et al. 2014
	Root dry weight	P	Bailey et al. 2002; Karrenberg et al. 2003
	Cross-sectional area of root/diameter	P	Anderson et al. 1989; Riestenberg 1994; Dupuy et al. 2005; Norris 2007; Docker and Hubble 2008
	Tortuosity	P	Schwarz et al. 2010; Schwarz et al. 2011
	Strength	P	Mikcovski et al. 2007; Norris 2007
	Stiffness	P	Ennos 1990; Mikcovski et al. 2007; Mikcovski et al. 2010
	Branching angle		Stokes et al. 1996; Dupuy et al. 2005
	Branching nodes	P	Schwarz et al. 2010; Schwarz et al.2011
	Number of branch axes	P	Stokes et al. 1996; Bailey et al. 2002; Schwarz et al. 2010; Schwarz et al. 2011; Dupuy et al. 2005
	Angle of dip/orientation		Wu et al. 1988
	Depth	P	Anderson et al. 1989; Stokes et al. 1996; Nilaweera and Nutalaya 1999; Mickovski et al. 2007
	Lateral root spread	P	Mickovski et al. 2005
	Above-ground height	P	Mickovski et al. 2005
	Above-ground dry mass	P	Bailey et al. 2002
	Topology	Dichotomous, Branching order	Mickovski et al. 2007, Wu et al. 1988, Dupuy et al. 2005
Root-Soil Interface	Interface friction	P	Mickovski et al. 2010; Dupuy et al. 2005; Schwarz et al. 2011
	Shear strength		Ennos 1993; Ennos 2000; Mickovski et al. 2010
	Surface Area	P	Ennos 1993; Ennos 2000; Operstein and Frydman 2000
Soil	Stress condition	P	Mickovski et al. 2010; Dupuy et al. 2005; Schwarz et al. 2011
	Saturation/water content	P	Mickovski et al. 2007; Mickovski et al. 2010; Schwarz et al. 2011
		N	Ennos 1990; Easson et al. 1995; Edmaier et al. 2014
	Shear Strength	--	Ennos 1989
	Cohesion	P	Ennos 1993; Dupuy et al. 2005
	Sediment Size	N	Karrenberg et al. 2003; Edmaier et al. 2014

2.3.6.4 Mechanical Properties of the Soil-Root System

2.3.6.4.1 Tensile Strength and Young's Modulus

Root elastic modulus and tensile strength are known to have inverse power law relationships with root diameter, as shown in Equation 1, where mechanical properties are in units of megapascal and diameter in millimeters (Nilaweera and Nutalaya 1999, Operstein and Frydman 2000, Abernethy and Rutherford 2001, De Baets et al. 2008). In Table 2-4, typical values for fitting coefficients, *a* and *b*, are listed. Both tensile strength and elastic modulus are known to increase with cellulose content and with the ratio of the density of the plant cells to the density of cell walls (Niklas 1992, Genet et al. 2005, Gregory 2006). Initial studies, which demonstrated that the strength of root members increased with decreasing root diameter sparked the initial conclusion that fine roots were both beneficial for resource acquisition and anchorage, however, with pullout studies on mutants without root hairs, root hairs were found to contribute negligibly to the global pullout response (Ennos 1990, Bailey et al. 2002).

$$\sigma_{ult} = ad^{-b}$$
$$E = ad^{-b}$$

(1)

Table 2-4. Root diameter-to-mechanical property power law fitting parameters.

Mechanical Property	a	b
Ultimate tensile strength, σ_{ult} [MPa]	8-60	0.19-1.8
Young's Modulus, E [MPa]	450-1100	0.24-0.6

2.3.6.4.2 Soil-Root Interface Friction

The expected ratio between the soil-root interface friction angle and the soil friction angle is between 0.7 and 0.9, depending on the orientation of the wood grain relative to direction of shearing, wood hardness and roughness, and particle shape (Potyondy 1961, Frost et al. 2002). However, modelling the soil-root interface response by the soil-dry wood interface response is a dubious assumption; many additional factors are present including exudates, root hairs, mycorrhizae growth, sloughing cells, water saturation and suction which could act to augment or diminish the shear strength of the interface.

2.4 Geotechnical Anchorage Systems

The purpose of geotechnical anchorage elements is to stabilize above-ground infrastructure that experiences uplift forces. A variety of embedded structural elements, including anchor plates and piles, soil and rock nails, ground anchors, and geogrids, are designed to provide supplementary stability to larger infrastructure, and these elements enhance infrastructure stability by transferring loads to the subsurface by engaging the shear strength of the soil. A detailed synopsis of the mechanical pullout behavior of select anchorage elements follows.

2.4.1 Anchor Plates

Anchor plates are embedded strip, square, or circular plates constructed of steel or concrete and connected to external infrastructure via steel rods. Numerous analytical (Balla 1961, Matsuo 1967, Meyerhof and Adams 1968, Vesic 1969), experimental (Baker and Konder 1966, Kananyan 1966, Ovesen 1981, Dickin 1988) and numerical (Davie 1973,

Rowe and Davis 1982, Tagaya et al. 1988) research has investigated the pullout response

of these anchorage systems, and the findings are translated to the design of a variety of

other anchorage systems including anchor and helical piles and embedded pipes. The

majority of the research is concerned with the peak pullout resistance (i.e. pullout capacity)

and the displacement at which that pullout capacity occurs. In contrast, investigation into

initial load transfer and pullout stiffness has been marginalized, which is primarily due to

the assumption that the anchor element is rigid. The failure mechanisms involved in the

uplift of anchor plates have been studied in detail, and the two primary type of failure

observed during pullout include: 1) breakout-type failure (i.e. uplift of a volume of soil),

and 2) anchor flow failure (Balla 1961, Vesic et al. 1965, Meyerhof and Adams 1968,

Dickin and Leung 1983, Ilamparuthi and Muthukrishnaiah 1999, Cheuk et al. 2008, Liu et

al. 2012). In particular, the mechanisms are dependent upon the void ratio and depth-to-

width ratio, where breakout failure dominates in denser specimens with lower depth-to-

width ratios, and anchor flow failure is the typical mechanism observed in looser soils with

greater depth-to-width ratios. Furthermore, a critical embedment depth-to-width ratio has

been proposed to depict the transition of the governing mechanism from the uplift of a

volume of soil to the flow and compression of soil and is dependent upon the shear strength

of the soil (Meyerhof and Adams 1968, Vesic 1969). For the case of the uplift of a wedge

of soil, a visible shear band that rapidly evolves into a failure surface is often

distinguishable. The prediction of pullout capacity, which is analyzed in more detail in

Chapter 8, requires an assumption regarding the shape of the failure surface, and various

analytical shapes have been proposed to represent the experimental results, though no

consensus has been reached. Generally, pullout capacity, P_{max}, is equivalent to the sum of

the weight of uplifted soil volume, W_{soil}, and the shear force on the failure surface, F_{shear}, as depicted in Figure 2-4. For the case of soil compression and flow, minimal research into the prediction of pullout capacity has been completed with the notable exception of *Vesic 1969*, who utilizes a cavity expansion approach for deep anchors. Overall, pullout capacity increases with increasing depth-to-width ratio and soil peak friction and dilation angles up until the critical depth-to-width ratio is reached. Studies on secondary effects such as soil-anchor interface friction angle and particle size on pullout capacity have produced conflicting results. Additionally, displacement at pullout capacity is shown to increase with increasing depth-to-width and decreasing relative density; however, the trend appears to reverse after a critical depth-to-width ratio is attained (Dickin 1988, Illamparuthi et al. 2002).
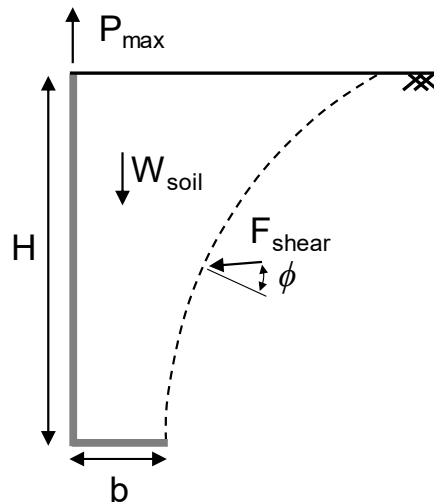
Figure 2-4. Free body diagram of plate anchor uplift (axisymmetric conditions).

2.4.2   Belled Piles

The pullout behavior of belled piles, or enlarged based piles, is similar to that of anchor plates. Belled piles are of particular interest to this project due to the changes in the

pullout response with varying bell angles and base diameters. More so, pullout capacity and pullout factor increase with increasing internal bell angle, when measured from the vertical and for constant base diameter (Dickin and Leung 1990, Dickin and Leung 1992). Additionally, displacement at pullout capacity has been shown to increase with increasing internal bell angle, and the effect is magnified for looser soils (Dickin and Leung 1990, Dickin and Leung 1992).

2.4.3   *Planar Soil Reinforcement*

Soil reinforcement inclusions including geogrids, geotextiles, steel strips, and wire meshes, are planar elements commonly used in soil stabilization applications for slopes, retaining walls, roadway subbases, and foundations. To establish the additional reinforcement these elements contribute to the infrastructure, they have been extensively tested in pullout. The mechanisms involved in the pullout process are dependent upon the shape and mechanical properties of the reinforcements. In particular, for solid, steel strips the primary mechanism is shearing of soil along the reinforcement interface, and as such, the pullout capacity is a function of the confining pressure and soil-structure interface friction angle. For webbed or gridded elements, two additional mechanisms arise in addition to soil shearing along the reinforcement which includes: 1) soil bearing resistance due to the contact of soil particles with the advancing element, and 2) the shearing of soil particles contained within the open sections of the reinforcement with soil immediately above and below the reinforcement. Consequently, pullout capacity is the result of some contribution of each mechanism (Jewell et al. 1985). In addition, an optimal particle size-to-reinforcement aperture exists such that at a certain ratio, particles are trapped in the reinforcement openings and mobilize the full shearing resistance of the soil. For

geotextiles, in particular, pullout capacity is greatly affected by the ability of the soil particles to become embedded in the reinforcement surface. Furthermore, a primary concern, especially critical with polymer-based elements, is the load transfer behavior, where the relative contribution of pullout resistance along the length of the reinforcement element evolves with displacement. The reinforcement-to-soil stiffness ratio is of critical importance to this mechanism, where more extensible elements reach pullout capacity at smaller displacements. (Palmeira and Milligan 1989, Abramento and Whittle 1995, Texeira et al. 2007)

2.4.4   Soil Nails and Ground Anchors

Soil nail and ground anchor elements are utilized in a multitude of geotechnical applications including grade separation systems, tunnels, slope stabilization, dams, towers and infrastructure subjected to buoyancy forces. Both systems are constructed of steel bars or tendons that are usually grouted in place. Primary differences include: 1) ground anchors are longer in length and thus sustain larger loads, and 2) for wall infrastructure, ground anchors have an unbonded length within an assumed failure surface. Soil nails and ground anchors can experience four failure mechanisms: 1) failure of surrounding soil mass in shear, 2) tensile failure of steel rod or tendon, 3) shear failure at the soil-grout interface, and 4) shear failure at the grout-tendon/rod interface. Additionally, just as for planar soil reinforcements, the load transfer mechanism is dependent upon the soil-to-anchor or nail stiffness ratio, and the relative contribution to pullout resistance along the length of the grouted portions varies with pullout displacement in a form of progressive resistance. When the soil nail or anchor is first displaced, the relative contribution to resistance along the element is not uniform; shearing resistance along the soil-grout interface is mobilized

only for a certain length of the element closest to the displacement front. With further displaced, an increasing percentage of the shearing resistance along the length of the element is mobilized, and locations first mobilized enter residual behavior. Pullout capacity is therefore obtained when the shearing resistance along the entire length of the soil-grout interface is mobilized.

2.5   Root System-Inspired Geotechnics

Root-inspired geotechnics refers to the utilization of root system principles in geotechnical engineering and offers a novel approach to conventional geotechnical design through the incorporation of the multifunctional, adaptable, and efficient properties of plant root systems into geotechnical design for the creation of sustainable and resilient infrastructure. One of the first documented examples of root-inspired geotechnics is a *pali radice* structure, or root pile, which are commonly utilized in underpinning and soil and slope stabilization applications. Due to their often reticulated and battered design, *pali radice* stabilization systems mimic the shape of a fibrous root system. Root piles, referred to as micropiles, are relatively small diameter piles (i.e. less than 12" in diameter) that are drilled, structurally reinforced, and grouted-in-place and are versatile due to their ability to act as both compressive and tensile members. Additional examples of plant root-inspired geotechnic applications include, particulate filters inspired by flexible filter walls (e.g. plasma membranes, kidneys, skin, cell walls) (Valdes and Santamarina 2003), root cap-inspired contact sensor for tunneling robot (Lucarotti et al. 2014), root-inspired osmotic actuator for tunneling robot (Mazzolai et al. 2008), and high bearing capacity root-inspired large diameter piles (i.e. 6m) with 3.6m long root branches that are driven horizontally

through templates in the pile wall into surrounding soil with an almost two-fold increase

in bearing capacity (Wang et al. 2014).

CHAPTER 3. X-RAY COMPUTED TOMOGRAPHY FOR BIO-GEOTECHNICS

The purpose of this chapter is to describe the utilization of x-ray CT imaging in geotechnics in general and its potential central role in bio-inspired geotechnics. For benchscale experimental models, field samples, and laboratory specimens, x-ray CT offers unparalleled soil behavior insights by means of the complete visualization of internal processes and structure within geomaterials, and this chapter seeks to support this statement and to provide the relevant information to demonstrate such a role in bio-geotechnics. The fundamentals of x-radiation and x-ray computed tomography are reviewed, and following, the design of an economical x-ray CT scanner is discussed along with some sample tomographic results.

3.1 Fundamentals of X-ray Computed Tomography

X-ray computed tomography (CT) provides a non-destructive means to assess the internal structure of a specimen. The product of CT is an approximate three-dimensional, discrete map of the x-ray absorptive capabilities (i.e. a measure of the attenuation coefficients, which is largely a function of density) of the specimen. A CT dataset is constructed through tomographic reconstruction of a set of radiographs (i.e. two-dimensional images of the attenuated x-ray beam), acquired at various angles around the specimen. Within this section, a complete description of the x-ray CT proves is provided, including a review of the physics of x-rays and the procedure and algorithm required to transform radiographs into a three-dimensional tomographic image.

3.1.1   X-radiation

A review of the physics of x-rays is first provided with a particular focus on the generation of x-rays, their various interactions with matter, and their detection. X-radiation, or x-rays, is a type of electromagnetic radiation that has a wavelength ranging from 0.01 to 10nm. X-rays are composed of photons, the mass-less, charge-less elementary particle of electromagnetic radiation. In general, photons are derived from atoms and act to transfer electromagnetic forces. The energy of a photon is directly proportional to its oscillation frequency through Planck's constant.

3.1.1.1   <u>Generation</u>

X-radiation is produced when photons are released from the electric field of an atom. The two primary forms of x-ray beam generation is, 1) Bremsstrahlung or braking radiation, which is where photons are emitted upon the rapid deceleration of a stream of electrons, and 2) Characteristic radiation, where photons are released upon the movement of an electron from an outer to an inner electron shell. In the laboratory, x-ray beams are generated in vacuum tubes through the following prescribed process: 1) electrons of the cathode electrode filament material are liberated from the outer electron shells of the atoms when a current is applied, heating the filament and causing thermionic emission, 2) a large voltage is applied by the x-ray tube power source between the cathode and anode electrodes causing recently liberated electrons to rapidly accelerate towards the anode while the electrons are focused by an electrostatic lens on a refined spot on the anode target, and 3) electrons are rapidly decelerated when they interact with atoms of the target material producing Bremsstrahlung or characteristic radiation depending on the interaction. Due to

differences in the magnitude of deceleration an electron experiences, a polyenergetic, also termed polychromatic, x-ray beam is created, meaning the beam is comprised of photons of various energies (Figure 3-1). As well, a polyenergetically-produced beam can also be due to fluctuations in the applied voltage as well as the interaction of multiple electrons with a single atom. The efficiency of the production of x-rays by Bremsstrahlung radiation is proportional to the atomic number of the target material and the applied voltage; therefore, anodes are typically made of materials with a large atomic radius and high melting point, such as tungsten or molybdenum. When an x-ray beam is produced in an x-ray tube, a percentage of the beam is produced by characteristic radiation. When an accelerated electron strikes and removes an electron in an inner shell of an atom of the target material, a higher energy electron in the outer shell replaces the released electron and produces a photon of energy equal to that of the difference in electron shell energy levels. The process of x-ray beam generation by Bremsstrahlung radiation is inefficient as most electrons simply interact with the much larger nuclei of the target atoms resulting in heating of the anode target.
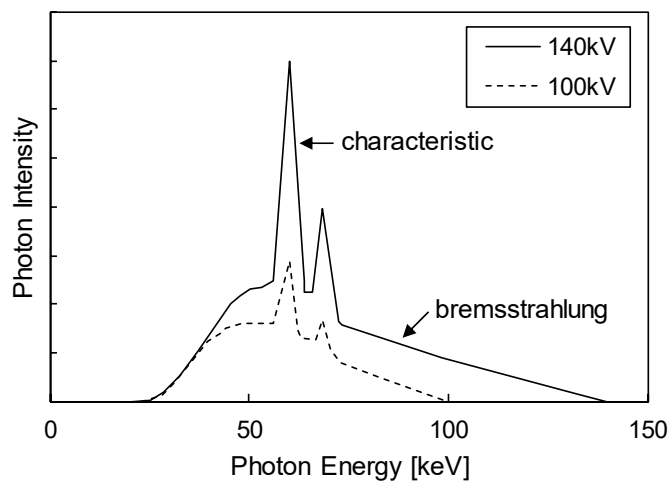
Figure 3-1. Characteristic x-ray spectra produced from an x-ray tube with tungsten anode at operation voltages of 100kV and 140kV.

In industry terms, the generated x-rays can be divided into two categories, hard (x-radiation > 5kV) and soft x-rays (x-radiation < 5kV), which is based on the x-rays ability to penetrate materials. Additionally, an x-ray beam can be generated through synchrotron radiation, where photons are emitted as atoms are accelerated radially; a monochromatic beam can be generated from the main beam via a monochromator due to the relative high intensity of synchrotron emissions.

3.1.1.2 <u>Interactions</u>

X-rays are attenuated as they are advance through any material, and the two main processes describing the interaction between the x-ray photons and the atoms of the material they are passing through are absorption and scattering. The absorption of photon energy after the photon strikes and ejects an electron of lesser energy in an inner orbital electron shell followed by the generation of characteristic radiation due to the replacement by an outer electron is termed the photoelectric interaction. The probability of photoelectric absorption occurring is proportional to the atomic number of the material and inversely proportional to the photon energy which is related to the applied voltage. Scattering of the x-ray beam occurs by two mechanisms, coherent or incoherent scattering. Coherent scattering, also known as Rayleigh, classical, or elastic scattering, is due to photons colliding with electrons of greater energy causing the photon to be reflected in a different direction but of equal energy. Incoherent or Compton scattering, on the other hand, occurs when photons strike electrons of lower energy in outer electron shells, ejecting the electrons as Comptons, and photons proceed on a different path with lower energy. As a result, the probability of Compton scattering occurring is reduced while the possible effect is increased as the applied x-ray tube voltage is increased; however, the effect due to

photoelectric interactions diminishes even more than Compton scattering as the applied x-ray source voltage is increased, which is demonstrated in Figure 3-2. Acknowledging these factors is critical to the success of an x-ray CT scan because scattering will create a noisy image; therefore, it is critical to maximize the photoelectric effect. As well, a percentage of the photons of the x-ray beam pass through the specimen with zero interactions.

Following the Beer-Lambert law for the attenuation of electromagnetic radiation (Equation 2), the original intensity, I_0, of the x-ray beam, which describes the quantity of photons at a particular energy level, attenuates exponentially as a function of the linear attenuation coefficient, μ, of the materials along the photon path. The equation applies for a narrow, monoenergetic beam through a heterogeneous medium.

$$I = I_0 \cdot e^{-\int \mu(s)ds} \tag{2}$$

The half-value layer, which specifies the penetration depth at which half of the intensity has been attenuated for a material, is often provided in industry applications particularly for shielding requirements. The Beer-Lambert is one of the fundamental equations of x-ray tomographic reconstruction, where the inverse problem solves for specimen attenuation coefficients in space.

The total linear attenuation coefficient of a material specifies the percentage of the x-ray beam absorbed and scattered per unit length of material. As shown in Figure 3-2, the behavior of radiated atoms as alluded to previously is non-linear, where the efficiency of the interaction mechanisms (e.g. photoelectric absorption, Compton scattering, Rayleigh scattering) varies with photon energy. Databases, such as NIST XCOM Photon Cross

Section Database, exist that document the attenuation behavior of all elements (Berger et al. 2010). Typically, attenuation values are listed in the form of mass attenuation coefficients, μ/ρ, since μ is dependent upon density. The total attenuation coefficient for a specimen is approximated as the summation of photoelectric absorption and Compton scattering (Equations 3), where Z, is the atomic number, A, the mass number, ρ, material density, and $f(E)$, function to define the energy dependency of the interaction.

$$\mu_{photo} \propto C_1 \frac{Z\rho}{f(E)A}$$

$$\mu_{Compton} \propto C_2 \frac{Z^{3.8}\rho}{f(E)A} \quad (3)$$

$$\mu_{total} = \mu_{photo} + \mu_{Compton}$$

Additionally, the attenuation coefficient for compounds and mixtures of elements is simply determined at the mass average of the elemental components.
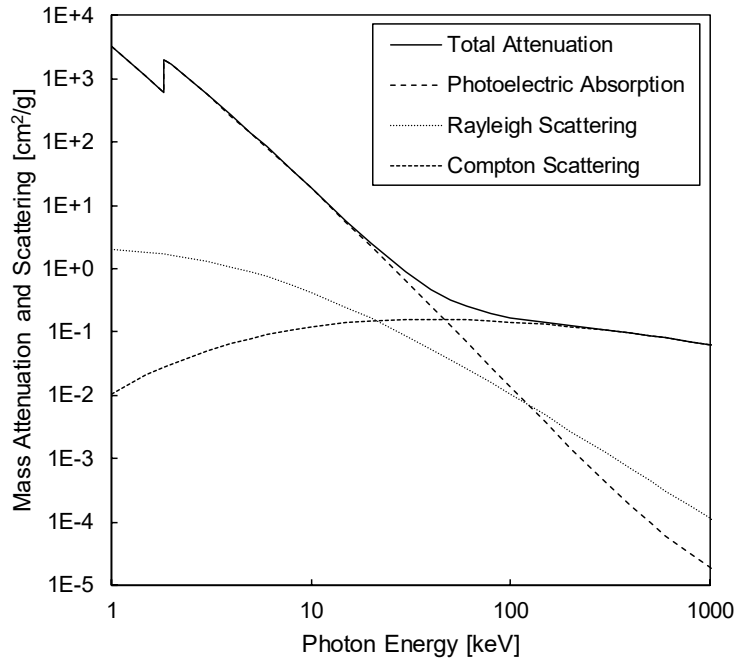
Figure 3-2. The various forms of mass attenuation and scattering that contribute to the total mass attenuation coefficient, μ/ρ, for silica, SiO₂ at various photon energies (NIST XCOM database, Berger et al. 2010).

3.1.1.3   Detection

The detector is the point of exposure in an x-ray CT system. Since the discovery of x-rays, the methods of detection have evolved significantly from photographic film to digital flat panel detectors (FPDs). Detectors produce a measure of the attenuation properties of radiated material through two general methods, 1) indirect detection, where the high frequency x-ray beam is first translated to more accessible electromagnetic radiation frequency (e.g. visible light) via a scintillation material and then the converted information is captured, and 2) direct detection, where photons are converted to electron-hole pairs and then collected at the detector electrodes (Esposito 2017). The reaction of a scintillation material to an incident photons is energy dependent. For a set exposure time, the brightness of the scintillation material is magnified with increasing photon interactions. Currently, in

the case of CT scanning, digital detectors are utilized due to the ease of image acquisition and time-savings. Two types of digital detectors exist, 1) energy integrating, that produces a signal proportional to the total energy of all individual photons that interact with the detector, and 2) photon-counting, that records either the energy of each photon or simply counts the number of incident photons.

3.1.2 Scanner Arrangement

An x-ray CT scanner is comprised of five principal components, 1) an x-ray source, 2) an x-ray detector, 3) a positioning system, 4) radiation shielding, and 5) a control center. The configuration of an x-ray CT scanner is dependent upon the specimen, where for the imaging of geomaterials and other inanimate objects, industrial-type scanners are utilized versus medical ones. For industrial systems, the x-ray source and detectors are stationary while the specimen rotates between the two components, and for medical systems, the x-ray source and detector rotate around a stationary specimen. Additionally the geometry of the scanner is dependent upon the shape of the x-ray beam and the detector. Scanner technology has gradually evolved from a point source and detector to a two-dimensional fan beam and linear detector to a three-dimensional cone beam and two-dimensional planar detectors. Contemporary industrial x-ray scanners utilize a cone beam x-ray source and a two-dimensional flat panel detector. The scanner geometry is dependent upon a plethora of parameters and input specifications and is detailed in the design section of this chapter. For most industrial scanners, the source-to-detector distance is fixed depending on the detector size, cone beam angle, specimen size, and required magnification.

3.1.3 Scanning Procedure

Establishing the proper scanning setup for the tomographic imaging of a specific specimen is an empirical process that requires significant experimentation to achieve the desired result. Some of the numerous scanning parameters to be optimized are displayed in Table 3-1.

Table 3-1. Effect of scanning parameters on output radiograph.

	Scanning Parameter	Effect
Source	voltage	controls range of photon energies, controls contrast
	current	controls photon intensity (i.e. count), ↑current →↑SNR
Detector	frame rate	controls exposure time, ↓ frame rate→↑SNR
	image stacking count	↑image stacking count →↑SNR
Rotary Stage	rotation increment	controls number of acquired projections
Geometry	source-object distance (SOD)	controls magnification

The operating voltage controls the range of photon energies, and the operating current controls the photon count. Selection of the operation voltage is specimen specific, and an optimal contrast between specimen material constituents is achieved when the difference in grey values amongst varying materials remains within a range such that the contrast is discernible yet not exceedingly large as to cause image artifacts. Increased current improves the SNR at the risk of detector over-saturation. For the detector, the two primary scanning parameters include the frame rate, which controls the exposure time, and image stacking count. Lower frame rates act to improve the SNR at the risk of over exposure (i.e. image saturation), and image stacking effectively averages a select number of radiographs.

For accurate tomographic reconstruction, sufficient projections at various increments of rotation must be acquired. As a general guideline, the number of equally

spaced projections, N, is detailed in Equation 4, where D is the width of the detector and d is the pixel pitch (i.e. width of pixel) (Flannery 1987).

$$N = \frac{\pi D}{2d}$$ (4)

Finally, the source-to-object distance is variable depending on the desired magnification. The principal parameters that dictate the source-to-detector distance are the sizes of the typical specimen and of the detector.

3.1.4 Tomographic Reconstruction

Tomographic reconstruction is an algorithm that seeks to find an approximate representation of the internal structure of a specimen from projections around the specimen. If the attenuation capabilities of a specimen in space is known, projections of the object at any angle can be perfectly constructed by applying a transformation operator to the known specimen. However, when only projected radiographs are known, an inverse problem is formulated. Rigorously, the matrix of measured radiographs, r_{ijk}, composed of two-dimensional radiographs indexed by the ith row and j^{th} column at the kth angular increment, is formed by applying a non-linear transformation operator, T, to the attenuation function, f, of the specimen (Equation 5).

$$r_{ijk} = T_{ijk} f$$ (5)

There are three main classes of tomographic reconstruction algorithms: analytical, algebraic, and statistical (Van Eyndhoven and Sijbers 2017), and all algorithms are based

upon two governing theories, namely the Beer-Lambert law for attenuation and the Radon transform for the projective description of an object based upon line integrals through an object at various angular increments. With the Radon transform, an attenuation matrix of a specimen can be decomposed into a sinogram, which is constructed by evaluating the complete specimen projection at various angles through the specimen (Figure 3-3). In computed tomography, the sinogram is constructed from the known projections, and the inverse Radon transform is applied to reconstruct the specimen's attenuation information.
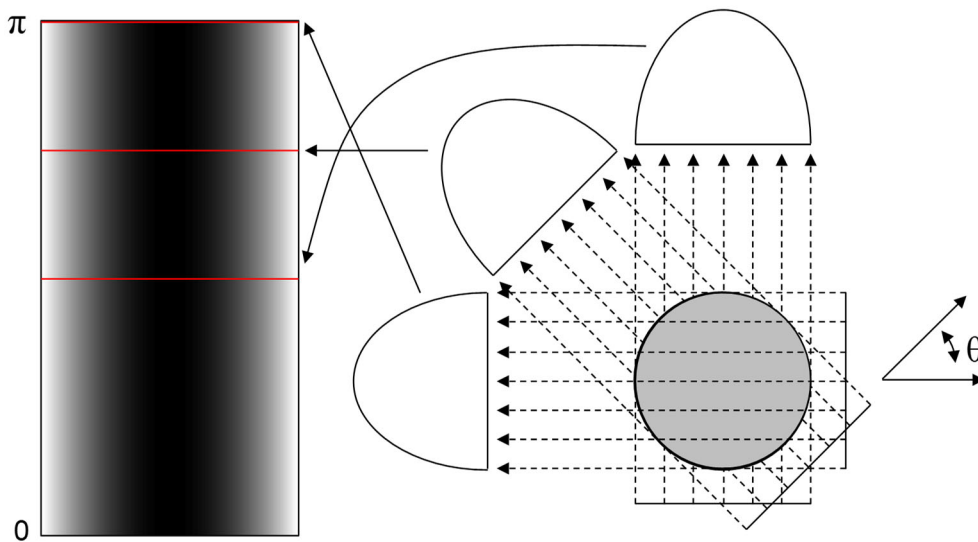
Figure 3-3. Illustration of Radon transform applied to a known circular specimen to produce sinogram (left) at various angles, θ.

The critical distinction for analytical-type reconstruction algorithms is the utilization of the projection-slice theorem, such that the advantages of a frequency-based analysis can be realized. The projection-slice theorem states that the one-dimensional Fourier transformation of a projection at a specific angle is equivalent to a slice at the same angle through the two-dimensional Fourier transformation of the entire specimen. Consequently, the inverse Fourier transform can be applied to the constructed sinogram in

the frequency domain to reconstruct the specimen. However, interpolation is required to create the sinogram in the frequency domain, which leads to poor image quality upon inversion. To mitigate the interpolation error, the Filtered Back Projection (FBP) method, perhaps the most well-known tomographic reconstruction algorithm, was formulated, which applies a high-pass filter to the 1D Fourier transformation of the projection data and then applies the inverse Fourier transform. Algebraic reconstruction algorithms directly project the radiographic projection data onto a discretized map to reconstruct the attenuation information of the specimen. These methods generally reconstruct the specimen through successive iterations in an attempt to optimize each pixel value. Many algebraic methods allow the user to input known specimen information to improve pixel optimization. Statistical reconstruction algorithms utilize the inherent statistical nature of x-ray generation, interactions, and detection to improve upon algebraic methods.

The Radon transform, the basis for all tomographic methods, assumes the emitted x-ray beam is perpendicular to the detector across the entire projection. However for cone beam sources, the beam radiates outwards from the focal spot, and the projection data contains information from rays at various angles to the normal. As such, for cone beam tomographic reconstruction, a coordination transformation is performed on the sinograms of the projection data to reflect a parallel beam geometry, and then a correction factor is applied to account for the divergent beam in the z-direction. As such, an inherent geometric distortion is present in all voxels beyond the central plane. The FDK (Feldkamp, Davis and Kress) method, a type of filtered backprojection algorithm, is the most widely used method for cone beam CT systems (Feldkamp et al. 1984), which was adapted from the two-

dimensional fan beam reconstruction method. For any 3D reconstruction applications, any improvement in the resolution increases the requirement on computer to the power of three.

Critical to reconstruction algorithms are description of the x-ray beam and detector geometries, the actual scanner layout, and the corrective measures to handle the incongruences between algorithmic assumptions and reality. Common to contemporary industrial CT scanners are the utilization of cone beam sources and flat panel detectors

3.2   Design of an X-ray Tomographer

The design of a geotechnics laboratory x-ray tomographer is outlined. The critical design input parameters include the typical size range of the specimen, the specimen material composition including container, and the desired resolution, where as an approximate, specimen features less than four times the image resolution are imperceptible. Given these inputs, an iterative design process is conducted that gradually maximizes the scanner functionality based on numerous specification tradeoff decisions. The selection of the source, detector, and motion control components is first discussed, focusing on the critical design specifications, which is then followed by the geometric layout design of the frame. The extent of the design problem is confined to systems suitable for the development of a reliable, feasible, and economically viable geotechnics scanner; both archaic and overly specific and expensive technologies are not represented.

3.2.1   X-ray Source

The source is comprised of an x-ray tube, which produces the x-ray beam, a generator, which supplies the required electrical energy, and a cooling system, since

approximately 90% of the input energy is converted to heat. Sources are available in variety of options for different imaging requirements; a few options include nano- and microfocus, wide beam, high-power, dual head (two focal spots) and conventional medical sources. The following x-ray source specifications are highlighted, with specific emphasis on the specification tradeoffs and their effect on the final reconstructed image.

3.2.1.1 Voltage and Current

The applied voltage is the difference in electrical potential across the cathode and anode electrodes and is usually given as a range. The x-ray tube current dictates the amount of electrons that flow between the electrode over time, and the power applied is the product of the voltage and current. For geomaterials specimens less than 10cm in diameter, a source with a maximum operating voltage of 100kV is sufficient, unless the specimen is contained in a high density chamber, such as steel. To determine the required maximum voltage for a specified geomaterial specimen, a simple calculation utilizing the Beer-Lambert law can be performed after the original equation (Equation 2) is rearranged in terms of the diameter of the specimen, D (Equation 6). Given a water saturated silica sand specimen with a void ratio equal to 1, the mass attenuation coefficient, μ/ρ, for the specimen is 0.169cm^2 g^{-1} at 100keV (obtained from the NIST XCOM database). For a transmittance, T, of 0.1, a specimen diameter of 7.5cm is penetrable ($\rho_{sat} = 1.825$g cm^{-3}).

$$D = -\ln(T)\frac{\rho}{\mu}\frac{1}{\rho} \qquad (6)$$

An inherent tradeoff in voltage selection during scanning consists of the balance between image contrast and signal-to-noise ratio, where lower voltages allow for larger

differences in attenuation coefficients and therefore greater contrast, yet, SNR decreases with significant beam attenuation. Additionally, scattering, which degrades image quality, contributes more significantly to beam attenuation for larger input voltages. The SNR due solely to photon material interactions is directly proportional to the square root of the number of photons; as such, increased current acts to improve image quality.

3.2.1.2 Focal Spot Size

The focal size is the width of the area from which the radiating x-ray photons originate, and it limits the obtainable image resolution due to blurring, which is discussed further in Section 3.2.4. An inherent compromise controlled within the source between the focal spot and the applied power exists such that for a certain input power, the focal spot size must be managed to prevent permanent damage by heating; as such, the focal spot size and minimum achievable resolution increases with applied voltage.

3.2.1.3 Beam and Beam Angle

The beam and beam angle, β, refer to the geometries of the emitted beam, where the two most common types, fan and cone beams, can be described as a planar, triangular beam and a three-dimensional, conical beam, respectively. The angle of the beam is measured internally. Both are controlled by the dimensions of the source window which attenuates most photons that do not pass directly through the window opening. For x-ray source selection, beam angle should completely radiate the detector area, such that the inequality (Equation 7) is satisfied, where D is the width of the detector and SDD is the source-to-detector distance (Figure 3-4).

58

$$\beta \geq 2\tan^{-1}\left(\frac{D}{SDD}\right) \tag{7}$$

3.2.1.4 Intensity Spectrum

When operating a polychromatic source, the input voltage accounts for only a small percentage of the beam's intensity and defines the upper energy limit of the x-ray spectra. The beam hardening artifact is the resultant of a polychromatic source, and all economical solutions will be of the polychromatic variety.

3.2.1.5 Minimum Source-to-Object Distance

The minimum source-to-object distance is the length between the focal spot position and the outer edge of the x-ray source housing. This distance restricts the maximum geometric magnification of the specimen.

3.2.1.6 Leakage Radiation

The leakage radiation is solely due to the radiation from the source at maximum power measured behind or to the side of the source at maximum power and does not include any effects from the primary beam; most manufactured x-ray sources have some form of internal shielding.

3.2.1.7 Lifespan

The lifespan of the source must also be considered for an economic and sustainable solution. Factors decreasing the life of a source include both environmental conditions

(high humidity, dust) and usage factors (regular operation at maximum voltages, repeatedly turning on and off, disregarding warm-ups).

3.2.2 Detector

All information within this section is related to digital radiography (DR) detectors as opposed to film and computed radiography detectors (i.e. x-ray film cassettes) due to the many advantages of DR detectors including automated and immediate image acquisition as well as greater dynamic range, spatial resolution, and detector efficiency. Digital detectors include both image intensifier (II) detectors and flat panel detectors (FPD), and as a general comparison, FPDs are more stable, have a greater dynamic range, and induce no image distortions, yet are more expensive and provide a lower spatial resolution. Image intensifiers effectively amplify the brightness of a radiograph through the following process: 1) x-ray photons are converted to visible light with a phosphor layer, typically cesium iodide, 2) the visible light photons are transformed into electrons via a photocathode, 3) an electron optic system focuses and multiplies the electrons onto a phosphor at the back of the image intensifier unit, and 4) a charge-coupled device (CCD) or complementary metal oxide semiconductor (CMOS) camera is responsible for acquiring the image of the output phosphor. Flat panel detectors include both direct and indirect varieties, though the indirect kind are most common. In the indirect method, photons are converted to visible light photons after interacting with a scintillation layer, and subsequently, the light is converted to an electric charge via a photodiode. In the direct method, x-ray photons are directly converted into an electric charge with photoconductive material, commonly selenium, through the photoelectric effect. For both types of FPDs, the electric charge is collected, amplified, and sent to the analog-to-digital converter by the

detector sensors (i.e. thin-film transistors (TFTs), CMOSs, or CCDs). Indirect FPDs produce an energy-integrated image, where the pixel values are directly proportional to the cumulative energy of the incident photons. Direct FPDs can produce both energy-integrated and photon-counting images and typically generate higher resolution images due to the elimination of the blurring in light conversion process. The utilization of photon counting detectors in CT imaging is an active area of research and is not widely available currently. Preliminary studies suggest that significant improvements in both SNR and spatial resolution can be achieved and that beam hardening artifacts can be eliminated (Yu et al. 2016, Willemink et al. 2018).

3.2.2.1 Detector Area, Pixel Number and Pitch

The responsive area of a digital detector is digitized by a matrix of individual sensors, which correspond to pixels of the image. The length of each sensor is termed the pixel pitch. Most flat panel detectors are formed by a square matrix of a binary number of sensors, typically in the range from 2^9 to 2^{12}. Combined together, these factors control the majority of the image spatial resolution.

3.2.2.2 Frame Rate

The frame rate of a detector is analogous to the shutter speed of a camera. At higher frame rates, the detector sensors are exposed to x-ray radiation for shorter periods, and consequently, the magnitude of the signal and the SNR for a single image is reduced, producing a lower quality image, which can be partially abated by stacking multiple projections at one position. For fluoroscopic imaging, though, a high frame rate is critical for capturing fast processes.

3.2.2.3 Scintillation and Photoconductive Materials

Detectors employ a variety of scintillating and photoconductive materials. Some common scintillating materials include cesium iodide (CsI), sodium iodide (NaI), Gadolinium oxysulfide (Gd2O2S), and zinc cadmium sulfide (ZnCdS). These materials are usually graded based upon their conversion efficiency, luminescent decay time, response linearity with dose and intensity, spatial resolution, x-ray stopping power (Nikl 2006). Amorphous selenium (a-Se) is the dominant photoconductive material in the market due to its development for photocopiers and is largely responsible for the detectors overall sensitivity and the detective quantum efficiency (Kabir et al. 2007). To protect the lifespan of the scintillation material, it is common practice is to place a highly attenuating material (e.g. lead) directly in front of the source window to shield the detector during the warm-up process of an x-ray source. An apparent tradeoff governing frame rate selection exists such that a slower frame rate allows for a higher SNR; however, the rapidity by which the scintillation material refreshes decreases with increased exposure time, causing a reduction in the temporal resolution due to blurring.

3.2.2.4 Analog-to-Digital Conversion

The A/D converter is either incorporated directly into the detector sensors or is placed just afterwards and is responsible for digitizing the continuous charge into a discretized signal. The compartmentalization of the charge is dependent on the bit size of the converter, which is always in binary form. Therefore, higher bit converters provide a more accurate representation of the real charge signal.

3.2.2.5 Energy Range

All detectors manufacturers provided a certain x-ray energy range over which a detector can effectively produce an accurate signal. Emitted x-rays with energies below this range are undetectable, while those above this range can permanently damage the detector.

3.2.2.6 Comparison standards

A number of performance standards are used to compare detectors based upon contrast, spatial resolution, and energy response (Table 3-2).

Table 3-2. Performance standards for detector comparison.

Standard	Acronym	Description
Point/Line spread function	PSF/LSF	Ability of detector to transfer the contrast of a point/line to screen at different spatial frequencies; common unit: lp mm^{-1}
Modulation transfer function	MTF	Ability of detector to transfer contrast from object to screen at different spatial frequencies; common unit: lp mm^{-1}
Signal-to-noise ratio	SNR	The ratio between signal intensity and background noise
Noise power spectrum	NPS	The intensity of the noise at different spatial frequencies
Detective quantum efficiency	DQE	Efficiency of detector to convert x-ray radiation to signal; combination of MTF, SNR, and NPS
Contrast-to-noise ratio	CNR	The ratio between the difference in signal intensity between two different regions and background noise
Dynamic Range	DR/DNR	The ratio between the largest and smallest dose the detector can send as a signal

3.2.2.7 Resolution

Just as for the x-ray source, numerous inherent and causal tradeoffs exist due to the design of the detector and the selection of detector scanning parameters. The detector acts as the ultimate determinate of image resolution. The finest possible resolution of the

radiograph is defined as the diameter of the specimen over the width of the detector in terms of the number of pixels. Further deterioration of the image resolution is inexorable. The detector limits the projected image resolution in all steps of the conversion of the x-ray photons to the resultant image, including scattering at the scintillation or photoconductive material, blurring during x-radiation to visible light conversion, and sampling, gain and aliasing errors in the A/D conversion.

3.2.3 Specimen Positioning System

The precise geometric positioning of the specimen during scanning is mandatory for generating high quality reconstructed images. The required precision of the manipulators is dependent upon the size of the specimen, the detector area and pixel pitch, and the desired resolution. Unspecified movement of the object during scanning as well as imprecise angular positioning results in image blurring. The complete motion control system is comprised of a rotary stage for angular movements and linear actuators for positioning in the x, y, and z directions. The specifications of the angular controller are the most critical for an industrial x-ray CT scanner, where primary specifications include the resolution, accuracy, repeatability, range, and maximum weight capacity. As a first order approximate to the required angular specification of the rotary stage, the minimum of the specified rotation resolution, repeatability, and accuracy, α, is a function of the pixel pitch, p, detector width, D, and pixel error threshold (i.e. the fraction of specimen projected outside of the detector pixel), ε (Equation 8). For a pixel pitch of 0.127mm, detector width of 130mm, and a pixel error threshold of 10% of a pixel, the rotary stage should have an accuracy, repeatability, and resolution less than 0.01°.

$$\alpha \le 2\sin^{-1}\left(\frac{p\varepsilon}{D}\right) \tag{8}$$

While three-dimensional control of the specimen within the scanner is not mandatory, it aides in acquisition time due to trail-and-error specimen positioning.

3.2.4   Scanner Geometric Layout

The source-detector distance, SDD, plus the width of the detector and source dictates the total length of the system. The focal spot size, FS, and the source-object distance, SOD, in conjunction with the SDD determines the geometric magnification and distortion of the object. A simple schematic of a CT scanning system with the controlling distances is shown in Figure 3-4.
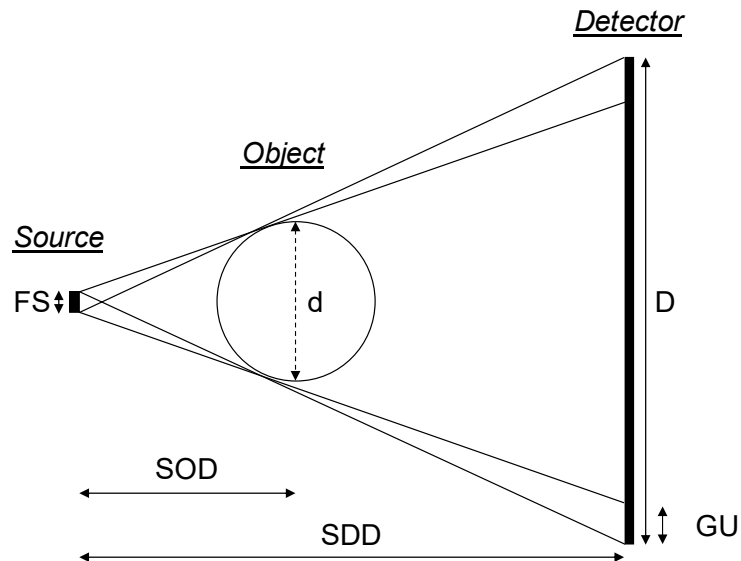
Figure 3-4. Plan view schematic of geotechnics laboratory CT scanner geometry.

The geometric magnification refers to the projected augmentation of an object on to detector area and is determined as the ratio of SDD to SOD. The geometric unsharpness,

GU, restricts the resolution of final image due to blurring and is formulated as the projection of FS on to the detector plane (Equation 9). When the unsharpness is backprojected on to the specimen, the resolution limit, RL, is defined (Equation 10).

$$GU = FS \cdot \left(\frac{SDD - SOD}{SOD} \right) \qquad (9)$$

$$RL = FS \cdot \left(\frac{SDD - SOD}{SDD} \right) \qquad (10)$$

An inherent tradeoff to the layout of the CT scanner components is the optimal specimen magnification, such that an increase in magnification will also increase the geometric unsharpness. Selection of the SDD is dependent upon the width of the detector, specimen size, and desired specimen resolution.

3.2.5 Control Center

A computer is required for the control of the individual components of the scanner (i.e. the source, detector, and positioning system) as well as image acquisition. Proprietary or open-source software is available to link the various components together, such as iRad, LabView, and PyLab_Works. Control computers often serve as the host for the tomographic reconstruction software. As such, computer demands can include additional network cards, large memory (≥32GB) and hard drive (multiple TBs), and GPU or CPU requirements (dependent upon reconstruction, visualization, and image processing software).

3.2.6 Safety Requirements

We are exposed to radiation every moment of our lives (e.g. medical x-ray imaging, air travel, watching TV, consuming food, cosmic radiation), and to sustain a healthy life, it is critical to limit the radiation we are exposed to. The Federal Nuclear Regulatory Commission mandates all radiation workers to maintain below a total effective dose equivalent of 5rems per year, where the average person receives 0.35rems per year (US NRC 2017).

Numerous safety requirements are enacted at the federal, state, and institution levels to ensure the safety of x-ray operators. Conventional industrial x-ray CT scanners are required to be placed in a lead shielded cabinet or room, where the lead thickness is determined based upon maximum source voltage, operation time, location of personnel relative to scanner location, and presence of additional attenuating structures (e.g. concrete columns, steel beams). Regular inspections via Geiger counter or ionization chamber are generally required to ensure the radiation dosage at maximum operating voltage is below the institute requirement. Areas in the direct line of the x-ray beam as well as openings in the shielding including doors and baffles are particularly vulnerable to leakage. . If determined that the radiation dosage at peak operational voltages is greater than background radiation, a dosimeter badge is to be worn by the operator and checked quarterly for received radiation. The door to the cabinet or room is to be equipped with a dual interlock switch, such that operation of source is dependent upon a closed switch. An emergency switch is to be mounted on the outside of the shielding in case of an emergency. The operation of the x-ray CT scanner should be well documented; an operational log book and standard operating and emergency procedures should be readily accessible. Signage in

conjunction with an x-ray in use light are to be obvious to alert bystanders that a radiation source is in the area and if it is in operation

3.3 Design Example: Laboratory Scanner

As part of the research studies presented in this thesis, a laboratory scanner was designed specifically for the imaging of a partially saturated clay specimen within an aluminum chamber (40mm diameter, 3.5mm thick wall) with the ability to scan geomaterial specimens up to 100mm in diameter (Figure 3-5). The desired resolution of the imaged clay specimen was approximately 75-100μm.
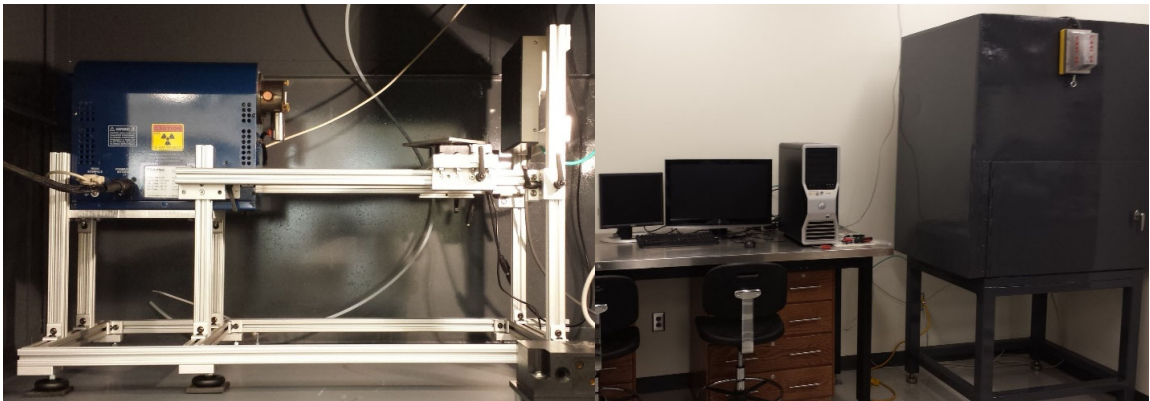
Figure 3-5. Image of x-ray CT frame, source, rotation stage, and detector (left) and image of control center and lead shielded cabinet (right).

Given the aforementioned input parameters, the laboratory x-ray CT scanner was designed, while constrained by a monetary budget of $100,000, a value approximately 1/5 to 1/10 of a commercial scanner. The complete list of specifications by scanner component is listed in Table 3-3. Specimen contrast for the relevant imaged materials is optimized at lower energy levels as illustrated in Figure 3-6. For a saturated kaolinite sample with an approximate void ratio of 1, a transmittance of 5% and 30% is achievable with an incident beam energy of 40keV and 100keV, respectively, for the specified specimen. As such, a

microfocus, cone beam source with a maximum operating voltage of 130kV was selected

to minimize penumbra effects while providing sufficient power.

Table 3-3. Specifications of the laboratory x-ray CT scanner by component.

System Component	Specification	Item
Source	Model	ThermoFisher PXS10
	Type	microfocus, cone beam, polychromatic
	Operating Voltage	20-130kV
	Maximum Power	16W
	Focal spot size	6μm at 4W, 21μm at 16W
	Cone beam angle	53°
Detector	Model	Varian PaxScan 1313
	Type	indirect, flat panel detector
	Area	130mm x 130mm 1024x1024pixels
	Pixel Pitch	127μm
	Maximum frame rate	10fps at 1x1 binning
	Energy range	40-160 kV
	Scintillator Material	DRZ-plus scintillator (trademark of Mitsubishi Chemical Corporation)
	Limiting resolution	4lp mm^{-1}
	A/D Conversion	14-bit
Rotary Control	Model	Zaber T-RS60
	Diameter	60mm
	Maximum Capacity	45kg
	Resolution	0.00023°
	Accuracy	0.05°
	Repeatability	0.02°
X,Y, Z positioning	Type	manual, linear rail system
Frame	Material	1" T-slotted aluminum
	SDD	400mm
	SOD range	20-400mm, specimen size dependent
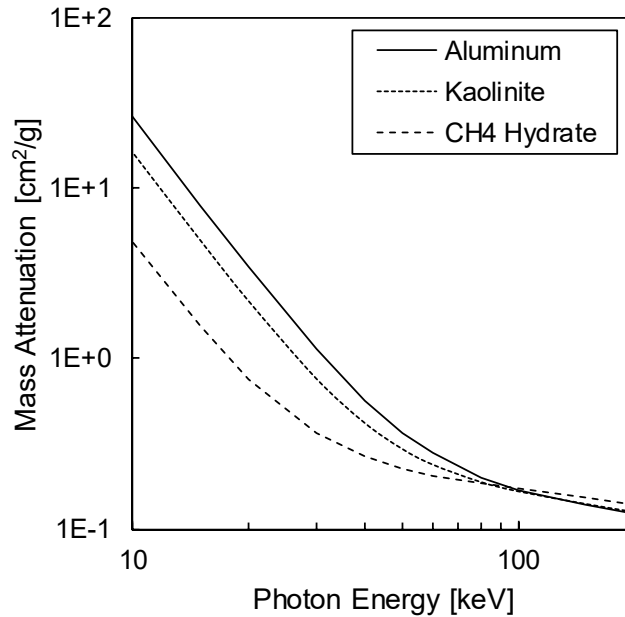
Figure 3-6. Mass attenuation coefficients relevant to the imaging of a hydrate-bearing clay specimen in an aluminum chamber.

Due to the typical specimen size, imaging requirements, and budgetary concerns, a petite flat panel detector (130mm wide) was selected, with an energy range compatible with the x-ray source. For a full specimen scan, the maximum possible resolution is approximately 40μm (geometric magnification of 3.25x), while 100μm resolution was achievable. For the rotary stage, the standard of the system were relaxed (i.e. the allowable pixel accuracy was broadened to 50% from 10%) due to ease of implementation into the controlling software, iRad. Substantial cost reduction was achieved through elimination of an xyz-positioning system. The source-detector distance was selected based upon the size constraints of a donated lead shielded cabinet (rated for a 250kV source) and the size of the specimen relative to the detector. The total price of the self-assembled scanner was approximately $80,000.

3.3.1   Sample Reconstructed Images

Select scans are presented as evidence of the imaging capabilities of the designed

x-ray laboratory tomographer (Figure 3-7-Figure 3-9).
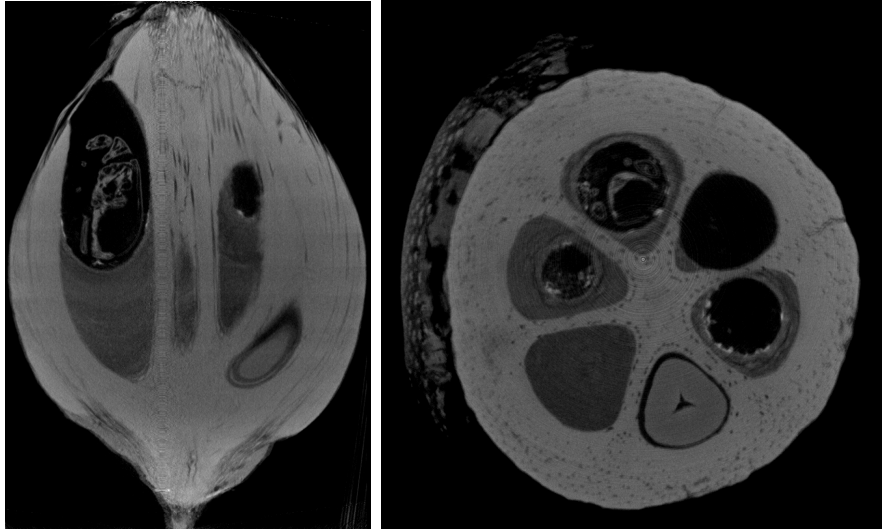
Figure 3-7. Vertical (left) and horizontal (right) slices through a scan of a full Brazil nut fruit with deceased burrowed beetle.
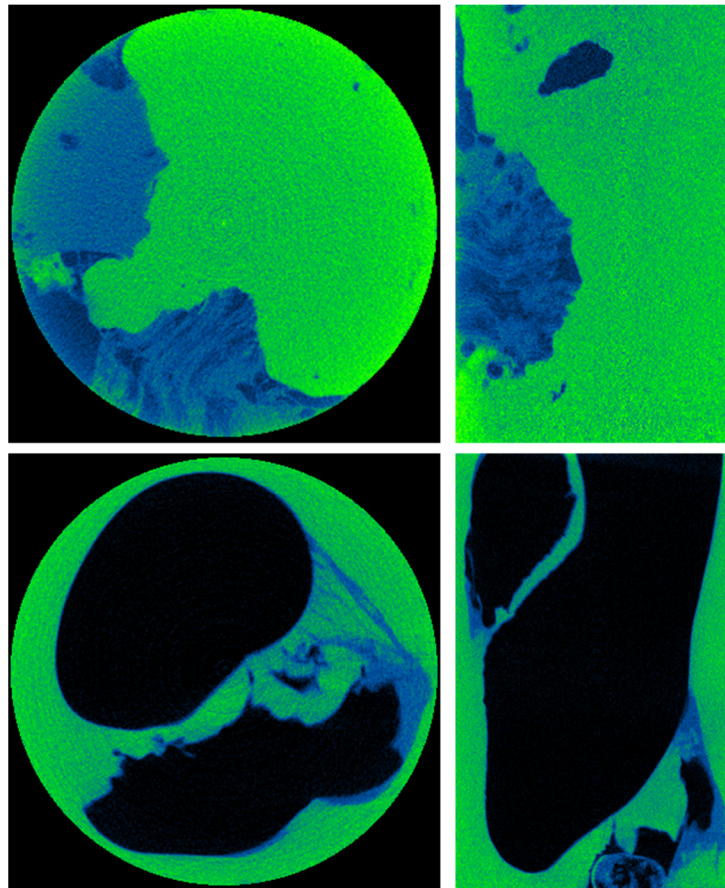
Figure 3-8. Evidence of CO₂ hydrate formation in a partially saturated kaolinite specimen utilizing two unique formation procedures (top and bottom).
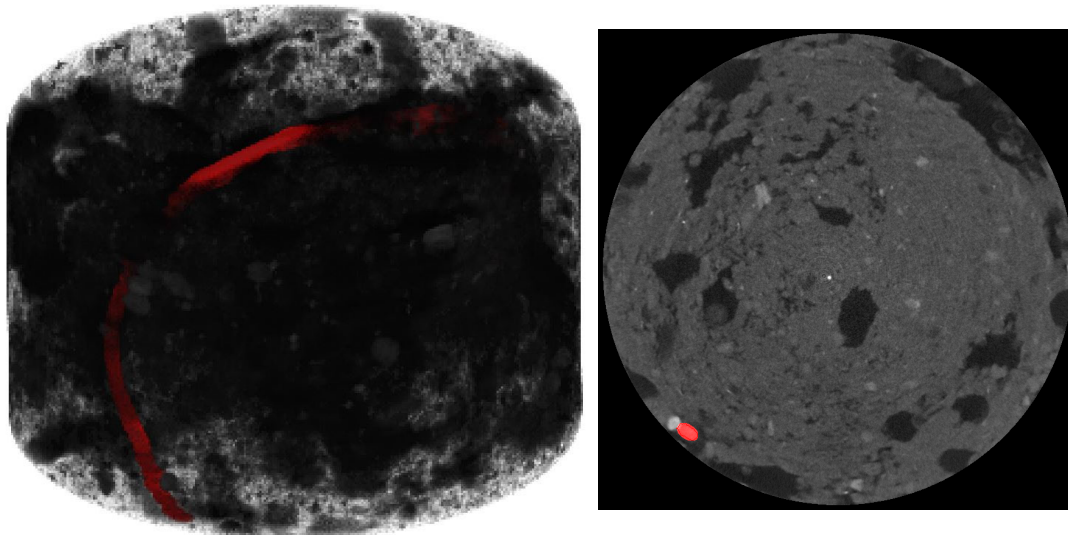
Figure 3-9. Images of earthworm tunneling through soil sample, full volume (left) and horizontal slice (right).

3.4 Geometric Correction

Cone beam reconstruction algorithms are based upon a scanner geometry with prescribed constraints, such that x-ray source focal spot is in-line with center of the detector, that the cone beam is normal to the detector plane, and that the rotation axis of the specimen is perpendicular to the axis between the source and detector center and parallel to the vertical orientation of the detector, as illustrated in Figure 3-10. Before reconstruction, the projections must be corrected based upon the actual scanner geometry to minimize image artifacts. Geometric misalignments are backcalculated from angular projections of a constructed x-ray phantom (Noo et al. 2000, Andò 2013, Ferrucci et al. 2015).
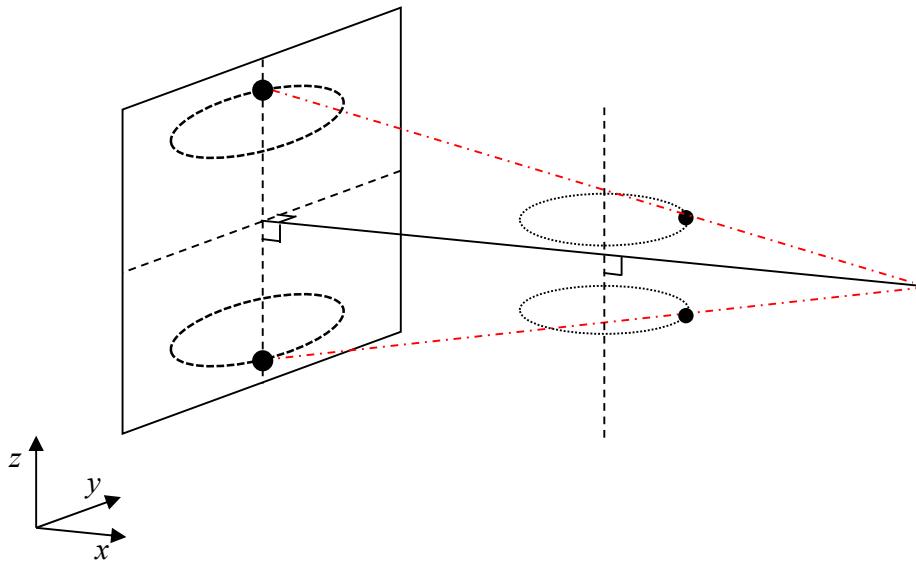
Figure 3-10. Schematic representation of the prescribed geometric constraints as well as illustration of the ellipsoidal trajectories of the geometric correction phantom.

The geometric correction algorithm identifies the source-detector distance, source-object distance, unit normal vector of the detector, the horizontal and vertical offset of the

focal spot alignment from the center of the detector and tilt of the rotation axis of the specimen. All parameters are determined from the cumulative projections of an x-ray phantom. The phantom is fabricated by mounting steel balls at a known separation distance around a cylindrical object, in this case a 1.5" diameter Delrin rod. Projections of the phantom are obtained with the same scanner geometry as for the imaged specimen. The process of obtaining the elliptical orbits of the high-density spheres by overlaying consecutive angular projections of the geometric correction phantom is illustrated in Figure 3-11.
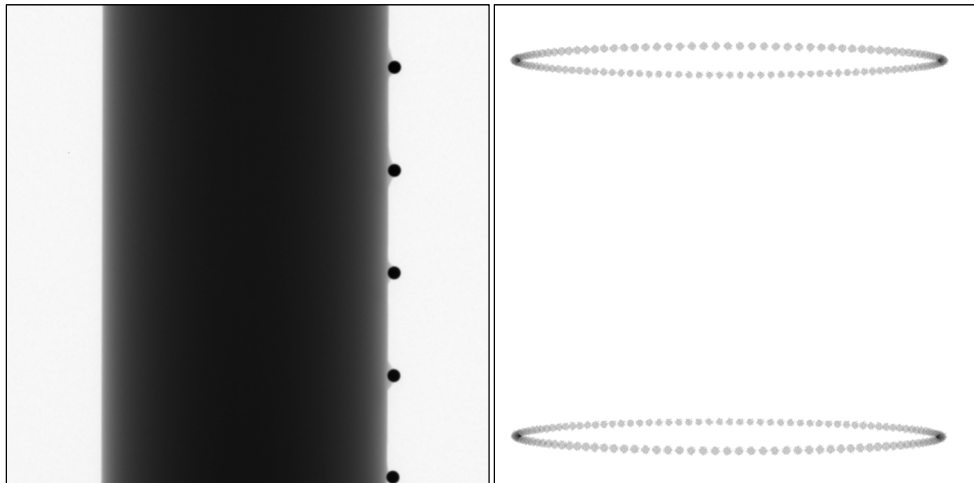
Figure 3-11. Sample radiograph of geometric correction phantom (left), and cumulative, extracted ellipsoidal trajectories of select spheres (right).

The entire algorithm is based upon the elliptical trajectories of the high-density spheres. The first obtained parameter is the rotation axis of the specimen, which is determined by finding the tilt between the centers of the top and bottom elliptical paths. All subsequent coordinates are then corrected by this tilt angle. Following, a least squares analysis is performed to fit an ellipse to the orbits of the spheres. The equation to describe the ellipse is described by a 4th order polynomial. With an analytical description of the trajectories,

the source-detector distance, the detector unit normal vector, and the offset is determined. Finally, the source object distance (SOD) is iteratively determined given the distance between the top and bottom spheres.

3.5 Image Processing

Image processing broadly refers to the manipulation of an image or set of images. This section provides select commercial and open-source software necessary to reconstruct, analyze, and present the tomographic images.

3.5.1 Reconstruction and Visualization

Numerous commercial and open-source software is available to perform tomographic reconstruction depending on the x-ray CT scanner layout. Viable open-source reconstruction software includes OSCaR, Reconstruction ToolKit, GSECARS, TIGRE and ASTRA. Some common issues or limitations in open-source reconstruction software include large computer memory demands, compiling requirements, inefficient algorithm implementation, software bugs, and no inclusion of beam hardening and geometric artifact corrections. Additionally, for visualization of reconstructed three-dimensional images sets, open-source software is available, including Image J/Fiji (developed at NIH), VTK, Open DX, Blob3D, and 3D Slicer.

3.5.2 Image Artifacts and Corrections

Reconstructed x-ray CT data sets are prone to a variety of image artifacts that deteriorate the image quality and are problematic for further qualitative and quantitative analyses. A variety of corrections can be applied to mitigate these errors. Artifacts are the

fictitious manifestations of the imprecision of the x-ray CT scanner and tomographic reconstruction algorithm and are inherent to all x-ray CT image sets. Consequently, the presence of image artifacts and the applied artifact corrective treatments to an image set should be acknowledged when the image sets are used in subsequent analyses.

3.5.2.1   Beam Hardening

Beam hardening arises due to the mismatch between radiographs produced with a polychromatic x-ray beam and the assumption within the tomographic reconstruction algorithm that the beam is of a single energy. Beam hardening manifests itself within the reconstructed images through two primary means, 1) cupping artifact, where image values artificially diminish in the interior of a specimen, 2) streaking artifact, where erroneous linear streaks appear in the image at originating from objects with high contrast. Overall, beam hardening is the due to the hardening of the polychromatic beam, which means that an upwards shift occurs in the average beam energy due to a reduction in intensity of the lower energetic portion, and this phenomenon occurs because the lower energetic portion of the beam is attenuated more readily. Consequently, the cupping artifact arises because the beam is hardened to a greater extent when the trajectory is through the middle of the specimen versus the sides, and thus, the interior of the specimen appears to attenuate the beam to a lesser degree causing the reconstructed image values to be less. Similarly, the streaking artifact occurs when x-ray trajectories pass through materials that harden the beam significantly, and thus creates the appearance that material in the vicinity of the highly hardening material, is less attenuating than reality. Additionally, steaking also arises due to photon starvation (i.e. complete attenuation of a beam ray), and the severity is magnified with undersampling and scatter.

For a purely monochromatic x-ray beam, no beam hardening occurs. For a polyenergetic beam, one method for diminishing the effects of beam hardening is to place a physical filter directly in front of the x-ray beam before the specimen to harden the beam before it intercepts the specimen. Additionally, several types of beam hardening correction algorithms exist to minimize beam hardening artifacts either before, during, or after reconstruction (Sources).

3.5.2.2 Ring Artifact

Ring artifact is the appearance of concentric rings around the rotation axis of the image and is due solely to acquisition method of flat panel detectors. Flat panel detectors are fabricated with row arrays of individual detectors, and during analog-to-digital conversion, minute variations in the gain of the analog signal per row array cause certain rows of the radiographs to have artificially low or high values. After reconstruction, the lines in radiographs appear as cylindrical shells in the 3D image space. Furthermore, variations in the photon response of individual detectors are also present.

The most robust method to suppress ring artifact is to normalize the radiographs with dark field (i.e. image acquired with the source deactivated, the baseline image) and bright field (i.e. radiograph obtained with x-ray source voltage set to scanning voltage) field images (Equation 11). A median filter can be applied to reduce unabated rings in the reconstructed image.

$$\mathrm{Im}_{corr} = \frac{\mathrm{Im}_{orig} - \mathrm{Dark}}{\mathrm{Bright} - \mathrm{Dark}} \tag{11}$$

3.5.2.3   Image Blurring

Inadequate spatial or contrast resolution results in the appearance of blurring. Some of the many causes of blurring include specimen movement, partial volume artifact, and scattering. Partial volume artifact arises when materials of varying attenuation capabilities are captured with the same discrete detector, and the resultant pixel is an average of the materials radiated. Additionally, blurring due to scattering increases in prominence with applied voltage as can be concluded from Figure 3-2.

3.5.3   Image Analysis of Reconstructed Images

Often, a quantitative analysis is performed on the reconstructed image data. Commonly applied image processing algorithms include geometric transformations (e.g. scale, rotation, shear, binning), standard mathematical operations (e.g. subtraction, division, multiplication), filtering (e.g. median, lowpass/highpass frequency, Gaussian smoothing, Laplacian), segmentation (e.g. thresholding, clustering, edge detection), binary processing (e.g. mask formation, dilation, distance maps, skeletonization), and feature detection (e.g. matching, tracking).

3.6   X-ray Tomography in Geotechnics

X-ray technology began to be applied to the study of soils and rocks in the 1960s with the imaging of marine sediments and rock cores (Calvert and Veevers 1962; Hamblin 1962; Bouma 1964, Baker and Friedman 1969). Initially, the scanning of geologic materials was stimulated from purely visualization motives but gradually progressed into more quantitative. Some significant areas of x-ray application in geotechnics include model tests,

strength-related behaviors, particle shape and structure, pore structure, and fluid flow. Some of the initial model tests were performed to investigate earth pressure behind a rotating retaining wall structure, where radiographs at subsequent increments of wall rotation were captured and the relative displacement of embedded lead shot was analyzed (Arthur et al. 1964, Bransby 1968, Roscoe 1970). Other examples of model tests performed with x-ray include foundation bearing capacity (Morita et al. 2007), soil-pile interaction (Otani et al. 2006, Doreau-Malioche et al. 2018), and geogrid pullout (Ochiai et al. 1996). As well, significant progress has been made in the association of macro-to-micro soil behavior (e.g. global stress-strain behavior to local particle kinematics and forces) at four main laboratories, Laboratoire 3SR at Universite Grenoble Alpes, Alshibli's Group at University of Tennessee Kentucky, X-Earth Center at Kumamoto University, and the LINXS group at Lund University. With small scale biaxial and triaxial testing of geomaterials, significant insight into strain localization and particle-level behavior during shear has been analyzed through particle tracking, void ratio and strain field maps, particle forces, and particle crushing (Alshibli and Sture 2000, Otani et al. 2000, Viggiani et al. 2004, Wang et al. 2004, Lenoir et al. 2007, Hall et al. 2010, Andrade et al. 2011, Hall et al. 2011, Andò et al. 2012, Watanabe et al. 2012, Takano et al. 2015, Kawamoto et al. 2016, Imseeh et al. 2018). Additionally, significant development in the relationship between pore and fracture structure and fluid flow has been investigated (Cassel et al. 1990, Wildenschild et al. 2002, Sugawara et al. 2004, Brusseau et al. 2006, Zhu et al. 2007, Alajmi and Grader 2009, Kumar et al. 2010, Watanabe et al. 2011, Peng et al. 2012).

3.7 X-ray in Bio-Geotechnics

The exploration of bio-mediated and bio-inspired processes in geomaterials is in its nascent stages; yet, significant advances in bio-geotechnics have already been achieved through the explorative power of x-ray CT imaging and associated analyses. Some initial investigations include the local deformation analysis of a MICP-treated sand specimen (Tagliaferri et al. 2011), the visualization of the formation of fire ant tunnels and its accompanying mechanics investigation (Monaenkova et al. 2015), the pullout behavior of plant root-inspired anchors (Mallett et al. 2018), and more recently, the particle kinematics during plant root growth (Anselmucci et al. 2019).

3.8 Conclusions

- For geotechnical applications, x-ray CT provides an approximate density map of the soil specimen, and when a CT scan is performed during a prescribed process (e.g. mechanical loading, controlled displacement, fluid flow), even greater insight into internal soil behavior can be revealed.

- The design of an x-ray CT scanner requires an optimized tradeoff analysis based upon a few input parameters: (standard) specimen diameter, desired resolution, and price.

- A cost-effective geotechnics laboratory scanner can be fabricated in-house at the fraction of the cost of an industrial scanner.

- Image artifacts are inevitable and are due imperfections in the tomographic reconstruction algorithm and the scanner components and geometry; when performing quantitative analyses of reconstructed image sets, the image artifact

mitigation method should be stated, since the processing inevitable effects the results of the analysis.

3.9   Acknowledgements

CHAPTER 4. MATERIALS AND METHODS

The purpose of this chapter is to fully describe all materials and methods utilized within this body of research. The various soil samples utilized in the experimental endeavors as well as all root-inspired anchor model materials are documented in this chapter. Additionally, all relevant experimental details including equipment specifications, specimen preparation, experimental procedure, and data conditioning are listed. Furthermore, numerical simulation methods such as model setup and calibration are described.

4.1 Materials

Numerous materials, including geomaterials, plants, and anchor model materials, were utilized in this research and are described in following sections.

4.1.1 Geomaterials

A variety of sand and glass ballotini samples are utilized within this work. The particulate materials, their characteristics, and their use within this dissertation are shown in Table 4-1. Additionally, Figure 4-1 contains images of the three soil types used at the Port Airport Research Institute in Japan. All Ottawa sand samples were sourced from U.S. Silica, while the source of the Japanese geomaterials is unknown. The US sourced glass ballotini were purchased from Potters Industries. Two recognized points of contention regarding the selection of the geomaterial specimens include, 1) the use of an inconsistent fine sand, coarse sand, and glass bead source, and 2) the use of clean, fine sand for studying plant root pullout behavior. In regards to the first contention, a standard set of geomaterials

was not specified due to the challenges in transporting geomaterials between countries. Furthermore, Ottawa F75 sand was used in place of Ottawa F110, both fine sands, for the living root system pullout experiments due to the current unavailability of F110 sand (extensively being used in shale fracking) and the large quantities required. Despite the inconsistent geomaterial use, similar medium characteristics (i.e. mean grain size, coefficients of curvature and uniformity, roundness, and friction angle) were maintained amongst the fine and coarse sand and glass bead samples. In response to the second contention, it is not without notice that the typical soil medium for optimal plant growth contains organic material, providing increased water retention as well as nutrients. Yet, the geomechanical behavior of clean, fine sands are well documented, and for a novel study, minimization of the effect of the unknowns, including organic matter and fine particles, is advantageous.

Table 4-1. Properties of soil specimens.

Geomaterial	d_{50} [mm]	C_u	C_c	G_s	e_{max}	e_{min}	R	ϕ_{cs} [°]	Chapter - Use
Ottawa F110 sand	0.120	1.67	0.96	2.65	0.85	0.54	0.45	32.0	Ch. 6, Ch. 10
Ottawa F75 sand	0.185	1.79	1.03	2.65	0.79	0.51	0.39	30.0	Ch. 5
Toyoura sand	0.165	1.52	0.97	2.65	0.98	0.61	0.40	34.0	Ch. 7
Ottawa 20-30 sand	0.72	1.19	0.96	2.65	0.72	0.51	0.56	31.0	Ch. 6, Ch. 10
Soma no.4 sand	0.85	2.06	0.84	2.65	0.81	0.58	0.34	34.0	Ch. 7
Glass Beads (J)	0.20	1.23	0.99	2.52	0.75	0.57	1.00	23.5	Ch. 7
Glass Beads (US)	0.1	1.47	0.98	2.5	0.67	0.58	1.00	24.0	Ch. 6, Ch. 10

Toyoura Sand   Soma Sand no.4   Glass Ballotini (J)

d_{50}: 0.165mm d_{50}: 0.85mm d_{50}: 0.2mm
R: 0.40   R: 0.34   R: 1.0
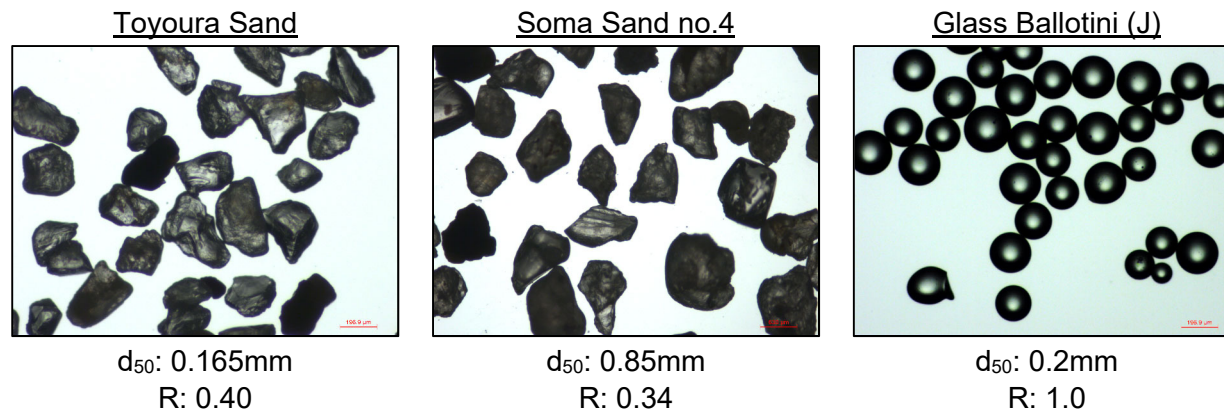
Figure 4-1. Images of particulate materials utilized at PARI in Yokosuka, Japan.

Ottawa 20-30 Sand   Ottawa F110 Sand

d_{50}: 0.72mm d_{50}: 0.12mm
R: 0.56   R: 0.45
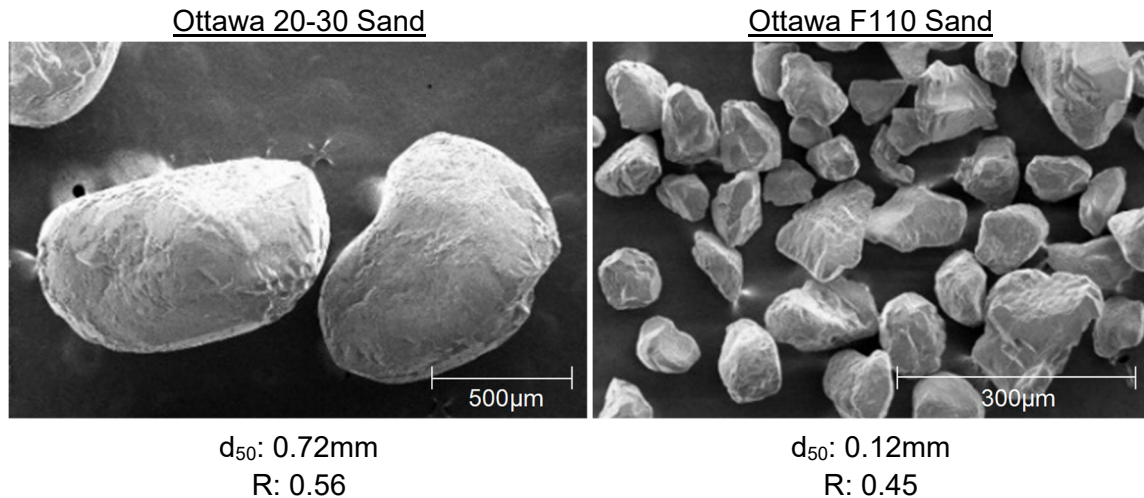
Figure 4-2. Images of select Ottawa sands utilized at Georgia Tech (Kim et al. 2019).

4.1.1.1   Geomaterial Characterization

Testing standards from both the Japanese Geotechnical Society, JGS, and ASTM International were utilized to characterize the various soil specimens in this research and were used in the respective research location of the origin of the standard. In general, results across the standards are similar, though concern regarding differences in maximum and minimum void ratios exist.

4.1.1.1.1   Specific Gravity, G_S

ASTM D854 Method B, "Specific gravity of soil solids by water pyncometer," and JGS 0111, "Test method for density of soil particles," were followed to determine the specific gravity of the geomaterials, and in both standards, a pyncometer device was utilized. Complications arose in determination of the specific gravity of glass ballotini due to the existence of dual porosity. Significant vacuum pressure was applied for an extended period of time to eliminate internal air voids.

4.1.1.1.2 Grain Size Distribution

Particle size distribution methods according to ASTM C136, "Standard test method for sieve analysis of fine and coarse aggregates," and JGS 0131, "Test method for particle size distribution of soils," were followed. Results of the sieve analysis for all samples is shown in Figure 4-3 in terms of percent finer by mass. Besides an unspecified mechanical agitation period for the JGS method, the standards for determining particle size distributions are identical. The coefficient of uniformity and curvature, C_u and C_c, are calculated as d_{60}/d_{10} and $d_{30}^2/(d_{60}d_{10})$, respectively.
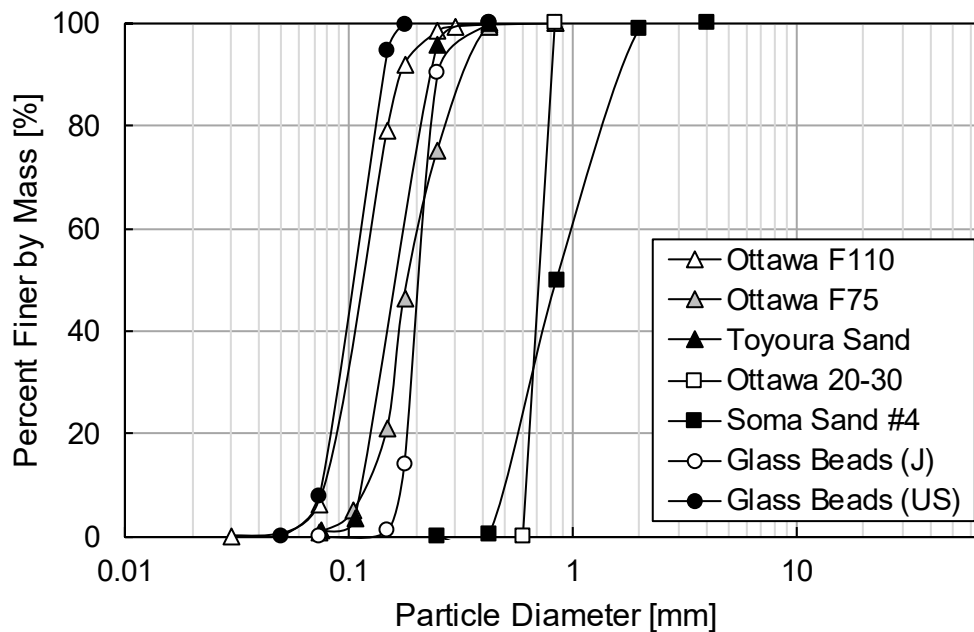
Figure 4-3. Particle size distributions of all geomaterials utilized within this research.

4.1.1.1.3 Void Ratio Limits

Comparison of material behavior based on maximum and minimum void ratios determined with the two standards demands attention due to the general concept of void

ratio limits as well as the striking differences in equipment requirements. First of all, void ratio limits are inherently dependent on the testing standard and as currently defined, do not provide a characteristic or absolute limit of the loosest or densest state of a particulate material. A concise description of both methods is listed in Table 4-2. Though JGS 0161, "Test method for minimum and maximum densities of sands," mentions the use of a wooden mallet to impact the mold, an automated apparatus that delivers equal energy blows was utilized. Conversely, ASTM D4253 Method 2A specifies the use of a cam-driven vertically vibrating plate to achieve minimum void ratio. The means of achieving the maximum void ratio is similar among the standards with the exception of the mold size. In general, minimum void ratio measurements are more method dependent than maximum void ratio measurements, especially as the fines content increases (Tavenas and La Rochelle 1972, Cubrinovski and Ishihara 2002, Lunne et al. 2019). More so, the JGS Standards are known to produce larger minimum void ratio values than ASTM standards (Ishihara et al. 2016). Since the relative density state of a soil influences the soil behavior, a direct comparison of results among materials tested with varying standards will not be performed.

Table 4-2. Comparison of JGS and ASTM standard methods to determine the maximum and minimum void ratios of a particulate medium.

Standard	Minimum void ratio	Maximum Void ratio
JGS 0161	Deposit particles in 10 equal lifts and tap mold (Ø60mm, H=40mm) 100 times equally around circumference for each lift	Fill test specific funnel (Spout Ø12mm) with particles and slowly deposit particles in mold (Ø60mm, H=40mm) over 20-30 seconds
ASTM D4253 Method 2A	Fill mold (Ø152.4mm, H=155.2mm) with particles utilizing funnel and vibrate sample with surcharge for 8 minutes at 60Hz	--

ASTM D4254 Method A	--	Fill test specific funnel (Spout Ø13mm) with particles and slowly deposit particles in mold (Ø152.4mm, H=155.2mm) with spiraling motion

4.1.1.1.4 Particle Roundness

Particle roundness, R, in this body of research, follows the two-dimensional definition as specified by *Wadell 1932*, which defines roundness as the arithmetic mean of the radii of curvature of particle corners normalized by the radius of the maximum inscribed circle. The values listed in Table 4-1, are the average of manual and automated measurements (Vangla et al. 2018).

4.1.1.2 Critical State Friction Angle

For the determination of the critical state friction angle, ϕ_{cs}, a simplified approach based upon the angle of repose is used (Cho 2001, Santamarina and Cho 2001). A volume of water saturated particulate material, is gradually tilted from the horizontal, and the average angle of the constant portion of the sloped material is determined.

4.1.2 Fibrous Root System-Inspired Anchor Models

Two distinct types of fibrous root system-inspired anchor models were designed for this research, 1) morphology-type (Figure 4-4), and 2) topology-type (Figure 4-5) and were developed specifically for the parametric evaluation of the contribution of root system architectural features on pullout behavior. Additionally, pile and plate anchor models (Figure 4-6) were established for the purpose of comparative evaluation and analytical

model validation. The design of the root-inspired anchor models is detailed extensively in

Chapter 5.
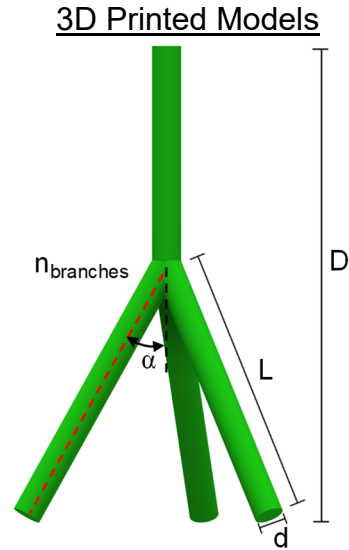
Figure 4-4. Primary, morphology-type, fibrous root system-inspired anchor model with emphasis on geometric feature parametrization.
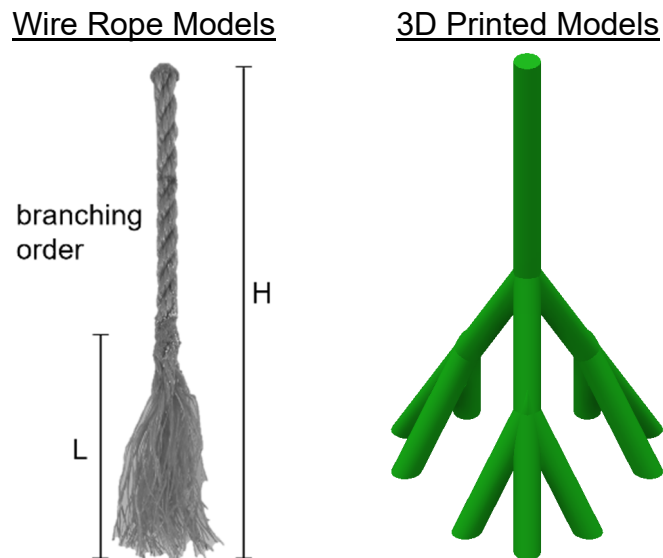
Figure 4-5. Secondary, typology-type, fibrous root system-inspired anchor models with emphasis on topological order variation.
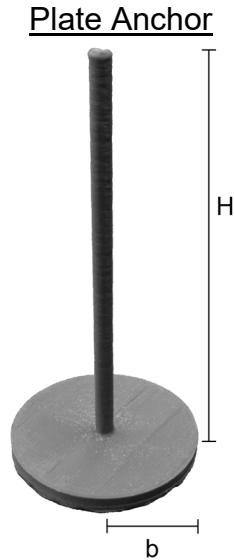
Plate Anchor

Figure 4-6. Plate anchor model for comparison and calibration purposes.

The morphology-type models are geometrically described in Figure 4-7, where the main components include the stem, branch axes, and the point of dichotomy. All branch axes are equally spaced when viewed from plan view, and the individual angle between adjacent branch axes is termed the branch spacing angle, θ, which is calculated as $2\pi/n$. The morphology-type models follow the following example nomenclature: n3a30L50d5D90 , where "n" refers to the number of branch axes, "a" the internal branching angle, "L" the length of the branch axes, "d" the diameter of models, and "D" the embedment depth.
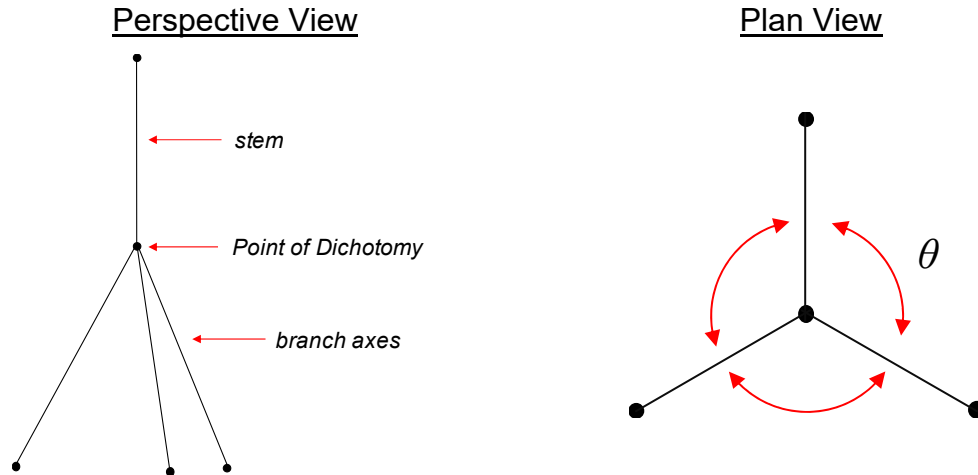
Figure 4-7. Schematic drawings of the primary components of the morphology-type models as viewed from perspective and plan views.

The topology-type models can be described in a similar fashion, where a point of dichotomy occurs at every branching point. For all cases, the point of dichotomy exists at half the length of the parent axis.

4.1.2.1   Anchor Model Fabrication

The morphology-type anchor models were fabricated either by welding for the steel models or through the fused filament fabrication (FFF) additive manufacturing method for the 3D printed models, which is comprehensively covered in the following section. For the wire rope, topology-type models, polymer or steel wire rope was cut to the appropriate length and unraveled to the specified branching order. Both the polymer and steel wire ropes contain three levels or orders of raveling, which are conventionally referred to as the wires, the strands, and the rope, in progressing order of braiding. The polymer wire rope is composed of 3 strands of 45 wires per strand, and the steel wire rope is composed of 7 strands of 18 wires. The nomenclature is 3x45 and 7x18, respectively.

4.1.2.1.1   3D Printed Model Fabrication

All 3D printed models, utilized in this research, were fabricated with a Lulzbot TAZ 6 fused filament fabrication printer (Figure 4-8). The general manufacturing process is as follows: 1) generate the computer-aided design of model and export as a stereolithography file (.stl), 2) import the .stl into a 3D slicer program, select printing parameters, and export the g-code to 3D printer, 3) execute the g-code. All models were designed with Autodesk Inventor, and the design methodology is as follows, 1) generate and import coordinates of the stem and branch members, 2) sketch circles of appropriate diameter normal to the axis of all members, 3) extrude sketches along axis of all members, 5) add additional 25mm of stem solely for use as an attachment point, and 6) export model as a stereolithography (.stl) file. A 3D slicer program, in this case CURA, divides the stereolithography file into individual printing layers and constructs the path of the printing head to efficiently deposit material based on the print parameters. Various object parameters and printing settings are incorporated into the g-code file, which directly controls the action of the 3D printer. Object parameters can be specified for each of the four primary components of a print, which include infill, shell, support, and base layer. The infill refers to all hidden material contained within the outer shell of the print. The support is all removable material required to print models with overhanging vertical layers, and a base layer is necessary to ensure the print remains adhered to the printing bed throughout the entire printing process. The standard adjustable infill parameters include the infill density, pattern, and orientation, and for the shell, thickness and orientation are primary variables. Common modifiers for the support material include support pattern and overhang threshold angle, and for the base layer, thickness and feature additions such as brim, skirts, and rafts can all be controlled

for the optimal print object-printing bed bond. The range of values of the typical variable printing settings are governed by the filament material and the desired object quality. The primary variables include printing bed and nozzle temperature, printing speed, layer thickness, and filament flow rate.

4.1.2.1.2   3D Printer Specifications

The Lulzbot TAZ 6 3D printer features a 280mm x 280mm x 250mm print volume and an automated z-axis leveling process that ensures the printing bed remains normal to the nozzle through the entire printing process. The print resolution, determined by the layer thickness, can be adjusted from approximately 0.1mm to 0.4mm for the 0.5mm diameter nozzle. Maximum printing bed and nozzle temperature are 120°C and 290°C, respectively.
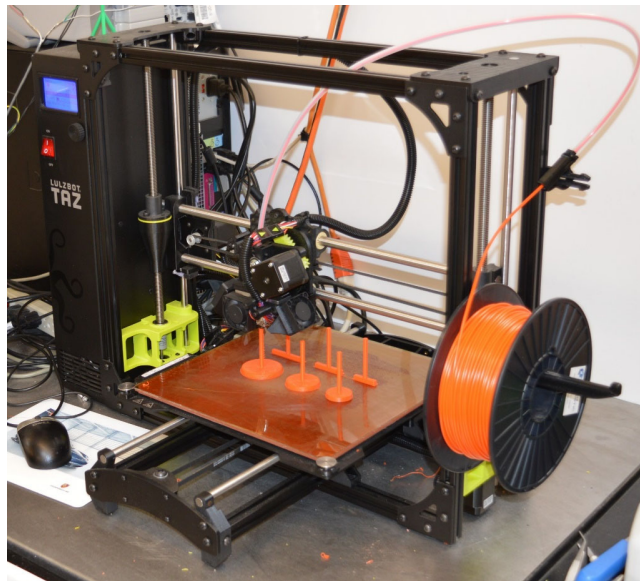
Figure 4-8. Image of Lulzbot TAZ 6 3D printer.

4.1.2.2   Anchor Model Material Properties

The 3D printed morphology-type models were all fabricated with acrylonitrile butadiene styrene (ABS) thermoplastic, one of the most commonly used 3D printing filaments. ABS material is known for its ease of 3D printing and relatively high strength and stiffness compared to other readily available products. The 2.85mm diameter filament was sourced from Push Plastic. The mechanical properties of bulk ABS plastic and other 3D printed plastic filaments in general are known to degrade with printing and with time. Furthermore, the mechanical properties (e.g. ultimate strength and elastic moduli) are affected by both the object parameters (e.g. infill density, shell thickness, shell and infill orientation) and printing settings (e.g. nozzle and printing bed temperatures, layer height, printing speed) (Giordano et al. 1996, Rodriguez et al. 2001, Tymrak et al. 2014, Dizon et al. 2017). The elastic modulus and ultimate strength of printed ABS plastic were determined following ASTM D638. Type I coupons were printed with the same print object parameters and printing settings as the root-inspired anchor models and then loaded in tension with a benchtop Instron tensile testing machine. Results of the tensile tests are documented in Table 4-3. The steel morphology-type models were fabricated from a low carbon, 5mm diameter steel rod. For the topology-type fibrous root system-inspired anchors, either galvanized steel or low density polyethylene was used. The mechanical material properties of all root-inspired anchor models are listed in Table 4-3.

Table 4-3. Mechanical properties of root-inspired anchor model materials.

Material	ρ [kg m^{-3}]	E [GPa]	ν	σ_{ult} [MPa]
ABS Plastic (printed)	1100*	1.5	0.35*	~60
Low-carbon steel rod	7850*	200*	0.29*	
Galvanized Steel 7x18 Strand Cable	8000*	200*	0.26*	
LDPE 3x45 Braided Rope	920*	0.5*	0.35*	

* Engineering ToolBox 2001

4.1.3 Interface Direct Shear Plates

To test the interface shear response between sands and 3D printed surfaces, a series of plastic plates were fabricated with Lulzbot TAZ 6 machine using either ABS or high impact polystyrene (HIPS), whose mechanical properties are listed in Table 4-4. For the interface direct shear tests on smooth 3D printed plastic, the specimens were prepared by sanding the surface with sandpaper of gradually increasing fineness. Four levels of sandpaper were used, 150, 320, 600, and 2000 grit sandpaper, with corresponding average particle sizes of 100μm, 46.2μm, 25.8μm, and 10.3μm, respectively. For the study of the effect of deposition orientation with respect to shearing direction, the orientation of the outer shell was varied in increments of 15° from 0° to 90°, where θ is the angle between the direction of shearing and filament orientation (Figure 4-9).

Table 4-4. Mechanical properties of 3D printed plates.

Material	ρ [g cm^{-3}]	E [GPa]	v [ ]	σ_{ult} [MPa]	Shore D Hardness [ ]
ABS Plastic (printed)	1.1*	1.5	0.35*	22-36	80.05
HIPS (printed)	1.1	--	0.4*	15-25	75.7
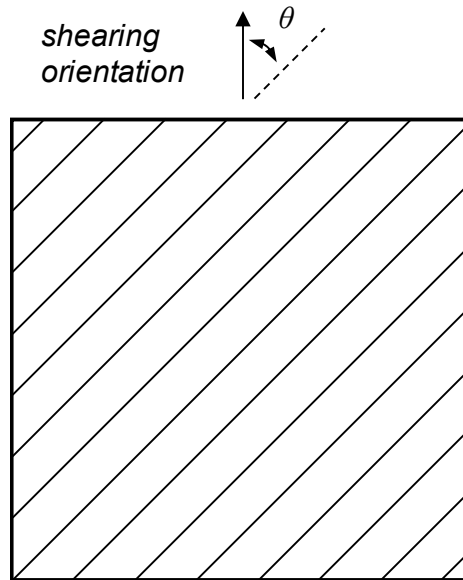
Figure 4-9. Illustration of the filament orientation relative to shearing direction.

4.1.4   Fibrous Root Systems

Two plant species were selected and grown for the pullout of living plant root systems experiment. The criteria for selection of plant the species were, 1) contains a fibrous root system, 2) all root members of the root system are sufficiently large so as to allow for ease of measurement, and 3) plants grow quickly and with minimal care. Spider plants (*Chlorophytum comosum*) and King Richard leeks (*Allium porrum*) satisfied all of these criteria. The King Richard leek seeds were sourced from Johnny's Selected Seeds, and the liquid fertilizer solutions were obtained from General Hydroponics.

4.2   Experimental Program Equipment
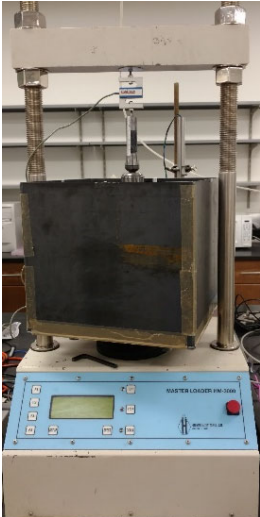
A multitude of devices were utilized in the execution of the entire experimental endeavor. A list of the equipment employed in each experimental program is archived in Table 4-5. The known specifications of the primary pieces of equipment are listed in Table

4-6. Specific details of the two x-ray computed tomography (CT) scanners utilized in this research are detailed in Table 4-7 and displayed in Figure 4-10.

Table 4-5. Experimental equipment per test program.

Test Program	Chapter	Equipment
Ring Pullout Tests	5	Ring pullout apparatus (custom), reaction frame (Humboldt HM-3000), 3 jaw chuck (Jacobs), 500lbf capacity load cell (Interface SM-500), 140mm range LVDT (Trans-tek 0245), data acquisition (Agilent 34792A)
Living Root System Pullout	5	Reaction frame (Humboldt HM-3000), 3 jaw chuck (Jacobs), 50lbf capacity load cell (Interface SSM-50), 140mm range LVDT (Trans-tek 0245), data acquisition (Agilent 34792A)
Anchor Model Pullout	6, 10	Reaction frame (Humboldt HM-3000), 3 jaw chuck (Jacobs), 50lbf capacity load cell (Interface SSM-50), 140mm range LVDT (Trans-tek 0245), data acquisition (Agilent 34792A)
Failure Surface Visualization	7	X-ray µCT scanner (Comscan ScanXmate D200RSS900), soil container and loading device (custom), 200N capacity load cell (Kyowa Dengyo LUR-A200NSA1), laser displacement sensor (Keyence LB-01), data acquisition (unknown)
Interface Direct Shear Tests	10	Interface direct shear apparatus (custom), 2x 1000lbf capacity load cells (Interface SM-1000), 3x LVDT ((2)Trans-tek 0244, (1) Trans-tek 0245), data acquisition (Agilent 34792A)

Table 4-6. Equipment specifications.

Device (Manufacturer and model)	Device Image	Specifications
Reaction Frame (Humboldt HM 3000 Master Loader)		Displacement control: stepper motor Maximum displacement rate: 50mm min^{-1} Maximum compression load: 50kN Maximum extension load: 9kN Soil box attachment: 342mm x 342mm x 330mm open top Fabricated from 1/8" steel plates Not watertight
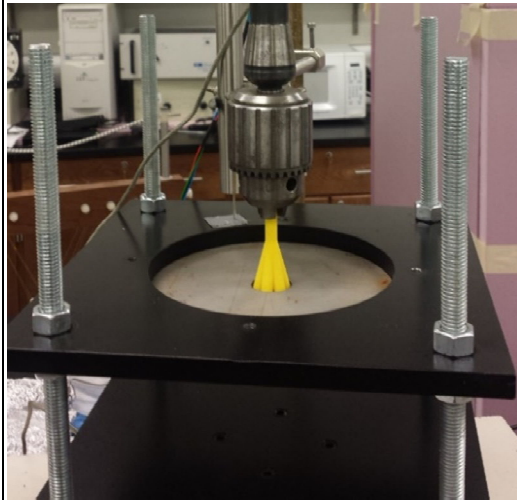
Ring Pullout Apparatus (Custom fabricated at Georgia Tech)		Reaction frame attachment Removable ring plates of varying diameter (Ø25, 50 ,75, 100), fabricated from 3/16" thick steel plate that attach to underside of top plate Base plate (3/8" thick) and top plate (1/2" thick) bolted together with 1/2"-13 all thread bars
Soil container and self-reacting loading device (Custom fabricated at PARI)		Displacement control: Chain drive, stepper motor Self-reacting: motor reacts against the soil container Container: acrylic, internal diameter of 114mm, height of 270mm. 8mm wall thickness
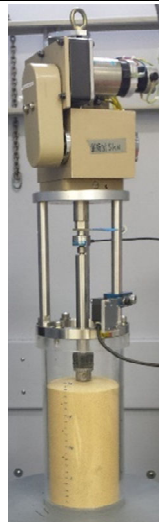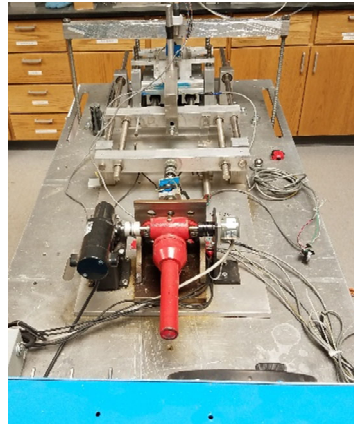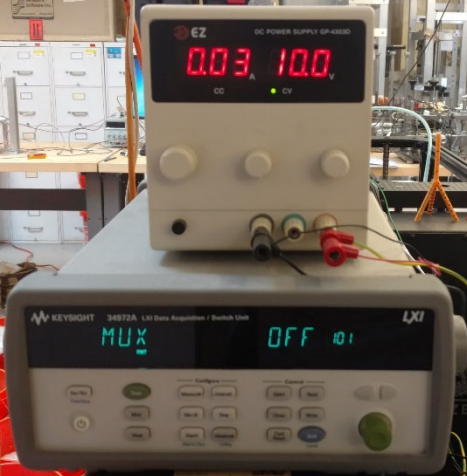
Interface Direct Shear Apparatus (Custom fabricated at Georgia Tech)		Horizontal displacement control: ActionJac ball screw jack driven by Bodine Electric 130VDC electric motor Normal load control: Bellofram double-acting pneumatic cylinder Maximum Pressure: ~80psi Soil container dimensions: 101.6mm x 101.6mm x 61mm with a 12.8mm thick top cap
3-jaw chuck (Jacobs)		Max. diameter: 1/2" Tensile holding capacity: ~450N Rigid connection, no eccentric loading control

15V Power supply and Agilent 34792A Data acquisition system		250 Channel per second capacity USB connection BenchLink Data Logger 3 software
Interface Load Cells (SM-50, SM-500, SM-1000)		S-type load cell capable of compressive and tensile loading Max. Load Capacity: 50, 500, 1000lbf, respectively Max. excitation voltage: 15VDC Rated Output: $3mV\ V^{-1}$ Non-repeatability: 0.01% of rated output Nonlinearity: 0.03% at full scale
Trans-tek DC LVDT (0244, 0245)		Linear variable differential transformer Max. excitation voltage: 30VDC Working range: 50.8mm and 101.6mm, respectively Nonlinearity: 0.5% at full scale
Keyence LB-01 Laser displacement sensor		Infrared semiconductor laser 785nm wavelength Max. Output: 2.5mW Working range: 80mm Nonlinearity: 1.6% at full scale Resolution: 10μm at 500ms acquisition time

Kyowa Dengyo LUR-A200NSA1 Compact load cell		Pancake style load cell capable of compressive and tensile loading Max Load Capacity: 200N Max. Excitation voltage; 7VDC Rated Output: 0.5mV V^{-1} Nonlinearity: 0.5% at full scale

Georgia Tech X-ray CT Scanner   PARI X-ray CT Scanner
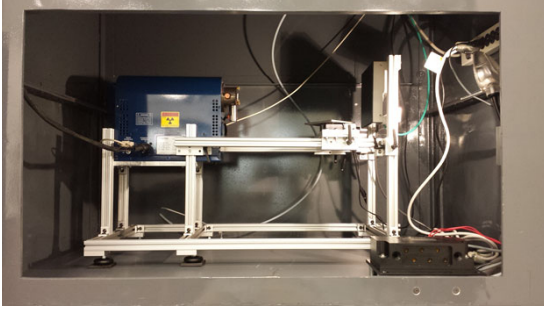
Figure 4-10. X-ray tomographers at Georgia Tech (left) and PARI (right).

Table 4-7. Specifications of x-ray tomographers at Georgia Tech and PARI.

		Georgia Tech	PARI
Source	Model	ThermoScientific PXS10	Hamamatsu L10801
	kV Range	20-130kV	20-230kV
	Max. Current	500µA	1000µA
	Min. focal spot	4µm	4µm
	Beam Angle	53°	40°
Detector	Model	Varian PaxScan 1313	Varian PaxScan 4343
	Pixel Area	1024x1024	3072x3072
	Pixel Pitch	127µm	139µm
Positioning	Model	Zaber T-RS60	Custom
	Max. Weight	45kg	100kg
	Accuracy (x,y,z, rot)	N/A, N/A, N/A, 0.05°	5µm, 5µm, 3µm, 0.002°

4.3   Experimental Program

Details for each of the experiments are described in the following sections, where particular focus is placed on the specimen preparation, experimental procedure, and data analysis.

4.3.1   Ring Pullout Test

A unique experimental setup was required for investigating the mechanical pullout behavior of root-inspired anchor models without the additional complexity of soil, and

consequently, a ring pullout apparatus was developed at Georgia Tech for assessing such pullout response (Figure 4-11). The device was constructed from steel with insertable plates of varying aperture, ranging from 25mm to 100mm in diameter in 25mm increments. A simple, elastic structural model in Comsol Multiphysics revealed that for testing of 3D printed anchors, 3/16" steel was of adequate rigidity for the replaceable ring plates to neglect plate deflection from the pullout response.
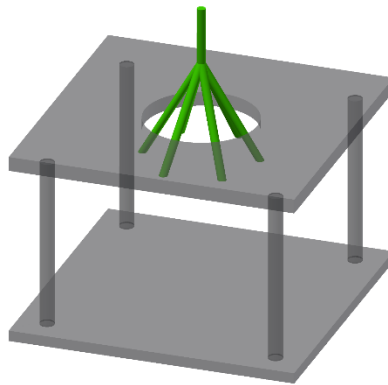
Figure 4-11. Model representation of ring pullout apparatus.

4.3.1.1   Specimen Preparation

The 3-jaw chuck was tightened around the root-inspired anchor model stem as close as possible to the point of dichotomy to minimize the contribution of the stem to the pullout response. The model was then positioned with the branch members in close proximity to the plate aperture without contact and with the axis of the model stem and of the ring aperture in alignment.

4.3.1.2   Procedure

With specimen preparation complete, the root-inspired anchor model was displaced upwards at a constant rate of 10mm min^{-1}. As the model was displaced, force and

displacement measurements were recorded every 0.5s. A 10VDC excitation voltage was applied to both the load cell and LVDT. The displacement and data recording was terminated with either the failure of a model branch or once the model was completely pulled through the plate opening.

4.3.1.3   Data Analysis

The initial load, which includes the weight due to the root-inspired anchor model and the jaw chuck as well as the load cell offset, was subtracted from all resistance values. Additionally, the displacement values were offset based upon the displacement at which the model became in contact with the ring apparatus. Both load and displacement values before contact were removed.

4.3.2   Living Root System Pullout Test

An experimental program was developed to identify the features of fibrous root systems that enhance pullout stability. All plants were grown inside within the Sustainable Geotechnical Systems Laboratory, which does not supply advantageous growing conditions.

4.3.2.1   Specimen Preparation

The soil containers were prepared first by slowly depositing 24kg of dry Ottawa F75 sand from a constant fall height of 10cm in 5-gallon HDPE buckets. The buckets contained 1" diameter holes at the base to allow for drainage. Numerous leek seeds were germinated, and of those, 68 seedlings were transplanted after one week of growth into the center of the buckets. Additionally, 15 plantlets with a single root less than 15mm in length

were harvested from a mature spider plant and transplanted into soil specimens. During the maturation period, the plants were watered daily and given nutrients in the form of soluble fertilizer weekly. Due to poor lighting conditions, all plants experienced stunted growth, in particular the leek plants. After a total growth period of ~230 days for the leek plants and ~100 days for the spider plants, the root systems were tested in pullout, and from the initial planting of 68 leek and 15 spider plants, 29 leek and 7 spider plants were tested.

4.3.2.2   Procedure

Before testing, the specimen containers were filled with water, and after 30 minutes of constant flow, the bottom openings were plugged with rubber stoppers. The containers were then filled with water again and allowed to equilibrate for 48 hours. Before testing, the surface water was siphoned off to approximately 1-2mm above the soil surface. As well, the above-ground portion of the plant was trimmed to approximately 30mm above the soil surface. The specimen was then carefully transported to the reaction frame, and then positioned such that the central axis of the jaw chuck and the above-ground portion of the plant were in alignment. The container was then positioned vertically such that when the 3-jaw chuck was tightened around the plant stem, the tip of chuck was at the soil surface. After installing the LVDT, ensuring the data acquisition system was active, and providing 30 additional minutes to allow any excess pore pressure to dissipate, the container was lowered at a steady rate of 10mm min^{-1}, while force and displacement readings were collected every 0.25s. After the plant was displaced from the soil for a total of 70-90mm of displacement, the pullout process was terminated.

4.3.2.3   Anatomical Examination

After the pullout procedure was complete, the plant was removed from the jaw chuck, and the remaining root structure was gently lifted from the soil by liquefying the soil container. A number of anatomical measurements were then recorded for the plant. For the intact root system, the maximum length of the root system initiating at the soil surface, the dry mass, the number of secondary root segments, and the length of each secondary root segment were logged. Additionally, the soil was excavated and wet sieved to collect all root segments that ruptured and detached during the pullout process. For the above-ground portion of the plant, the length of longest member measured from the soil surface, the dry mass, and the diameter of the stem at the soil surface were recorded. For all length measurements, the individual root segments of varying tortuosity were gently stretched, and the value of maximum length was recorded. Within the plant biology literature, guidelines vary substantially on the procedure for drying roots; for this study, the most common trend was followed which entailed drying plant members at 70°C for 48 hours (Bohm 1979).

4.3.2.4   Data Analysis

Using the load cell and LVDT calibration factors, the change in voltage was converted to force in Newtons and displacement in millimeters. The force and displacement data was trimmed and zeroed at the time when the plant began to be uplifted.

4.3.3   Root-Inspired Anchor Model Pullout

A soil box fabricated from 1/8" steel plates measuring approximately 340mm in all directions was attached to the Humboldt reaction frame. The box is not watertight currently, and consequently, experiments were conducted with dry sand only.

4.3.3.1 Specimen Preparation

A root-inspired anchor model was first attached to the reaction frame via a 3-jaw chuck. The soil box was then vertically positioned such that a specified distance between the top of the model and bottom of the soil box was attained based on the embedment of the model. A mass of geomaterial was then slowly deposited into the box in a spiraling motion via a funnel at zero height from the soil surface. The opening of the deposition device is 1". After a specific mass of soil was placed, the soil box was then systematically tapped with a rubber mallet for a number of repetitions based on the desired relative density and geomaterial sample. Densification was achieved by administering a blow three times on three equidistant locations on each side of the soil box, for a total of 36 blows per repetition. Before the final repetition, the soil surface was leveled to allow for visualization of surface heave and evidence of a circular failure surface.

4.3.3.2 Procedure

Before pullout testing commences, the positioning of the LVDT is corrected, and a 10VDC excitation voltage is applied to the load cell and LVDT. The soil box was then lowered at a constant displacement rate of 10mm min^{-1}, while the force and displacement readings was logged every 0.25s. The model was displaced from the geomaterial for a minimum of 40mm or until the point of dichotomy reached the soil surface. After displacement of the model was halted, the diameter of the failure surface at the soil surface was measured if visible.

4.3.3.3 Data Analysis

The recorded voltage changes with time were converted to force values in Newtons and displacement readings in millimeters for the load cell and LVDT, respectively. Since the soil was densified around the anchor models, a certain initial load on the anchor models was present. Consequently, the force reading was not zeroed but corrected by the load cell offset, the weight of the jaw chuck and associated connections and the weight of the root-inspired anchor model. Additionally, the displacement readings were zeroed at the time at which the pullout processes was initiated.

4.3.4   *Visualization of Failure Surface during Root-Inspired Anchor Pullout*

The pullout tests were completed with a lightweight, self-reacting loading device. The bottom portion is a soil chamber with an internal diameter of 114mm and height of 250mm, fabricated from 8mm thick acrylic. The low-density acrylic, in comparison to silica, minimally attenuates the x-radiation, allowing the beam to pass through the entire specimen. The top portion, which resides above the field of view of the x-ray scanner, consists of a loading motor and three steel rods that react against the soil chamber. An externally attached, high-resolution laser displacement sensor and an in-line, low-profile load cell are utilized to record displacement and force, respectively; both devices are connected to an all-in-one data acquisition and power supply system. A three-jaw chuck is attached to the end of the loading rod to grip the root-inspired anchor models. The following procedure was followed for the pullout tests completed within the x-ray microtomographer at PARI versus Georgia Tech due to specimen size restrictions.

4.3.4.1   Specimen Preparation

For sample preparation, the root-inspired anchor was first attached to the loading device via a 3-jaw chuck. Subsequently, a prescribed mass of soil was air pluviated through a hose at zero fall height around the anchor model. With a rubber mallet, the soil chamber was tapped systematically to achieve the desired relative density of 80%. The identical densification method as for the root-inspired anchor model pullout tests was followed, where the soil container was tapped three times at four equidistance locations around the circumference of the container and at three locations vertically for a total of 36 blows per cycle.

4.3.4.2 Procedure

Once the specimen was prepared, the loading device was carefully positioned onto the stage of the x-ray CT scanner. For all scans, the soil and anchor models were imaged at a voltage of 160kV and current of 130μA for preferred image contrast. As well, the positioning of the specimen was held constant for each test. Within each scan, a radiograph was captured every 0.24° for a total of 1500 images. First, an initial scan of the specimen was performed before any model pullout. Subsequently, the anchor model was uplifted from the soil at a rate of 10mm min^{-1} to 0.5mm of displacement, and following, an additional scan was performed. The sequence of 0.5mm of upwards model displacement and corresponding x-ray CT scan was reiterated for a minimum total of 3mm or 7 image sets. During the entire scanning procedure, the force and displacement readings were monitored and recorded to ensure image sets were obtained before and after pullout capacity was attained.

4.3.4.3 Data Analysis

The force and displacement data was converted from voltage changes to force and displacement values in Netwons and millimeters, respectively. Additionally, the force and displacement readings were zeroed based on the initial readings. For the images, 3D image sets were reconstructed from the angular radiographs based upon the spatial scanning configuration. Following, a beam hardening correction and 7x7 median filter was applied to minimize image artifacts and noise.

4.3.5 *Interface Direct Shear Test*

A series of interface direct shear tests were performed to assess the interface shearing behavior of the silica sand-3D printed surface system. Additional details of the interface direct shear device can be found in *Dove 1996* and *Zettler 1999*.

4.3.5.1 Specimen Preparation

The 3D printed surfaces were securely fixed to the interface direct shear apparatus via rigid bars screwed through the outer edge of the specimen into the testing bed of the apparatus. With an air pluviation device, sand was deposited into the soil box to form a specimen with a bulk relative density of 67-80%. The sand was carefully leveled with a brush, and the loading cap was then positioned on top of the sand specimen. The self-reacting loading device and vertical LVDT was then centered on the loading cap, and the loading pressure was gradually increased to the specified normal pressure as the change in vertical displacement was recorded.

4.3.5.2 Procedure

The interface was then displaced at a constant rate of 1mm min^{-1}, as the horizontal and vertical load and displacement measurements were recorded every second.

4.3.5.3 Data Analysis

The force and displacement readings were zeroed by subtracting the initial values from all readings.

4.4 Numerical Modelling

The pullout of root-inspired anchor models was simulated with the commercial finite volume software, FLAC3D. The details of numerical model including geometry, boundary conditions, mesh generation and size convergence, input parameters, and calibration, are provided.

4.4.1 Geometry and Boundary Conditions

For the numerical extension of the experimental 1g pullout tests, the radius of the container between the experimental and numerical was kept consistent (i.e. r=171mm), while the depth was reduced to D=150mm to minimize mesh count. Owing to the symmetry of the problem, the size and corresponding number of elements can be reduced by a factor equivalent to the number of branch axes of the root-inspired anchor model, as illustrated in Figure 4-12, where pullout resistance is adjusted by multiplication of the number of branch axes. For boundary conditions, the bottom of soil was fixed vertically and horizontally, while rollers (i.e. zero displacement normal to face) are added to the external radius of the soil and to the symmetric cuts. Additionally, the pullout process is displacement rate controlled, where for a rigid simulation all nodes of the anchor model are prescribed the

same upwards vertical rate while for an elastic simulation only the top surface of the stem of anchor model is controlled. The simulation maintains consistent units as dictated in Table 4-8.
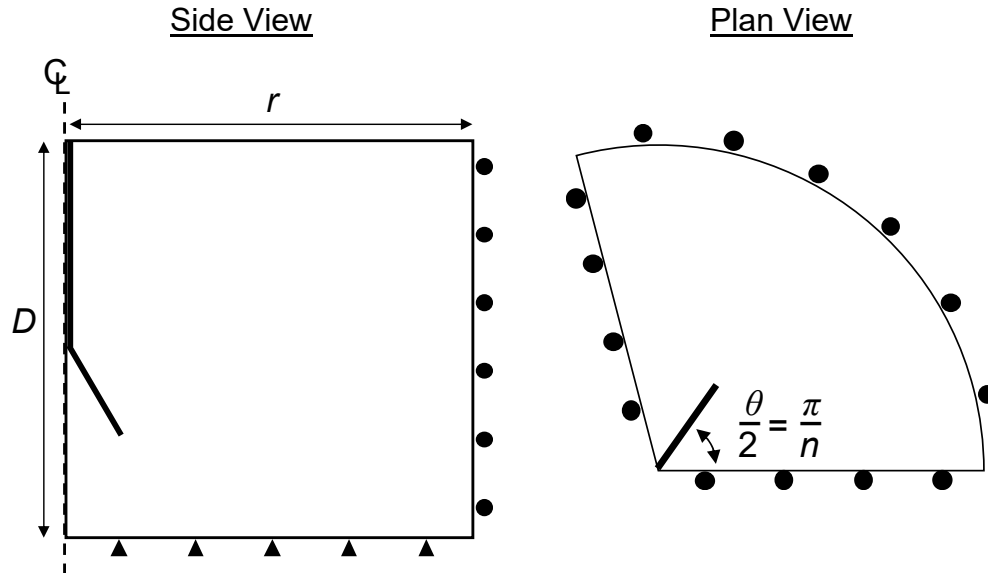
Figure 4-12. Schematics of numerical model geometry clarifying both dimension and boundary conditions.

Table 4-8. Consistent units implemented in the numerical model.

Quantity	SI mm units
Length, L	mm
Mass, M	tonne
Time, T	s
Force, M L T^{-2}	N
Stress, M L^{-1} T^{-2}	MPa
Density, M L^{-3}	tonne mm^{-3}
Gravity Constant, L T^{-2}	9.81x10^{-3} mm s^{-2}

4.4.2 Mesh Generation

Both the soil and the root-inspired anchor were modeled with solid, tetrahedral elements. For parametric implementation, a more simplistic method to model the anchor was sought (i.e. solely shell elements or a combination of beam and shell elements), yet,

was impossible with the version of the operable software at the time. As such, the soil and anchors were modeled individually using a more time consuming process. The open-source platform, Salome, was used to generate all meshes, and the following procedure was performed for all cases: 1) generate a computer-aided model of soil and anchor geometry in Autodesk Inventor and export as a step file, 2) import geometry in Salome and with the partition tool, define the soil, anchor, and soil-anchor interface groups, 3) mesh the geometry with "1D-2D-3D Netgen" meshing algorithm and export the solid mesh as a .med file and the anchor surface as a .stl file, 4) utilize the open-source software Gmsh to convert from .med files to FLAC3D readable .inp files (Geuzaine and Remacle 2009). The mesh generation methodology was enacted due to the difficulties in selecting and defining irregular surfaces in FLAC3D.

The effect of mesh size on pullout capacity was assessed through a mesh convergence study (Figure 4-13). Pullout capacity reaches an asymptotic value at approximately 50000 elements, where the minimum mesh size is 1mm or less.
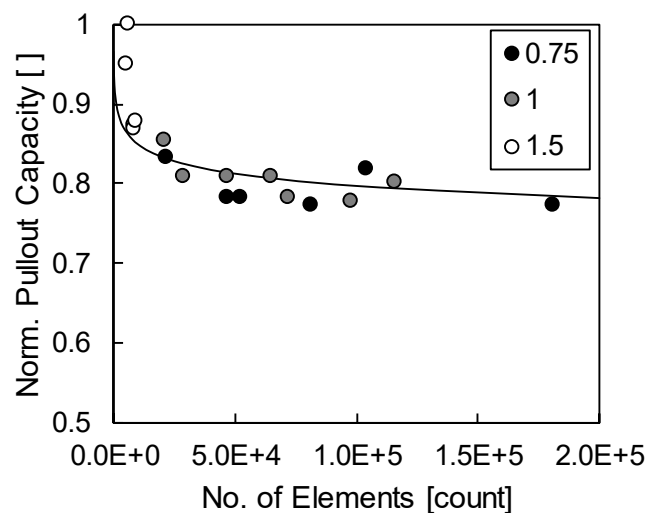
Figure 4-13. Mesh convergence by number of elements with varied minimum mesh size.

Critical to the finite volume method implemented with an explicit scheme is the selection of a suitable time step, which must be less than the critical time step for stability. As such, the displacement rate of the root-inspired anchor was selected based on the plateauing of the pullout capacity value with decreasing displacement rate (Figure 4-14). As well, damping is applied to equations of motion to achieve the equilibrium threshold at a faster rate.
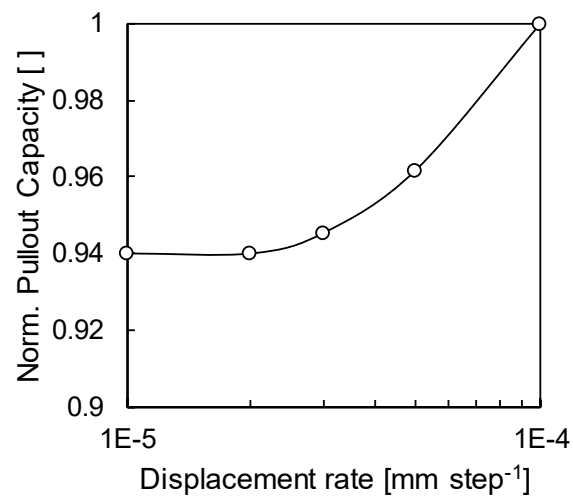
Figure 4-14. Numerical stability check with varying displacement rates.

4.4.3   Input Parameters

The input values, both the range of values for the parametric study and the calibrated values, are documented in Table 4-9.

Table 4-9. Range of input properties and calibrated values for numerical model.

	Input Parameter	Range	Calibrated Value
	Elastic Properties		
Anchor	Young's Modulus, E [MPa]	1.5×10^0-1.5×10^5	1.5×10^3
	Poisson's ratio, v [ ]	0.35	0.35
	Initial State		
	Density, ρ_{dry} [kg m^{-3}]	1650	1650
	Earth Pressure Coefficient, K	K_{active}-$K_{passive}$	1
	Elastic Properties		
	Young's Modulus, E [MPa]	1.5-1500	15
Soil	Poisson's ratio, v [ ]	0.2	0.2
	Plastic Properties		
	Critical State Friction angle, ϕ_{cs} [°]	31	31
	Dilation angle, ψ_{max} [°]	0-31	10
	Cohesion, c [Pa]	0	0
	Tension cut off, σ_t [Pa]	0	0
	Normal contact stiffness, k_n [MPa mm^{-1}]	15-15000	150
Soil-Anchor Interface	Shear contact stiffness, k_s [MPa mm^{-1}]	15-15000	150
	Interface friction	0-ϕ_{cs}	2/3ϕ_{cs}

4.4.4   Material Constitutive Models

The soil elements are defined as an elastic-plastic material where the plastic yield and flow are defined by the Mohr-Coulomb constitutive model. As well, the elements are prescribed a mass equivalent to that of the experimental study. The root-inspired anchor elements are given elastic properties only, and the Young's modulus was selected from Table 4-3.

4.4.4.1   <u>Contact Model</u>

A contact model is given to the interface elements defining the surface between the anchor and soil elements. The change in shear and normal force at each node is computed

with the relative shear and normal displacement and specified normal and shear stiffness along the area of the interface element. A Coulomb failure criterion is also supplied to the interface elements, such that if the shear force exceeds the failure shear stress dictated by the interface friction angle, then sliding occurs.

4.4.5 Model Calibration

The numerical model was first calibrated with experimental plate anchor pullout data from tests conducted in Ottawa F110 sand with a relative density of 80%. A set of eleven models were used for input parameter calibration, and the parameters were optimized through the minimization of the RMSE over the pullout resistance-displacement response, and a coefficient of determination of 0.98 was achieved between the numerical calculation of pullout capacity and the experimental response (Figure 4-15).
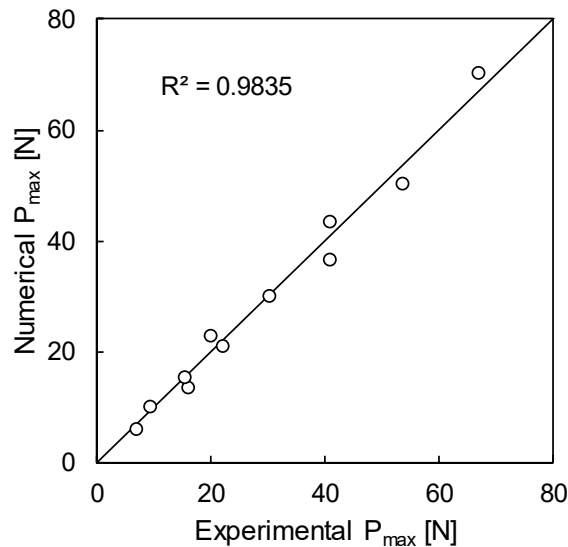
Figure 4-15. Comparison of pullout capacity values determined experimentally and with the calibrated numerical model.

Special Recognition: Tom Jenkins (REU from Jackson State University) and Taylor Martin (Young Scholar from Alpharetta High School) performed manual particle roundness

calculations and F75 Ottawa sand particle size distribution and void ratio limits, Nimisha

Roy performed automated particle roundness calculations.

CHAPTER 5.   THE DESIGN OF A ROOT-INSPIRED ANCHOR

The primary goal of this dissertation is to design a root-inspired infrastructure element to replace or enhance a conventional geotechnical structure. The purpose of this chapter in particular is to fully utilize the concepts developed within biologically inspired design to create a root-inspired element. The entire design process progression is documented from the identification of fibrous root system features to the development of root-inspired anchor models. Additionally, select physical properties of the root-inspired anchor models are detailed.

5.1   Root-Inspired Design Process

The nature of this bio-inspired challenge is solution-based, meaning the designer seeks to develop a product based upon a fixed biological solution to solve an unknown problem. The root-inspired geotechnics design process can be broadly described by the flowchart shown in Figure 5-1.

1) Investigate and organize plant root system attributes	→	2) Investigate current geotechnical challenges and align attributes	→	3) Design and evaluation of root-inspired elements	→	4) Select and design operational root-inspired product
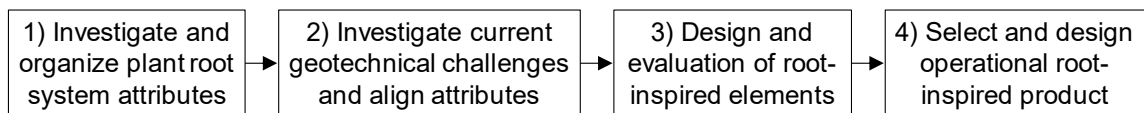
Figure 5-1. Design flowchart for a solution-based root-inspired geotechnics project.

While the logic flowchart is shown as a linear series of operations, the design process in practice is irregular and features iterative loops at various points within the process, which ultimately enhances the final design. Additionally, information is cumulative and consequently, aides in subsequent design iterations. For this particular project, three primary cycles were performed terminating at successive steps in the design

process. Within each operation, various techniques were utilized. For example, functional decomposition charts and four-box comparison diagrams were utilized to assimilate deductions. Functional decomposition is a method of dissecting a process into various levels of cognition typically by answering successive questions of how or why. Additionally, four-box comparison diagrams are utilized in both problem formulation and biology-design translation and are formed by amassing organism or design features into four determined problem-defining categories, operational environment, functions, specifications, and performance criteria (Helms and Goel 2014). The complete evolution of the root-inspired design following the prescribed design flowchart is described below.

Step 1) Investigation, organization, and selection of plant root system attributes

For step one, a thorough literature review was performed to develop a foundation of knowledge of plant root systems and to identify attributes of plant root systems. Attributes refers to all properties and principles involved in the life of a plant root. For the literature review, the bulk of the resources are from plant biology, with more minor contributions from soil science and geotechnical engineering. This was combined with communication with biologists to confirm comprehension and to assimilate additional attributes. The result of this literature review is found in Chapter 2. With successive iterations, design-specific plant root system attributes were gradually identified. In the first iteration, a general accumulation of root system properties pertaining to all aspects plant life was attained. After realizing the collected root system features were not sufficient as to enhance or develop the identified geotechnical problems, a focus on the anchorage principles of root systems was enacted. Finally in the third iteration, after the alignment of

fibrous root and anchorage systems and the recognition of the augmentation potential of a root-inspired anchor, root system features essential for resisting uplift forces were targeted.

Step 2) Investigation of current challenges in geotechnical engineering and alignment of root attributes with those challenges

For this step of the design process, various geotechnical challenges were accrued and analyzed through discussions with practicing engineers and investigations of geotechnical infrastructure failures. Within each iteration, the list of geotechnical challenges was narrowed, and the specifics of the problem space were more clearly defined. For example, the first iteration was terminated on this step after it was concluded that the root systems attributes first set forth were not sufficient in specificity to proceed with further design steps. In the second iteration loop, plant root system attributes were aligned with specific problems in the various highlighted geotechnical infrastructures. The term align in this context refers to associating the solution space with the problem space, where particular attributes are connected to specific challenges. Finally, in iteration three, the specific challenge area of anchorage elements, including ground anchors, anchor plates and piles, and tie-downs, was selected.
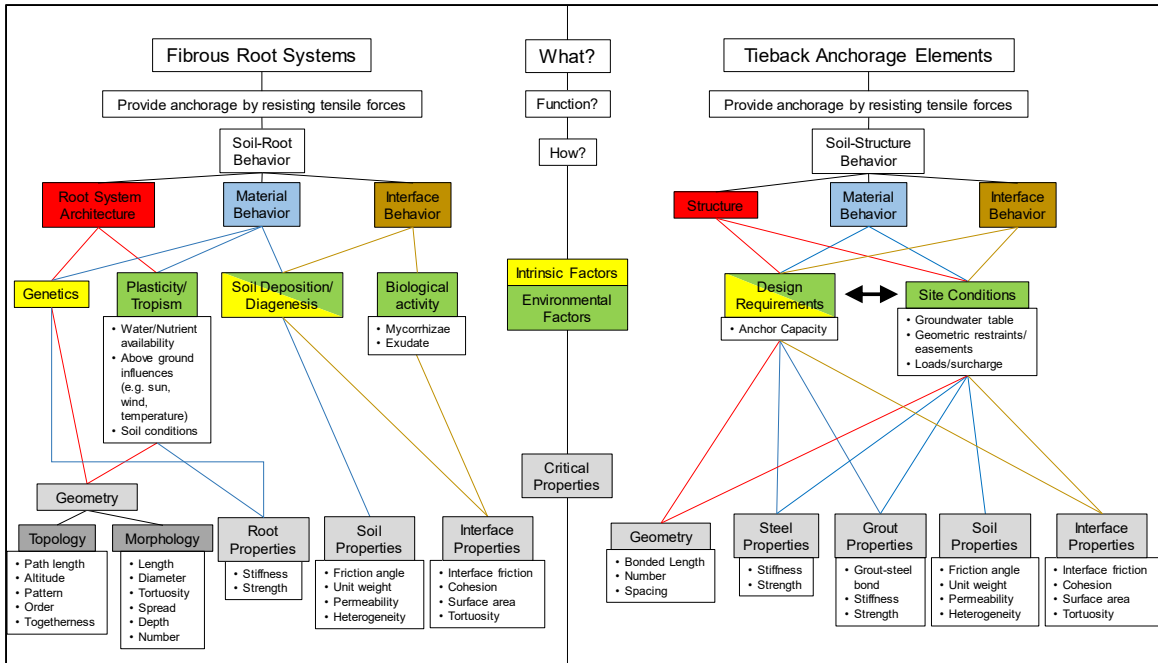
Figure 5-2. Example of the alignment of anchorage principles of fibrous root systems and ground anchors through use of a functional decomposition.

Step 3) Design and evaluation of a root-inspired element

For step three of the design process, root system attributes were translated into a proposed root-inspired geotechnical design. Translate in this context refers to the process of transferring attributes of the root system to a geotechnical design. The various root-inspired designs were then evaluated through both traditional design methodologies and geotechnical analyses depending on the iteration cycle. For example, in the second iteration, various proposed root-inspired designs were evaluated using four-box comparison diagrams as shown in Table 5-1 and Table 5-2. Additionally, in iteration three, two fibrous root system-inspired anchor models were designed and evaluated, and the results of this work comprises all of the subsequent research in both this chapter and all subsequent chapters.

Table 5-1. Four-box comparison diagram for wind turbine foundations (product of Iteration 2).

Root-inspired Wind Turbine Foundations	
Operational Environment	**Functions**
- Wind turbines are constructed both on- and offshore in a variety of soil conditions	- Support self-weight of structure o Wind turbine tower, blades, and nacelle (~150 tons) - Resist bending moment due to wind loads - Resist wave loads (offshore)
Specifications	**Performance Criteria**

- Materials
  o Typical geotechnical foundation materials (concrete and steel)
- Construction
  1. Horizontally drill laterals
  2. Jet grout laterals (pressurized grout injection)
	- Settlement
	  o Total Settlement
	  o Differential settlement
	- Bearing capacity
	  o Must exceed self-weight, wind, and wave loads
	- Efficiency
	  o Equivalent capacity with less cost of material

Table 5-2. 4-box comparison diagram for ground anchors (product of Iteration 2).

Root-inspired Anchors	
Operational Environment	**Functions**
- Used to reinforce retaining walls - Anchored into soils with sufficient resistance - Typically used in sands, gravels, and stiff clays	- Provides added stability to retaining wall
Specifications	**Performance Criteria**

- Materials
  o Steel tieback (cable or rebar) and grout
- Construction
  o Pre-tensioned steel
  o Tieback grouted past active horizontal stress ratio line
- Branching Construction
  1. Horizontal drill branches
  2. Percussion hammer branch structure in soil (spread with wedge)
	- Design Pullout Resistance
	- Testing Regimen
	  o Proof and performance loading requirements
	  o Must meet state codes

Step 4) Selection and design of an operational root-inspired product

To this end, the bio-inspired design process is incomplete. This dissertation goes so far as to design and evaluate root-inspired anchor models. Not only does the proposed design need to be scaled to practical conditions, but also a market for this design must exist.

5.1.1 Iterative Progression

The root-inspired geotechnics design process featured three primary iterations. The eventual selection of a fibrous root system-inspired anchorage element was only achieved in the third iteration. Table 5-3 provides a synopsis of the activities completed in each cycle of the design process. The termination of a cycle is recognized when the information accumulated previously does not allow for the completion of the current step.

Table 5-3. List of tasks completed in each step of the design process per iteration.

	Iteration 1	Iteration 2	Iteration 3
Step 1	**Action:** General accumulation of root system principles into five overarching categories (i.e. biological, chemical, hydrological, mechanical, thermal)	**Action:** Accumulation of anchorage specific principles	**Action:** Accumulation of specific anchorage principles of fibrous root systems
Step 2	**Action:** Identification of geotechnical problem areas **Halt:** Insufficient accumulation of root system principles to provide solution to geotechnical problem space **Decision:** Inadvertent focus on mechanical attributes	**Action:** Alignment of root system anchorage principles with select geotechnical issues	**Action:** Alignment of anchorage principles of fibrous root systems and geotechnical anchorage elements
Step 3	--	**Action:** Ideation of three root-inspired geotechnical elements and comparison with four-box diagrams	**Action:** Development and evaluation of root-inspired anchor through pullout tests

		Halt: Insufficient details of uplift anchorage mechanics of fibrous root systems **Decision:** Focus on fibrous root system-inspired anchor elements	
Step 4	--	--	**Action:** In progress, selection of root-inspired anchor model features for upscaled uplift test

5.2 Identification of Biological Inspiration

Within this section, the logical selection of fibrous root systems as the principal source of biological inspiration as well as the selection of specific root system architectural features beneficial to uplift anchorage are described.

5.2.1 Plant Root System Utilization

Plant root systems have existed for over 400 million years and have undergone extensive evolutionary adaptations. As such, sufficient information is contained within extant root systems which can act as a source of biological inspiration. Moreover, the multifunctionality (i.e. nutrient absorption, anchorage, vegetative reproduction, energy storage), material efficiency (e.g. evolutionary adaptations, I-beam cross sections), and adaptability (e.g. phenotypic plasticity, tropic responses) aspects of root systems are appealing to geotechnical engineers with sustainability and resiliency initiatives. Resiliency (i.e. the ability to withstand and recover rapidly from major threats) and sustainability (i.e. the process of achieving present goals while recognizing future social, economic, and environmental needs) can be incorporated convergently and synergistically

in geotechnical infrastructure if the principles of root systems can be properly utilized. Furthermore, plant root systems serve as prime source of inspiration for anchorage-focused geotechnical designs. Root systems are ubiquitous, provide mechanical stability for most of the Earth's biomass, and provide a critical functionality for most plants, since plants will perish if anchorage is comprised. Furthermore, the thigmotropism ability of root systems reveal that plant roots actively sense and adapt to mechanical loads and internal stresses to improve their anchorage capacity, and therefore, root systems contain information within their architecture to enhance their anchorage ability.

5.2.2 Fibrous Root System Selection

As described in the root-inspired geotechnics design process, the selection of fibrous root systems as the primary source of biological inspiration was a multistage development. The properties of fibrous root systems were first targeted after the initial discovery that plant biologists theorize that fibrous root systems contain optimized architecture features to resist uplift forces due to evolutionary pressures from grazing herbivores (Ennos 2000). Despite the fact that fibrous root systems are only required to provide a greater resistance than the tensile strength of the plant stem, undoubtedly, by natural selection, plants that can achieve adequate anchorage with minimal resource consumption are favored. More so, though fibrous root systems experience forces and moments due to self-weight, wind, precipitation, and trampling amongst others, the ultimate load a fibrous root system can experience is a vertical uplift force due to foraging animals (Ennos 1989, Ennos 2000). As a result, the possible loading conditions were identified for each of the root system architecture classifications (Table 2-2), and for root-inspired designs, it provides a means to associate and relate a root system classification

with the mechanical loading conditions of the proposed bio-inspired design. The basis of the argument is presented as follows: since a root system architecture contains information to resist a primary force in a particular direction and a root-inspired design is subjected to a load in the same direction, the information contained in a root system architecture, therefore, can serve to inspire the design process. As an example of this concept, a plate root system can serve to provide valuable inspiration for the redesign of a foundation to stabilize wind turbines, since both elements (i.e. plate root and turbine foundation systems) share a common primary loading condition of lateral wind forces. Conclusively, Table 2-2 serves as an initial robust methodology for the alignment of the characteristic load and root system architecture as well as for the initiation of a root-inspired anchorage design. The final selection of fibrous root systems as the chief source of inspiration was the result of a direct comparison of the uplift anchorage mechanics between fibrous root systems and ground anchors, where numerous similarities were revealed (Figure 5-2).

5.2.3   Feature Selection

With the determination of a fibrous root system-inspired anchorage element as the objective of the root-inspired project , the goal of feature extraction was to identify the properties of root systems that could most effectively enhance the pullout behavior of a conventional anchorage system. The features of fibrous root systems were gradually accumulated and refined through the root-inspired design process. An emphasis was solely placed on uplift anchorage characteristics, while features not directly associated with the mechanical behavior of root systems were neglected. The methodology for the identification of pullout behavior enhancing root system architecture characteristics consisted of an extensive examination of documented root and root analog pullout tests as

well as an experimental program and ensuing analysis on the pullout behavior of fibrous root systems. Root system architectural properties that displayed a positive relationship with pullout behavior indicators were highlighted and detailed in Table 2-3.

5.2.3.1 Pullout Tests of Fibrous Root Systems

A series of pullout experiments were performed on two plant species with fibrous-type root systems, King Richard leek plants (*Allium porrum*) and spider plants (*Chlorophytum comosum*). These plant root systems were selected due to their relatively high root diameter to length aspect ratio, ease of growth, and existence of published pullout data. Complete details of the experimental program including plant selection and cultivation, specimen preparation, pullout procedure, and anatomical examination are included in Chapter 4: Materials and Methods. In summary, 36 root systems, 29 leek plants and 7 spider plants, were uplifted from a semi-saturated fine silica sand while force and displacement measurements were recorded. After the root systems were extracted from the soil, the anatomical features of both the intact root system and dismembered roots were quantified, and their relationship with pullout behavior indices was analyzed.

5.2.3.1.1 Pullout Behavior

Figure 5-3 displays the typical force-displacement curve generated from the pullout of the fibrous root systems of spider and leek plants. The force-displacement trajectory is an expression of the global pullout response of a root system. Multiple ongoing and competing mechanisms are captured simultaneously forging a convoluted global pullout response, and the overall behavior is the resultant of three system constituent behaviors, the soil response, the root system response, and the soil-root interaction response. For

example, as a root system is lifted from the soil, some resistance is provided by the rigidity of the individual roots, where various elongation processes occur including material deformation, extension of tortuous members, and alignment of eccentrically located members in relation to the loading direction. Additionally, resistance develops due to shearing at the soil-root interface and effective soil-root cohesion due to cementation (e.g. chemical precipitation, biological growth), suction, and geometric restrictions (e.g. lateral branching, tortuosity). Furthermore, soil particles are mobilized due to the movement of the root system and engage the shearing resistance of the soil mass. To add further complexity, both geomaterials and plants behave non-linearly and non-elastically upon loading due to Hertzian and Mindlin contact theory, respectively, for particulate media, and due to the cellular structure for plants (Ashby and Medalist 1983). As well, the strength of both materials is strain dependent. The behavior of cellular structures is dictated by cell arrangement and geometry as well as mechanical properties of the cell walls. Upon tensile loading, the stress-strain response of plant materials is characterized by three unique regimes, 1) a linear elastic regime at small strains, 2) a non-linear plastic regime due to cell buckling and wall failure, and 3) a strain hardening or densification regime (Ashby and Medalist 1983, Niklas 1989).

Within the force-displacement curve, several unique features are present in comparison to those produced in most geotechnical analysis, which can be mainly attributed to the qualities of the root system including root system architecture and the mechanical behavior of plant tissue. Firstly, a bimodal force-displacement curve pre-peak pullout resistance exists for the pullout of all plant root systems tested and is clearly evident when analyzing the tangent stiffness (Figure 5-4). This behavior indicates that an initial

elongation of the system occurs before the full resistance of the system is engaged, and a potential explanation includes the alignment of the primary root system axis with the loading direction, involving lateral and elongational movement of the below-ground stem and the passive resistance of the soil. The soil-root system deforms as a greater pullout force is applied until the peak pullout resistance (i.e. pullout capacity) is reached, after which immediate reductions in pullout resistance are observed due to the tensile failure of individual root axes.
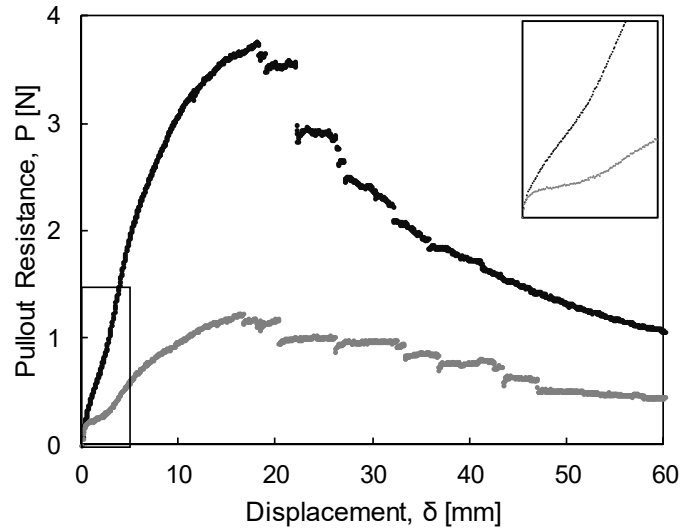
Figure 5-3. Typical force-displacement curves for the uplift of fibrous root systems (black and gray curves correspond to the spider and leek plants, respectively).
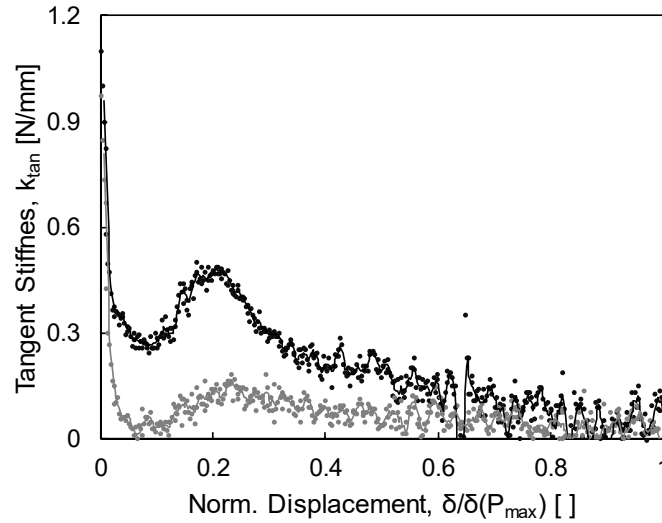
Figure 5-4. Tangent stiffness up to pullout capacity (black and gray curves correspond to the spider and leek plants, respectively).

5.2.3.1.2   Feature Selection Analysis

The primary goal of testing fibrous root systems in pullout was to identify the prominent predictors of pullout behavior as characterized by pullout behavior indices. Traditional statistical and machine learning techniques were used to identify the salient features. For all techniques, a matrix with pullout behavior indices, soil conditions (i.e. void ratio and unit weight), and root system anatomical attributes was manipulated to extract the desired outcome.

5.2.3.1.2.1   Correlation Coefficients

In the first analysis, Pearson's correlation coefficient, which determines the linear correlation between variables, was utilized, where the correlation coefficient, *C*, is computed for each feature set, *f*, and each dependent pullout behavior index, *D*, among all test observations, *n* (Equation 12).

$$C(f,D) = \frac{1}{n-1} \sum_{i=1}^{n} \left(\frac{f_i - \mu_f}{\sigma_f} \right) \left(\frac{D_i - \mu_D}{\sigma_D} \right) \tag{12}$$

Consequently, a matrix of correlation values was generated and is displayed visually in Figure 5-5, where the more saturated red and blue colors represent higher positive or negative correlations, respectively. The matrix is comprised of 17 or 18 rows (depending on the plant system of interest) corresponding to the number of features, and 3 columns corresponding to the pullout behavior indices, (1) pullout capacity, (2) displacement at pullout capacity, and (3) secant stiffness. The features list is as follows: (1) soil void ratio, (2) saturated unit weight, (3) above-ground dry mass, (4) below-ground dry mass, (5) above-to-below ground dry mass ratio, (6) maximum above-ground length, (7) maximum below-ground length, (8) above-to-below ground maximum length ratio, (9) number of intact roots, (10) cumulative root length of intact root system, (11) mean root length of intact root system, (12) maximum root length of intact root system, (13) number of dismembered root segments, (14) cumulative length of dismembered root segments, (15) mean length of dismembered root segments, (16) maximum length of dismembered root segment, (17) root system diameter at soil surface, and (18) mean root segment diameter. Feature 18, mean root segment diameter, is not present in the leek study because an accurate measure of the diameter of the leek rook segments could not be achieved with the utilized caliper.

The linear regressions of the leek plant root system features with the highest absolute Pearson's correlation coefficients are shown in Figure 5-6. In all cases, the p-value is much less than 0.01, indicating statistically significant values. Due to the small sample

size of tests conducted on Spider plants, stronger correlations, both positive and negative,

occurred. When results from both leek and spider plants were combined, the above- and

below-ground dry mass features provided the strongest correlation with pullout capacity

and secant stiffness, respectively (Figure 5-7).
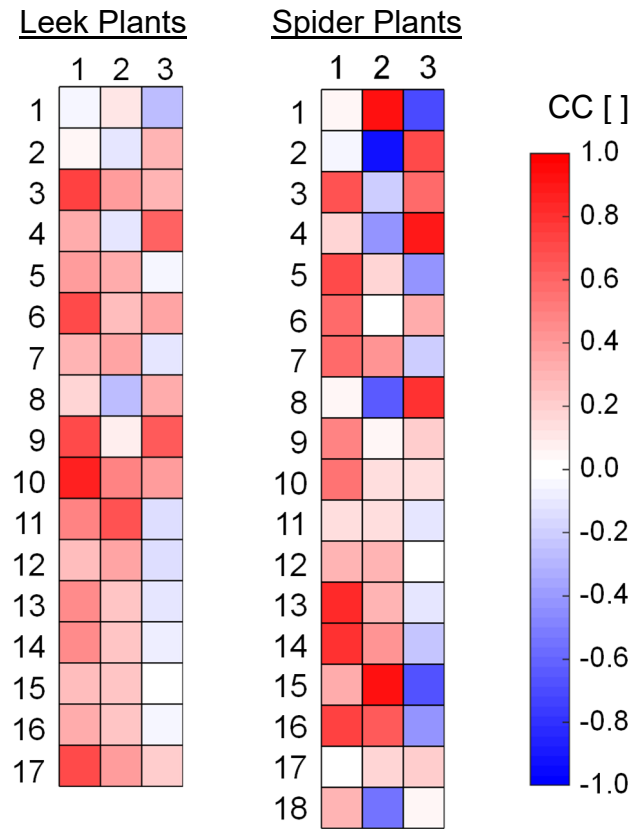
Figure 5-5. Correlation coefficient matrices for leek and spider plants.
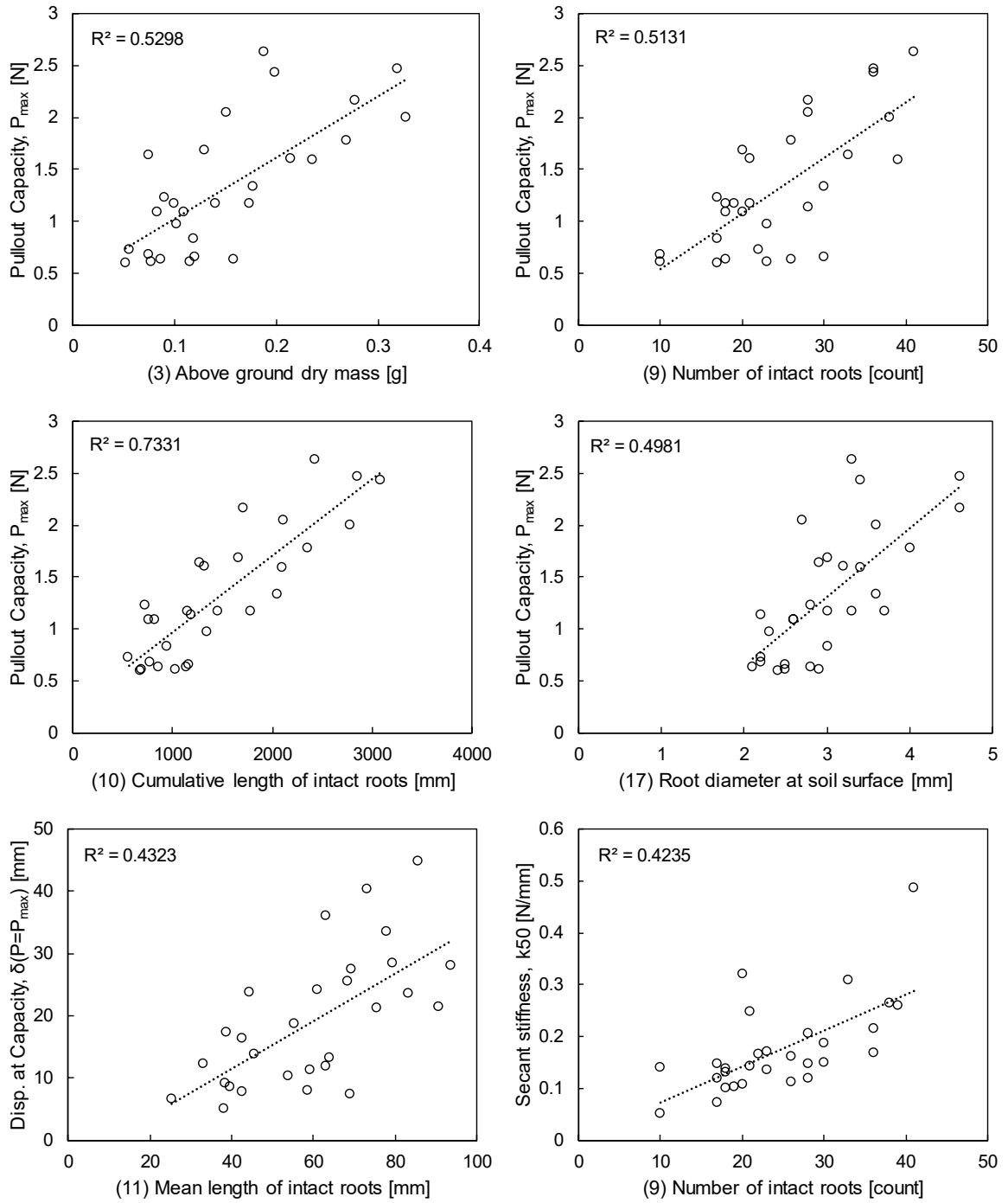
Figure 5-6. Compilation of best linear regressions between pullout behavior indices and leek plant root system features as determined by Pearson's correlation coefficient.
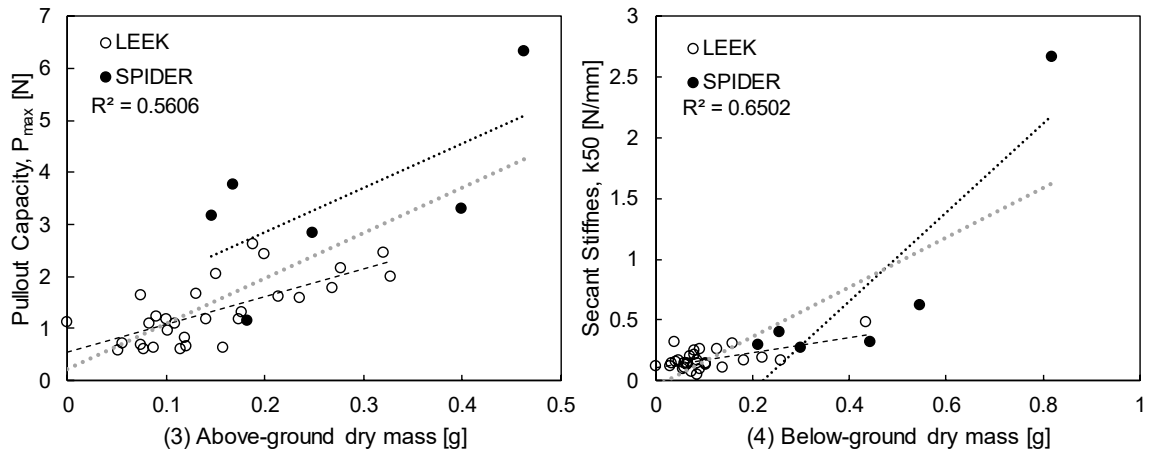
Figure 5-7. Best linear regressions for combined leek and spider plant data sets as identified by Pearson's correlation coefficient.

5.2.3.1.2.2 Random Forest Analysis

In machine learning, algorithms are utilized to generate predictions given sample data. The random forest algorithm is one such machine learning algorithm that constructs a group or forest of decision trees and provides the mean prediction (Ho 1995). For each decision tree, a subset of the total number of observations is used and then error tested with the unsampled observations. Additionally, for each node within each decision tree, a subset of the number of input features is tested for the best split and then selected. From the original Classification and Regression Tree (CART) algorithm implemented in Matlab, the best split is determined based upon the maximum Gini index. For this analysis, feature importance is estimated through permutations of the observations within a selected feature and then determining the error from permuting those observations, and if the error remains the same through all permutations, the feature is not important. More precisely, the importance of the individual features to the various pullout behavior indices are determined by identifying the lowest normalized mean error among sampled and unsampled observations for all decision trees.

For the leek plant data set, a Random Forest analysis with 200 trees revealed the salient features necessary to predict the three pullout behavior indices (Figure 5-8). For the prediction of pullout capacity and secant stiffness, common salient features were identified including cumulative length of intact root system, number of intact roots, maximum above-ground length, root system diameter at soil surface, and number of dismembered roots.
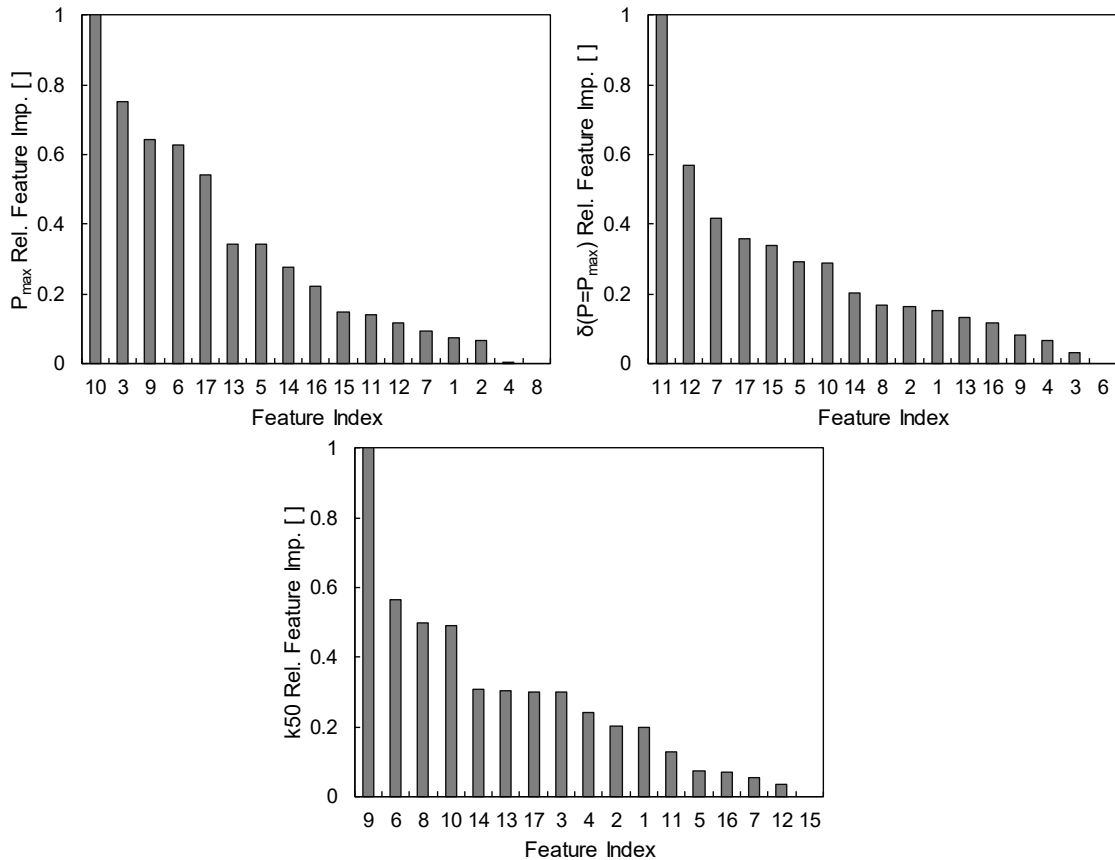
Figure 5-8. Relative feature importance for the three pullout indices as identified from a Random Forest analysis of the leek plant pullout data.

With the abundance of machine learning algorithms ubiquitous in most high-level programming platforms, accurate predictions are obtainable given the multitude of literature data on almost any geotechnical problem. In fact, predictive models of anchor pullout capacity have employed a variety of machine learning algorithms, including

artificial neural networks, genetic programming, and support vector machine (Alavi et al. 2011, Muduli et al. 2013, Cheng et al. 2014, Moayedi and Rezaei 2019). Using the limited data set, a random forest model was developed in Matlab to predict pullout capacity from either one or two readily measureable above-ground leek features and was then compared to a linear regression model. With the sole use of the above-ground height feature of leek plants, a random forest model achieved a coefficient of determination of 0.65, in comparison to 0.49 for the linear regression model (Figure 5-9(left)). When adding the root system diameter at the soil surface feature to the models, the coefficient of determination values improved to 0.67 and 0.56 for the random forest and linear regression models, respectively (Figure 5-9(right)).
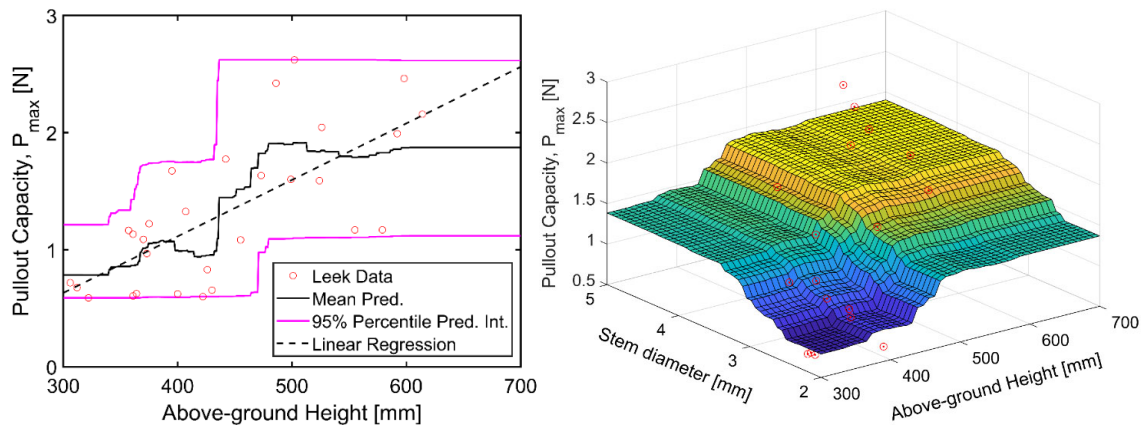
Figure 5-9. Random Forest models for the prediction of pullout capacity utilizing (left) one or (right) two above-ground leek plant features.

5.3 Root-Inspired Anchor Models

5.3.1 *Objectives/Constraints*

Two main objectives for the design of a root-inspired anchor model were as follows: 1) to strategically incorporate selected root system features in a manner that allows

for decipherable parametric studies, and 2) to develop models capable of being described by simple analytical descriptions that would allow for rapid and repeatable fabrication and would aid in evaluation. Together both of these objectives act to constrain the translation of biological principles into the design space.

5.3.2 Salient Fibrous Root System Features

Analysis of both documented pullout experiments and those conducted for this research revealed several salient features of fibrous root system architecture to root system pullout behavior, with an emphasis on pullout capacity. From the experimental endeavor specifically, the cumulative length of the root axes and the number of root axes were the top predictors of pullout capacity and secant stiffness, neglecting above-ground specific plant features, while mean root axis length, maximum root length, and maximum depth were the best indicators of failure displacement. From Table 2-3, several additional features, including dry weight, root axis diameter, tortuosity, branching angle, depth, lateral spread, and topology, positively correlate with pullout capacity. Features that did not have a strong correlation with the pullout behavior indices or those that were not important for predicting pullout behavior were deemed irrelevant and were not purposefully incorporated into the root-inspired anchor models.

5.3.3 Feature Incorporation and Model Description

Two distinct models were devised to incorporate as many of the extracted fibrous root system features into a conventional anchorage element as feasible. The primary concept for the design of both models was to metamorphose a linear anchorage element into a bifurcating structure through specific and systematic transformations. First, a morphology-

type root-inspired anchor model was generated that incorporates six identified fibrous root system features, which includes 1) model depth, H, 2) number of branch axes, n, 3) length of individual root branch axes, L, 4) diameter of root members, d, 5) root system breadth, b, and 6) internal branching angle, α (Figure 4-4). To note, internal branching angle, branch length, and root system breadth are interrelated and therefore, oppose the first objective since the effect on pullout behavior of changing these parameters cannot be definitely resolved. Second, a topology-type root-inspired anchor model was devised to elucidate the role of topology on pullout behavior. Models were formed by unraveling steel or polymer wire at various branching orders (Figure 4-5). Specific details of the models including fabrication and material components are described in Chapter 4.

5.3.3.1 Limitations to Design

Through the entire design process, several adverse factors acted to restrain the ultimate design. First, an intrinsic bias is imparted on the project due to the mechanically-focused geotechnical engineering affinities of the primary actor. The entire process tended towards the anchorage mechanics of the soil-root system, and this effectively neglected the various other root system principles in the arguably more researched realms of root system biology, hydraulics, chemistry, and thermal performance. To mitigate this bias in future root-inspired geotechnic studies, a multidisciplinary design team is proposed, comprised of both plant biologists and engineers, as well as required checkpoints, where full reasoning concerning actions at every design step must be provided and agreed upon. In addition, only a select group of root system features were systematically studied and extracted for incorporation. Though other root features and soil-root phenomenon were ignored, they were not considered negligible to the anchorage of plant root systems. Examples of

neglected fibrous root features and soil-root phenomenon include root hairs, root tortuosity, actual root strength and stiffness properties, mucilage effects (dry or wet), soil densification due to root growth, and soil moisture. Furthermore, features of the fibrous root system architecture vary with time and space and are not the sole expression of a particular root function but rather the integrated resultant of both endogenous and exogenous factors. As such, features of the root system architecture beneficial for pullout anchorage are not specific to the anchorage functionality, but belong to the integrated environmental system of the plant. As a result, the engineer recognizes that the fibrous root system features selected to enhance the pullout behavior of geotechnical anchorage elements contain information regarding a variety of other processes, such as geotropism, hydrotropism, and nutrient acquisition. Finally, the development and fabrication of the root-inspired models were constrained by the fabrication processes. Selected features of the root system were studied within the confines of the ability of the 3D printer, which dictates the minimum achievable root diameter and obtainable material physical properties. However, for each print, the properties of the printing algorithm were kept constant. Additive manufacturing was selected as the principle method of model creation due to the rapidity, precision, and economic viability of the system. Furthermore, this study recognizes the irreconcilable differences in material properties between living plant root axes and the various materials used for model fabrication, and undoubtedly, the global pullout response is affected by this choice. However, due to the constraints on geotechnical anchorage systems, in particular the system displacement restrictions and capacity requirements, utilization of materials for 1g model tests with strength and stiffness properties abiding to the laws of similitude (i.e. representative properties when scaled) is logical. Overall, this section serves to expose the

weaknesses of the developed root-inspired anchorage models with the purpose of, 1) fully detailing the design process so as to provide limits on extrapolated expectations and conclusions of the design, 2) elucidating specific areas of potential improvement for future bio-inspired geotechnical designs, and 3) rationalizing the inherent or induced faults.

5.3.4   *Properties of Root-Inspired Anchor Models*

The properties of the root-inspired anchor models are detailed with a specific focus on the properties utilized in the analysis of pullout behavior.

5.3.4.1   Geometric Description

The morphology-type models are comprised of two main parts, the stem and the branch members, where the point of dichotomy is defined as the location where branching initiates. Additionally, all branch members are equally spaced as viewed from plan view. Given the geometric constraints, the models can be fully described mathematically with five morphology-type parameters (i.e. embedment depth, H, branch axis length, L, branch axis diameter, d, internal branching angle, α, and number of root branch axes, n). Additionally, for the topology-type models, the branch axis length-to-embedment depth ratio, L/H, is held constant at 1/2.

5.3.4.1.1 Model Volume

Model volume is required for the determination of the material efficiency index, Π_M, where pullout capacity is normalized by the unit weight of the root-inspired models (i.e. the product of material density and model volume). The material efficiency index therefore provides insight into the optimal model geometry per volume of material used. The full

solution to the volume of the defined morphology-type root-inspired model is not performed due to the rigorous analysis required. For simplicity, an empirical model inspired from the solution to a Steinmetz solid was developed (Equation 13). A select group of models were used to calibrate the empirical model, where the true volume of the models were obtained from Autodesk Inventor, and with a fitting parameter, X, of 1/15, the percent error is less than 0.2%.

$$V \approx \frac{\pi}{4} d^2 \left(L_s + nL - X \frac{dn^2}{\sin \alpha} \right) \tag{13}$$

For the wire rope topology-type models, the volume is that of a cylinder.

5.3.4.1.2 Projected Area

For the branched portion of the morphology-type root-inspired anchor model, the ratio of the external surface area to the surface area of a cone (i.e. when the branched portion is completely filled with branches) is shown in Equation 14. As a simplification, the surface area of the branched section only includes the intersecting area of a cone with the same internal branching angle and length with the branched portion.

$$\frac{A_{roots}}{A_{cone}} = \frac{nd}{2\pi L \sin \alpha} \left[\frac{\sin\left(\frac{\pi}{n} - \sin^{-1}\left(\frac{d}{2L\sin\alpha}\right)\right)}{\sin\frac{\pi}{n}} + 1 \right] \tag{14}$$

5.3.4.2 Physical Properties

Relevant physical properties, including effective pullout stiffness and surface roughness, of root-inspired anchor models are presented.

5.3.4.2.1 Pullout Stiffness of Root-Inspired Anchor Models

Ring pullout tests were performed on morphology-type root-inspired anchor models with the Ring Pullout Apparatus, which was designed to evaluate the stiffness of root-inspired anchor models of various geometric morphologies. A semi-analytical equation was developed to predict pullout stiffness of morphology-type anchor models. In particular, knowledge of anchor stiffness is critical for proof and performance testing as well as infrastructure system strain compatibility. Details of the apparatus and experimental procedure are contained within Chapter 4. The goal of these pullout tests was to explore the pullout behavior of root-inspired models without the complexity of soil.

5.3.4.2.1.1 Ring Pullout Tests

Ring pullout stiffness, k_R, for these models is defined as the vertical pullout force, P, over the vertical displacement, δ_y., as shown in Figure 5-10. For the parametric analysis, number of branch axes and the interior branching angle were varied with different ring diameter configurations.

$$k_R = \frac{P}{\delta_y}$$
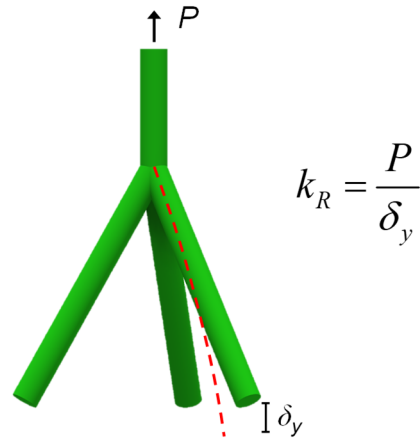
Figure 5-10. Schematic defining parameters involved in the determination of ring pullout stiffness.

From the ring pullout tests, the initial stiffness was determined from the initial linear portion of the vertical pullout force versus vertical displacement data, which is illustrated in Figure 5-11.
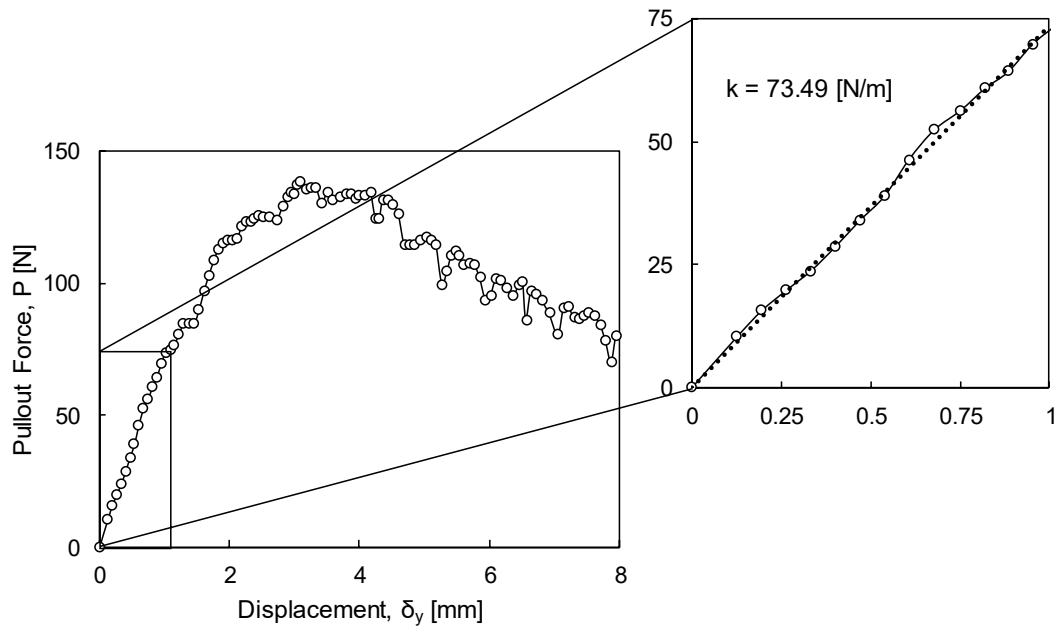
Figure 5-11. Sample ring pullout force versus displacement curve (model: n4a45L75d5) and enlarged region for stiffness determination.

144

5.3.4.2.2 Pullout Stiffness Analytical Model

A simple analytical model to predict stiffness was derived from the basic equation for the deflection of a cantilever beam subject to a point load on the free end, as schematically shown in Figure 5-12, where R corresponds to the pullout apparatus ring aperture radius. The reaction force, R_F, due to the contact of the upwardly displaced model and the fixed ring pullout apparatus is normal to the axial axis of the branch and occurs at some length along the root-inspired model branch. Ring pullout stiffness is calculated from the initial portion of the pullout response since the beam deflection equation, derived from the Euler-Bernoulli beam equation, is applicable only for small deflections (i.e. $\delta < 0.1L$). For greater movements, a two-dimensional analysis must be completed (Bisshopp and Drucker 1945).
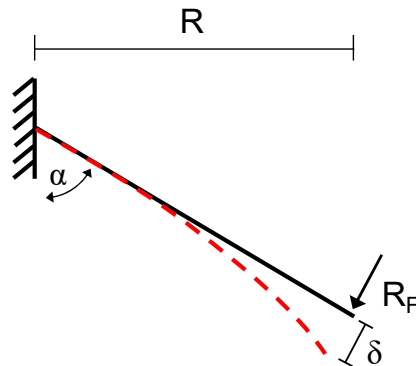
Figure 5-12. Representation of the deflection of a cantilever beam at a described angle.

The vertical pullout resistance, P, is the result of the summation of vertical components of the reaction forces on each branch, assuming the axis of the ring aperture and axis of the anchor model are aligned (Equation 15).

$$P = \sum_{i=1}^{n} R_{Fy,i} = nR_F \sin \alpha \qquad (15)$$

The deflection, δ, of a fixed cantilever beam due to a point load on the free end is the foundation of the derivation and shown in Equation 16.

$$\delta = \frac{R_F L^3}{3EI} = \frac{R_F}{3EI} \left(\frac{R}{\sin \alpha} \right)^3 \qquad (16)$$

Substituting Equation 15 and 16 into the definition of ring pullout stiffness, k_R, produces the final model (Equation 17).

$$k_R = \frac{P}{\delta_y} = 3nEI \left(\frac{\sin \alpha}{R} \right)^3 \qquad (17)$$

5.3.4.2.2.1 Model Validation

In general, the analytical model underpredicts pullout stiffness by a factor of two, which suggests an additional mechanism is missing from the model. One possible explanation is that the models are materially fortified in the immediate vicinity of the point of dichotomy, which would augment the pullout stiffness especially for models with greater number of branch axes, larger branch axis diameters, and with shorter cantilever arms. However, for a first order approximation of pullout stiffness, a simple correction factor of two provides satisfactory results, as executed in Equation 18 and shown in Figure 5-13.

146

$$k \approx 6nEI \left(\frac{\sin \alpha}{R} \right)^3 \tag{18}$$
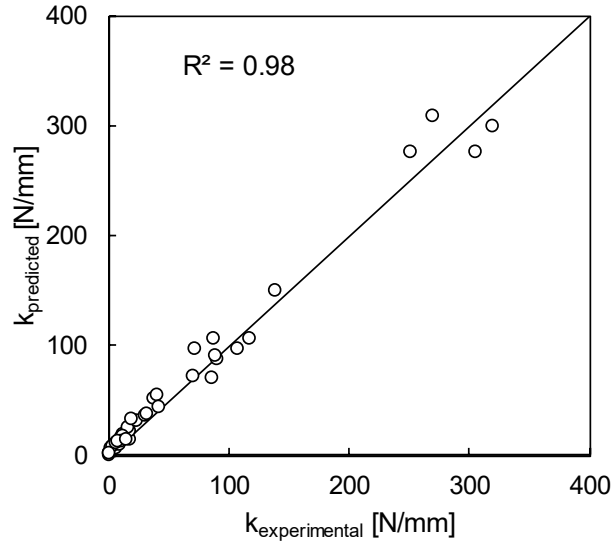
Figure 5-13. Analytical versus experimental pullout stiffness for the simple cantilever model.

5.3.4.2.3 Full Model Ring Pullout Stiffness

Thus far only the stiffness of the branched portion of the morphology-type root-inspired anchors has been considered; however, the stem portion also contributes to total model stiffness. Ring pullout stiffness of the entire root-inspired model can be determined as a combination of the stiffness values of the stem and the branched section in series, where the stiffness equation for the entire model is shown in Equation 19.

$$k_{model} = \frac{k_b k_s}{k_b + k_s} = \frac{3\pi n d^4 E \sin^3 \alpha}{12 n d^2 L_s \sin^3 \alpha + 32 R^3} \tag{19}$$

With the addition of stem length, all models will experience a reduction in pullout stiffness, and models with larger diameters experience a greater stiffness reduction.

5.3.4.2.4 Pullout Stiffness of Plate and Conical Anchor Models

Additionally, within this dissertation, root-inspired models are compared to conventional plate anchors, and for this purpose, the stiffness of plate anchors is approximated using plate theory. For a plate of thickness, *b*, simply supported in the center with a line load on the edge, the stiffness is defined in Equation 20 and is applicable for small deflections and for small thickness-to-width ratios (i.e. $\delta/d < 0.1$ and $d/b < 0.1$).

$$k_{plate} = \frac{4\pi E d^3}{3(1-v)(3+v)b^2} \tag{20}$$

Furthermore, comparisons in anchor pullout behavior are made between root-inspired models and conical models, which represent models that have the maximum number of branch axes (i.e. branch spacing angle is equivalent to 0). A demanding analysis with shell theory is required to compute pullout stiffness for a conical model, as opposed to the simplistic equation for plate models. (Altman and Young 1968, Tavares 1996). Pullout stiffness of a complete cone subjected to a compressive axial load with a fixed base is shown in Figure 5-14a, where the stiffness is normalized by the maximum stiffness, and this analysis has been completed following the work of *Tavares 1996*. Furthermore, for a truncated cone subjected to a compressive axial force on the top and fixed at the bottom boundary, pullout stiffness has been determined via an elastic FEM analysis performed in Abaqus, and the results are highlighted in Figure 5-14b. Both models demonstrate an exponential increase in stiffness with increasing internal branching angle, and for the 90° case, which is equivalent to a plate, the analytical shell method and FEM analysis predict the same stiffness value as in Equation 20.
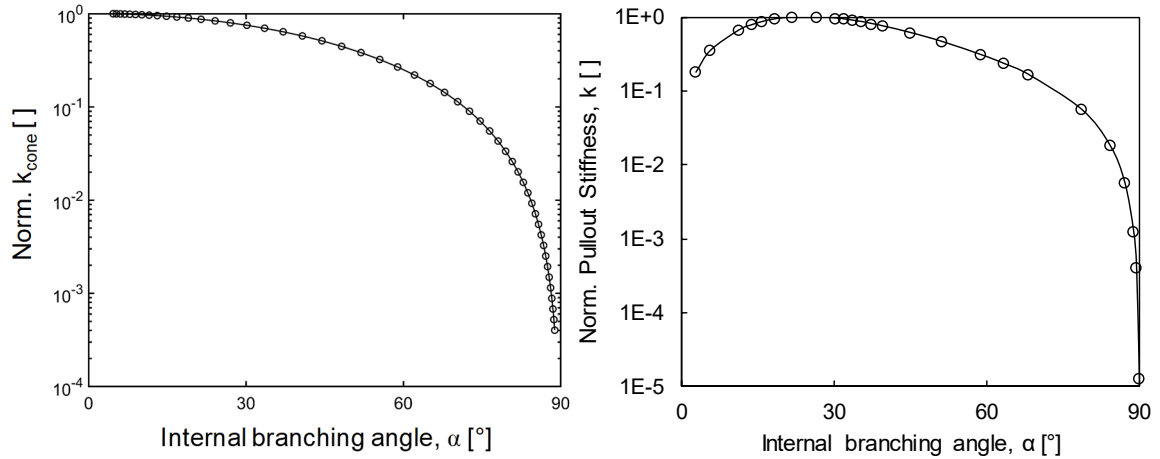
Figure 5-14. Normalized pullout stiffness of a complete (left) and truncated cone (right) subjected to a compressive axial load and fixed at the base.

5.3.4.3 3D Printed Model Surface Roughness

For all models fabricated with the Lulzbot TAZ 6 3D printer, the models were printed in the same orientation as shown in Figure 4-4. Filament layers were deposited in 0.18mm increments. When scanned with a 3D optical profilometer (i.e Zygo NewView 8300), filament ridges occur every 0.15mm, which is finer than the prescribed layer thickness (Figure 5-15). Surface-particle interlocking can occur for geomaterials with particle sizes less than the 0.15mm, and as such, differences in interface shear behavior is expected between relatively similar geomaterials with varying size distributions about and below the 3D printing resolution (e.g. Ottawa F110 and Ottawa 20-30), as documented in Chapter 10.
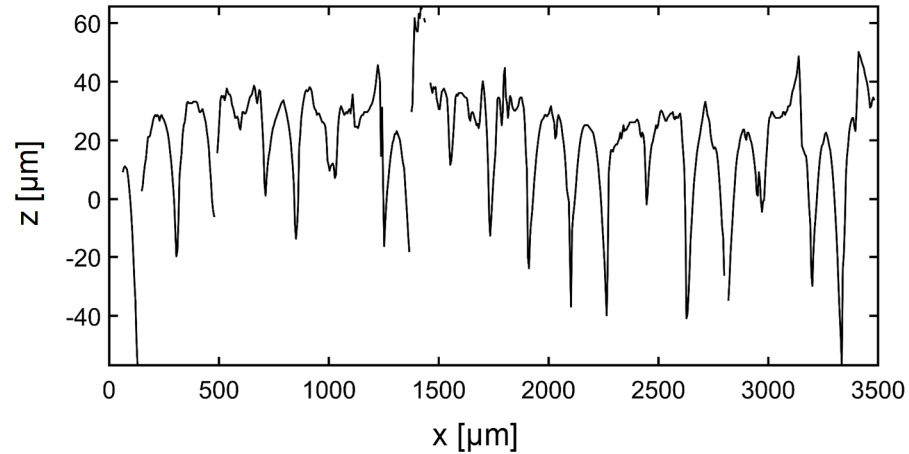
Figure 5-15. Linear surface profile of a 3D printed ABS cylinder.

5.4   Conclusions

A few of the salient conclusions derived from this chapter are as follows:

•   The multifunctionality, adaptability, and material efficiency aspects of root systems offer themselves as prime sources of inspiration for sustainable, resilient geotechnical infrastructure design.

•   Fibrous root systems contain information within their architecture to resist pullout forces (e.g. grazing herbivore induced evolutionary adaptations, plasticity, thigmotropism).

•   As indicated from the literature and from pullout tests on leek and spider plant root systems, the total length of the root serves as a principal indicator of root system pullout capacity.

•   Association of root system architecture and common loading condition serves as a robust initial methodology for providing inspiration for root system-inspired geotechnics that seek to enhance anchorage behavior, be that resistance to pullout, lateral, compression, or combinatory loads.

•   Two types of root-inspired anchor models were designed that incorporate the morphological and topological properties of fibrous root systems; yet, a few limitations of the design and design process are acknowledged, including the inherent design bias due in part to the interests of the principal designer, incorporation of root system features for anchorage enhancement that actually exist for a multitude of functions, and anchor model fabrication constraints.

•   Ring pullout stiffness of a root-inspired anchor model can be well captured using a spring-in-series model incorporating both stem stiffness and branch axis stiffness, modeled as cantilever beams.

•   The surface roughness of root-inspired anchor models manufactured with fused filament fabrication 3D printing is governed by the layer thickness of filament deposition, and the mean particle diameter-to-characteristic layer thickness ratio will be important for assessing the geomaterial-3D printed plastic interface strength.

Special Recognition: Rodrigo Borela, Sangameshwar Hanumasagar, and Caroline Colbert for assistance with fibrous root system experiment; Mahdi Roozbahani for assistance with Machine Learning; Ben Kalziqi and Prashanth Vangla for assistance with surface profilometry of 3D printed plastic surface

CHAPTER 6.   PULLOUT BEHAVIOR OF ROOT-INSPIRED

ANCHOR MODELS: EXPERIMENTAL ENDEAVOR

The purpose of this chapter is to evaluate the global pullout response of root-inspired anchors. The term global signifies that the behavior of the entire soil-anchor system is investigated, which is in direct comparison to analyzing the behavior of the soil or root-inspired anchor model individually at the local scale. Before the relatively geometric complex root-inspired models were tested, a series of pullout tests was performed on anchor piles and plates to form a basis of comparison (i.e. to quantify the enhanced pullout behavior of root-inspired anchor over conventional pile and plate anchors) and validate the experimental procedure. Following, a parametric study was performed on the effect of the geometric features of root-inspired anchor models as well as soil parameters on pullout behavior. The overall goal of this chapter is two-fold: 1) to systematically study the effect of incorporated plant root features and soil parameters on pullout behavior of a root-inspired anchor, and 2) to provide constraining bounds on the optimal root-inspired anchor shape for specific soil conditions and constraints.

6.1   Pullout Behavior of Anchorage Systems

Pullout behavior is the mechanical response of the soil-structure system as an embedded element is displaced in the direction of a pullout force. The source of the pullout force depends upon the application, and examples include vertical uplift forces due to grazing herbivores on root systems and horizontally-orientated pullout forces induced by lateral earth pressures on retaining walls, which are resisted by ground anchors. The

response of the system is dependent upon the properties of the individual constituents of the system as well the interaction-specific properties between various components. Even more, the relative difference in constituent properties can incite dramatically different responses. A review of pullout behavior of plant root systems and various geotechnical systems is provided in Chapter 2.

6.1.1 Preface

Vertical pullout tests were selected as the primary means to assess the pullout behavior of root-inspired anchor models. Though the primary axis of conventional anchorage systems can range in orientation from perpendicular (e.g. tiedowns, anchor plates, anchor piles) to parallel (e.g. soil nails, ground anchors) to the soil surface, vertically loaded anchor model tests were selected due to, 1) the ease of experimentation (i.e. equipment design and setup, specimen preparation, and procedure), 2) the extraction of a complete pullout response, and 3) the wealth of literature data on vertically uplifted anchor plates and pipes (i.e. means of comparison). Undoubtedly, pullout resistance varies as the primary axis of the root-inspired anchor model, the orientation of the soil surface, and the loading direction is rotated. However, for shallow embedments (i.e. model depth-to-width ratio less than the critical embedment ratio), the primary mechanism remains the same, where a failure surface develops and the pullout resistance is mainly due to the uplift of a mass of soil and frictional resistance along the failure surface, though the shape of the failure surface is altered. Even more, pullout capacity increases as the model axis is rotated from perpendicular to the soil surface to parallel, due to the increase in mean confining stress (Vesic 1969, Ovesen 1981, Geddes and Murray 1991). Additionally, when evaluating the variation in pullout behavior for a particular feature, every other variable

within the system is controlled as much as feasibly possible. The primary exception is the relation between internal branching angle, branch axis length, and width; not only is the effect on pullout behavior for each individual feature difficult to ascertain due to their geometrical connection but also since the geostatic stress distribution along the branch axis varies, which influences pullout behavior. Furthermore, only a select group of root system features are systematically studied. Other root features and soil-root phenomenon are intentionally ignored but are not considered negligible to the pullout behavior of a living root system. Examples of neglected fibrous root features and soil-root phenomenon include root hairs, root tortuosity, actual root strength and stiffness properties, mucilage effects (dry or wet), soil densification due to root growth, and soil moisture.

6.1.2 *Validity of Model Pullout Tests*

6.1.2.1 Validity of 1g Model Tests

The validity of 1g model tests has been scrutinized since the nascence of geotechnical engineering. The two principal concerns with 1g models are the inherent existence of scale effects and the potential formation of dissimilar or additional failure mechanisms in comparison to field applications. In defense of model tests, the value of the results is dependent upon the analysis methodology and purpose or utilization of the results, wherein insightful contributions to the understanding of soil behavior and soil-structure interaction are generated upon a precise experimentation description and without broad conjecture. Furthermore, if models are designed and analyzed with proper employment of model similitude, the purpose of models can be advanced from solely as means to expose or verify soil mechanisms and behaviors to the production of predictive data (Rocha 1957,

Roscoe 1968). Similitude in this case refers to the concept by which an actual application and scaled model are compared and made similar typically through means of dimensional analysis. In reference to 1g model pullout tests on root-inspired anchor models, potential scale effects, including particle size and stress state effects, have been noted for model pullout tests on uplift resistive structures (Ovesen 1981, Dickin 1988, Tagaya et al. 1988, Sakai and Tanaka 1998, Bradshaw et al. 2016, Athani et al. 2017). For particle size effect, smaller anchor diameter-to-d_{50} ratios lead to larger pullout capacity values as well larger displacement at pullout capacity. For anchor pullout problems, an appropriate anchor diameter-to-d_{50} ratio based upon a comparative analysis has not yet been provided, though *Garnier et al. 2007* suggests $2b/d_{50} > 48$. For the more contested issue of stress state effect, the primary concern resides in the fact that soil behavior is stress and strain dependent. More precisely, for coarse-grained soils at the same initial void ratio, the rate of dilation is greater at lower stress levels and leads to greater peak friction. However, if the 1g model is designed within a proper stress-strain framework, such as Critical State theory, the results can be representative of full-scale tests (Altaee and Fellenius 1994, Bradshaw et al. 2016). Likewise, the author supposes that the results of a 1g model test can be upscaled in the same manner, and further discussion is provided in Chapter 11.

6.1.2.2 Test Repeatability and Reproducibility

For the experimental parametric endeavor, a single test was typically performed for each unique set of parameters. Before the initiation of the experimental program, the repeatability of the testing procedure was determined by performing a pullout test five times on a root-inspired anchor model with identical geometric properties, sample preparation, and experimental procedure (Figure 6-1). Analysis of the results revealed that

the standard deviations in the pullout behavior indices, including pullout capacity, displacement at pullout capacity, maximum tangent pullout stiffness were 0.55N, 0.056mm, and 21.3N mm^{-1}, respectively. Additionally, two additional students participated in the pullout of root-inspired anchor model program. When all data was analyzed collectively, the standard deviation in the pullout indices increased slightly for the first two indices to 0.70N and 0.076mm and decreased for the last index to 18.3N mm^{-1}. Variance in the experimental data is expected primarily due to the specimen preparation method. Repeatability statistics are usually neglected in anchor plate uplift studies, though *Murray and Geddes 1987* performed tests with pullout capacity values ranging between ±2.5% of the mean.
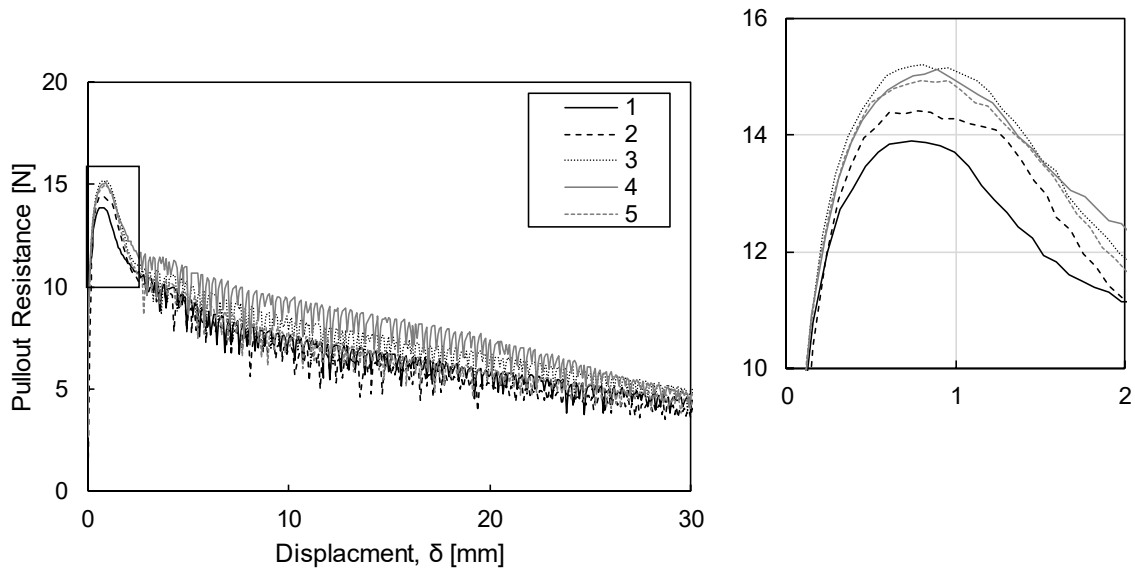
Figure 6-1. Pullout resistance-displacement responses of model n6a30L50D90 uplifted from Ottawa F110 sand prepared at a relative density of 80%, where the test was repeated five times.

6.1.2.3 Displacement Rate Dependency

For all pullout tests, the models were uplifted from the geomaterial at a rate of 10mm min^{-1}. Compared to displacement rates from the literature of standard geotechnical pullout tests of model plates and pipes, the rate prescribed is approximately an order of magnitude larger, though experiments have been performed at much higher rates (Giampa et al. 2016). However, a series of pullout tests controlled for displacement rate were performed, and as the results in Figure 6-2 demonstrate, no clear trends or significant variations in pullout behavior are discernable for the range of displacement rates tested. Even more so, the shearing behavior of sand, and in particular dry sand, is known to be relatively independent of strain rate (Yamamuro and Lade 1993, Tatsuoka et al. 2002, Lade et al. 2009).
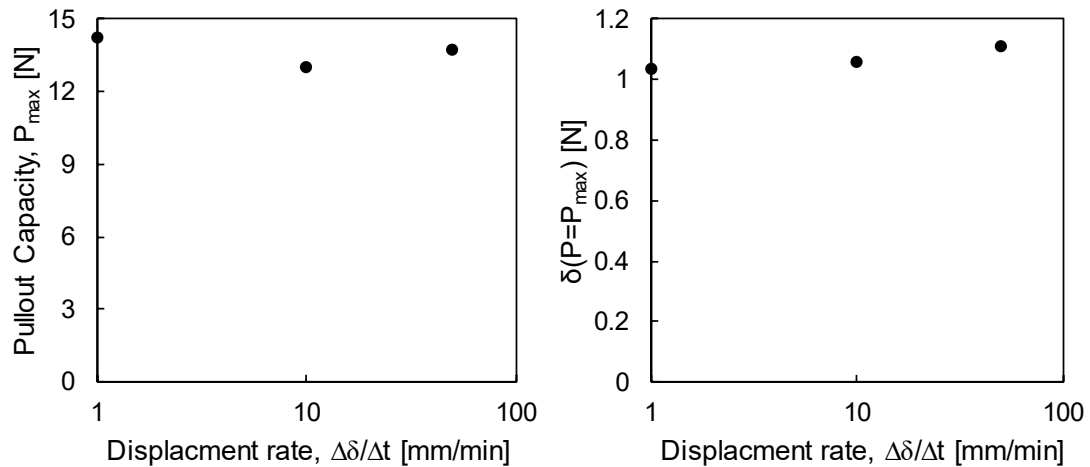
Figure 6-2. Effect of pullout displacement rate on pullout behavior indices.

6.1.3   Pullout Behavior Indices

For this experimental study, a series of six pullout behavior indices are provided for each investigation. The first four are direct characteristics of the pullout resistance-displacement response including initial pullout resistance, P_0, peak pullout resistance or pullout capacity, P_{max}, displacement at pullout capacity, $\delta(P=P_{max})$, and maximum tangent

157

stiffness, max(k_{tan}), as shown in Figure 6-3. An initial, non-negligible pullout resistance exists due to the specimen preparation procedure, and when normalized by the weight of the soil cylinder immediately above the anchor branch axes, insight into initial soil stress state is provided. Maximum tangent stiffness is calculated as the maximum derivative of the pullout resistance-displacement curve up to pullout capacity. Together, displacement at pullout capacity and maximum tangent stiffness are critical design parameters for infrastructure displacement compatibility as well as proof and performance testing necessary for post tensioning. Pullout or breakout factor, $N\gamma$, which is the common non-dimensional method for presenting pullout capacity for plate anchors, is determined by dividing pullout capacity by the weight of soil cylinder above the root-inspired anchor (Equation 21). The weight of the cone of soil below the model is removed to allow for an equivalent comparison with plate anchors. Pullout factor not only provides insight into the factors contributing to pullout capacity, but also provides an initial step in determining the optimal root-inspired anchor shape per volume of utilized soil. Furthermore, an index of material efficiency, Π_M, is determined by normalizing the pullout capacity by the weight of the root-inspired anchor model and is an important index for assessing infrastructure sustainability. Likewise, material efficiency is directly related to pullout capacity divided by the total root-inspired anchor length for models of equal diameter, which becomes important for evaluating drilling priorities.
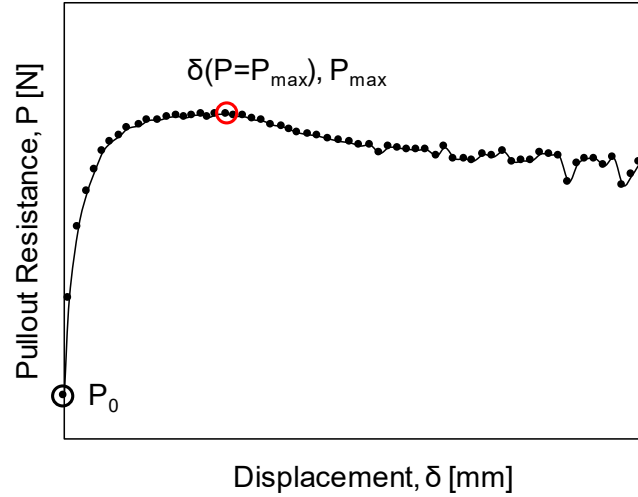
Figure 6-3. Characteristic pullout resistance-displacement response with overlain pullout behavior features.

$$N\gamma = \frac{P_{max}}{\gamma \pi b^2 H'} = \frac{P_{max}}{\gamma \pi b^2 \left(H - \dfrac{b}{3 \tan \alpha} \right)} \qquad (21)$$

6.1.4 Pullout Behavior of Anchor Piles

To evaluate the pullout efficiency of root-inspired anchor models versus conventional anchors, several pile models were prepared and tested with the identical procedure. The pile models varied in diameter from 5-10mm and in depth from 90-150mm. Pullout capacity and material efficiency versus the depth-to-pile diameter ratio of the pile models are presented in Figure 6-4.
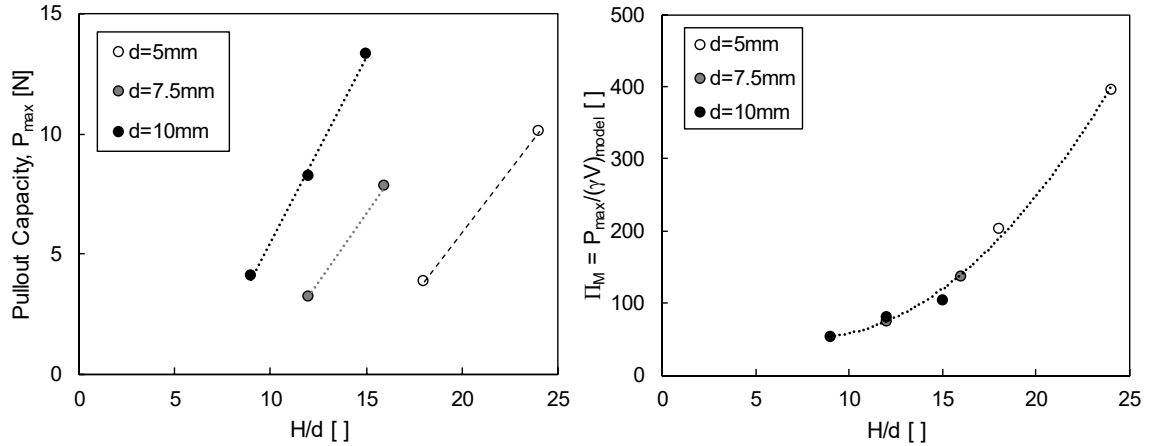
Figure 6-4. Pullout capacity and material efficiency of anchor pile models.

In general, pile pullout capacity increases quadratically with the depth-to-diameter ratio (Das and Seeley 1975), but this trend does not hold for the anchor pile models tested. This is most likely due to particle size effect since the pile diameter-to-mean particle diameter ranges from 83-42, and noticeable particle size effects have been observed for ratios less than 100 (Garnier and Konig 1998, Bałachowski 2007, Garnier et al. 2007).

Equation 22 is a simple pullout capacity model based upon lateral passive earth pressure and interface friction, $\tan\delta$, and a comparison of predicted and experimental values are presented in Figure 6-5. To note, the interface friction angle, δ, is calculated as 2/3 of the peak friction angle, ϕ_p.

$$P_{max} = \frac{\pi}{2}\gamma' dH^2 \tan\delta K_P \tag{22}$$
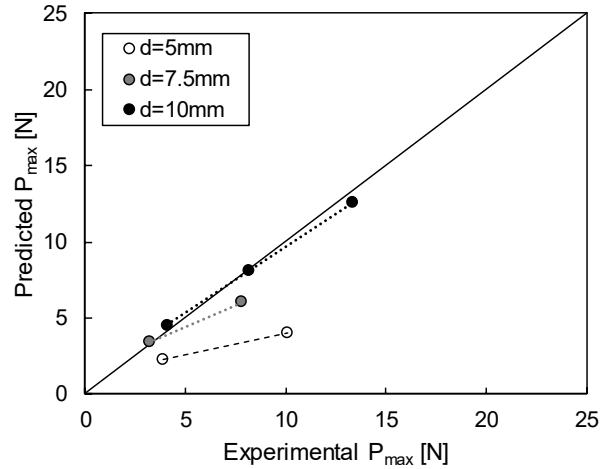
Figure 6-5. Predicted versus experimental pullout capacity utilizing Equation 22.

For the purpose of this study, a pullout capacity model that captures the particle size effects is required for the analytical comparison of root-inspired anchors and anchor piles, and Equation 23 is an empirical model inspired from the quadratic relationship between the material efficiency index and the depth-to-diameter ratio. Figure 6-6 demonstrates the relative predictive power of Equation 23 versus Equation 22 for the range of pile models tested. The fit is optimized when the coefficient, C, is equivalent to 1/12.

$$P_{max} = C\frac{\pi}{2}\gamma' H \tan\delta K_P \left(H^2 - Hd + d^2\right) \tag{23}$$
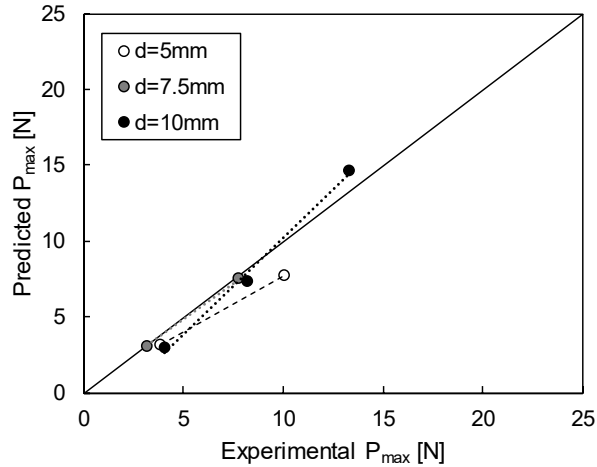
Figure 6-6. Predicted versus experimental pullout capacity utilizing Equation 23.

6.1.5   Pullout Behavior of Anchor Plates

Before the behavior of root-inspired anchor models is assessed, the uplift performance of a series of anchor plate models was analyzed. This data provides a means to validate the pullout tests through comparison of general trends with literature data as well as to validate an analytical pullout capacity model, which is fully described in Chapter 8. As a general trend, pullout capacity, displacement at pullout capacity, and pullout factor increase with greater depth-to-width ratios (Figure 6-7), which corroborates with previously reported trends. The maximum tangent stiffness, which is a representation of global pullout stiffness, increases with the depth-to-width ratio. For plate anchors of constant width and increasing depth, anchor model ring pullout stiffness, as approximated in Chapter 5, decreases with the depth-to-width ratio, which indicates that soil stiffness dictates the global pullout stiffness since the elastic modulus of soil generally increases exponentially with depth. Furthermore, the normalized initial pullout resistance is greater than one for all cases, which indicates that due to specimen preparation procedure, the soil stress state is greater than geostatic. In addition, the effect of relative density, particle roundness, and

particle size on pullout behavior of anchor plates is evaluated by performing pullout tests on identical plate anchors in varying geomaterial conditions.
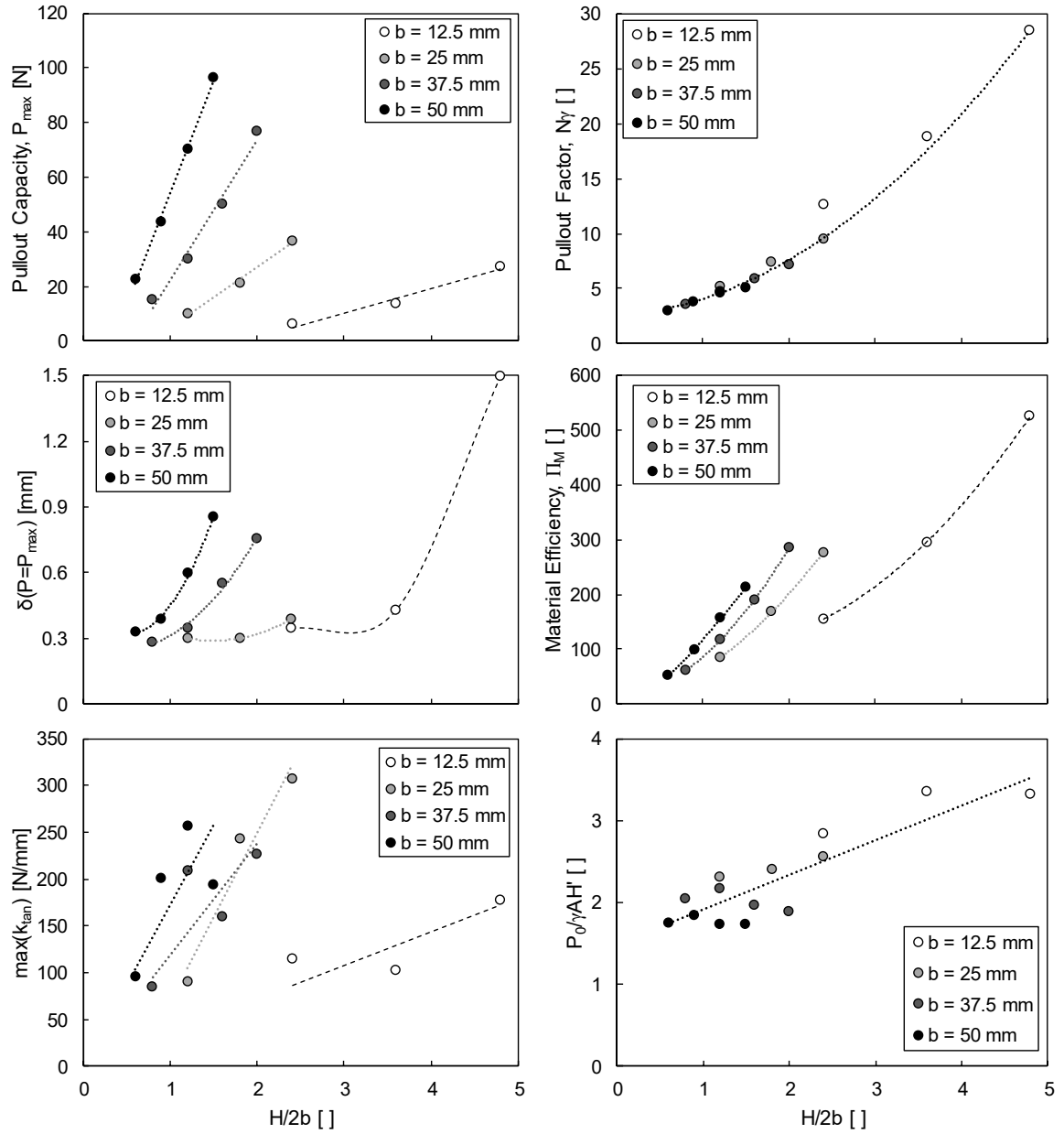
Figure 6-7. Compilation of pullout behavior indices for plate anchor model tests.

6.1.5.1 Effect of Relative Density

Variations in pullout response are analyzed for two geomaterial specimens, Ottawa F110 sand and glass beads, at varying relative densities (Figure 6-8). Both pullout capacity and pullout factor increase with increasing relative density for both geomaterials, which is entirely expected since inherently the weight of soil increases as well as the frictional resistance because the shear strength of coarse-grained materials improves due to dilation. Additionally, though the trend is not definitive, displacement at pullout capacity appears to increase with increasing relative density, which is contradictory to reported data (Dickin 1988, Illampurthi et al. 2002). Overall, displacement at pullout capacity is representative of the displacement required to mobilize the full shear strength of the soil and for dense, dilative specimens, to develop shear bands. As such, one hypothesis for this behavior would be that denser more dilative specimens have a larger failure surface and require additional magnitudes of displacement to reach pullout capacity (evidence in Chapter 7). In addition, knowledge of the state parameter or the difference in initial and critical state void ratios at the prescribed mean stress for each specimen would be beneficial. As well, a larger failure displacement with relative density could be explained by the model deformation behavior, since a greater distributed load on the branch axis would occur with greater relative densities and would translate to a more compliant pullout response. Maximum tangent stiffness, in general, increases with relative density, which is expected since soil stiffness increases with contact number and density.
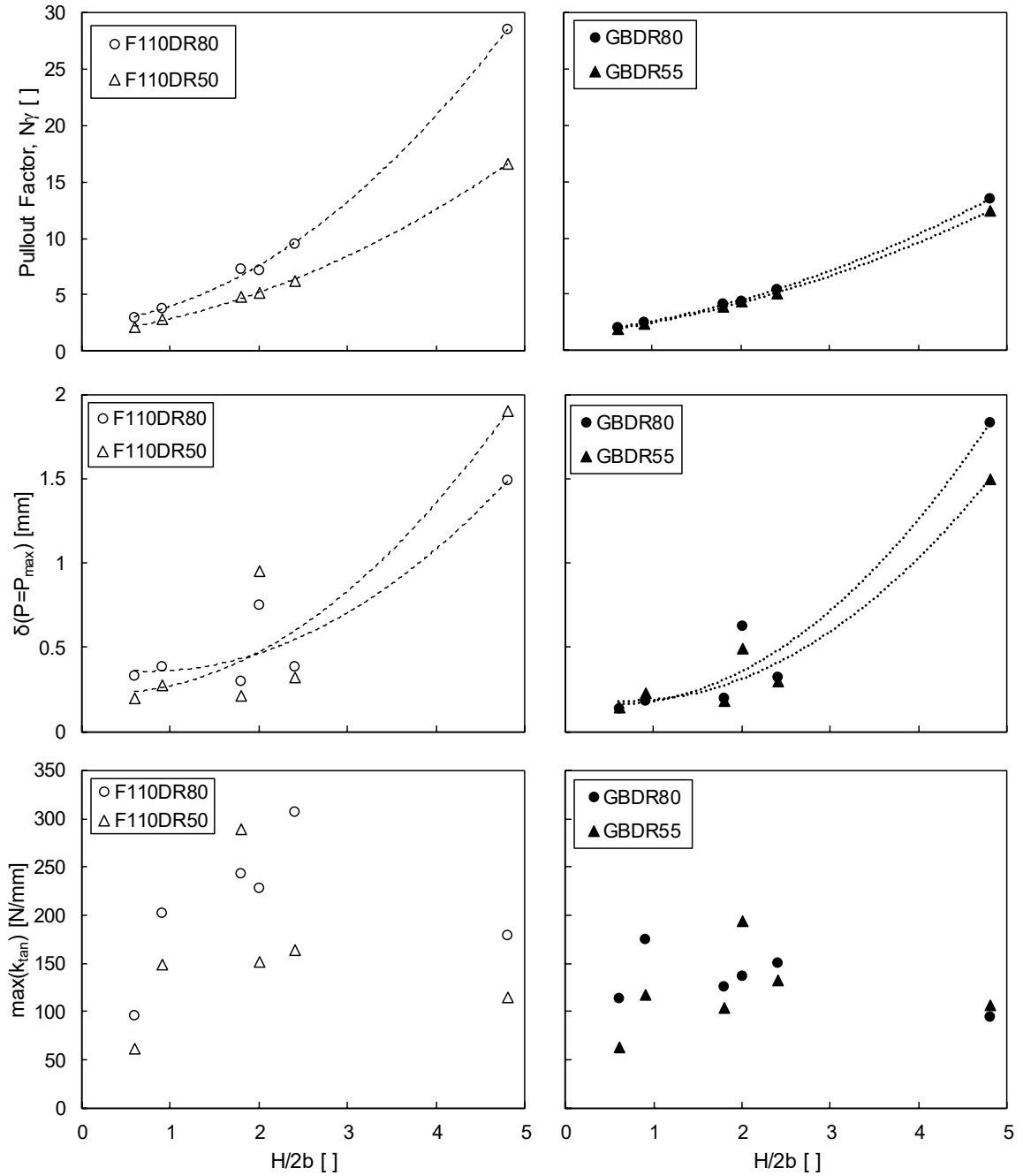
Figure 6-8. Effect of relative density on pullout behavior of plate anchor models uplifted from Ottawa F110 sand (left) and glass beads (right).

6.1.5.2 Particle Size

To evaluate the effect of particle size on uplift behavior, pullout tests were performed on Ottawa 20-30 and F110 sands, which contain similar characteristic properties

including particle morphology, mineral constituents, and critical state friction angle (Figure 6-9). Yet, the sands differ substantially in grain size distribution, where mean particle diameter is 0.72mm and 0.12mm for Ottawa 20-30 and Ottawa F110 sands, respectively. The comparison, however, is not perfect because the state parameter is unknown, and therefore the rate of dilation and peak friction angle might vary. Contrary to numerical results, pullout capacity and pullout factor determined experimentally decreased with particle size (Sakai and Tanaka 1998, Athani et al. 2017). Possible explanations for an increase in pullout factor for the sands includes, 1) variation in failure surface shape, 2) variation in achieved rate of dilation and peak friction angle, both of which are common particle size effects for dilative specimen behavior in model tests (Stone and Wood 1992). Displacement at pullout capacity logically increases with particle size due to the displacement required to develop shear bands and consequently, failure surfaces.
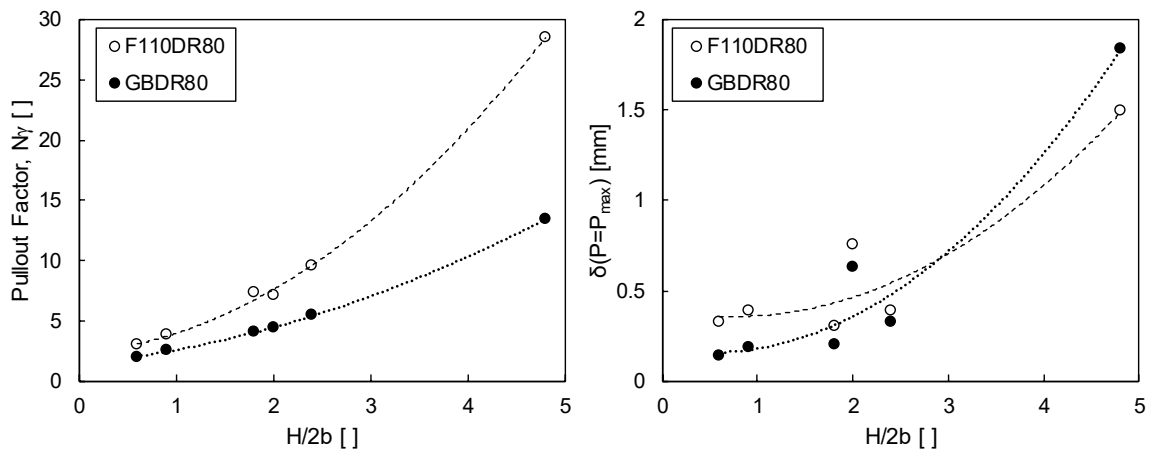
Figure 6-9. Effect of particle size on pullout behavior of anchor plate models.

6.1.5.3   Particle Roundness

The effect of particle roundness on pullout behavior was investigated by comparing the uplift response of plate anchors in Ottawa F110 sand and glass beads. The two

geomaterials have similar mean particle sizes, yet differ in other particle characteristics including particle shape and material constituents (i.e. quartz versus silica). Particle roundness is known to correlate well with critical state friction angle, and as shown in Figure 6-10, pullout factor expectedly decreases with particle roundness. In addition, shape of the failure surface is dependent upon the friction angle, where a larger volume of soil is mobilized in soils with greater friction angles. In general, displacement at pullout capacity decreases with increased particle roundness, where particle morphology, including roundness and sphericity, could influence the displacement required for localization. More so, particles with greater angularity, interlocking ability, and eccentricity would require greater displacements to mobilize the full shear strength.
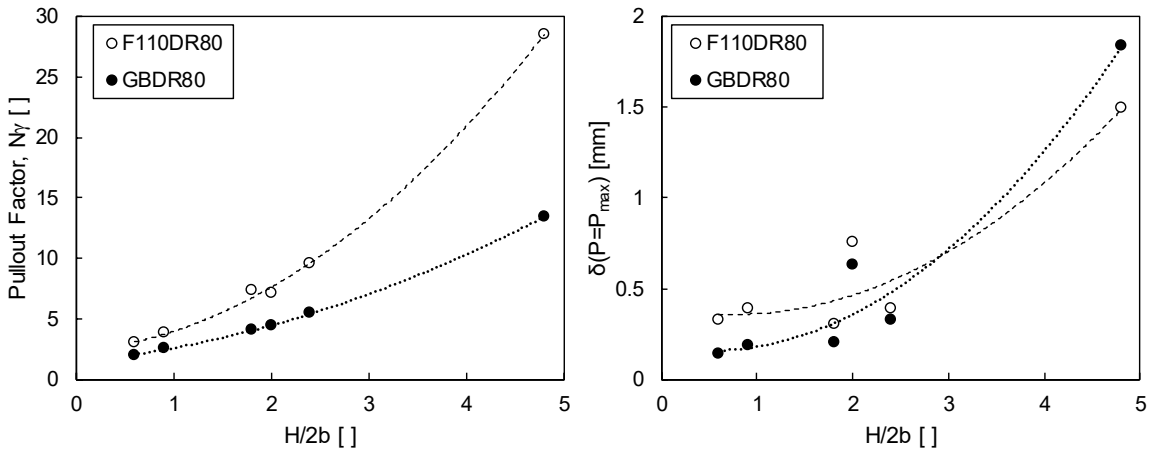
Figure 6-10. Effect of particle roundness on pullout factor and displacement at pullout capacity for plate anchor models.

6.2 Pullout Behavior of Root-Inspired Anchor Models

The pullout behavior of root-inspired anchor models is now analyzed, including the effect of varying anchor model morphological parameters and soil properties on the global

167

pullout indices. A sample of the characteristic force-displacement behavior occurring during root-inspired anchor model pullout is demonstrated in Figure 6-11.
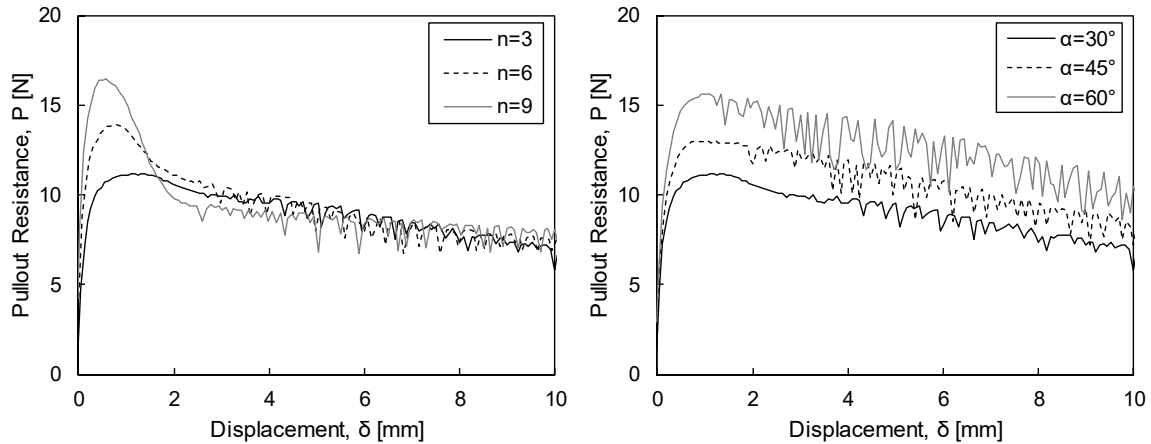
Figure 6-11. Sample pullout responses of root-inspired anchor models with varying number of branch axes, *n*, and internal branching angles, *α*.

6.2.1 Effect of Root-Inspired Anchor Model Morphology

6.2.1.1 Effect of Number of Branch Axes

For this series of tests, the effect of the number of branch axes on pullout behavior was investigated on models of constant width and depth but varying number of branch axes and internal branching angles. For most root-inspired anchor sets, the number of branch axes consisted of 2, 3, 6, 9, 12, and full models. In Figure 6-13, the various pullout behavior indices are plotted versus the angle between the equally spaced branch axes as from plan view, as schematically shown in Figure 6-12. Pullout capacity increases with an increase in the number of model branch axes, which suggests that that failure surface evolves such that a greater volume of soil is uplifted and/or a greater shearing resistance is mobilized. Additionally, pullout factor follows the same general trend with minor variations in the internal branching angle tendencies, where an internal branching angle less than 90° allows

for a more effective use of the overlying soil. Neglecting models with internal branching angles of 90°, displacement at pullout capacity increases with decreasing number of branch axes, and mechanistically agrees well with the opposite trend in maximum tangent stiffness. Anchor model ring pullout stiffness, as predicted in Chapter 5, increases with the number of branch axes, and for models embedded at approximately the same depth, variations in global pullout stiffness can therefore be primarily attributed to model stiffness. As a result, more flexible models result in a more compliant global pullout response and a greater displacement at pullout capacity is expected. Possible hypotheses for this trend includes, 1) soil arching mechanism, where models with fewer branch axes contain relatively larger spacing between consecutive branch axes, which would require a larger vertical movement of the anchor for arching to fully develop, and 2) root-inspired anchor stiffness, where models with fewer branch axes have a lower effective pullout stiffness, which would result in greater branch displacement. In terms of material efficiency, a local maximum occurs for root-inspired models with three branch axes, and the index increases with increasing branching angle. Though an increase in the number of branch axes typically leads to greater pullout capacity values, clearly the volume of the root-inspired anchor models increases at a greater rate. Furthermore, when initial pullout resistance is normalized by the weight of the cylinder of soil immediately above the root-inspired anchor, it becomes apparent that due to the specimen preparation method, anchors with a larger number of branch axes cause a greater disturbance to the surrounding soil.
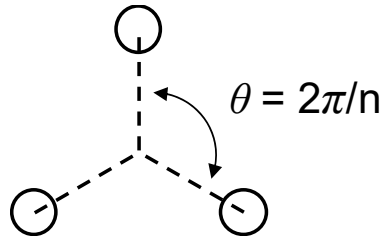
Figure 6-12. Representation of the branch axis spacing angle, θ, (the horizontal axis variable from Figure 6-13).
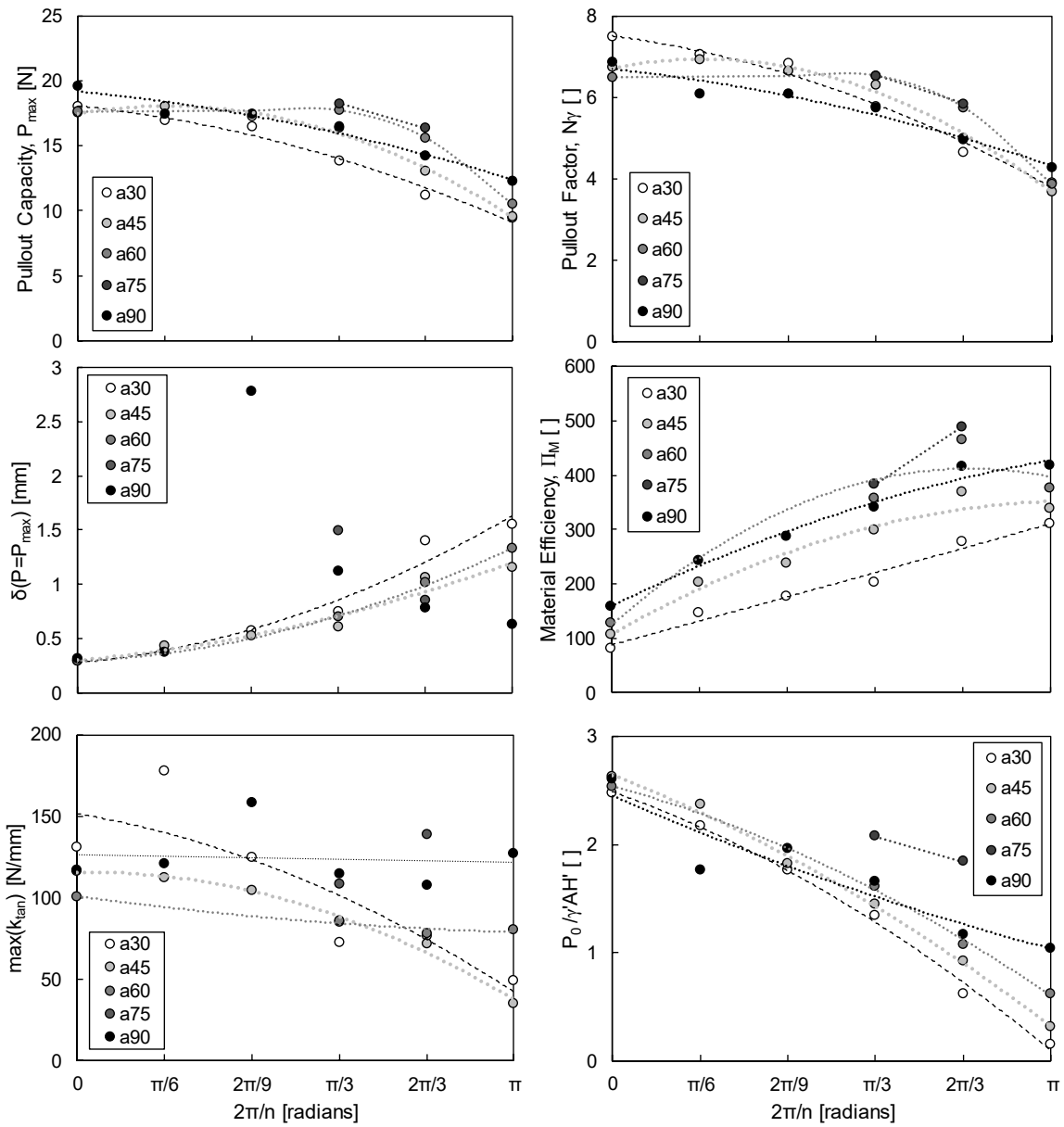
Figure 6-13. Effect of branch axis number on pullout behavior for models of varying internal branching angle.

6.2.1.2   Effect of Depth-to-Width Ratio

For this series of tests, the width, *b*, was held constant at 25mm, while the depth, *H*, was altered in 30mm increments from 60mm to 150mm, illustrated in Figure 6-14. Overall, the root-inspired models follow the same general trends as the plate anchor tests, where all indices increase with depth-to-width ratio, with the exception of initial pullout resistance that largely remains constant with depth (Figure 6-15). The increase in pullout factor with depth suggests that the volume of the failure surface increases with depth. The experiments reiterated the effect of the number of branch axes on both pullout capacity and pullout factor. Additionally, larger internal branching angles led to a more effective use of soil. More so, the material efficiency index improves with less branch axes and for greater internal branching angles. The displacement at pullout capacity and maximum tangent stiffness increase with increasing depth. No clear tendencies for displacement at pullout capacity and maximum tangent stiffness with respect to the number of branch axes and the internal branching angle are revealed through this test set.
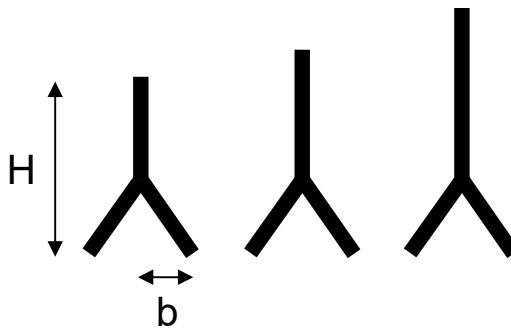
Figure 6-14. Schematic representation of root-inspired models utilized to identify the effect of the depth-to-width ratio on pullout behavior (constant width and increasing embedment depth).
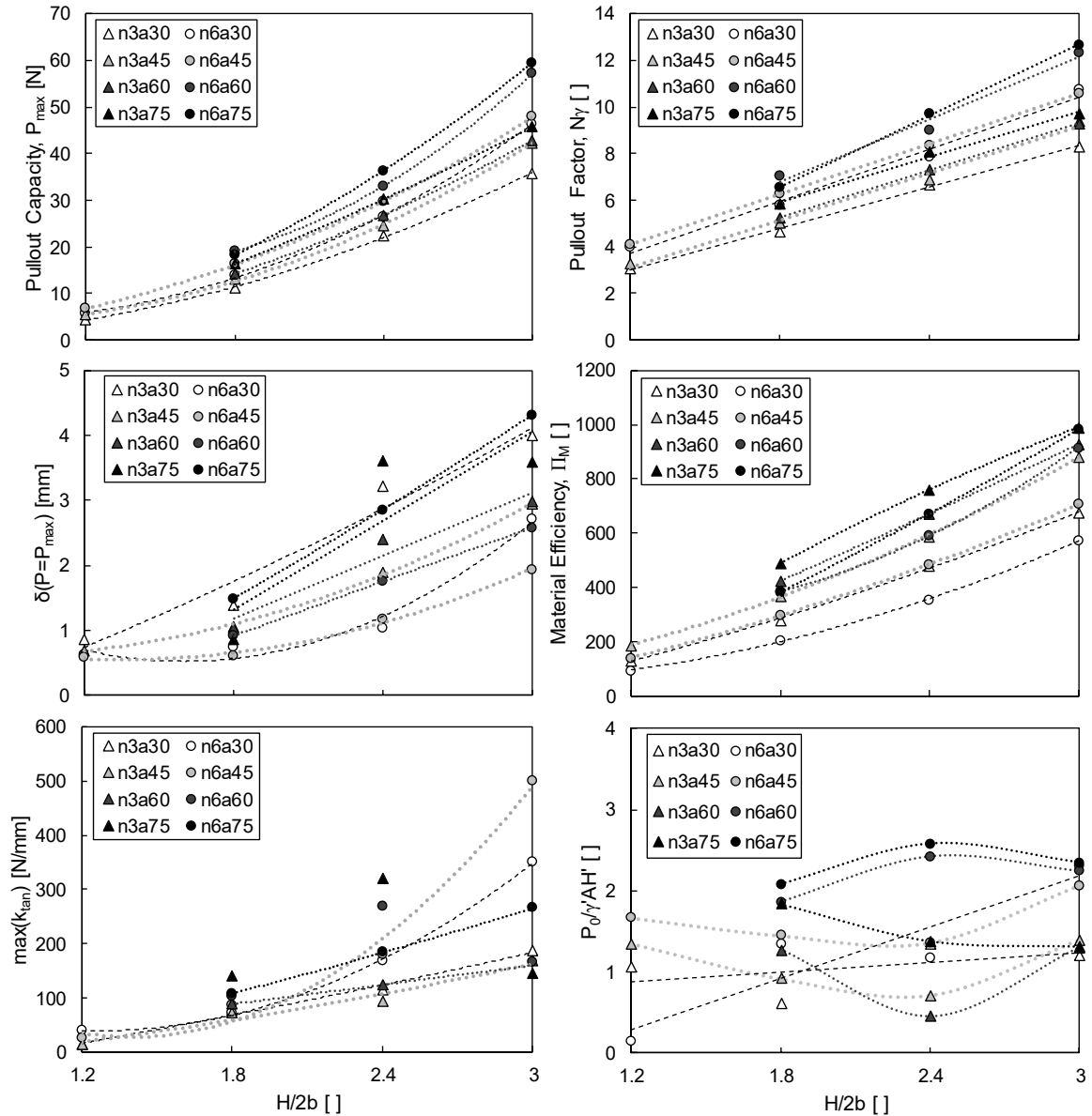
Figure 6-15. Effect of depth-to-width ratio, *H*/2*b*, of root-inspired anchors on pullout behavior.

6.2.1.3   Effect of Branch Length and Internal Branching Angle

The effect of branch length and internal branching angle is difficult to assess due to their geometric association with each other and the depth-to-width ratio. Consequently, the effect of branch length and internal branching is analyzed from two perspectives, 1) constant depth-to-width ratio with varying internal branching angle and branch length, and

172

2) constant depth with varying width. From Figure 6-16, a local maximum pullout factor occurs for root-inspired anchor models with an internal branching angle of 60° for models with both three and six branch axes, and the trend shifts to a wider branching angle for the material efficiency index, where the maximum occurs at an internal branching angle of 75°. The maximum tangent stiffness increases with internal branching angle due to the increase in model stiffness with decreasing branch length, and as well, the point of dichotomy increases in depth with larger internal branching angles, which causes the models to experience a stiffer bulk soil.
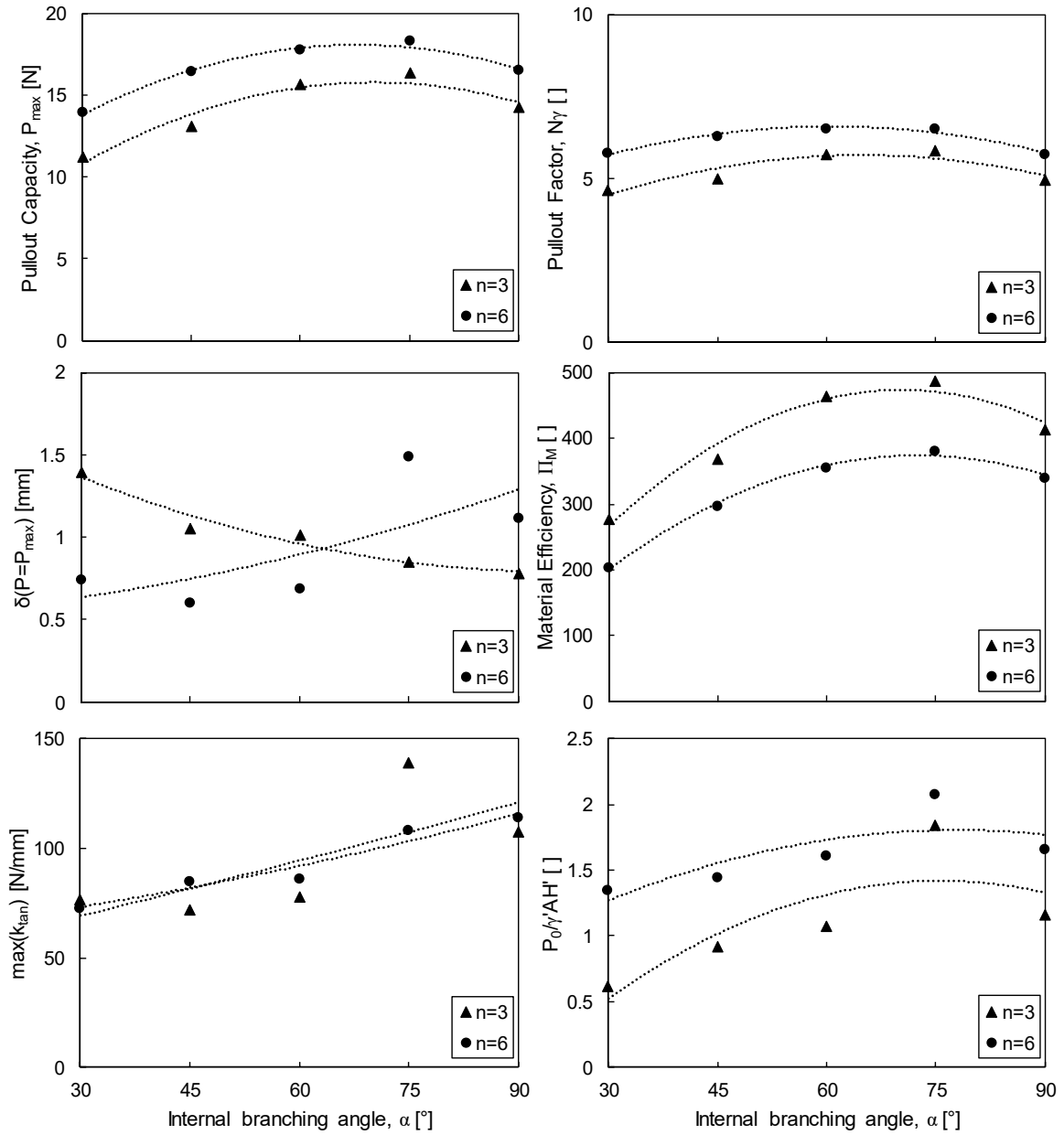
Figure 6-16. Pullout behavior with internal branching angle for root-inspired anchor models of constant depth-to-width ratio and varying branch axis length.

When branch axis length and depth are held constant and the depth-to-width ratio is varied (schematic provided in Figure 6-17), additional insights become apparent (Figure 6-18). Interestingly, similar pullout capacities are achieved for root-inspired models of the same branching angle and depth regardless of width and length. However, when the pullout capacities are normalized by the weight of the overlying soil, the effectiveness of root-

inspired anchor models decreases as the point of dichotomy becomes shallower. Furthermore, the material efficiency improves with greater internal branching angles. Displacement at pullout capacity increases dramatically for lengthier branch axes, demonstrating the effect of model stiffness on pullout stiffness.
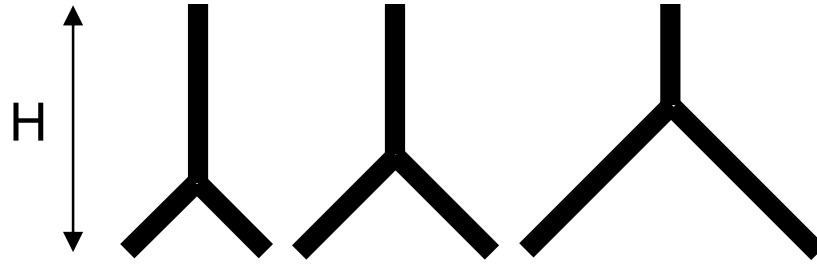
Figure 6-17. Representation of root-inspired anchor models utilized to determine the effect of branch axis length on pullout behavior (constant depth).
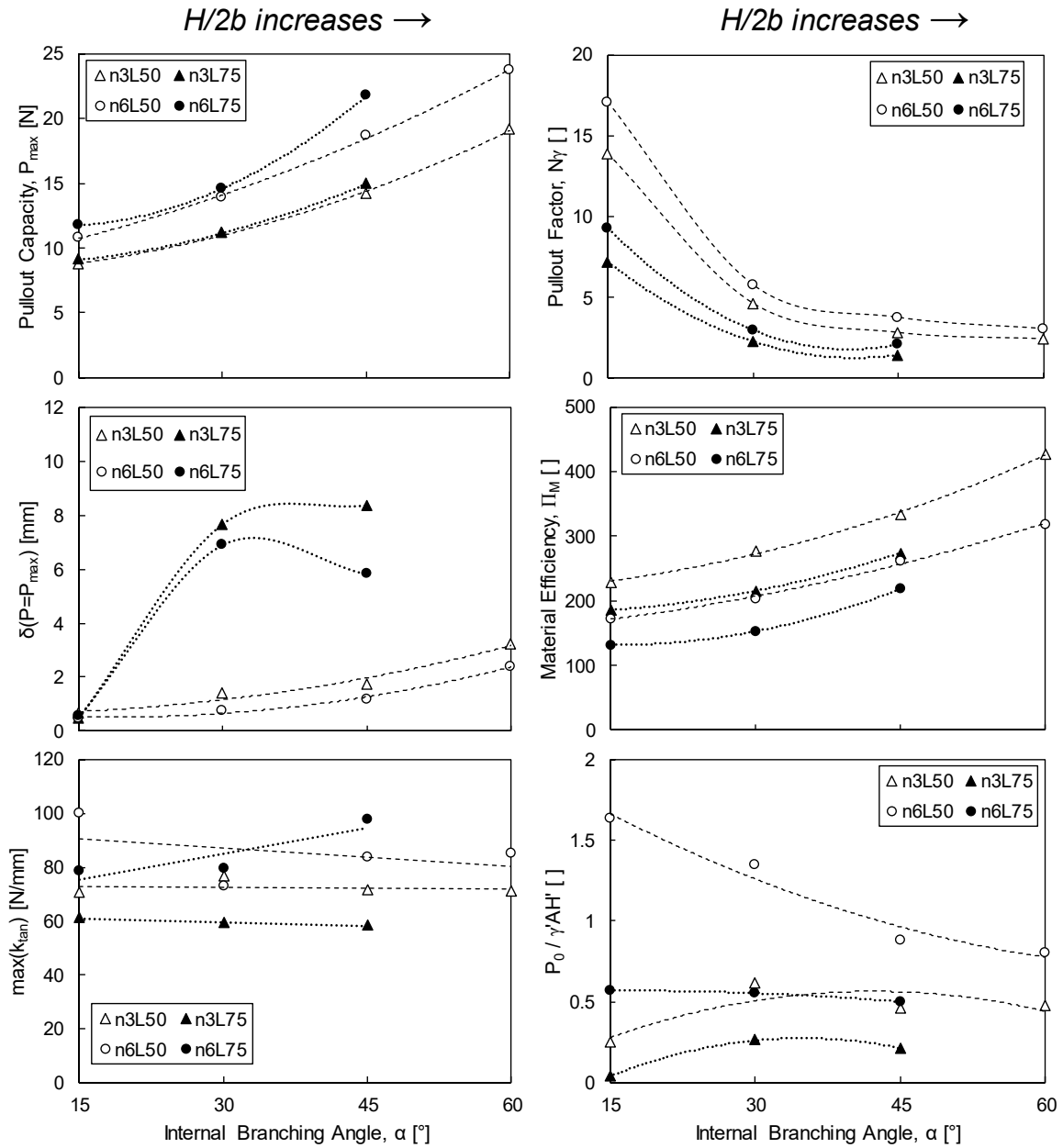
Figure 6-18. Pullout behavior indices with internal branching angle for models of constant depth and varying branch axis length and width.

6.2.2   Effect of Soil Properties

6.2.2.1   Effect of Relative Density

The role of relative density on pullout behavior is evaluated for two particulate materials, Ottawa F110 sand and glass beads. The first set of experiments clarifies the effect of relative density on pullout behavior for models of increasing depth-to-width ratio (Figure 6-19). For pullout capacity, which is a combination of the weight of uplifted material and the shear force on the failure surface, relative density acts to enhance both of these forces due to an increase in density and dilative tendencies. As experimentally determined, pullout capacity and pullout factor increase with relative density. Displacement at pullout capacity is dependent on model morphology and relatively independent of relative density, and on the other hand, maximum tangent stiffness is convincingly dependent on the soil modulus, which is dependent on both the void ratio and stress state.
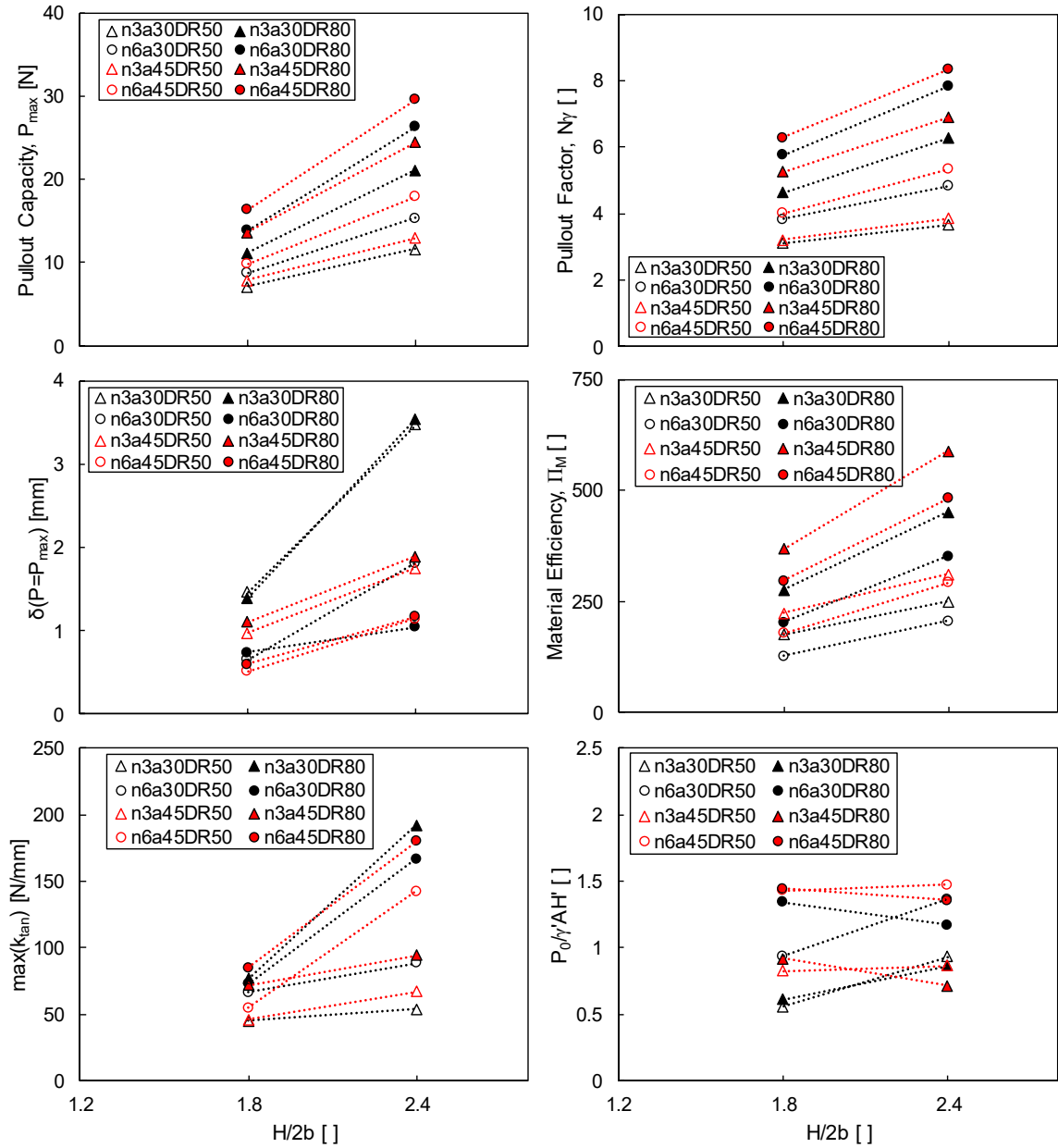
Figure 6-19. Pullout behavior indices of root-inspired anchor models of varying depth-to-width ratio at two relative densities of Ottawa F110 sand.

The role of the relative density of Ottawa F110 sand is again evaluated amongst anchor models of varying internal branching angle at constant depth (Figure 6-20). Pullout capacity, pullout factor, and material efficiency indices indicate an optimal internal

branching angle of 60° for models of three and six branch axes. Just as before, displacement at pullout capacity is sensitive with the geometric parameters of the root-inspired models.
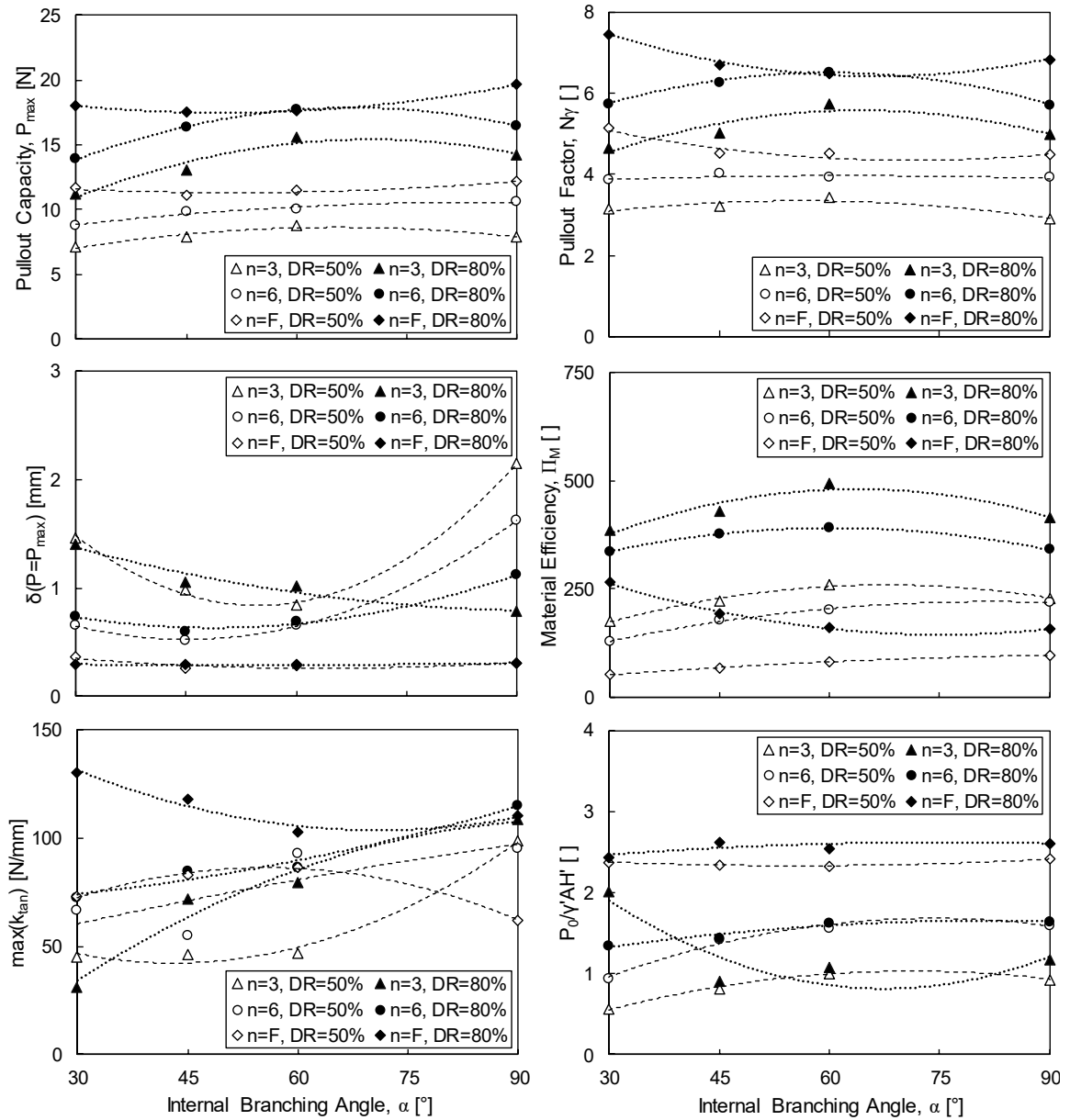
Figure 6-20. Pullout behavior indices with internal branching angle of root-inspired anchor models at varying relative densities of F110 sand.

The last set of experiments to evaluate the effect of relative density on pullout behavior was performed in a glass bead medium (Figure 6-21). Overall, relative density

has a more minor effect on pullout behavior for glass beads than F110 sand. For glass beads, the relative improvement in pullout capacity and pullout factor are minimal (Figure 6-22). In contrast to the tests performed with Ottawa F110 sand, both displacement at pullout capacity and maximum tangent stiffness display a higher dependency on model shape than soil stiffness.
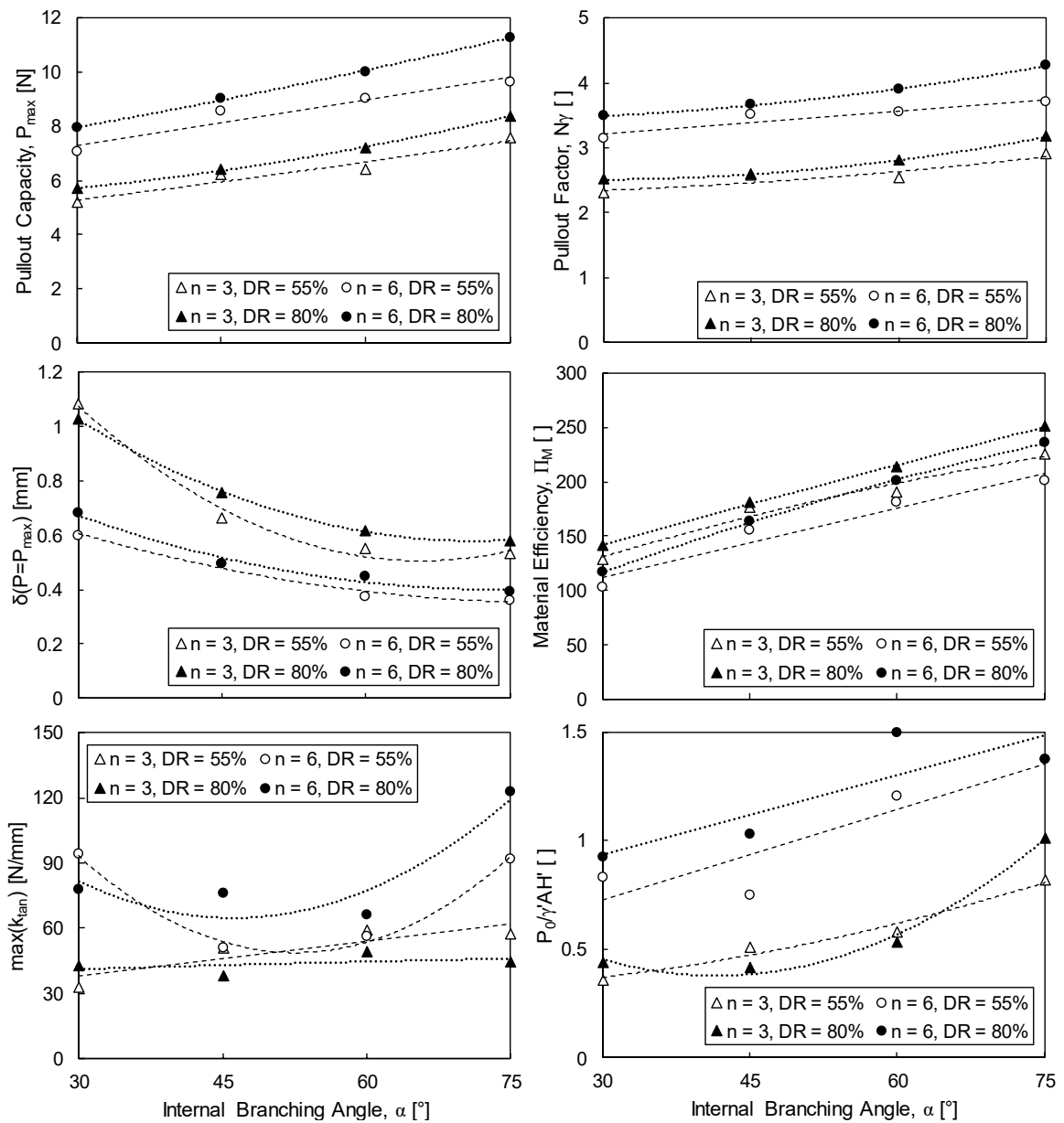
Figure 6-21. Pullout behavior indices with internal branching angle at varying relative densities of glass beads.
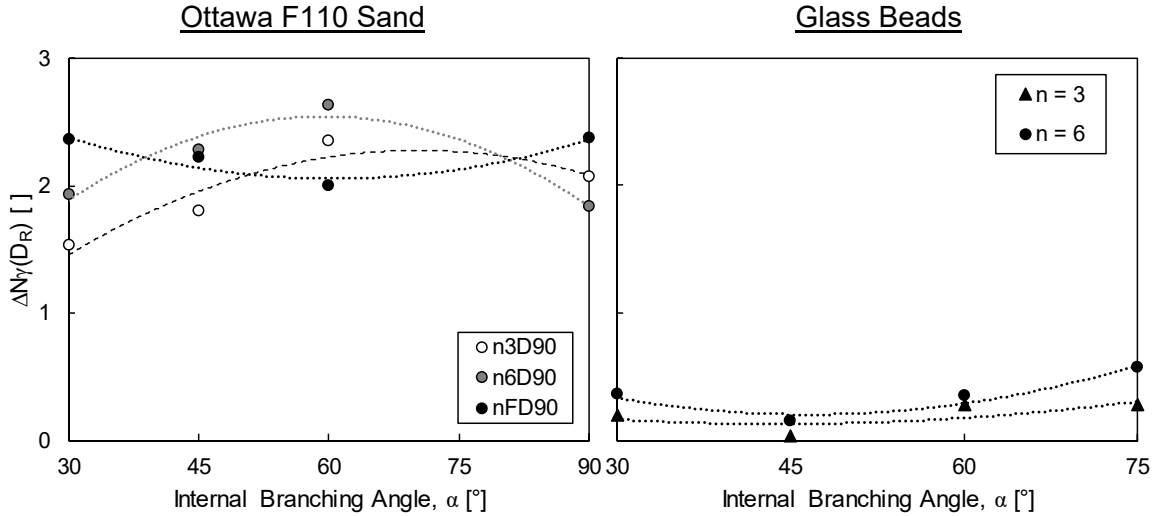
Figure 6-22. Change in pullout factor with relative density for Ottawa F110 sand and glass beads.

6.2.2.2 Effect of Particle Angularity

Just as for the plate pullout tests, the effect of particle angularity is investigated from pullout tests performed in Ottawa F110 sand (d_{50} = 0.12mm, Roundness = 0.7, ϕ_{CS} = 32°) and glass beads (d_{50} = 0.1mm, Roundness = 1.0, ϕ_{CS} = 24°). Pullout capacity, pullout factor, and material efficiency increase with particle angularity perhaps due primarily to the increase in friction angle with particle angularity. The observation of an optimal internal branching angle of 60° and 75° for pullout factor and material efficiency, respectively, is confirmed. A noticeable reduction in both displacement at pullout capacity and maximum tangent stiffness is observed with increasing particle roundness, and as hypothesized within the plate anchor tests, media comprised of more angular particles require greater particle displacement to mobilize the full shear strength.
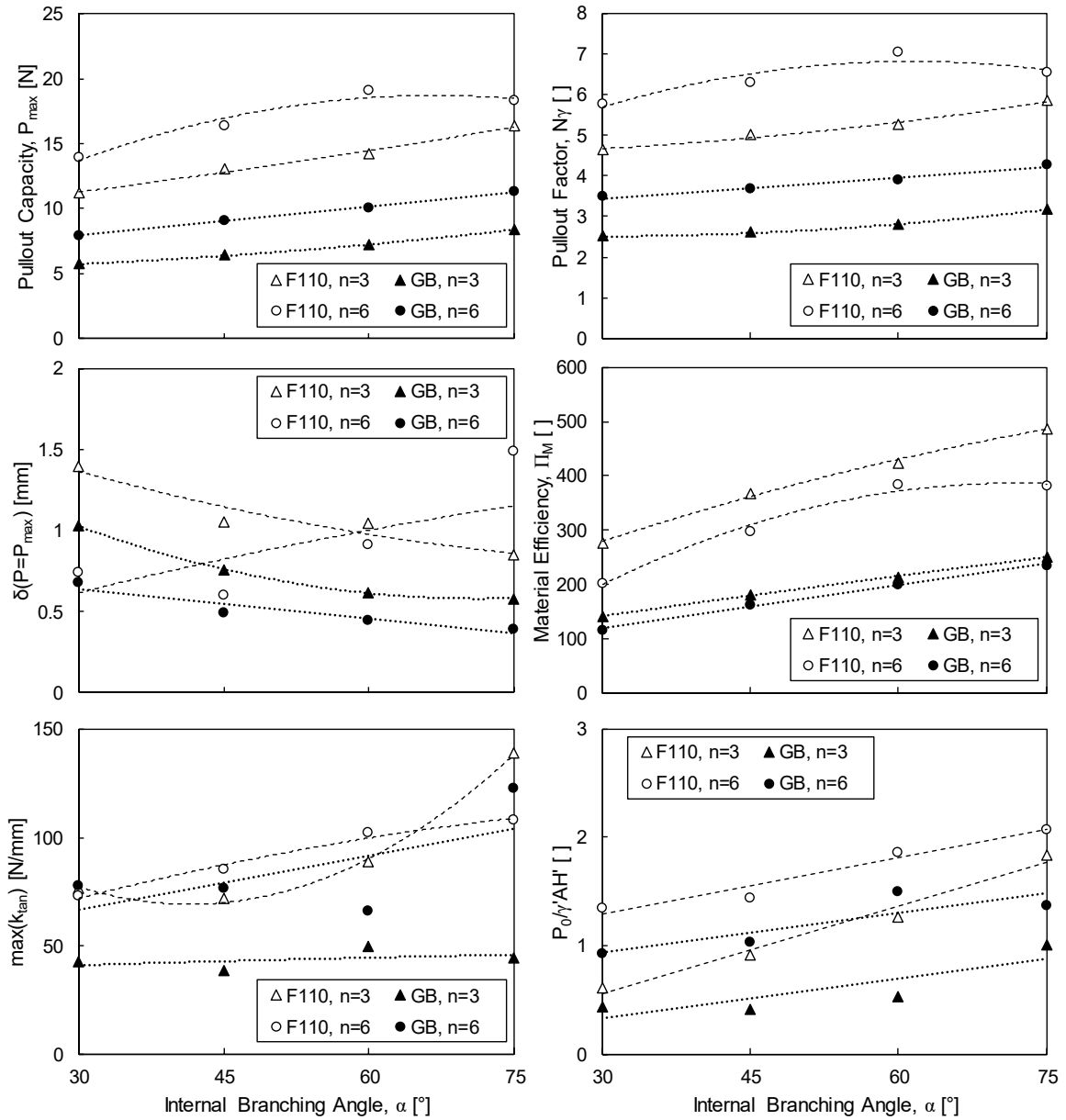
Figure 6-23. Pullout behavior indices with internal branching angle for models embedded in Ottawa F110 sand and glass beads.

6.2.2.3 Effect of Particle Size

For this series of tests, pullout behavior indices are compared from tests performed in two Ottawa sands of differing particle size. As described previously, comparison of pullout capacity and pullout factor values is not recommended for this case due to the

fallacy that the media (Ottawa 20-30 and F110) behave the same despite the their selected difference in particle size. However, the trends in pullout capacity, pullout factor, material efficiency with internal branching angle, number of branch axes remain the same. No consistent trends in displacement at pullout capacity or maximum tangent stiffness is obvious from direct comparison; though for the larger particles, a reduction in failure displacement with increasing internal branching angle and number of branch axes is present. The diminution in failure displacement with increasing internal branching could be attributed to the increasing embedment of the point of dichotomy, which positions the branched portion of the root-inspired model in a slightly stiffer soil matrix.
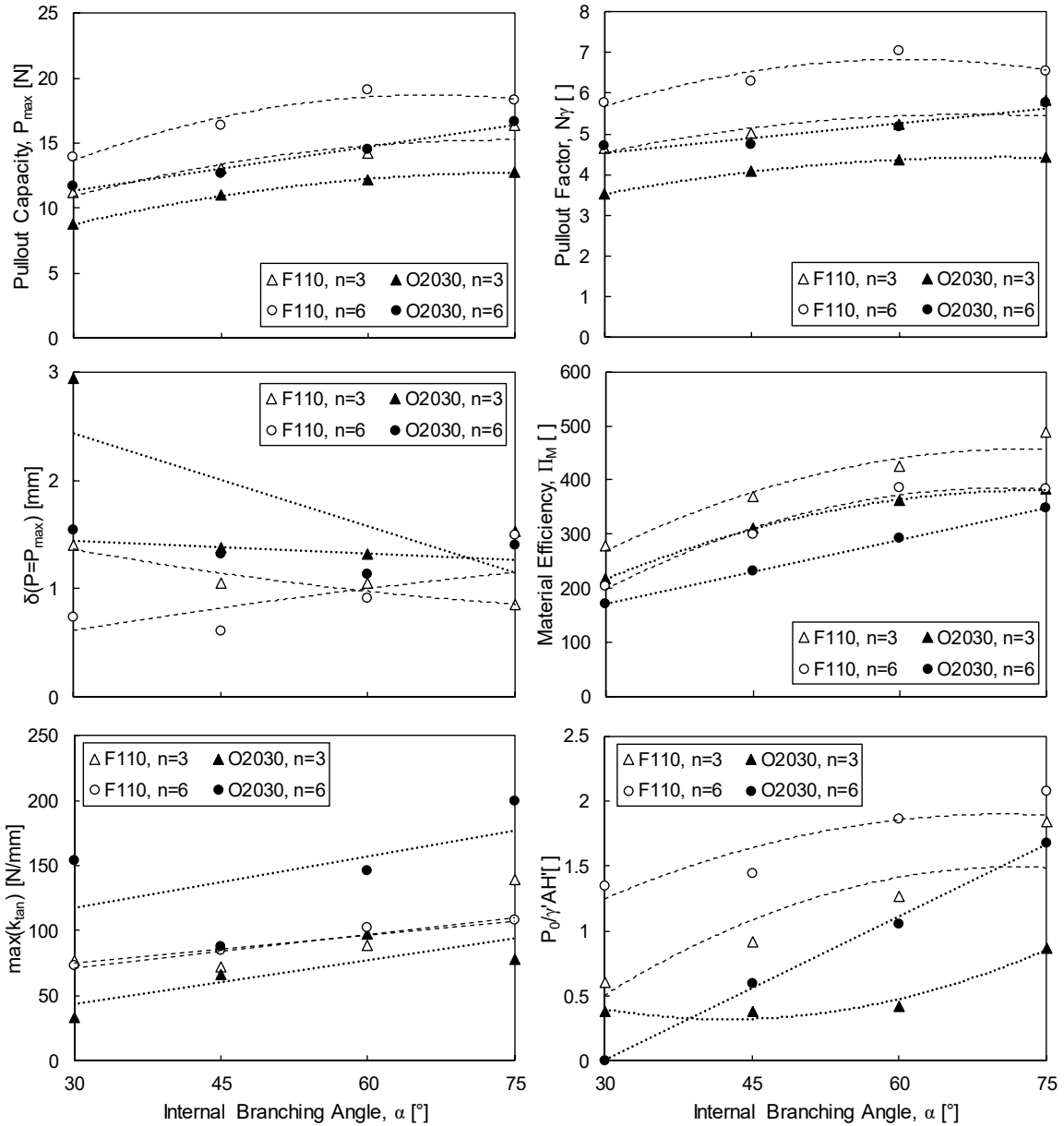
Figure 6-24. Pullout behavior indices with internal branching angle for models embedded in Ottawa 20-30 (d_{50}=0.72mm) and F110 (d_{50}=0.12mm) sands.

6.2.3 Summary of Trends

The correlation between pullout behavior indices and varied root-inspired anchor

model morphological parameters and geomaterial properties is documented in Table 6-1.

Again, for the trends in particle roundness, R, and mean particle size, d_{50}, the correlations

with pullout capacity dependent indices (P_{max}, $N\gamma$, and Π_M) are not valid since the comparison is not rigorous (i.e. solely the D_R is equal).

Table 6-1. Association of pullout behavior indices and root-inspired anchor model morphological parameters and geomaterial properties (P=Positive, N=Negative, I=indeterminate, a particular value is the optimal value).

Indices	Morphological Parameters			Geomaterial Properties		
	n	$H/2b$	α	D_R	R	d_{50}
P_{max}	P	P	75°	P	N	N
$N\gamma$	P	P	60°	P	N	N
$\delta(P=P_{max})$	N	P	I	I	N	P
$\max(k_{tan})$	P/I	P	P	P	I	I
Π_M	N/3	P	75°	P	N	N
P_0	P	P	75°	I	I	N

6.3   Conclusions

Analysis of numerous 1g model pullout tests (~200) revealed several critical insights for the evaluation of root-inspired anchors as a desirable replacement for conventional anchorage systems:

- Pullout capacity, P_{max}, is mandatory for anchorage design, and experimental pullout tests revealed an optimal internal branching angle of 75°, as well as a comparatively high capacity with even 3 branch axes.

- Pullout factor, $N\gamma$, provides an effective means to normalize P_{max} to allow for a fair comparison amongst models of varying morphology. Notably, an optimal internal branching angle range ($60°<\alpha_{opt}<90°$) was identified.

- Displacement at pullout capacity or failure displacement, $\delta(P=P_{max})$ along with maximum tangent stiffness serve as applicable indices to assess infrastructure

displacement compatibility as well as proof and performance testing (post-tensioning).

- $\delta(P=P_{max})$ is representative of the displacement required to mobilize the full shear strength of the soil, and for these pullout tests, it is dependent on the stiffness of the anchor model, where larger $\delta(P=P_{max})$ values occur when the anchor is less stiff.

- Global pullout stiffness, as represented by maximum tangent stiffness is more dependent upon the soil state as opposed to $\delta(P=P_{max})$, as highlighted by the relative density tests.

- Material efficiency is optimized for $2<n<6$, $60°<\alpha<90°$, and as the depth-to-width ratio increases. Limits to the depth-to-width ratio are imparted by the critical depth-to-width ratio and geometric constraints placed on models.

- Normalized initial pullout resistance reveals sample preparation effects, and in particular, values greater than one, reveal a loading greater than geostatic stress due to perhaps dynamic or pre-stress effects.

- In comparison to root-inspired anchor models of the same depth-to-width ratio, anchor plates achieve higher pullout capacities and pullout factor values; however, root-inspired anchor models surpass anchor plates by 1.04 to 2.9 times in terms of material efficiency, Π_M, where the enhancement is optimal for 3 branch axes and internal branching angles of 75°.

- In comparison to root-inspired anchor models of the same depth, anchor piles perform significantly poorer in terms of P_{max} and Π_M. In particular for H=90mm, the best performing pile model performed 4.2 and 2.4 times less effectively than

the best performing root-inspired model of 3 branch axes, in terms of P_{max} and Π_M,

respectively.

CHAPTER 7.   VISUALIZATION AND ANALYSIS OF BREAKOUT-TYPE FAILURE SURFACE DURING ROOT-INSPIRED ANCHOR MODEL PULLOUT

The purpose of this chapter is to identify the failure mechanisms involved in root-inspired anchor model pullout through the visualization of the soil deformation and particle kinematics. The visualization is achieved through incremental three-dimensional imaging, captured via x-ray computed tomography of the model soil-anchor system during the pullout process. The image sets were quantitatively analyzed using digital image correlation (DIC) to provide insight into the local soil displacement and strain behavior. The results of the DIC analysis reveal the development of shear strain localizations into mature failure surfaces. The shape of the failure surfaces are analyzed, and the variances in failure surface descriptors are associated with variations in pullout system features including root-inspired anchor morphology and geomaterial particle characteristics. This chapter adds clarity to the comprehension of the pullout process, providing evidence that corroborates with global pullout behavior conclusions, and as well, allows for the formulation of an equation to predict pullout capacity based on a known descriptive failure surface.

7.1   Background

Previous studies on experimental visualization of the pullout process of embedded geotechnical structures has been limited to two-dimensional analyses (i.e. plane strain and half-models). Former studies include common uplift problems such as anchor plates (Balla

1961, Baker and Konder 1966, Matsuo 1967, Meyerhof and Adams 1968, Ilamparuthi and Muthukrishnaiah 1999), passive trapdoors (Ladanyi and Hoyaux 1969, Tanaka and Sakai 1993), piled embankments (Hewlett and Randolph 1988), and pipes (Cheuk et al. 2008). These experiments were performed primarily to identify the governing failure mechanism and associated failure surfaces for the derivation of an analytical solution to describe the phenomenon. In addition, numerous numerical simulations have been conducted to supplementarily evaluate the soil kinematics during uplift of various embedded objects (Rowe and Davis 1982, Merifield and Sloan 2006).

7.1.1 Failure Surfaces

A failure or rupture surface in geotechnical engineering refers to the sliding surface or concentrated region within which the soil shears at failure. For typical geotechnical analyses, failure surfaces are considered as the narrow zone between two rigid bodies that displace relative to each other (Terzaghi 1943, Roscoe 1970). Examples of well-established failure surfaces that have been experimentally determined and idealized for analytical treatment include those developed for bearing capacity, slope stability, and retaining wall overturning problems. Failure surfaces are the result and maturation of the localization of shear strain into relatively thin zones, termed shear bands, where strain localization is the accumulation of deformation in a particular area. Shear band formation is a dilative process and as such, the band denotes the anomalous region of relatively higher void ratio compared to the surrounding soil. Additionally, the thickness of rupture surfaces is within the range of 10-20 times the mean particle size (Roscoe 1970, Muhlhaus and Vardoulakis 1987, Oda and Kazama 1998, Alsaleh et al. 2006). In Mohr-Coulomb failure criterion theory, a failure surface coincides with the plane of maximum stress obliquity and forms

at an orientation of $\pi/4$-$\phi/2$ to the principal stress direction. However, in plane strain experiments, discrepancies between actual and theoretical failure surface orientations arose and empirical formulations including dilation angle were produced accordingly (Roscoe 1970, Arthur et al. 1977).

7.2   Experimental Program

The goal of this study is to dissect the role of root-inspired anchor model morphology as well as soil properties on local and global soil behavior during pullout. As in the previous chapter, root-inspired anchor models are embedded in a geomaterial and vertically uplifted; however, in this experimental program, at set increments (i.e. 0.5mm of upward model displacement), the uplift is paused and the entire soil-model system is imaged with x-ray CT technology. To assess the local soil behavior, the images are then analyzed with digital image correlation to form displacement fields, and following with a continuum approach, strain maps are produced by tessellating the geomaterial volume.

For this experiment, to evaluate the role of model morphology on soil kinematics, the number of branch axes and internal branching angle of three 3D printed morphology-type root-inspired anchor models are varied. In addition, a typology-type root-inspired anchor model is evaluated to provide insight into the role of anchor topology on pullout behavior. All cases are compared to a conventional straight, shaft pile element. The models are embedded in three unique geomaterials, Toyoura sand (d_{50}=0.165mm, R=0.4), Soma No. 4 sand (d_{50}=0.85mm, R=0.34), and glass ballotini (d_{50}=0.2mm, R=1.0), to highlight the role of particle size and roundness on the soil uplift behavior. The complete testing matrix for this study is documented in Table 7-1.

Table 7-1. X-ray CT pullout parametric study testing matrix (X = Performed).

		Geomaterial		
		Toyoura	Soma No. 4	Ballotini
Model	n3a30	X	X	X
	n6a30	X	X	X
	n6a45	X	X	X
	pile	X		
	topo.	X		

Full information regarding the experimental apparatus, exact experimental procedure, including sample preparation and scanning routine, sand types, and anchor models are discussed in Chapter 4.

7.3   Image Processing

Within x-ray computed tomography, the reconstruction algorithm predicts the attenuation coefficients of the scanned specimen in space from the two-dimensional radiographs captured at various increments of rotation. As a result of the inverse nature of this problem, these images are prone to a variety of artifacts that arise from differences between the experimental scanning procedure and the assumptions within the reconstruction algorithm. For example, the beam hardening, which creates the appearance that a relatively homogeneous object attenuates less radiation in the center, is due to the incongruence between the polychromatic beam of the common commercial x-ray generator and the assumed monochromatic x-ray beam. To diminish image artifacts consistently, all data sets are image processed in an identical manner with a variety of techniques. First of all, the original radiographs undergo 2x2 binning to improve the signal-to-noise ratio (SNR) and to form more manageable file sizes. Subsequently, a beam hardening correction

and median filter are applied to minimize beam hardening and ring artifacts. Finally, for the 2D DIC analysis, radial slices parallel to the z-axis and intersecting the central anchor model axis were generated from the 3D image set through means of linear interpolation. All image processing was performed through a combination of Matlab and ImageJ software.

7.3.1 *Digital Image Correlation*

Digital image correlation (DIC) is an image processing technique utilized to match similar images with the purpose of identifying image differences and extracting positional information. For engineering in particular, DIC is a method of generating a displacement field by comparing two images of an object at different moments of deformation. DIC can be implemented in a multitude of ways, yet the underlying concept remains the same. Subsets or windows of an initial image are correlated to positions in the subsequent image; thus, for the midpoint of every subset, a displacement vector is determined. Neighboring midpoints can then be meshed together, and strain tensors for each element can be determined via continuum mechanics assumptions. Nominally, DIC, when performed on three dimensional image sets, is often referred to as digital volume correlation (DVC) or volumetric digital image correlation (VDIC), and particle image velocimetry (PIV) employs similar algorithms but is concerned with velocity fields.

7.3.1.1 Algorithm

For this particular research, both DIC and DVC analyses were performed. For the 2D DIC analysis, an open source Matlab package, OpenPIV, was utilized (Taylor et al. 2010), and for the DVC analysis, a script was written in Matlab. For both cases, the same

standard correlation algorithm is followed, as detailed and illustrated in Figure 7-1 and Figure 7-2, respectively. After importing two successive images, subset nodal points are defined based upon the size of the images and the specified subset size and spacing, where the spacing determines the subset window overlap. Subsets are then collected, and the standard cross-correlation implemented in the frequency space is performed. For DIC analyses where brightness and contrast do not remain constant through the image acquisition process, a normalized cross-correlation is mandatory; however, for the x-ray CT image volumes attained, the reconstruction algorithm maintained a relatively constant brightness. Additionally, to reduce computational time, the cross-correlation is equivalently determined in the frequency space through convolution. Following, the maximum correlation coefficient is located, and with a least squares regression, a polynomial surface is fitted to the neighboring correlation values to identify an inter-pixel maximum. The global maximum of the surface function is then selected and is mapped back to the image space. The sub-pixel displacement vector is then defined as the difference between the nodal point of subset and the matched point.
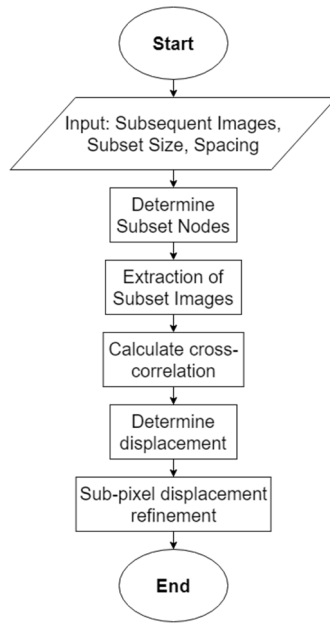
Figure 7-1. Flowchart for DIC/DVC algorithm.
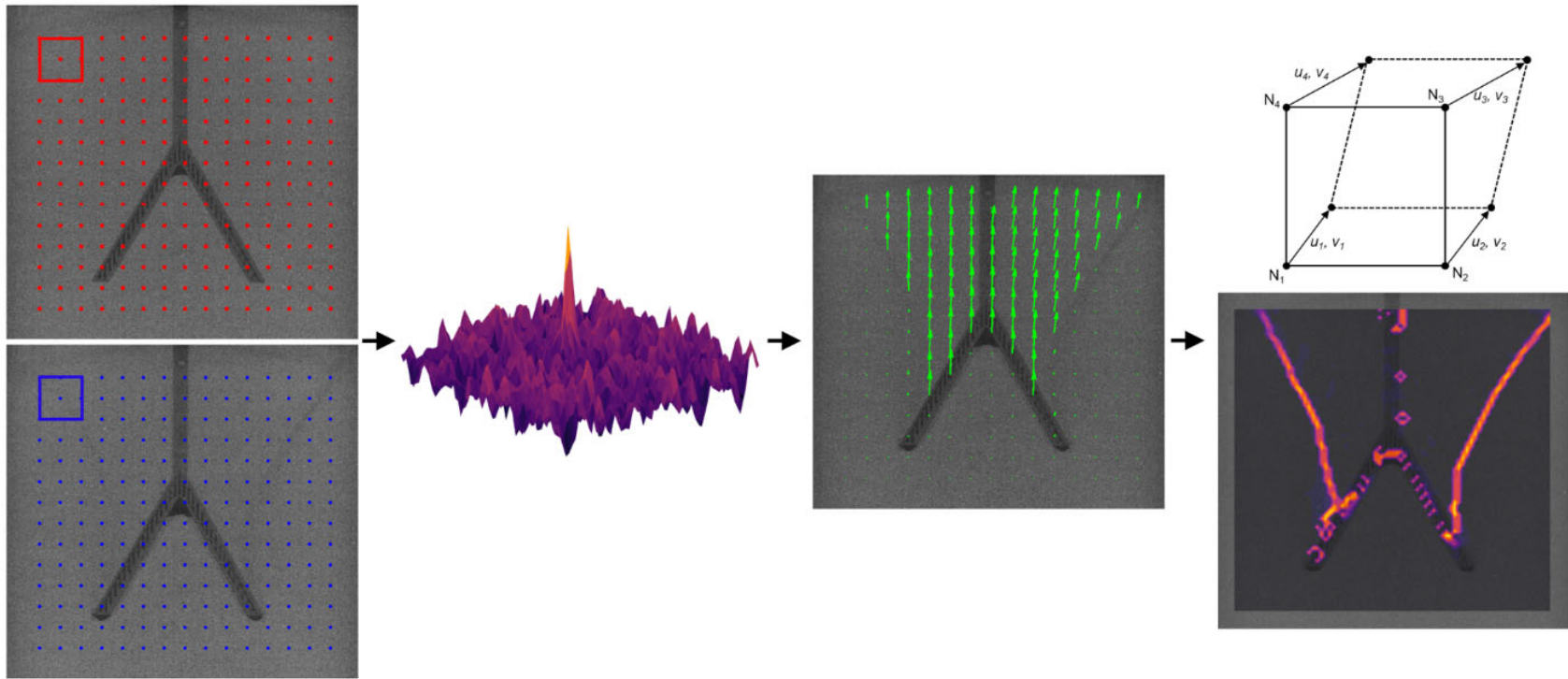
Figure 7-2. Illustrative example of DIC and strain mapping procedure.

7.3.1.2   <u>Subset Size and Spacing Selection</u>

Both the size and spacing of the subset windows control the resolution of the displacement fields and all supplemental analyses, including strain field, and the selection of these two parameters requires a tradeoff between desired resolution and error limitation. For subset size, larger windows, in general, result in higher correlation values but provide less displacement information; as well, excessively large windows can fail to capture more minute and localized phenomena. In Figure 7-3, the normalized correlation values for a DVC analysis are shown, which highlights that a more highly correlated result is achieved with increasing subset size; even more so, with increasing total soil deformation, the correlation diminishes slightly. On the other hand, errors associated with the selection of an insufficient window size are formally categorized under the term, the aperture problem (Sutton et al. 2009). One such example stems from the infeasibility of performing a correlation analysis with single pixels and another, from the selection of a subset size identical to the size of a replicating pattern within the image. For the subset spacing, the amount of overlap between subsets contributes an averaging effect, as well as providing additional data for a seemingly higher resolution result. For the case when the spacing between subset nodes is larger than the subset size, the primary consequence is a reduction in the resolution; however, for the opposite case, an excessive overlap can over-average the displacement values, resulting in erroneous gradient calculations critical to the determination of strain fields.
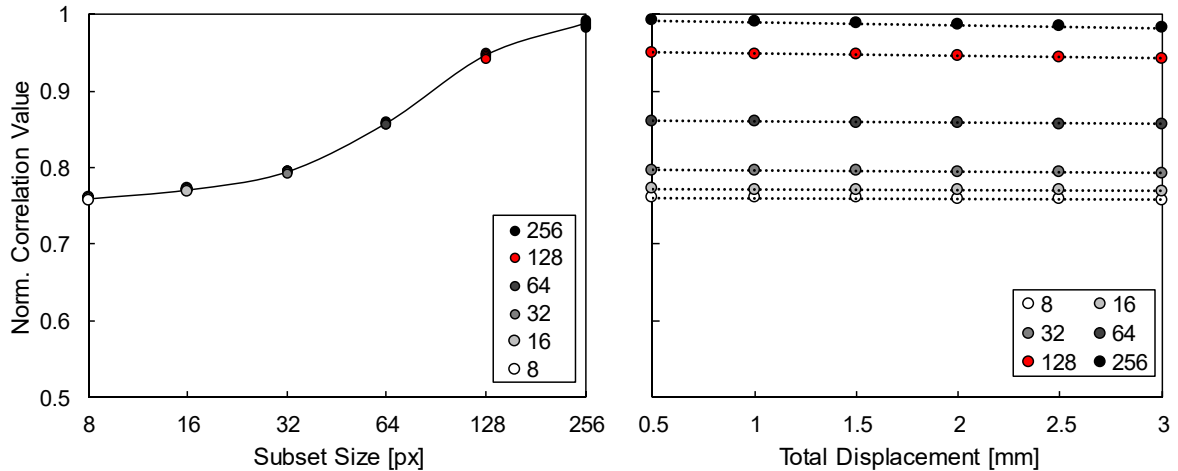
Figure 7-3. Normalized correlation values for the 3D DVC analysis of model n6a30 in Toyoura sand with varying subset size (left) and with increasing model pullout displacement (right).

7.3.1.3 DIC Performance

The performance of a DIC analysis is generally assessed in terms of the accuracy, precision, and resolution of the produced displacement field and is affected not only by the DIC algorithm but also by the image acquisition system (White et al. 2003). At the forefront, DIC is inherently an inverse problem, characterized by the lack of knowledge of the transformation from the initial to the deformed image state. Consequently, the DIC algorithm requires assumptions regarding the transformation model, which naturally introduces approximations and errors into the results. Multiple factors, including image quality and features, subset size, sub-pixel refinement algorithm, and image-to-object space transformation, can contribute to the performance of the DIC algorithm. In particular, accurate DIC analyses require that each subset contain a certain texture density (i.e. a pixel value variance density), often referred to as a speckle pattern (Sutton et al., 2009). Correspondingly, for geomaterials that can be distinguished and contain some degree of texture when imaged, the size of the subset is therefore related to the ratio of d_{50} of the

material to the image resolution. As well, accuracy related issues are primarily due to the transformation from the image-space to the physical-space (White et al. 2003). Precision, on the other hand, is largely due to algorithm related approximations, particularly within the selected sub-pixel refinement and mapping algorithms. However, image features including noise, histogram, and speckle pattern are known to influence the accuracy and precision of the DIC results (Bay 2008). As mentioned previously, the subset size governs the resolution of the displacement; no accurate measure of displacement can be obtained when the subset is larger than the period of the displacement field (Bornert et al. 2008).

7.3.1.4 DIC Implementation

For this study, both a two-dimensional DIC and a three-dimensional DVC analysis were performed for two distinct reasons, both relating to computational restrictions. The DIC analysis was executed on full resolution 2D radially sliced images (image size = 1504x1300pixels, resolution = 83µm) to achieve high detail information of the local soil kinematics and failure surface. Conversely, the DVC analysis, performed on 2x2x2 binned image sets (image size = 752x752x650 pixels, resolution = 166µm) of the original volume, allowed for the visualization of the complete failure surface, fully capturing the displacement field in all directions. The overall model, considering both soil and anchor elements, retains symmetry about the z-axis for each root branch section. Correspondingly, a 2D DIC analysis of a radial slice is representative of all slices at the same azimuthal angle both positive and negative from each root section. However, a 2D analysis of radial slices fails to capture the out of plane soil movement. A DVC analysis of all cases was also performed to capture displacement in all directions as well as to form a complete visualization of the failure surface.

The size of the subset for each scan and associated 2D and 3D correlation analysis was dependent upon the geomaterial. For each subset size selection, a balance between desired strain map resolution and correlation was achieved and the results are documented in Table 7-2. For all cases, the spacing, defined as the pixel distance between subset nodes, was maintained as half of the subset size. For verification, the correlation values for the 2D DIC analysis are displayed in Figure 7-4.

Table 7-2. Selected subset size per geomaterial.

Geomaterial	2D DIC	3D DVC
Toyoura	128	32
Soma No. 4	128	16
Ballotini	256	32
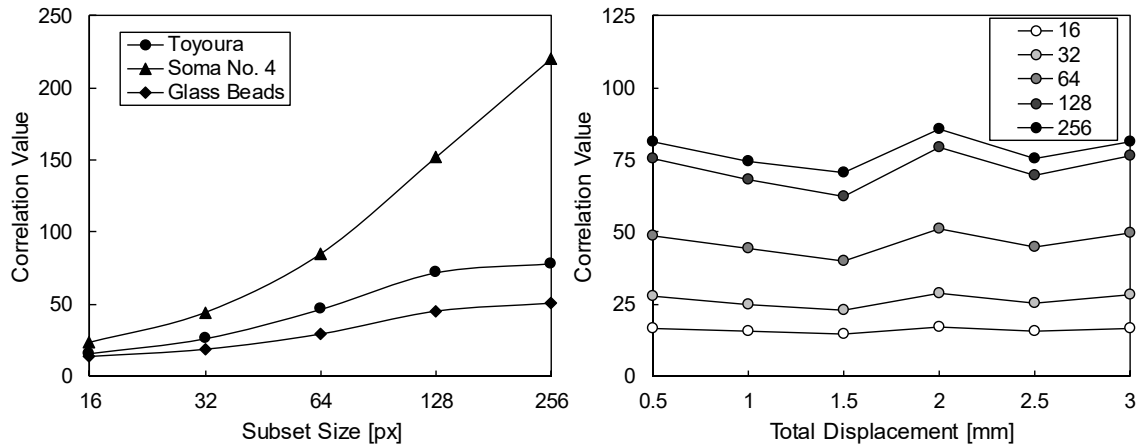
Figure 7-4. Correlation values for the 2D DIC analyses of model n6a30 in Toyoura sand, Soma No.4 sand, and glass beads with varying subset size (left) and with total displacement for the Toyoura sand case (right).

7.3.2 Strain Field Mapping

Strain field maps are the result of a continuum mechanics analysis of the local displacement fields. For ease of calculation, the nodes of the displacement field are tessellated into quadrilateral (for 2D) and brick (for 3D) elements. While increasing nodal

points reduces the error in interpolation, the use of triangular or tetrahedron elements limits the reduction in resolution when assessing strain maps. Due to the relatively large soil deformation during root-inspired anchor pullout, a finite strain approach is utilized, and as well, an Eulerian or spatial description (i.e. fixed mesh) of displacement is employed. As such, the gradient of the displacement tensor, ∇u is determined as shown in Equation 24.

$$\nabla u = \begin{bmatrix} \dfrac{\partial u_1}{\partial x_1} & \dfrac{\partial u_1}{\partial x_2} & \dfrac{\partial u_1}{\partial x_3} \\[2mm] \dfrac{\partial u_2}{\partial x_1} & \dfrac{\partial u_2}{\partial x_2} & \dfrac{\partial u_2}{\partial x_3} \\[2mm] \dfrac{\partial u_3}{\partial x_1} & \dfrac{\partial u_3}{\partial x_2} & \dfrac{\partial u_3}{\partial x_3} \end{bmatrix} \tag{24}$$

Following, the deformation gradient, F, and Eulerian strain tensor, E, are calculated with Equations 25 and 26, respectively.

$$F = \nabla u + I \tag{25}$$

$$E = \frac{1}{2}\left[I - \left(F^{-1}\right)^{T} F^{-1} \right] \tag{26}$$

Due to the large strain approach, solely a measure of the shear strain is utilized and is defined separately for the 2D and 3D cases using Equations 27 and 28, and finally, the volumetric strain is computed with Equation 29.

$$\varepsilon_{shear} = \varepsilon_1 - \varepsilon_2 \tag{27}$$

$$\varepsilon_{shear} = \frac{2}{3}\sqrt{\left(\varepsilon_1 - \varepsilon_2\right)^2 + \left(\varepsilon_1 - \varepsilon_3\right)^2 + \left(\varepsilon_2 - \varepsilon_3\right)^2} \qquad (28)$$

$$\varepsilon_{vol} = \det\left(F\right) - 1 \qquad (29)$$

7.4   Global Pullout Behavior

The global pullout behavior is the mechanical response of the entire geomaterial-anchor model system as the anchor model is gradually uplifted as viewed from a global or external perspective, and the behavior is captured in the form of anchor model pullout resistance versus model vertical displacement. The pullout resistance-displacement trajectories for each geomaterial set is presented in Figure 7-5 and Figure 7-6. The point in the pullout response where an x-ray scan is performed is noted by a marker. During each scan, anchor model displacement is halted to prevent image blurring, and during each pause in the pullout process, a corresponding period of force relaxation occurs, which is hypothesized to be the result of a relaxation in the chain component of the loading device and not of the geomaterial. Scanning is not initiated until the force reduction stagnates. After scanning and once model uplift is resumed, pullout resistance returns to the approximate value attained before scanning initiated. Table 7-3 details a comparison in global pullout behavior amongst the various anchor models and geomaterials, where the mechanical behavior is characterized by pullout indices as detailed in Chapter 6. In general, greater pullout capacities are attained in Soma No.4 sand and by n6a45 root-inspired anchor models.
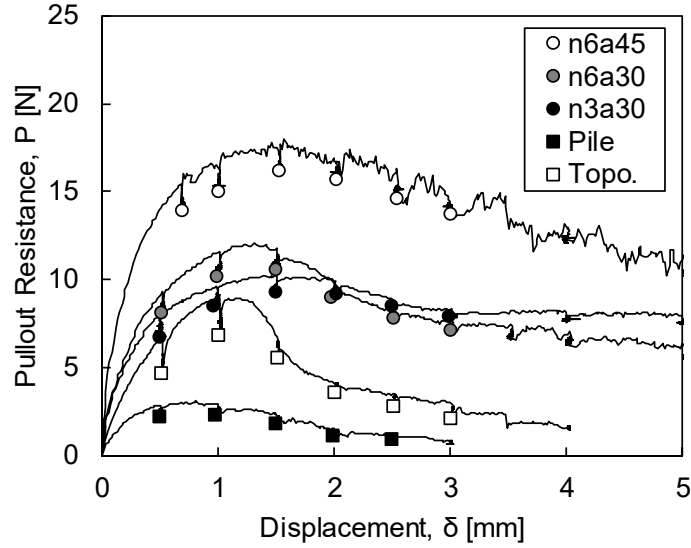
Figure 7-5. Pullout resistance-displacement curves for all models uplifted from Toyoura sand.
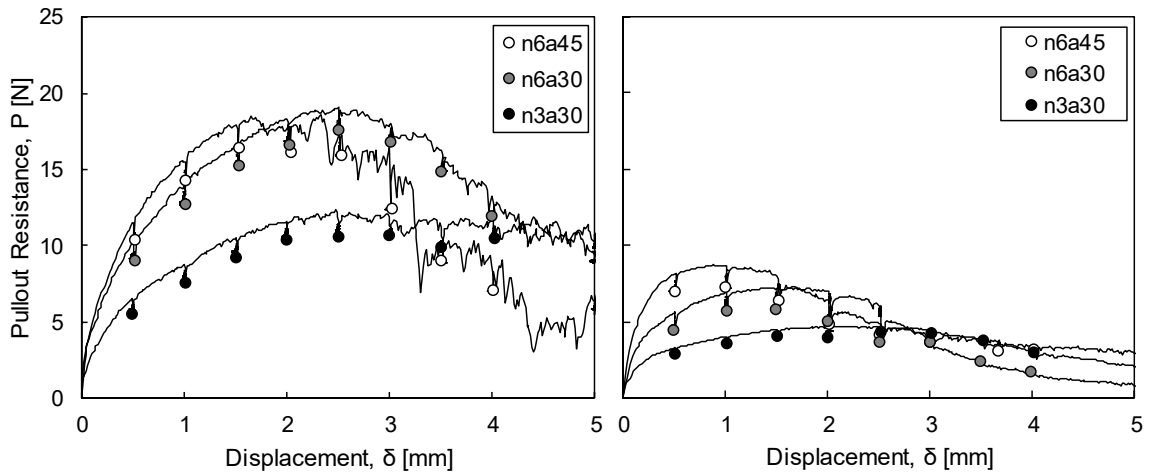
Figure 7-6. Pullout resistance-displacement response for all models uplifted from Soma No.4 sand (left) and glass ballotini (right).

Table 7-3. Compilation of select pullout indices for all cases tested (T = Toyoura sand, S = Soma No.4 sand, GB = glass ballotini).

Models	P_{max} [N]			$\delta(P=P_{max})$ [mm]			Π_M [ ]		
	T	S	GB	T	S	GB	T	S	GB
n3a30	10.2	12.4	4.7	1.40	2.47	1.85	247.7	301.1	114.1
n6a30	12.1	19.1	7.2	1.32	2.51	1.35	173.6	274.1	103.3
n6a45	18.0	18.6	8.8	1.57	2.34	0.89	320.4	331.1	156.6
pile	3.1			0.81			70.8		
topo.	8.9			0.98			457.9		

7.5   Local Pullout Behavior

Local pullout behavior herein refers to the regional, discrete behavior of the system in pullout, which is in direct contrast to global pullout behavior, or the cumulative mechanical response of the entire system. Whereas global pullout behavior is characterized by the overall pullout resistance-displacement response, the local pullout behavior is assessed in this research through visualization of the pullout process and the associated system kinematics and deformation behavior analyses.

7.5.1   *Displacement Fields (2D DIC)*

Displacement field maps are generated directly from the DIC analyses performed on radial slices of the 3D reconstructed images. The displacement field map compilations (Figure 7-7 - Figure 7-10) utilize linear interpolation between nodes of displacement values to produce a smoothed displacement map versus a pixelated version. Solely the magnitude of displacement is presented. Additionally, each displacement field is superimposed on the initial radial slice of the two increments considered in each DIC analysis.

Set 1: Toyoura sand

The compilation of displacement field maps for all anchor models uplifted from Toyoura sand are displayed in Figure 7-7 and Figure 7-8. In general, the intensity in the magnitude of displacement peaks at approximately the 3rd increment (1.5mm of vertical model displacement). The notable exceptions include the model n6a45, where the most intense soil deformation occurs in the first increment of displacement and is followed by a secondary increase in deformation in a more concentrated inner cone, as well as the anchor

pile model, where most soil mobilization occurs within the first and second increments of model uplift. Additionally, from the radial slices, a conical type volume of sand is uplifted with anchor models, with the exception of the anchor pile model, which solely disturbs the soil immediately adjacent to the pile suggesting a simple shearing pullout behavior.

Set 2: Soma No.4 sand

The collection of displacement field maps for models vertically displaced from Soma No.4 sand is shown in Figure 7-9. As for the anchor models uplifted from Toyoura sand, the models pulled vertically from Soma No.4 sand demonstrate similar soil deformation patterns, including a gradual intensification in soil deformation up until the 3rd and 4th increments of model displacement and then a gradual reduction in both intensity and extent in soil displacement in the 5th increment. As well, a curved conical volume of sand is uplifted with the anchor models.

Set 3: Glass ballotini

Displacement field maps for the anchor models uplifted from glass ballotini are presented in Figure 7-10. For the n3a30 case, a substantial reduction in the soil deformation intensity and extent is observed in direct comparison to the same model uplifted from both Toyoura and Soma No.4 sands,. Additionally for both n6a30 and n6a45 cases, an initial outward curving conical volume of glass ballotini is displaced during the initial 3 increments of displacement; yet, a more concentrated inwardly curved region of particle deformation is realized throughout all increments that later exists as the sole form of deformation in the 5th increment. The presence of an inwardly curved region of soil deformation for the n6a30 and n6a45 models and the dramatic reduction in soil

displacement for n3a30 model illustrates the effect of particle angularity on the particle kinematics during anchor model pullout, where reduction in geomaterial strength and increase in the ability of particle flow across similar stress conditions is observed for the models tested in glass ballotini.
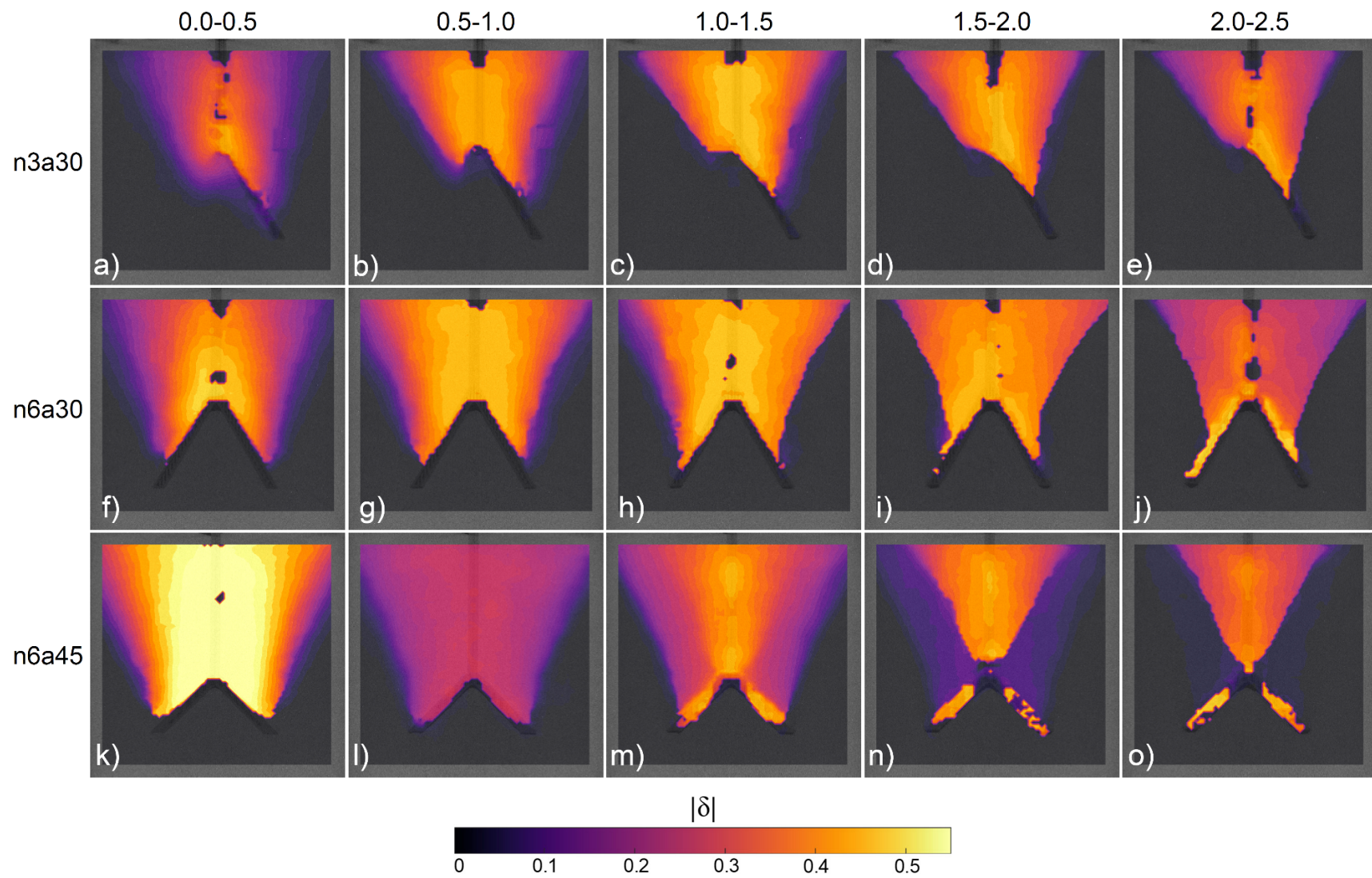
Figure 7-7. Compilation of displacement field maps for three morphology-type anchor models uplifted from Toyoura sand.
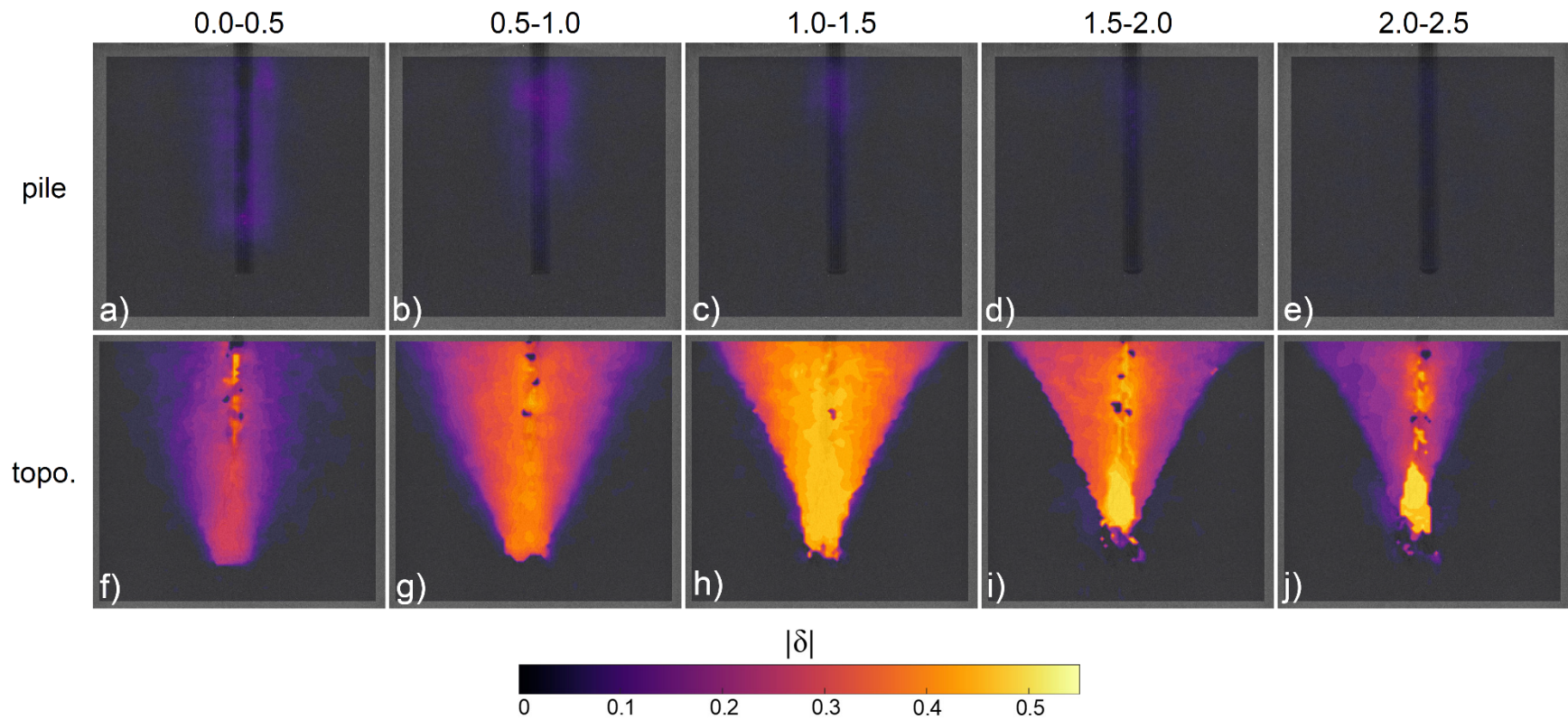
Figure 7-8. Compilation of displacement field maps for straight shaft anchor pile model and topology-type root-inspired anchor model uplifted from Toyoura sand.
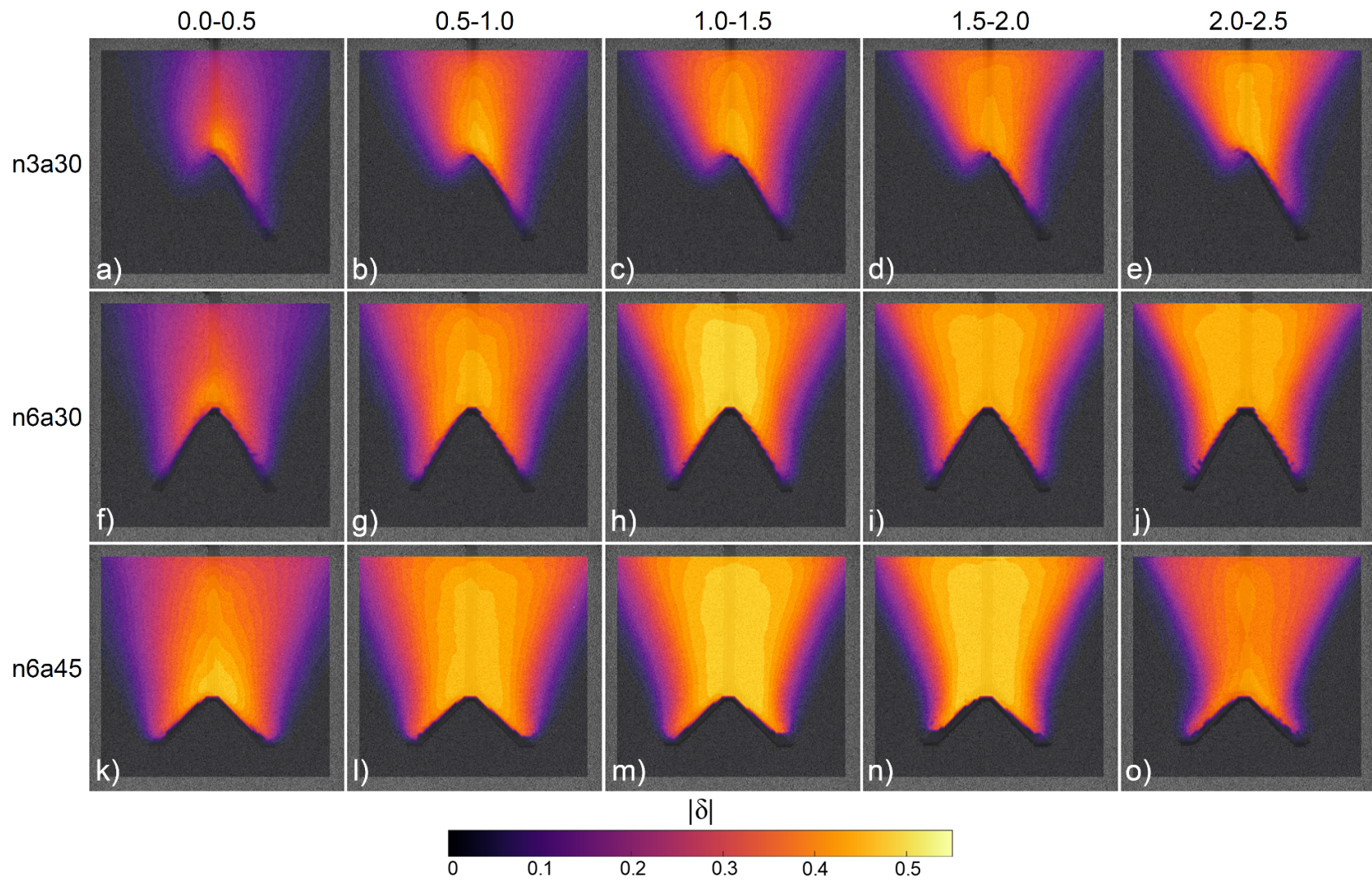
Figure 7-9. Compilation of displacement field maps for three morphology-type anchor models uplifted from Soma No.4 sand.
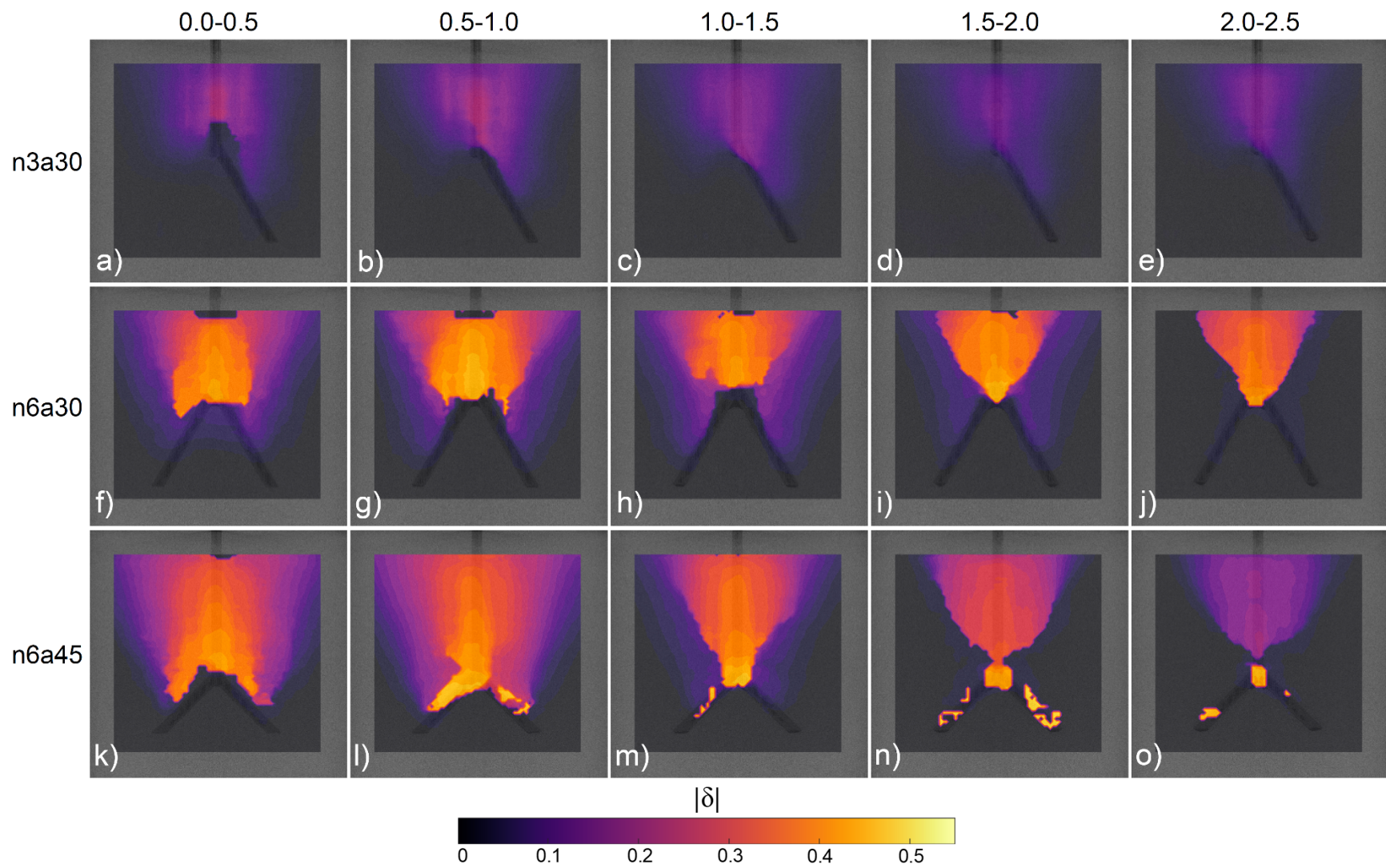
Figure 7-10. Compilation of displacement field maps for three morphology-type anchor models uplifted from glass ballotini.

7.5.2 *Maximum Shear Strain Fields (2D DIC)*

For all cases, the incremental maximum shear strain is displayed. Simplistically, maximum shear strain provides a measure of the gradient of displacement, where locations of significant differences in displacement values result in larger maximum shear strain values. The relative success of both the magnitude of displacement and the maximum shear strain maps, with the exception of the n3a30 model in glass ballotini, indicates that minimal out-of-plane particle movement occurs. Plots of maximum shear strain clearly resolve the location of the failure surface in space. While variations in the mature failure surface are present, most models demonstrate a breakout mode type pullout failure, identical to those from plate anchor studies. Additionally, for all geomaterials, the localization of shear strain occurs before pullout capacity is reached, which corroborates with previous experiments of the presence of failure surfaces in the initial strain hardening regime.

Set 1: Toyoura Sand

Maps of maximum shear strain for the morphology-type root-inspired anchor models uplifted from sand are shown in Figure 7-11, while those for the anchor pile and topology-type root-inspired anchor models are shown in Figure 7-12. For all models with the exception of the pile anchor model, shear strain accumulates into localizations within the first increment of displacement before pullout capacity occurs, and the definition and maturation of the failure surfaces gradually improves until the 4th increment. For the case of n6a45, the maps of maximum shear strain illustrates the initial accumulation of shear strain that initiates towards the end of the model branch axis (Figure 7-11l) and intersects the soil container wall in the 2nd increment (Figure 7-11m), is followed by a secondary,

inner accumulation of shear strain that initiates at the point of dichotomy in the 3rd increment of model displacement (Figure 7-11n), and is followed by the dissolution of the initial, outer failure surface and the full maturation of the inner shear band (Figure 7-11o). No clear failure is resolved in the anchor pile test, whereas a full breakout mode type failure is present for the topology-type anchor model (Figure 7-12).

Set 2: Soma No.4 sand

For the anchor models tested in Soma No.4 sand, maximum shear strain profiles are displayed in Figure 7-13. For this geomaterial, the shear strain localizes into substantially thicker shear bands, which is to be expected given the 5 fold increase in particle size compared to the other samples. As an approximation, the thickness of the mature failure surfaces are on average 2.5mm, 8.3mm, 3.3mm for tests performed in Toyoura sand, Soma No.4 sand, and glass ballotini, respectively, corresponding to 15, 10, and 16 times their respective mean particle diameter sizes, which coincides with previous studies of shear bands in the order of 5-20 particles thick (Roscoe 1970, Mulhaus and Vardoulakis 1987, Oda and Kazama 1998, Evans 2005, Alsaleh et al. 2006). However, this is not a robust measure of the shear band thickness due to the inherent resolution limits of the DIC data (i.e. defined by the spacing of the analysis) as well as the use of linear interpolation in the formation of contour maps

Set 3: Glass Ballotini

The compilation of maximum shear strain maps for anchor models uplifted in glass ballotini are displayed in Figure 7-14. Several disparities are present in terms of the maximum shear maps between the anchor models tested in glass ballotini and those tested

in Toyoura and Soma No.4 sand, which demonstrate the role of particle angularity and geomaterial friction angle on the pullout mechanisms and failure surface characteristics. Firstly, a clear dissimilitude is the existence of a convex rather than the concave failure surface shape present in the two sands. As well, for n6a30 anchor model, the failure surface intersects the model at the point of dichotomy versus some location closer to the middle of the branch axis for the other materials. However, for the n6a45 case, the identical shear strain accumulation mechanism occurs, where an initial outer shear strain localization is followed by an inner shear strain accumulation that nucleates at the point of dichotomy and results in a mature failure surface. The relatively low maximum shear strain and magnitude of displacement values obtained in the case of the n3a30 model could be due to poor performing DIC analysis due to relative consistency and similarity in particles, particle out-of-plane movement, or the occurrence of a flow mechanism, where the anchor model is displaced through the particulate medium with minimal influence on the particle kinematics (multiple DIC analyses were performed with various subset window).
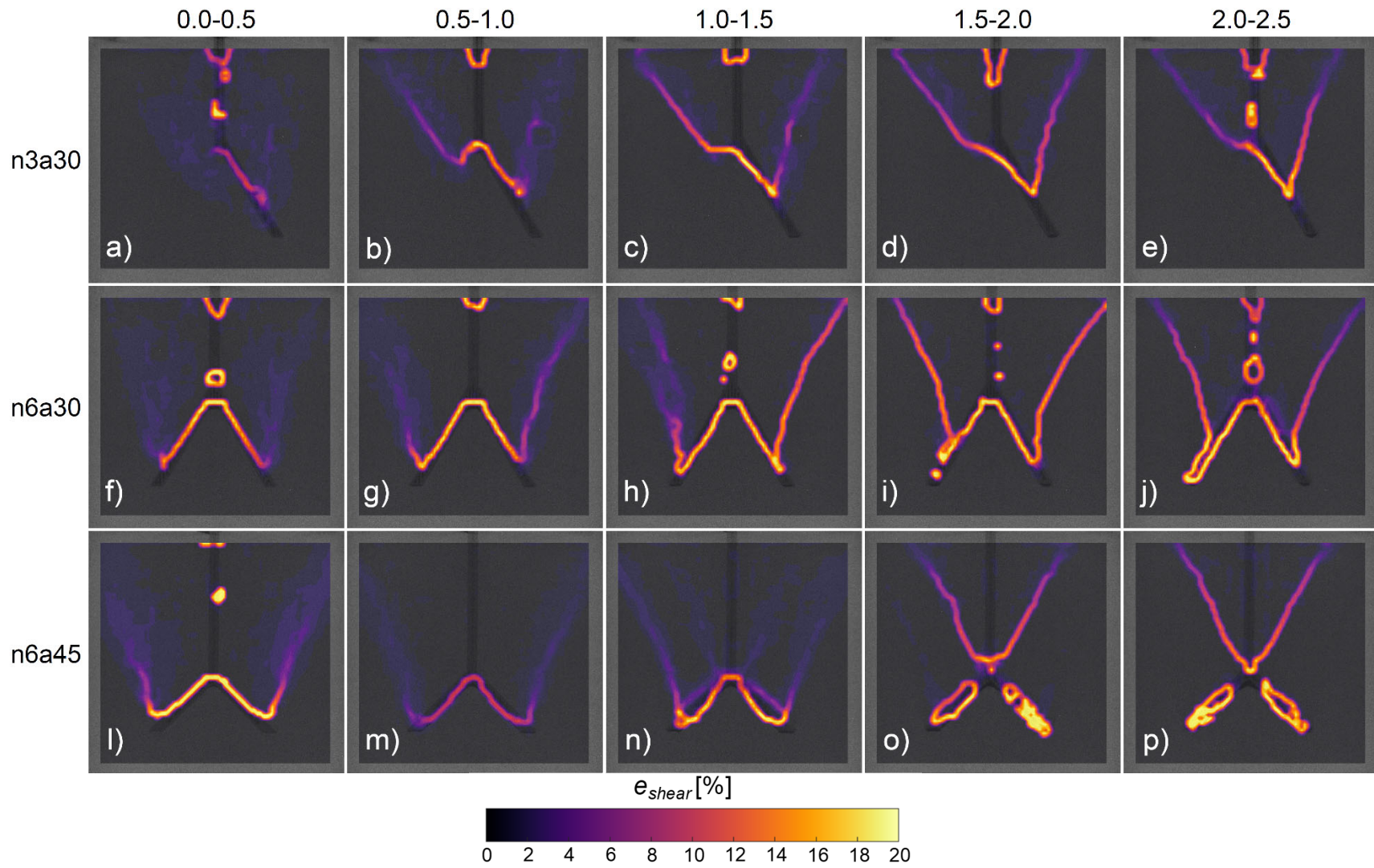
Figure 7-11. Maximum shear strain map compilation for morphology-type anchor models uplifted from Toyoura sand.
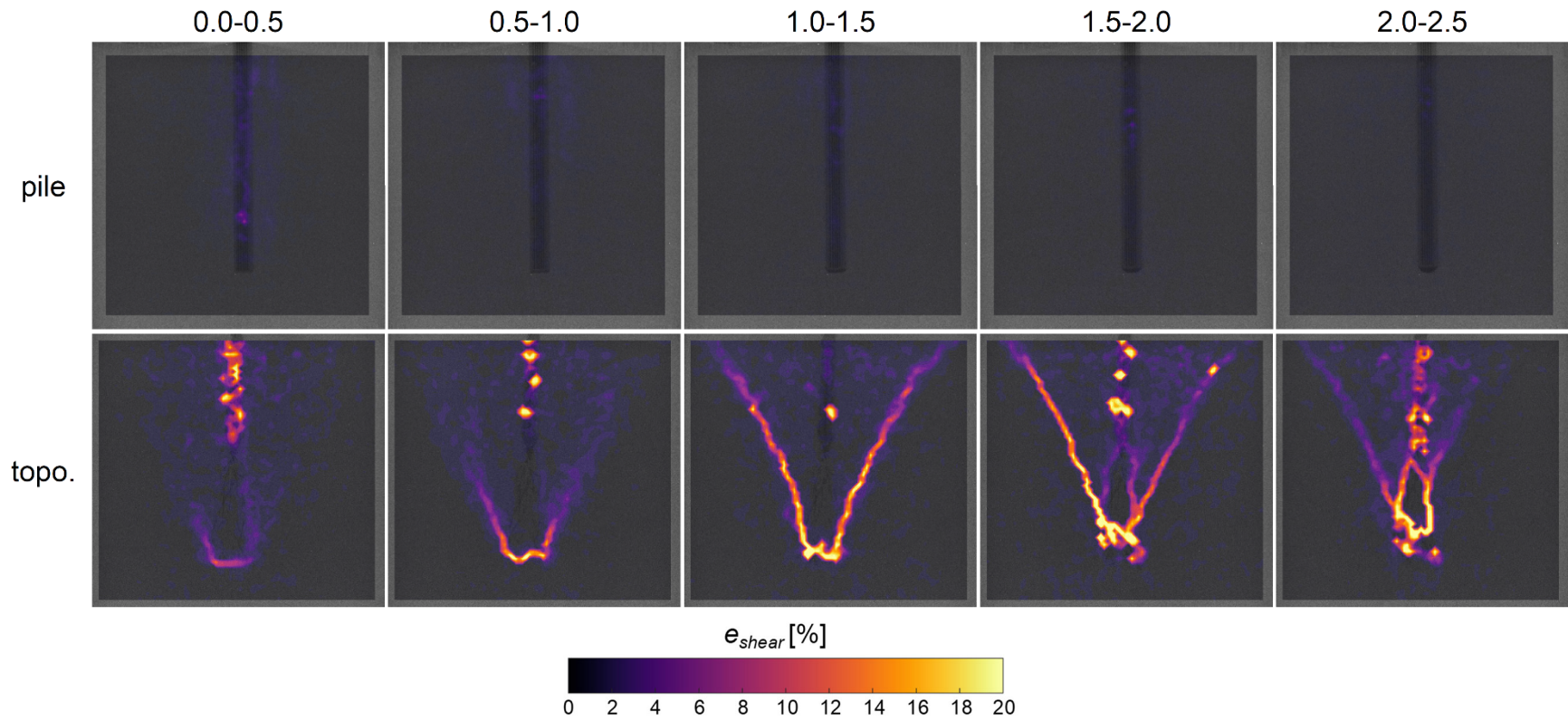
Figure 7-12. Maximum shear strain map compilation for anchor pile and topology-type root-inspired anchor models uplifted from Toyoura sand.
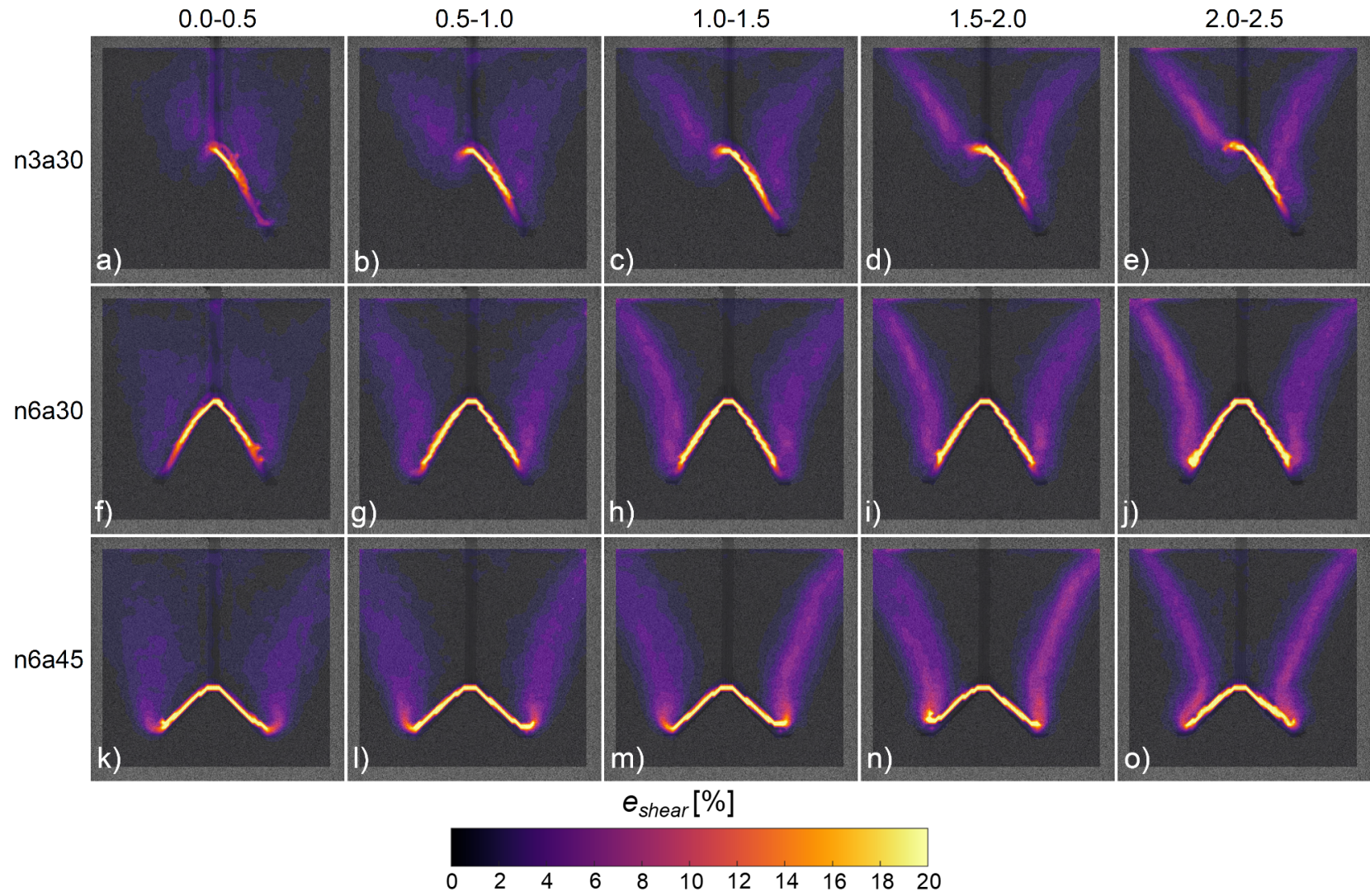
Figure 7-13. Maximum shear strain map compilation for morphology-type anchor models uplifted from Soma No.4 sand.
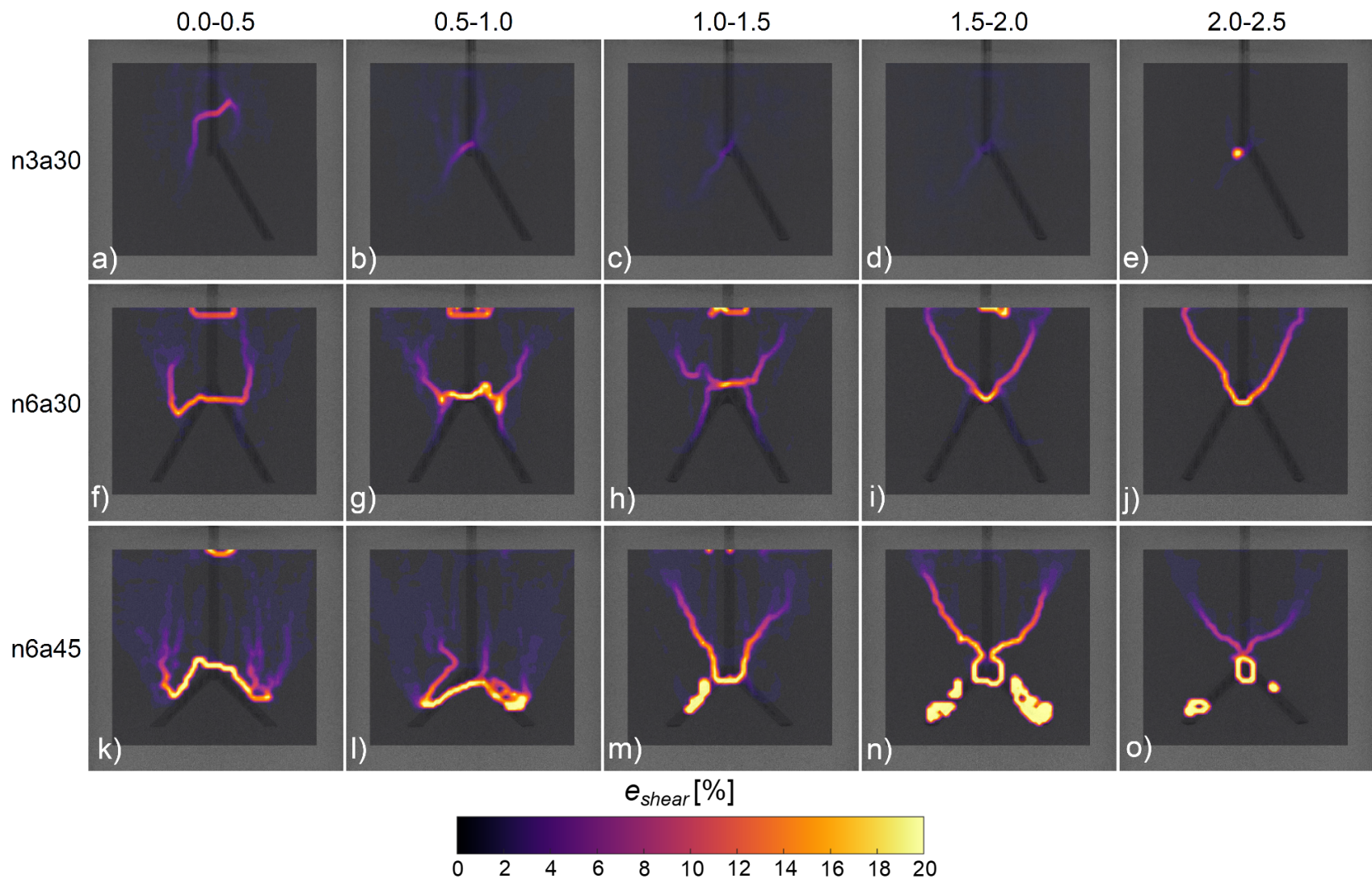
Figure 7-14. Maximum shear strain map compilation for morphology-type anchor models uplifted from glass ballotini.

7.5.3   Maximum Shear Strain Volumes (3D DVC)

With the three-dimensional maximum shear strain field obtained via DVC analyses, the resultant complete failure surface is visualized. For all cases, with the exception of the anchor pile model, the mature failure surface appears as a hyperboloid with a petaloid-type bottom. For all pullout tests performed, shear strain accumulation is present in all increments, and the increment at which the most clearly defined failure surface generally corresponds to the increment of model displacement after pullout capacity is attained. To note, a direct comparison of maximum shear values for the images presented is not advised due to the limitations in presenting three-dimensional data in two. For example, for the test of n6a45 in Toyoura sand, the external outer failure surface conceals the intensity of the inner surface; though some level of transparency is provided to allow for some visualization of the internal structure, actual shear strain values are not discernable.

Set 1: Toyoura Sand

The compilation of three-dimensional maximum shear strain maps for anchor models uplifted from Toyoura sand are shown in Figure 7-15-Figure 7-17. For the n6a45 anchor model test, the evolution in shear strain localization from an outer to inner failure surface is fully illustrated, wherein the boundary condition (i.e. rigid soil container wall) in the initial increments is clearly visible. Additionally, a DVC analysis allows for visualization of a failure surface for the anchor pile model test, albeit the strain level is five times less intense. As expected, shear strain localizes into a cylindrical volume around the pile shaft. The resemblance in failure surface shape between the topology- and

217

morphology-type models illustrates the significance of soil properties and conditions on the resultant rupture surface morphology.

Set 2: Soma No.4 sand

The three-dimensional maps of maximum shear strain for all morphology-type root-inspired anchor models uplifted from Soma No.4 sand are shown in Figure 7-18. Though the resolution of the 3D maximum shear strain maps is double that of those in the Toyoura sand set, the definition of the failure surface is less refined due to particle size and the increase in failure surface thickness. A noticeable decrease in the volume of the failure surface for the n6a45 case is apparent by the gradual increase in exposure of the branching portion of the root-inspired anchor; yet a dramatic shift in kinematics as in the Toyoura sand set does not occur. On first speculation, this distinction could be a particle size effect, such that insufficient soil deformation in relation to the particle size has occurred to allow for such a change in kinematics or a state variable difference, such that a relative density of 80% for the Soma No.4 sand reflects a stronger specimen than the Toyoura sand at the same relative density.

Set 3: Glass Ballotini

For anchor models uplifted from glass ballotini, the 3D maximum shear strain maps are displayed in Figure 7-19 and Figure 7-20, where the maximum shear strain scale for anchor model n3a30 is presented at half of that for the n6a30 and n6a45 models. As for the 2D DIC analysis, the indefinite, unclear failure surface is either a result of poor performance of the 3D DVC algorithm, more random particle kinematics, or a combination of the both.
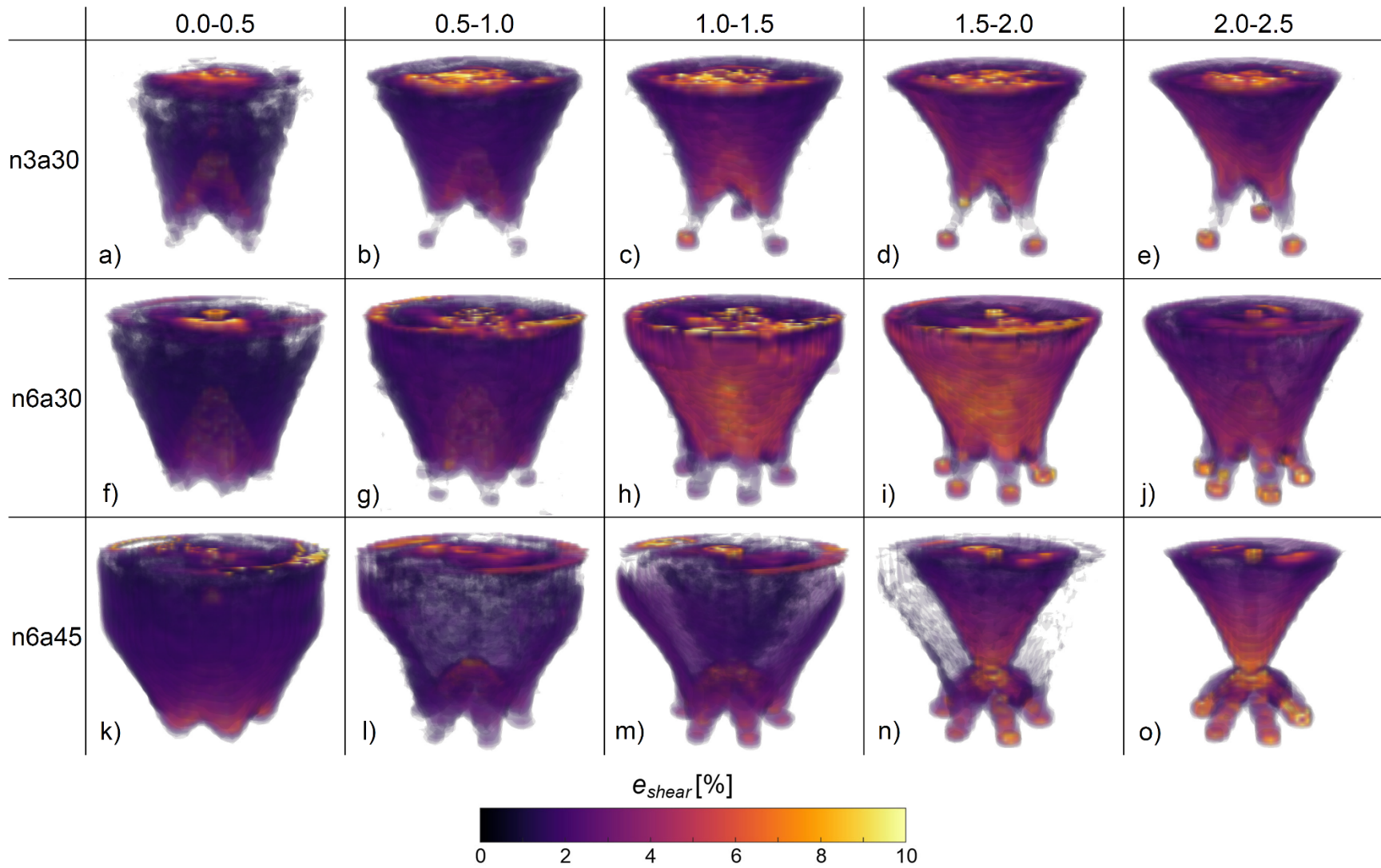
Figure 7-15. 3D maximum shear strain maps for pullout of morphology-type anchor models from Toyoura sand.
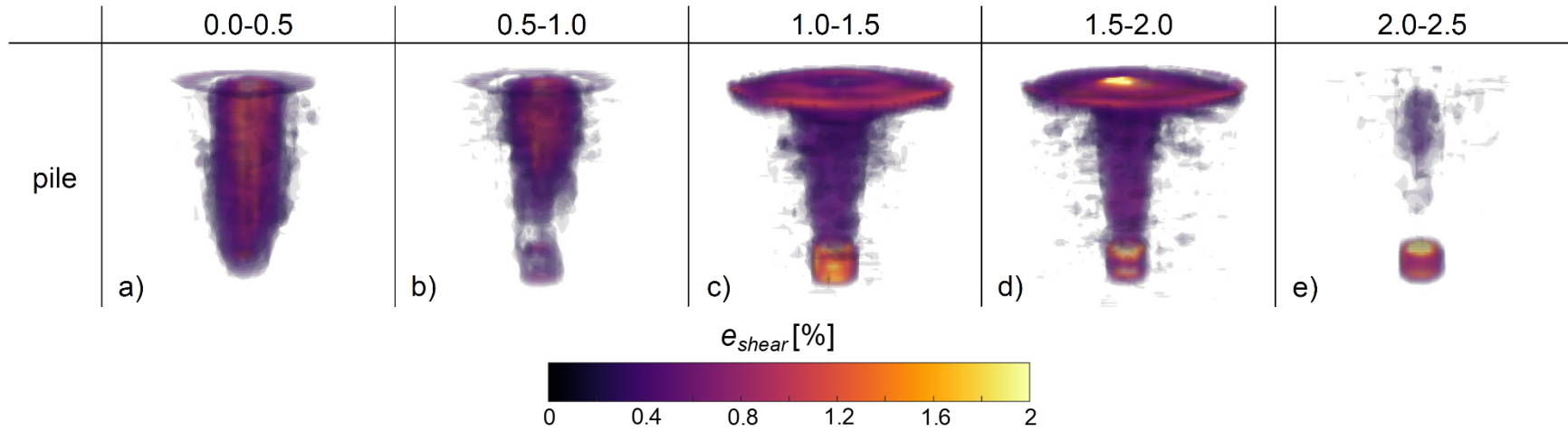
Figure 7-16. 3D maximum shear strain maps for pullout of anchor pile model from Toyoura sand.
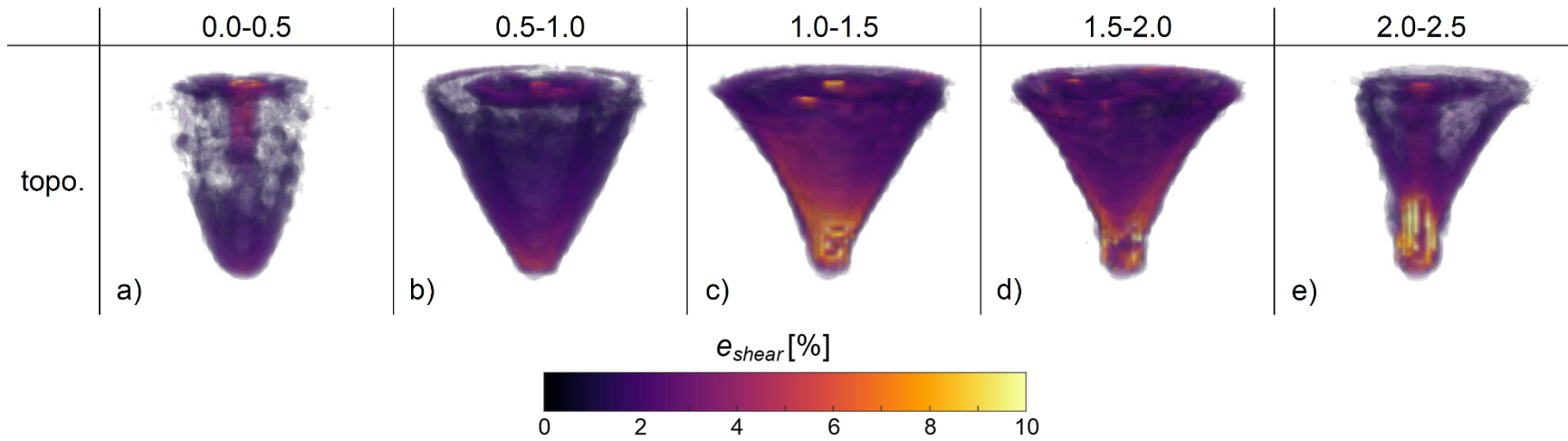
Figure 7-17. 3D maximum shear strain maps for pullout of topology-type root-inspired anchor model from Toyoura sand.
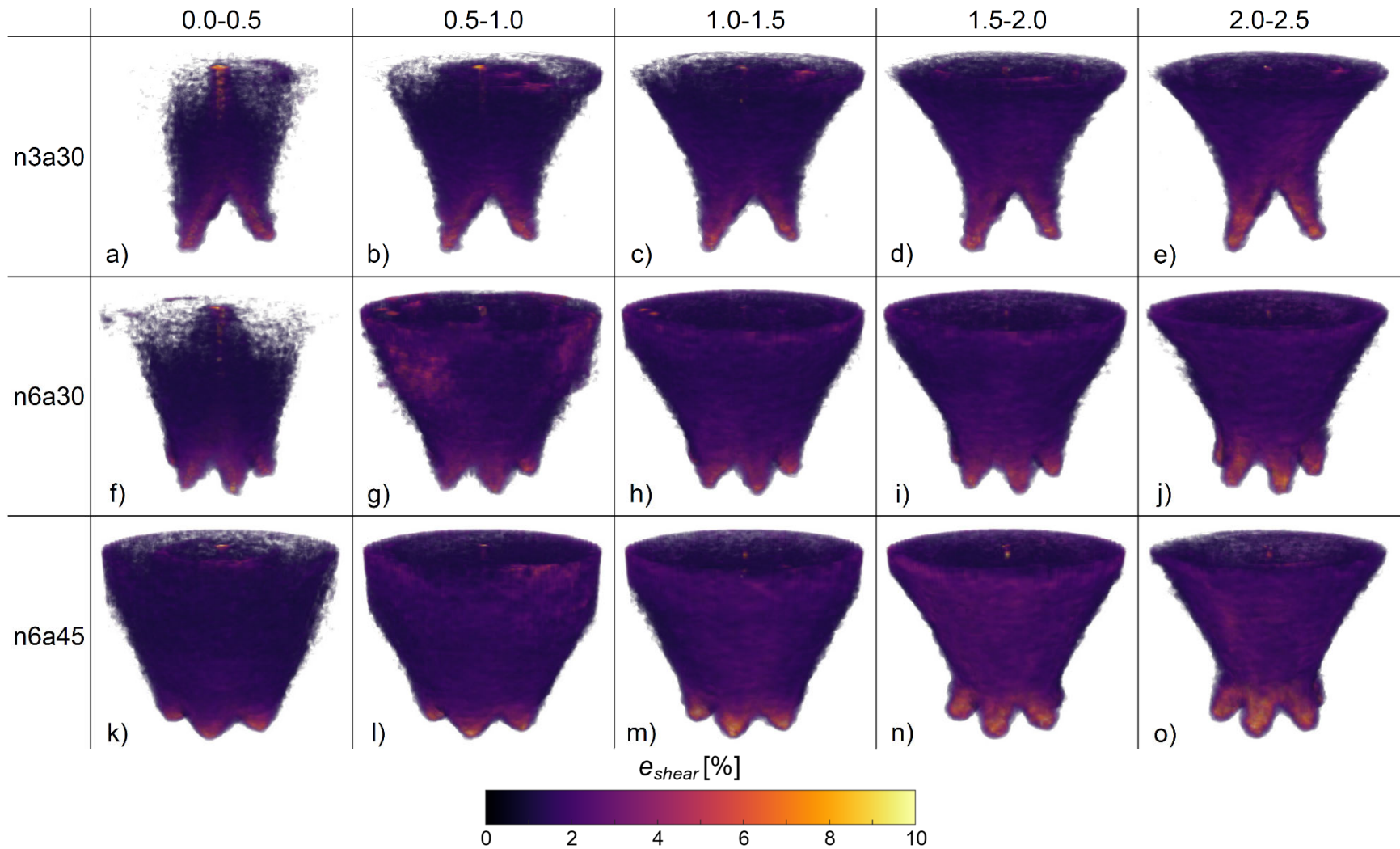
Figure 7-18. 3D maximum shear strain maps for pullout of morphology-type root-inspired anchor models from Soma No.4 sand.
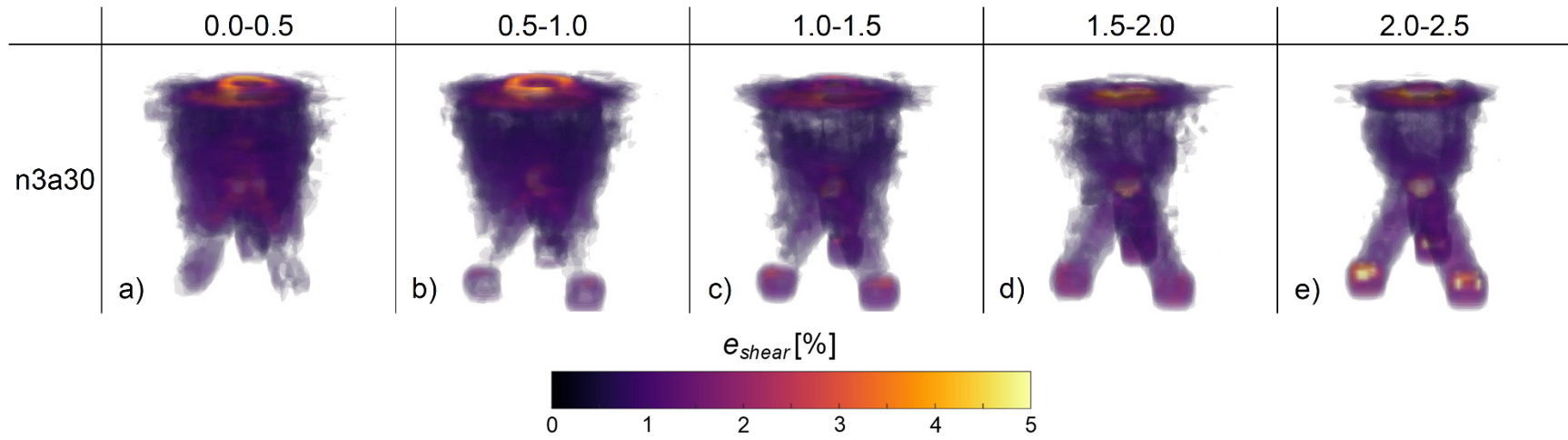
Figure 7-19. 3D maximum shear strain maps for pullout of n3a30 anchor model from glass ballotini.
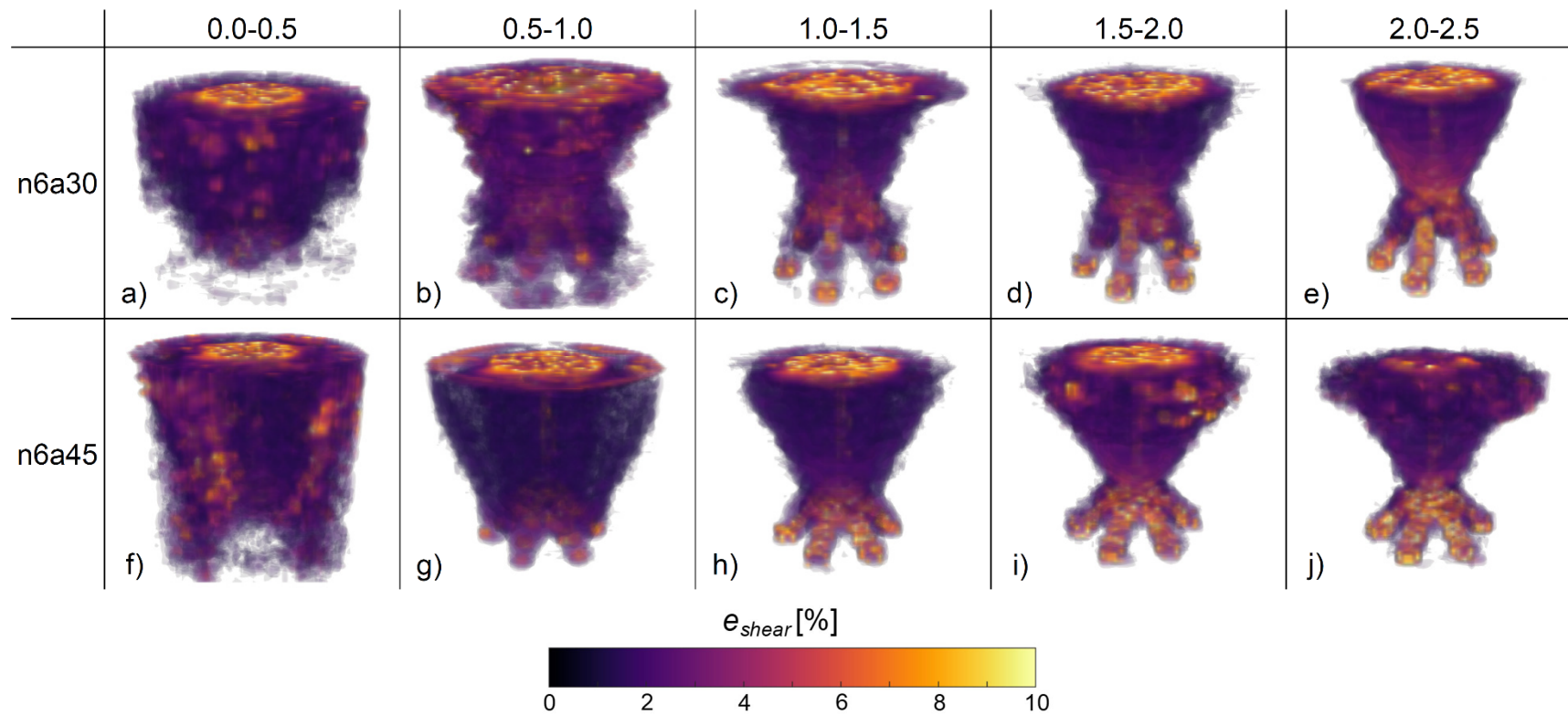
Figure 7-20. 3D maximum shear strain maps for pullout of morphology-type root-inspired anchor models from glass ballotini.

7.5.4   Association of Failure Surface and Global Pullout Response

The purpose of this section is to associate the local pullout behavior in terms of the particle kinematics and material shear strain localization to the global pullout behavior, namely the characteristic pullout resistance-displacement response. This section continues in the assumption that pullout resistance is due to both the weight of the uplifted soil mass as well as shearing force either amongst particles or at the particle-anchor model interface. As such, this section compares the weight of the volume of uplifted geomaterial to the global pullout response. The volume of uplifted material is approximated from the DVC analysis. For each incremental comparison, the displacement magnitude images are binarized through thresholding and common binary morphology operators (e.g. erosion, dilation, opening, and closing) are utilized to form an approximate volume of the uplifted geomaterial. Another attempt to associate the global and local behavior was through the determination of the rate of work utilized in the uplift of soil volume through the integration of incremental particle velocities (White et al. 2008).

Set 1: Toyoura Sand

The comparison between the global pullout resistance and the DVC analysis-determined weight of uplifted soil for the morphology-type root-inspired anchor models is displayed in Figure 7-21, whereas the results for the topology-type anchor and anchor pile models are illustrated in Figure 7-22. In general the approximated weight of uplifted soil is 2-3 times less than the pullout resistance at that increment of displacement, suggesting that a frictional resistance of the soil contributes to the uplift problem both along the failure surface and along the root-inspired anchor model that is sheared against the soil. The peak

DVC volume weight approximation either coincides with pullout capacity at the same model displacement increment (e.g. n6a30, topo.) or before (e.g. n6a45, n3a30). As well, the weight of soil gradually decreases with greater model displacements after capacity is reached. For the pile anchor model, the results further establish the argument that pullout resistance for the anchor pile model is solely due to shearing resistance proximal to the anchor pile shaft.

Set 2: Soma No.4 Sand

For all anchor models uplifted from Soma No.4 sand, the approximated weight of uplifted soil is substantially less than the recorded pullout resistance at the same increment of displacement (Figure 7-23). Furthermore, the displacement at which DVC approximate peaks is also substantially less than the displacement at which pullout capacity occurs. The DVC analysis provides information solely concerning the material kinematics. While the DVC analysis indicates that a volume of soil is displaced relative to its original positon, it cannot indicate whether the material has displacement sufficiently as to mobilize the full shear strength along the failure surface, where the previous 2D maximum shear strain maps indicate that shear strain is gradually accumulating into a localized failure surface until a fully, defined failure surface is achieved after pullout capacity is attained.

Set 3: Glass Ballotini

Due to the indistinct results of the DVC analysis, fluctuations in the DVC-determined uplifted soil weight value occur with displacement, though the general trend of a decreasing volume of soil with model uplift remains (Figure 7-24).
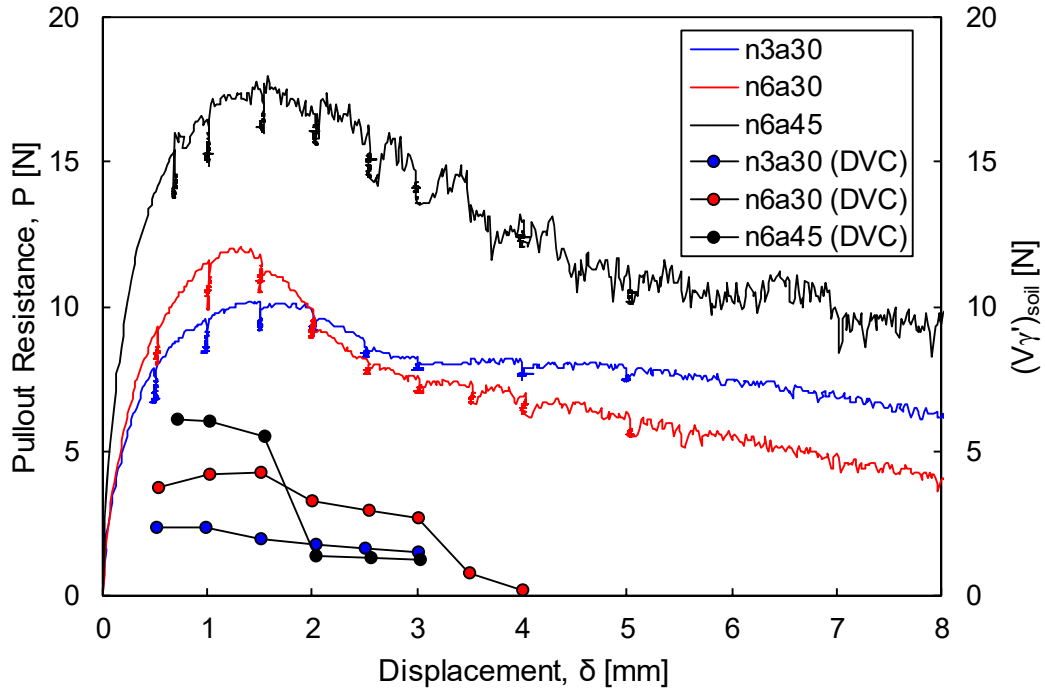
Figure 7-21. Comparison between pullout resistance and weight of soil within DVC-described failure surfaces with vertical displacement of morphology-type root-inspired anchor models from Toyoura sand.
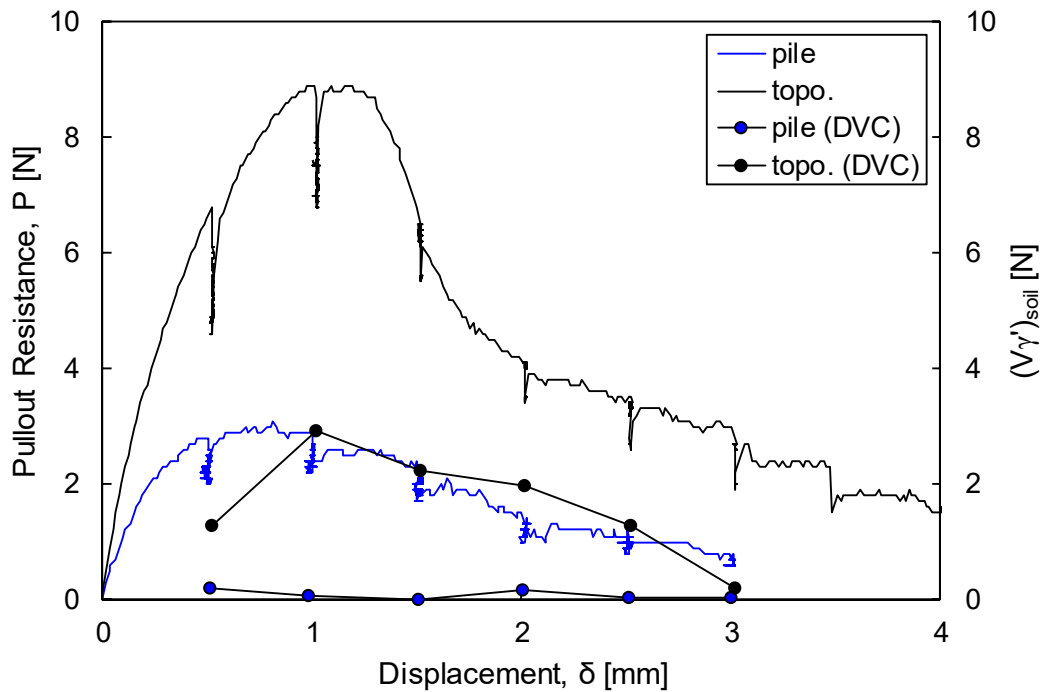
Figure 7-22. Comparison between pullout resistance and weight of soil within DVC-described failure surfaces with vertical displacement of anchor pile and topology-type root-inspired anchor models from Toyoura sand.
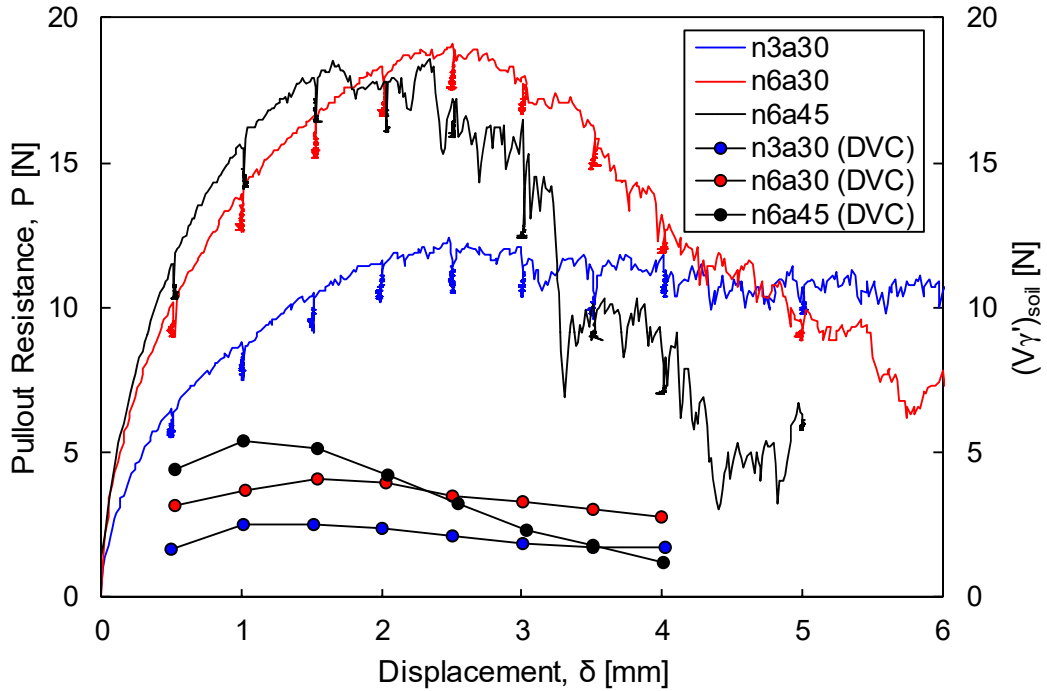
Figure 7-23. Comparison between pullout resistance and weight of soil within DVC-described failure surfaces with vertical displacement of morphology-type root-inspired anchor models from Soma No.4 sand.
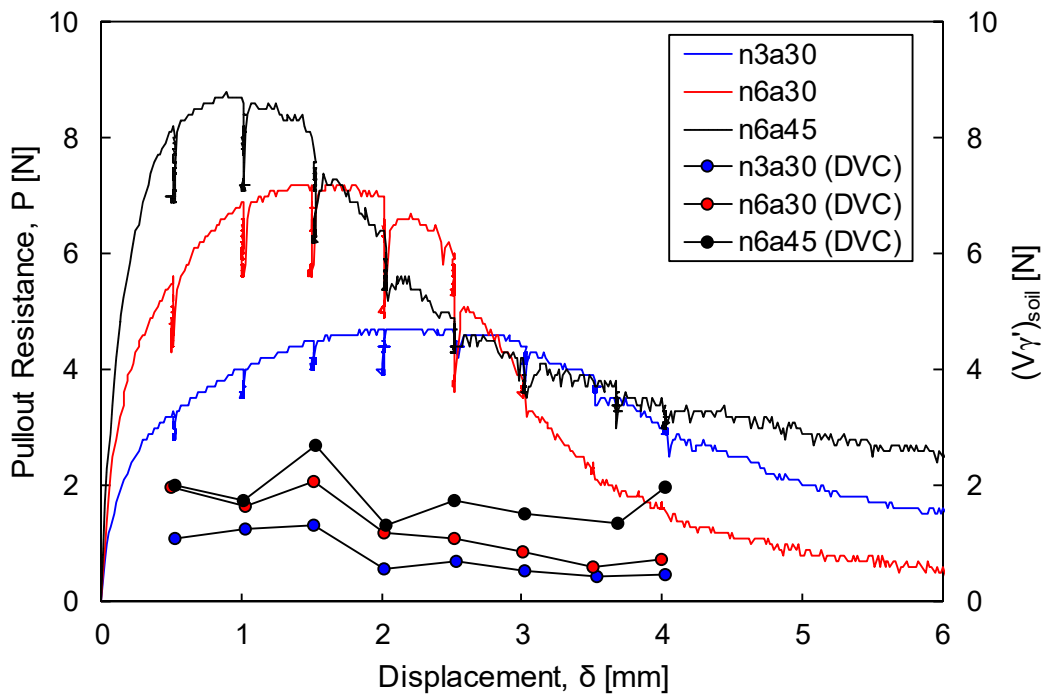
Figure 7-24. Comparison between pullout resistance and weight of soil within DVC-described failure surfaces with vertical displacement of morphology-type root-inspired anchor models from glass ballotini.

7.6 Failure Surface Morphology

The mechanics of the pullout process is contained within the shape of the failure surface. The purpose of this section is to analyze in detail the morphological characteristics of the failure surface to form a more precise understanding of the mechanics of pullout. As such, a mathematical analysis of the failure surface shape is conducted in conjunction with a mechanics-based rationale. The guiding questions for this section stimulated from the results of the DIC and DVC analyses are as follows:

• Why are the failure surfaces curved and not straight? More so, why are the failure surfaces concave for the sand samples and straight/convex for the glass ballotini sample?

• Why does the geomaterial between adjacent anchor branch axes displace upwards with the anchor model instead of the anchor model sliding through the particles?

• What leads to the development of secondary, inner failure surfaces for some of the models?

• Why does the failure surface initiate at some distance along the anchor branch axis versus at the point of dichotomy or the tip of the branch axis?

7.6.1 General Shape

In all cases, the failure surface initiates at some point along the branch axis and extends vertically and outwardly to the soil surface. For both the Toyoura and Soma No.4 sand samples, the failure surface is concave, where the surface curves inwards towards the central axis of the anchor model; yet, in the case of glass ballotini, convex failure surfaces

occur. For the pullout of a horizontally oriented plate from a homogeneous geomaterial sample, a straight inclined failure surface is expected when the normal stress on the failure surface remains constant during pullout. Additionally, given a constant normal stress, a straight inclined failure surface requires a constant mobilized friction angle with depth. However, in 1g model conditions with no surcharge, geomaterial samples are significantly influenced by particle dilation, and for identical stress conditions, the mobilized friction angle increases with decreasing stress. As such, for a material that experiences increasing dilation with decreasing depth (i.e. stress), a concave failure surface is expected. Furthermore, the likelihood of a constant normal stress at depth seems unlikely as shown by the magnitude of displacement maps, which indicates a uniform loading scenario, where the magnitude gradually grows as an expanding centrally located bulb. For the glass ballotini samples, the occurrence of straight and convex failure surfaces for the case of the n6a30 and n6a45 anchor models, respectively, only fully develops in the 4th increment, while with the displacement field maps an outer concave displacement is apparent. As such, perhaps the existence of mature straight and convex failure surfaces in the case of glass ballotini is due to a rotating stress state combined with less variation in mobilized friction angle with depth.

Additionally, the shape of the failure surface is not solely governed by the properties of the geomaterial; the anchor models undoubtedly alter the shape as evident by the individual differences within the same geomaterial (e.g. apparently smaller breakout geomaterial volumes, varying point at which the failure surface intersects the branch axis).

7.6.2   *Analytical Description: Logarithmic Spiral*

Within Mohr-Coulomb theory, a material at or beyond the yield surface undergoes volume change upon deformation and therefore, requires both tangential and normal geometric freedom to move. To allow for such behavior, both planar and logarithmic spiral surfaces can be utilized, whereas circular surfaces inhibit material deformation (Drucker and Prager 1951, Bolton 1986). In the analysis of several common geotechnical problems (e.g. bearing capacity, slope stability, and active and passive earth pressure problems), logarithmic spirals are favored to describe the rupture surface over kinematically inadmissible circular surfaces.

A logarithmic spiral is defined analytically in polar notation in Equation 30, where ρ is the radius of the spiral and ψ is the angle between the line tangent to the spiral and radius of the spiral. The beauty of the logarithmic spiral in relation to geotechnics is that the angle complementary to the tangential angle, ψ, is known based on the assumptions of the analysis and as well defines the displacement of the material relative to the failure surface. To note, for a failure surface that spans various stress conditions, a single logarithmic spiral cannot perfectly describe the kinematics of the problem since the radius of the spiral expands at a constant rate, which directly conflicts with a decreasing friction angle with depth.

$$\rho(\theta) = \rho_0 e^{\kappa\theta}$$
$$\kappa = \cot\psi = \tan\phi$$

(30)
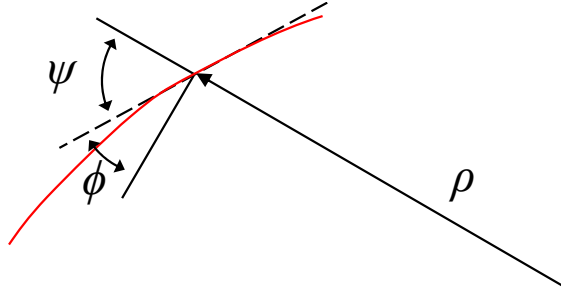
Figure 7-25. Schematic of logarithmic spiral with descriptors.

In parametric form, the logarithmic spiral is defined in Equation 31, where r describes the horizontal component of the spiral, z, the vertical component, and θ, the angle of the spiral from the horizontal.

$$r(\theta) = \rho \cos \theta + r_0$$
$$z(\theta) = \rho \sin \theta + z_0 \tag{31}$$

Furthermore, the failure surface in two-dimensions can be fit with a logarithmic spiral. The problem is composed of four unknowns, ρ_0, κ, r_0, and z_0. For the regression analysis, the various pixels of the maximum shear strain maps are used as the data points, where the pixel values are used as weights. As a result, error in the regression analysis is minimized as the logarithmic spiral function overlays the failure surface. The non-linear curve fitting analysis is implemented in Matlab and utilizes the fminsearch function, based upon the Nelder-Mead simplex method, to identify the centroid of the spiral, r_0 and z_0, and within that function, a linear least squares analysis to identify ρ_0 and κ. An image mask was formed to remove the locally intense maximum shear strain values adjacent to the anchor models. To note, in the analysis, no constraints were placed on the logarithmic spiral parameters, such that while visually and statistically, the fit performed well (i.e.

minimization of root mean square error), realistically, the model ignored the physicality of the model and erroneous parameter values were found, namely the value of κ.

The results of the logarithmic spiral fit are superimposed onto the maps of maximum shear strain along with overlain displacement quivers (Figure 7-26-Figure 7-29). With these figures, not only is it visually determined that a logarithmic spiral can well define the breakout failure surface, but also the orientation of the failure surface relative to geomaterial displacement is realized. As a general approximation, the angle varies significantly between negative and positive values. Additionally, conditions that appear to be kinematically inadmissible (i.e. regions where the particle trajectories intercept the failure surface) are demonstrated particularly in the case of pullout from Soma No.4 and glass ballotini. For a Coulombic material, the geomaterial undergoes a volume change in the plastic regime (i.e. dilation), and consequently, the material moves at some angle relative to the orientation of the failure surface. For materials that comply with the normality condition (i.e. associative flow), the angle is equivalent to the mobilized friction angle; yet, for non-associative flow, the angle is less than that of the mobilized friction angle. Based on the approximate results, these materials appear to violate the normality condition.
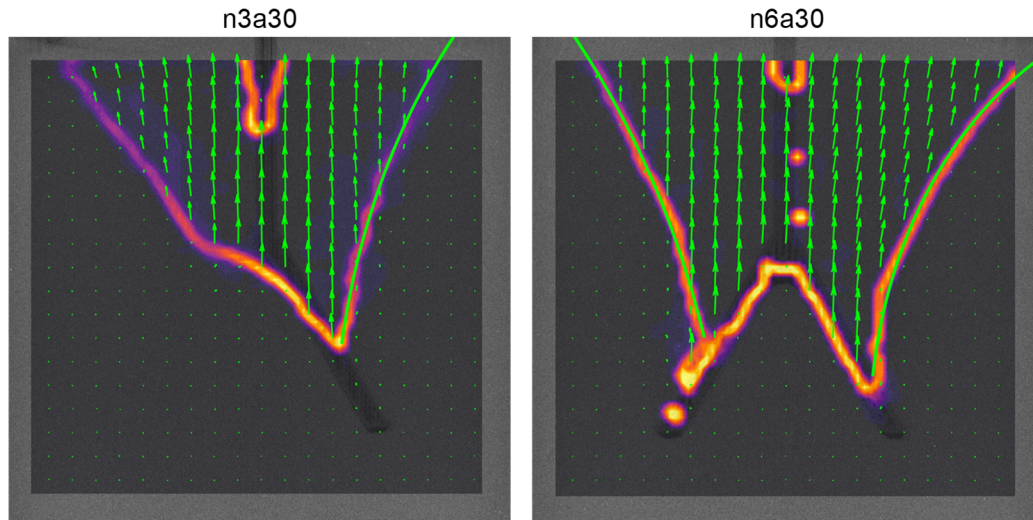
Figure 7-26. Fitted logarithmic spiral and displacement quivers superimposed on maximum shear strain maps for the pullout of model n3a30 (left) and model n6a30 (right) from Toyoura sand.
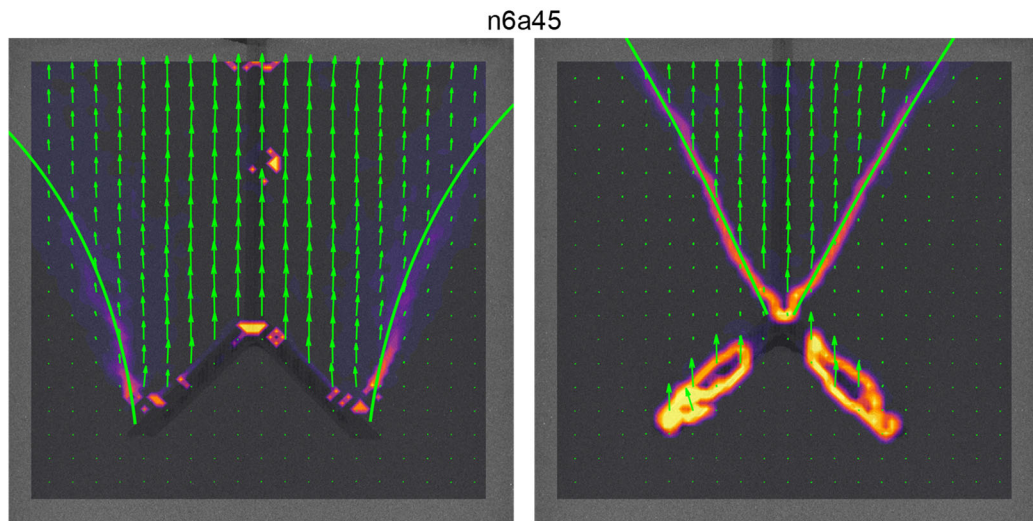
Figure 7-27. Fitted logarithmic spiral and displacement quivers superimposed on maximum shear strain maps for the pullout of model n6a45 in Toyoura sand at the 1st and 4th increments of displacement, respectively.
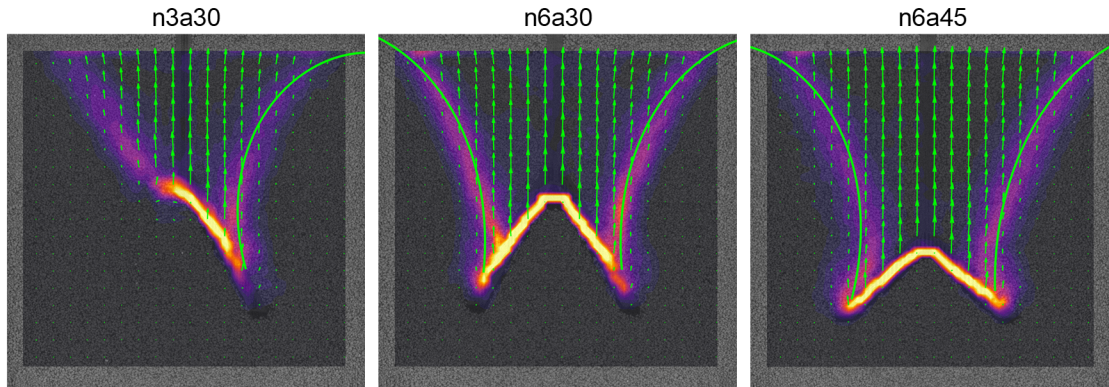
Figure 7-28. Fitted logarithmic spiral and displacement quivers superimposed on maximum shear strain maps for the pullout of root-inspired anchor models from Soma No.4 sand.
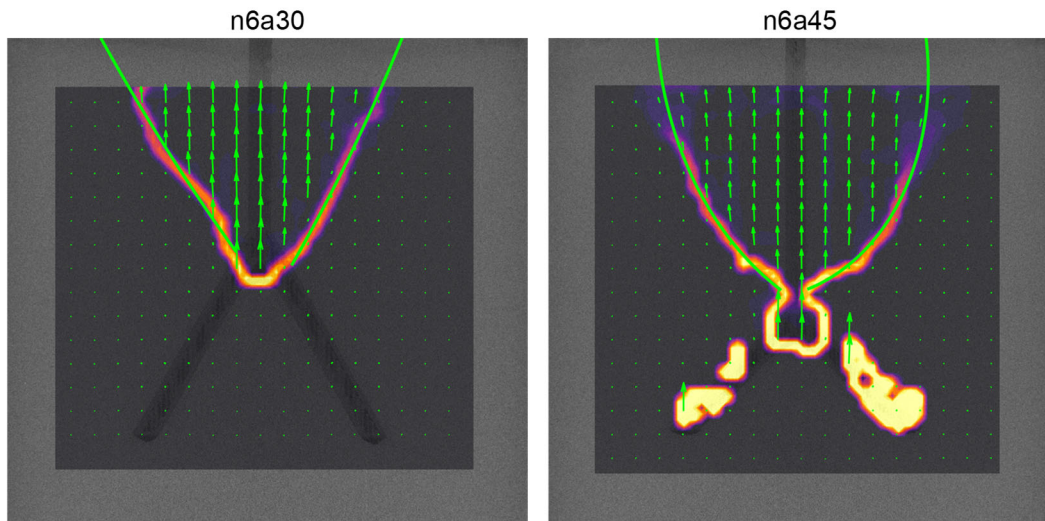
Figure 7-29. Fitted logarithmic spiral and displacement quivers superimposed on maximum shear strain maps for the pullout of model n6a30 (left) and model n6a45 (right) from glass ballotini.

7.6.3   Initiation and Termination Angles

The angle at which the failure surface intersects the root-inspired anchor models is critical to the description of the mechanics of the pullout process, as well as to the description of a logarithmic spiral-defined rupture surface. This angle, defined as the initiation angle, ω, is the angular difference in the orientation of particle flow immediately

around the anchor model to the orientation of the failure surface. As visualized in Figure 7-26-Figure 7-29, the particles immediately above the branch-axis circa the failure surface displace vertically with anchor model. Consequently, the initiation angle can be calculated simply as the tangent of initial portion of the failure surface to the vertical as shown schematically in Figure 7-30(right). For morphology-type root-inspired anchor pullout tests, the value of the initiation angle is displayed in Figure 7-30(left). In general, similar values are achieved amongst the n3a30 and n6a30 models within a geomaterial, while a greater initiation angle for the n6a45 is realized. This suggests that internal branching angle influences the initial rupture surface orientation. Furthermore, the mean initiation angles apparent in for the Soma No.4 vary minimally in comparison to the other geomaterials, which could be due to state variable effect as suggested earlier such that Soma No.4 is more stable and stronger at a relative density of 80% than the other materials. The initiation angle values confirm that all materials do not conform to the normality condition within plasticity theory.
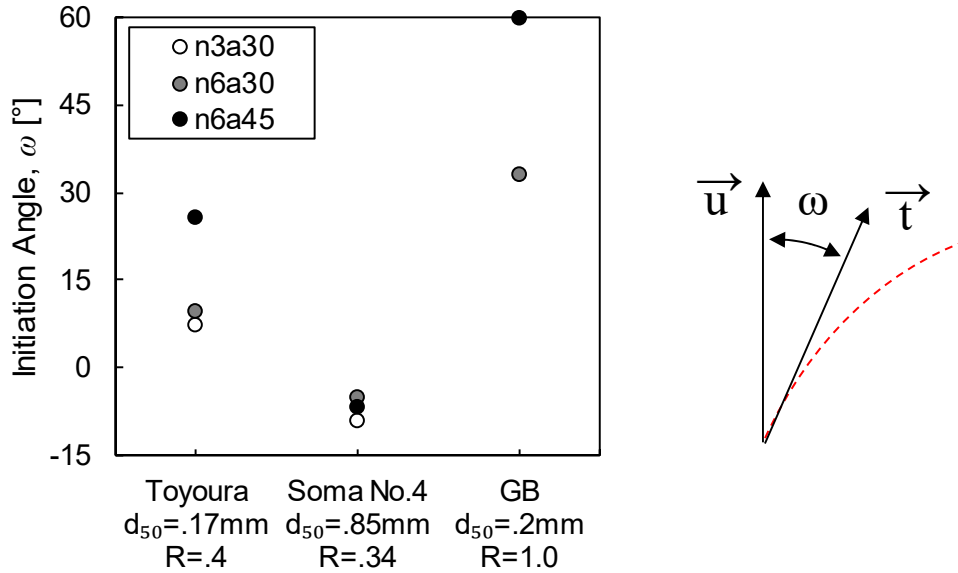
Figure 7-30. (left) Mean initiation angle, ω, with geomaterial type for the various pullout tests performed on morphology-type root-inspired anchor models, and (right) a schematic representation of the initiation angle, where vectors *u* and *t* represent the displacement vector and failure surface tangent vector, respectively.

The termination angle, which is defined as the angle between the tangent to the failure surface at the soil surface and the orientation of the failure surface, is not determined for all studies since significant blurring is apparent near the soil surface. However, for a statically admissible failure surface, the termination angle would be equal to $\pi/4-\phi/2$, since the horizontal stress is equal to the maximum principal stress at the soil surface.

7.6.4 Evidence of Soil Arching

As clearly visualized in both the figures of particle displacement and material maximum shear strain, a breakout-type failure occurs, where a volume of soil above the anchor models (with the exception of the anchor pile model) is uplifted with the anchor model. Consequently, a mechanism must exist to allow for the upward movement of the geomaterial between the branch axes. One likely explanation is the ubiquitous soil arching

mechanism, which is typically described from a continuum perspective as the transfer in stress from a yielding mass to an adjacent stationary mass, where the trapdoor and silo problems are the classic exemplars of this mechanism (Terzaghi 1943). From the three-dimensional visualizations of shear strain, a petaloid-type (e.g. plastic soda bottle) surface characterizes the bottom of the rupture surface in the region of the branch axes. As evident in Figure 7-31, while the failure surface approximately at mid-depth is concentric around the anchor model axis, closer to the branch axes, a lobed pattern emerges where the principal axis of the individual lobes follows the orientation of the branch axes. Furthermore, in Figure 7-32-Figure 7-35, the polar transformation of the 3D maximum shear strain maps with increasing radii, R, succinctly captures the arching mechanism, where arching patterns of shear strain are clearly visible across branch axes. These patterns reflect the ability of arch-like spans of particulate material to support itself as well as the weight of the material above it. In both Toyoura and Soma No.4 sand, a significant increase in the height of the arch above the branch axes is observed for n3a30 models versus n6a30 models. Additionally by increasing the radius at which the polar transformation is acquired, the observation of arching diminishes, where the failure surface evolves in a straight line at greater distances from the point of dichotomy.
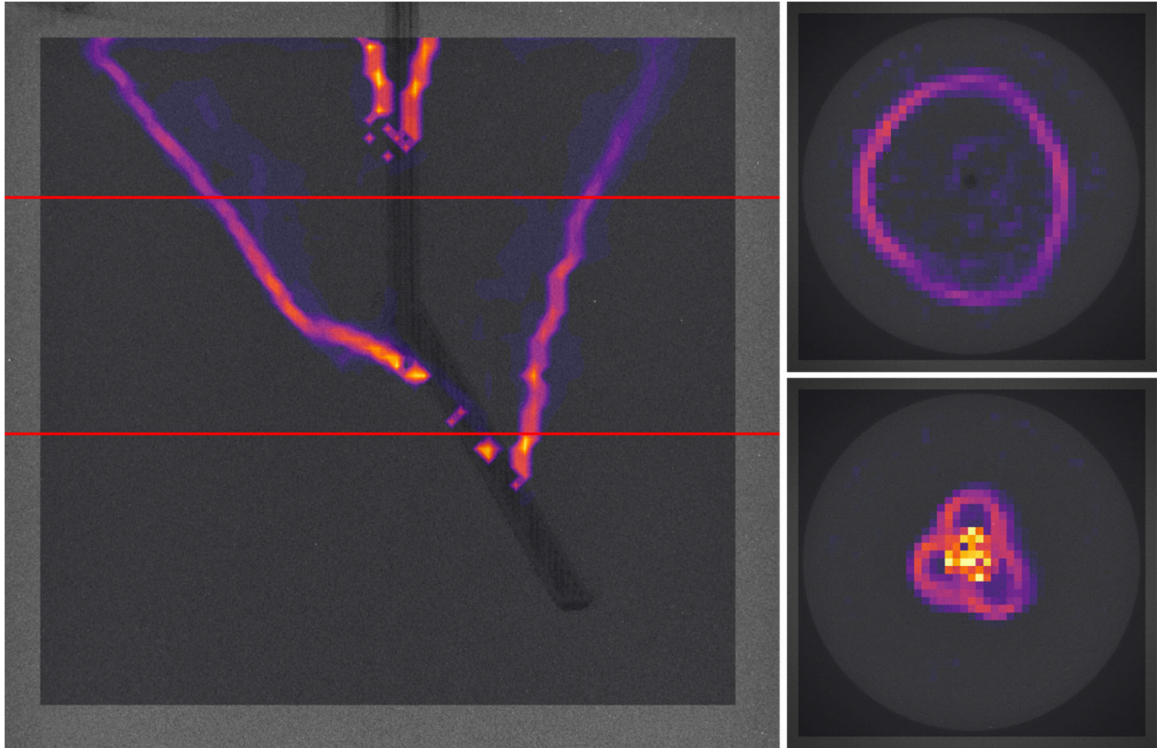
Figure 7-31. Evidence of arching mechanism in Toyoura sand through plots of maximum shear strain at various slices, (left) radial slice through model n3a30, (top right) plan view at position indicated by top red line in (left) figure, (bottom right) plan view at position indicated by lower red line in (left) figure.
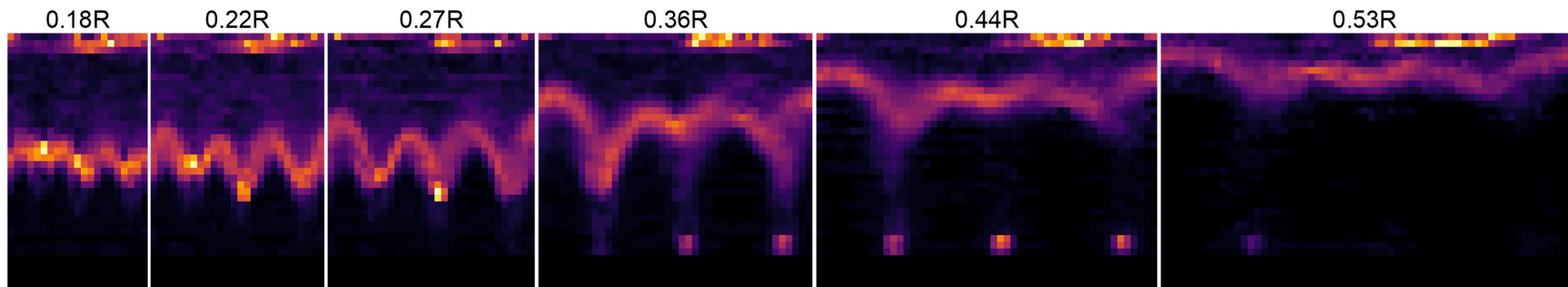
Figure 7-32. Polar transform of 3D maximum shear strain maps for model n3a30 in Toyoura sand with increasing radius.
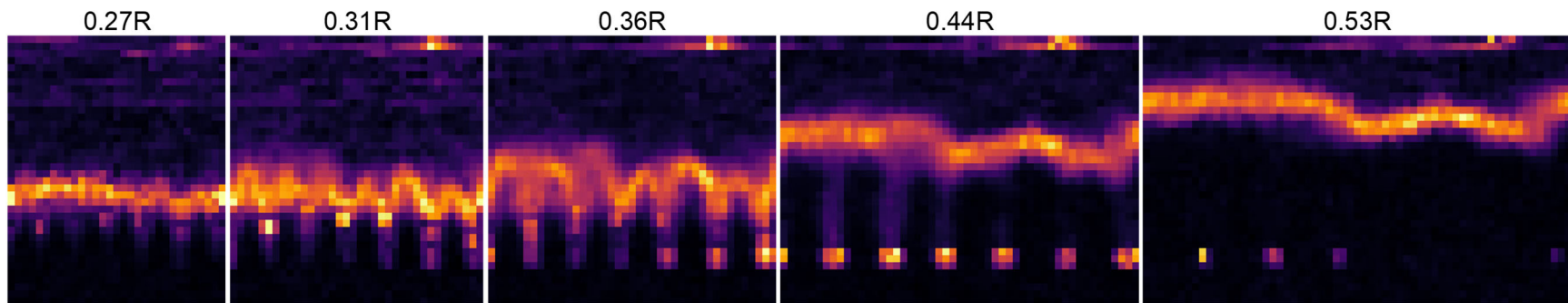
Figure 7-33. Polar transform of 3D maximum shear strain maps for model n6a30 in Toyoura sand with increasing radius.
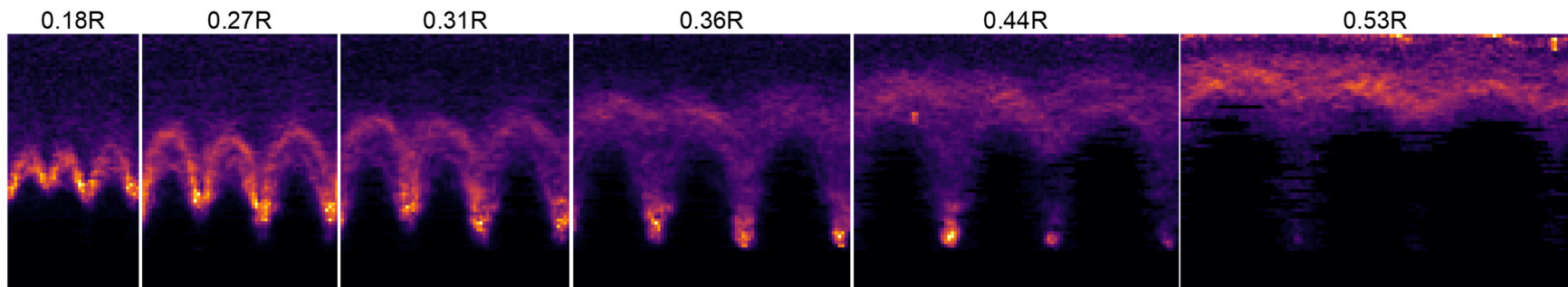
Figure 7-34. Polar transform of 3D maximum shear strain maps for model n3a30 in Soma No.4 sand with increasing radius.
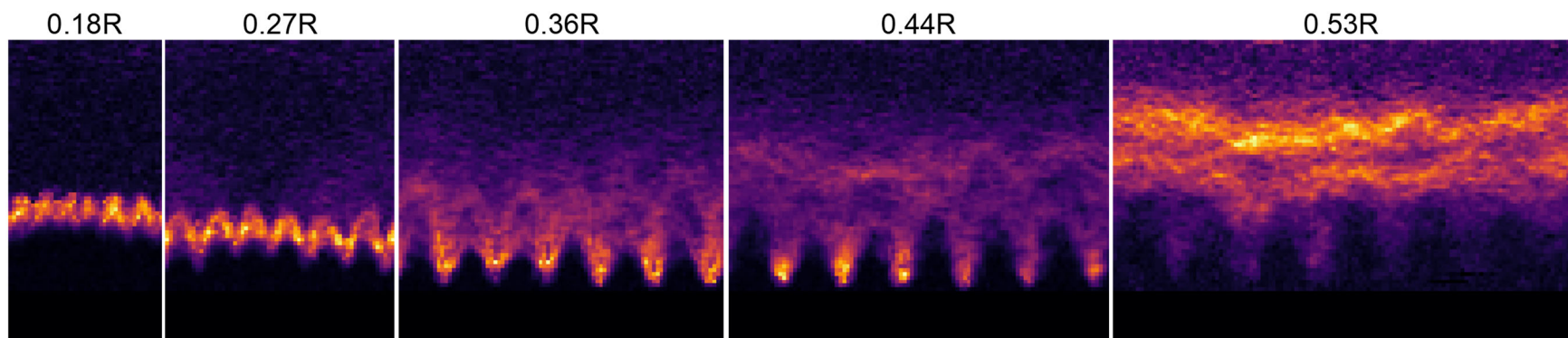
Figure 7-35. Polar transform of 3D maximum shear strain maps for model n6a30 in Soma No.4 sand with increasing radius.

7.6.5   Critical Failure Surface Intersection Ratio, f

A critical feature in the morphological characterization of the failure surface is the point at which the failure surface intersects the branch axis. When normalized by the overall length of the branch axis, the critical failure surface intersection ratio, f, is defined. For the three anchor models, f varies significantly between the sand and glass ballotini samples (Figure 7-36), which displays the average critical failure surface intersection ratio for all cases. Additionally, f is shown to decrease with fewer branch axes and with steeper internal branching angles, where f is determined for the initial failure surface. The results indicate that particle angularity and material friction angle promote more extensive failure surfaces, whereas particle size has negligible effect. In terms of the anchor model morphology, explanations for variations in f are hypothesized to be the sole or combined effect of particle-anchor model interface strength, the geomaterial-to-anchor model stiffness ratio, and/or soil arching. As evident by the previous section, soil arching is a dominant mechanism within the pullout process and is limited by the depth-to-branch axis spacing ratio as well as the strength of the geomaterial, such that soil arching is more probable in soils with greater friction angles and for anchor models that contain larger depth-to-branch axis spacing ratios. In terms of soil-to-anchor model stiffness, the effective anchor model stiffness increases with shorter and a greater number of branch axes, and consequently greater branch axis deflection would occur for less stiff anchors under the identical conditions, which would most likely promote a smaller f.
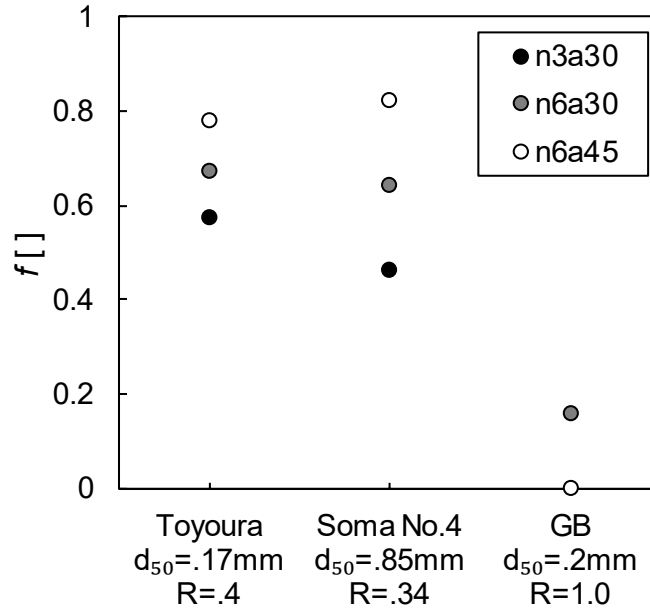
Figure 7-36. Average critical failure surface intersection ratio, *f*, for morphology-type root-inspired anchor models uplifted from Toyoura sand, Soma No.4 sand, and glass ballotini.

7.6.6   Subsequent Failure Surfaces

For the n6a45 anchor model in both Toyoura sand and glass ballotini, an initial outer failure surface nucleates at a point along the length of the branch axis, and with further anchor model displacement, an inner failure surface nucleates at the point of dichotomy, while the intensity of the shear strain in the outer surface deteriorates. The formation of subsequent failure surfaces in the gradual loading of a geomaterial is common phenomena (Bransby 1968, Lade et al. 1984, Stone and Wood 1992) and is due to sudden shift in the kinematics of the problem. For the n6a45 cases of interest, a mechanism inhibits displacement of the geomaterial constrained between the outer and inner failure surfaces. One unique feature of the deformation kinematics within the n6a45 pullout tests is the intersection of the particle trajectories with the soil container wall. This offers a possible explanation for the generation of an inner failure surface, where the soil container wall

impedes particle movement in the vicinity and actively disturbs the stress state of the material everywhere. This change in stress field offers the possibility for a relocation of failure conditions and associated shear localization within the soil mass.

7.7   Conclusions

- The breakout-type failure mode occurred for all root-inspired anchor models. For the conditions tested, root-inspired anchor models can outperform conventional pile anchor models in terms of pullout capacity due to the combined contributions of both the weight of the uplifted soil volume and the shearing resistance along the soil failure surface, whereas pile anchor models only mobilize the shearing resistance along the pile anchor-soil interface.

- The failure surface/s developed during the pullout process can be well described with a kinematically admissible, logarithmic spiral in two-dimensions, which allows for development of an analytical or numerical model to predict pullout capacity.

- With overlain maps of particle displacement orientation and maximum shear strain, a visual analysis leads to the conclusion that non-associative plastic flow occurred in all geomaterials tested during anchor model uplift.

- Evidence of soil arching is visualized, where the arching mechanism increases in relevance as the branch axis spacing angle increases.

- Using an initial approximation, the weight of the uplifted soil mass is insufficient to predict pullout resistance at a prescribed increment of anchor model uplift, and

consequently, the shearing resistance along the failure surface is a probable mechanism.

- The critical failure surface intersection ratio, f, increases with particle angularity and geomaterial strength, number of branch axes, and with internal branching angle, and is proposed to be governed by either one or a combination of the following mechanisms: soil arching, soil-to-anchor model stiffness, and soil-anchor model interface strength

CHAPTER 8.   PULLOUT CAPACITY OF ROOT-INSPIRED

ANCHOR MODELS: AN ANALYTICAL STUDY

The purpose of this chapter is to develop a model to predict pullout capacity of a root-inspired anchor model. The governing factors in pullout behavior of the soil-root system are highlighted, and additionally, previous derivations of pullout capacity for both plant root systems as well as infrastructure systems, such as ground anchors, pipes, and pile embankments are documented and assessed. Finally, from plasticity theory, a slip-line analysis is conducted for the uplift capacity of plate anchors, and supplementary methods for the adaptation of the derivation for plate pullout capacity to root-inspired anchor model pullout capacity are presented and evaluated.

8.1   Introduction

Pullout behavior refers to the mechanical response of a system as an embedded object is extracted from granular material, and within the pullout response, pullout capacity is the peak or maximum resistance that develops. Accurate knowledge of anchor pullout capacity is mandatory for infrastructure stabilization design, ensuring adequate pullout resistance can be provided and adequate factor of safety against failure is achieved. Furthermore, with regards to the analysis of pullout capacity, various assumptions are generally contrived to nullify certain aspects and to simplify the problem.

Though the material properties and architecture of plant roots and geotechnical anchor systems are remarkably different, numerous similarities in pullout behavior between the systems exist, where the primary difference in pullout response relates to the

striking contrast in scale. As such, in the progression towards a means to predict pullout capacity of a root-inspired system both root systems and conventional geotechnical anchorage systems are analyzed.

8.2 Pullout Capacity of Fibrous Root Systems

8.2.1 Single Root Axis

For the vertical pullout of a single root axis perpendicular to the soil surface, a simple force equilibrium analysis is employed (Waldron 1977, Ennos 1990, Gray and Barker 2004, Mickovski et al. 2010), and pullout capacity, P_{max}, is formulated in Equation 32.

$$P_{\max} = \pi dL\tau \qquad (32)$$

Assumptions regarding the shear strength of the soil-root interface vary significantly and include definitions such as a constant value or a limit equilibrium approach with a linearly increasing geostatic stress field.

$$\tau = \frac{\gamma L}{2} K \tan \delta \qquad (33)$$

In an attempt to model the complete pullout response more accurately, additional factors have been added to the mechanical description of root axis pullout including root axis tortuosity, soil-root interface bond strength, variable root axis diameter, and a point of dichotomy resistive term (Schwarz et al. 2010). From an alternative perspective, root axis pullout response has been analyzed by modeling root axes as beams or cables (depending on the relative magnitude of the root displacement) and the soil as a spring (Wu et al. 1988).

In this case, resistance is imparted to the system through the passive soil resistance determined through bearing capacity equations and the shearing resistance of the soil-root interface determined from a shear stiffness.

8.2.2 Fibrous Root Systems

For the uplift capacity of a root system, pullout capacity is determined as the summation of the individual resistances provided by each applicable root axis, given an assumption regarding the distribution of root axis diameter and length. Well established power law relationships between root axis diameter and additional model features, including tensile strength, elastic modulus, and root axis length, are utilized such that only knowledge of root diameter is required. All models consider the tensile strength of the individual root axes; however, for models that consider root axes of variable diameter (e.g. fiber bundle model, root distribution model), a non-null pullout resistance is still produced due to the presence of larger diameter roots (Pollen and Simon 2005, Schwarz et al. 2010). Additionally, some models generate the entire force-displacement pullout response through iterative means (i.e. strain or stress controlled) and consequently do not yield closed-form solutions for pullout capacity. However, for all of these models, an inherent assumption is that the root systems act individually and not as a collective mass. Depending on the various properties and conditions of the soil-root system, the formation of an uplifted soil-root mass is probable, particularly in the case of densely spaced root axes where the soil is more liable to fail on the circumference of the root system instead of at the individual root-soil interfaces.

8.3 Pullout Capacity of Anchor Elements applied to Root-Inspired Anchor Models

8.3.1   Failure Modes

The pullout capacity of various infrastructure elements subject to uplift loads, including anchor piles and plates, belled piles, ground anchors, helical piles, planar elements, pipes, soil nails, and tie-downs, has been derived implementing a variety of analytical techniques. The failure modes range significantly depending on the element morphology (e.g. depth-to-width ratio, embedment depth), soil conditions (e.g. undrained shear strength, relative density, stress state), and installation method (e.g. grouting/post-grouting, borehole cleaning, tensioning) as detailed in Chapter 2. More specifically, documented failure modes are schematically represented in Figure 8-1. "Pure shear," as document in Figure 8-1.1, occurs when a cylindrical failure surface develops at the soil-element interface or at a surface extending vertically to the soil surface from the external edge of the element, and pullout capacity is calculated as the integral of the shearing resistance along the surface. Breakout-type failure occurs (Figure 8-1.2) when a typically curved failure surface develops from the outer extent of structural element and all of the soil within the confines of the defined failure surface is displaced in the direction of the pullout force (Balla 1961, Mariupol'skii 1965, Baker and Konder 1966, Matsuo 1967, Meyerhof and Adams 1968). This is the typical observed failure mode for structures (e.g. anchor piles and plates, helical piles, pipes) with a depth-to-width ratio below the critical embedment ratio threshold. Pullout capacity for these failure modes is calculated as the resultant of the weight of uplifted soil and the shearing resistance along the failure surface. For loose or compressive soils in shallow or deep conditions, a combinatory soil compression (indicated by shaded area) and shear or breakout-type failure (inner or outer failure surfaces, respectively) can occur (Figure 8-1.3), where the soil near the end of structure is first compressed and then

followed by a sliding or breakout failure depending on the structure embedment (Vesic et al. 1965, Cheuk et al. 2008, Liu et al. 2012). Conventionally, pullout capacity is the summation of the force required to compress an assumed volume of soil above the structure extents, the shearing resistance along the shear or breakout failure surface, and the weight of uplifted soil. Additionally, a combined sliding and breakout failure (Figure 8-1.4) occurs in dense or stiff soils in deep conditions (Vesic 1969). Furthermore, other composite failure modes transpire, especially in layered soil profiles.
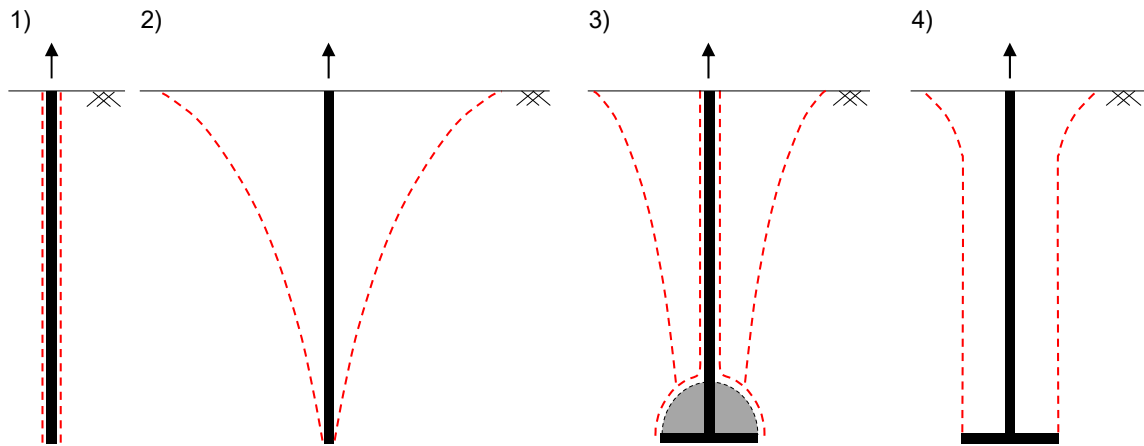
Figure 8-1. Schematic descriptions of commonly documented failure modes for uplifted structures.

Based on the failure analysis of an uplifted root-inspired anchor model observed in Chapter 7, the remainder of the chapter focuses on the breakout-type failure mode.

8.3.2   Model Assumptions

Assumptions are mandatory for the derivation of an analytical pullout capacity model. First, general definitions regarding the material properties and behavior of the system constituents are required. For example, the soil is often considered as a

homogeneous, continuum material obeying a Mohr-Coulomb failure criterion, while the infrastructure element is often considered to be a rigid structure. Additionally, the mechanisms that contribute to pullout capacity are defined. Common mechanisms reflected in the derivation include the weight of the uplifted soil as well as the shear and cohesional resistance along the failure surface. As well, a complete description of the failure surface shape is required. Failure surface geometries range in complexity, from cylindrical to surfaces generated from arc or logarithmic spiral generatrices. For models that incorporate a shearing resistance component, the stress state along the failure surface must be defined.

Within a general analytical framework, a failure surface, often referred to as rupture surface, separates two bodies of motion and defines the failure mode. For the breakout failure mode, all soil within the defined failure surface is displaced in the direction of loading, while outside of the failure surface, the soil body remains fixed. For most analyses, all soil along the surface is treated as being in a state of a failure as defined by the select material behavior failure criterion, and for pullout capacity predictions, the soil is assumed to be at a peak failure state versus a residual state.

Experimentally, a failure surface is typically defined and identified through a deformation analysis as a thin layer of soil that has experienced a localized strain. Also termed shear bands, failure surfaces can develop before peak strength is attained, meaning the soil is not in a failure state. Additionally, in the maturation of the failure surface, the soil transitions from a near elastic behavior at low strains to residual or critical state behavior at large strains, and soil located at various points along the surface can be at various stress states depending on the strain level (i.e. progressive failure).

8.4   Pullout Capacity of Root-Inspired Anchor Models

Select pullout capacity models are applied to root-inspired anchor models. All models are axisymmetric around the primary axis of the root-inspired anchor model (i.e. the stem axis). Additionally, pullout capacity models are categorized into their respective failure surface shapes. Unlike conventional bearing capacity solutions, the shape of the failure surface for uplift problems has not reached a consensus among researchers. For all models, only dry, coarse-grained sediments are considered, which implies that cohesion is neglected. Full derivations of pullout capacity and uplift coefficients are listed in the appendix.

8.4.1   General Form

The maximum pullout resistance, or pullout capacity, P_{max}, is determined as the summation of the weight of the uplifted soil contained within the failure surface and the frictional shear resistance along the failure surface, neglecting the weight of the anchor element, and the general form of the equation is shown in Equation 34.

$$P_{\max} = W_{soil} + F_{shear} \tag{34}$$

For comparison among various laboratories and soil and element types, pullout capacity is often normalized by the weight of the cylindrical volume of soil directly above the anchor model (Equation 35), where the radius and height of the cylinder are defined by the radius and depth of the anchor element. This dimensionless expression of pullout capacity is often symbolized as $N\gamma$, and is noted as the breakout or pullout factor.

$$N_\gamma = \frac{P_{max}}{\gamma' A H} = \frac{P_{max}}{\gamma' \pi b^2 H} \tag{35}$$

For the case of a root-inspired anchor element, an equivalent height variable, H', is introduced to normalize the pullout capacity by the weight of the cylindrical volume of soil minus the conical volume of soil under the angled root-inspired anchor (Equation 36).

$$H' = H - \frac{b}{3 \tan \alpha} \tag{36}$$

If the weight of soil in the cylindrical volume of soil directly above the anchor element is equivalent to the lower-bound pullout capacity, a breakout factor greater than one suggests that possibly the failure surface is ill described and that additional mechanisms are occurring (i.e. mobilized frictional resistance). Furthermore, the pullout capacity can be normalized by various other variables to ascertain additional insights. For example, if the pullout capacity is normalized by the weight of the anchor element, the material efficiency, Π_M, of an anchor model can be identified.

8.4.2 Cylindrical Failure Surface

The cylindrical failure surface model is one of the most simplistic models and is often credited to *Majer 1955*, and evidently, the failure surface is described by a cylinder (Figure 8-2). Pullout capacity is calculated by the weight of the soil within the cylindrical failure surface and the shear resistance along the cylindrical wall. A typical manner to solve this problem is to assume the soil is in a state of passive failure along the entire surface. If the

vertical stress increase with depth is solely geostatic, pullout capacity can be determined

as shown in Equation 37, as well as the associated breakout factor (Equation 38).
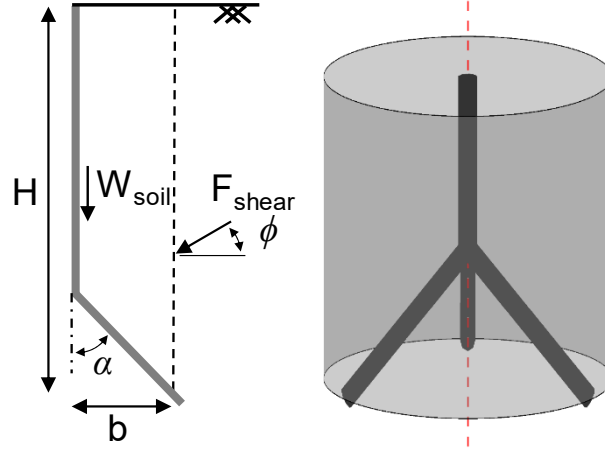
Figure 8-2. Free body diagram and three-dimensional failure surface for a cylindrical model.

$$P_{max} = \gamma' \pi b \left(bH - \frac{b^2}{3 \tan \alpha} + H^2 K \tan \phi \right) \tag{37}$$

$$N_\gamma = 1 - \frac{3 H^2 K \tan \phi}{b \left(\dfrac{b}{\tan \alpha} - 3H \right)} \tag{38}$$

8.4.3   Conical Failure Surface

Various authors have assumed a conical failure surface, illustrated in Figure 8-3.

However, the derivation of pullout capacity varies significantly depending on the treatment

of the shear resistance (Vermeer and Sutjiadi 1985, Ghaly et al. 1991, White et al. 2008),

where the most simplistic method assumes no shearing along the failure surface (Mors

1959). Assuming conical inclination angle, θ, is a function of the soil properties and state

conditions, the simple conical failure surface neglecting friction has been shown to

adequately model pullout capacity (Dyson and Rognon 2014). Pullout capacity and breakout factor for a conical failure surface neglecting frictional resistance are shown in Equations 39 and 40.
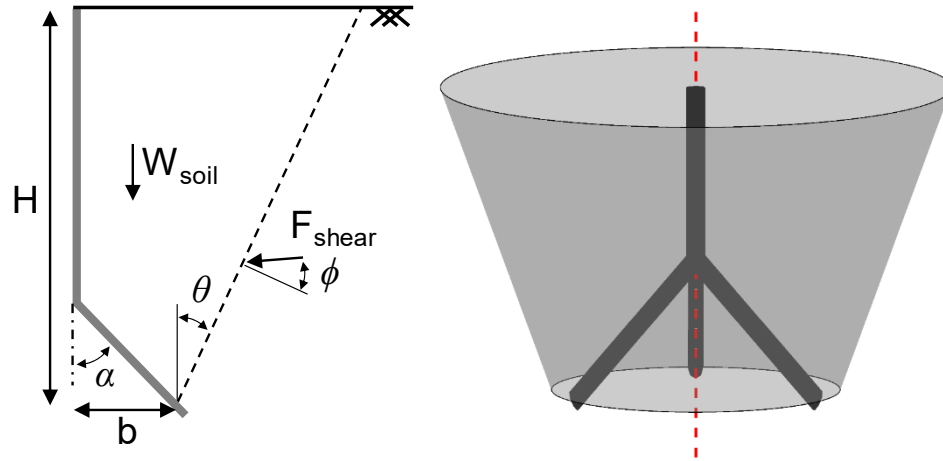
Figure 8-3. Free body diagram and three-dimensional failure surface for a conical model.

$$P_{max} = \gamma' \frac{\pi}{3} \left[\tan^2 \theta \left(\frac{b}{\tan \theta} + H \right)^3 - b^3 \left(\frac{1}{\tan \theta} + \frac{1}{\tan \alpha} \right) \right] \quad (39)$$

$$N_\gamma = 1 + \frac{H \tan \theta}{b} + \frac{H^2 \tan^2 \theta}{3b^2} - \frac{b}{3H \tan \alpha} \quad (40)$$

8.4.3.1 *Murray and Geddes 1987* Pullout Capacity Model

Both limit equilibrium (Equation 41) and limit analysis (Equation 43) approaches are utilized to provide bounds and approximations to pullout capacity. The specifics of the formulation are vague; in particular, no mention of the soil stress state and the stress along the failure surface is noted. However, assuming a rigorous derivation was performed, valuable bounds are supplied, highlighted in Equation 43.

$$P_{max} = \gamma' \pi b^2 H + \gamma' \pi b H^2 \xi + \gamma' \pi \frac{H^3}{3} \xi \left[\tan \theta + K \tan(\phi - \omega) \right] - \gamma' \frac{\pi}{3} \frac{b^3}{\tan \alpha} \quad (41)$$

$$\xi = \frac{\tan \theta \tan \delta_w}{\tan \delta_w - \tan(\phi - \omega)} \quad (42)$$

$$\gamma' \pi b^2 H' \leq P_{max} \leq \gamma' \pi \left[b^2 H' + b H^2 \tan \phi + \frac{H^3}{3} \tan^2 \phi \right] \quad (43)$$

8.4.3.2 *White, Cheuk, and Bolton 2008* Pullout Capacity Model

Relatively unique to this model, an assumption regarding the normal stress on the failure surface is stated, where the normal stress is determined from Mohr's circle given a geostatic vertical stress, a K_0 determined horizontal stress, and the conical inclination angle. The limit equilibrium solution provided within their paper is for a two-dimensional pipe uplift problem; consequently, a solution to the pullout capacity of a root-inspired anchor assuming a conical failure surface is formulated based upon their approach. The full derivation of Equation 44 is found in the Appendix.

$$P_{max} = \gamma' \frac{\pi}{3} \left[\begin{array}{l} \tan^2 \theta \left(\dfrac{b}{\tan \theta} + H \right)^3 - b^3 \left(\dfrac{1}{\tan \theta} + \dfrac{1}{\tan \alpha} \right) \ldots \\[2ex] + H^2 \left(\tan \varphi_P - \tan \theta \right) \left(\dfrac{1 + K_0}{2} - \dfrac{1 - K_0}{2} \cos 2\theta \right) \left(3b + H \tan \theta \right) \end{array} \right] \quad (44)$$

8.4.4 *Circular Failure Surface*

The circular failure surface refers to the failure surface generated by revolving a circular arc around the vertical axis of the anchor element. The surface intersects the ground

surface at a statically correct angle of $\pi/4 - \phi/2$ and with the anchor element at an angle of π, which stipulates that β is equivalent to $\pi/4 + \phi/2$. The typical free body diagram utilized in most research with an assumed circular failure surface is shown in Figure 8-4.
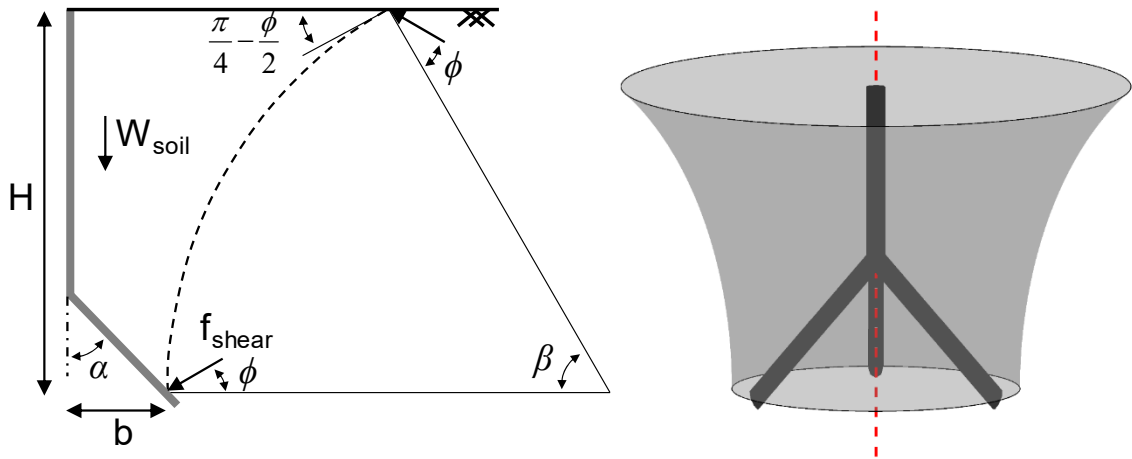
Figure 8-4. Free body diagram and three-dimensional schematic of a circular failure surface.

8.4.4.1 *Balla 1961* Pullout Capacity Model

To calculate pullout capacity, shear stress, determined via Kotter's equation, is integrated along the circular failure surface. Kotter's equation is a partial differential equation for the change in shear stress along a failure line that is derived through the equations of plastic stress equilibrium. While authors have presented critiques on this pullout capacity model, suggesting that the model is invalid due to neglection of normal stress on the slip surface, as well as derivation errors, this model was the first to utilize a slip line-type plasticity analysis to solve for pullout capacity (Vesic 1969, Murray and Geddes 1987). Consequently, this paper laid much of the groundwork for later plastic equilibrium models including *Vesic et al. 1965*, *Matsuo 1967*, *Saeedy 1971*, and *Rao and Kumar 1994*, to name a few.

8.4.4.2 *Vesic et al. 1965, Vesic 1969* Pullout Capacity Model

Vesic 1969 adapts previous research completed on the ultimate uplift pressure due to an embedded explosive point charge to pullout capacity of an embedded plate anchor. Two solutions are provided, one implementing cavity expansion theory and the other, implementing the Brinch Hansen approximate earth pressure equation, an expression derived from Kotter's equation. The latter solution follows the breakout failure mode and integrates the Brinch Hansen equation along a circular failure surface to calculate the frictional resistance due to both the normal and shear stress on the slip line (Equation 45). The shear resistance is then added to resistance due to the weight of soil within the failure surface and equated to the expansion pressure. As stated within the research, plane stress conditions inherent to the Brinch Hansen equation are assumed to approximate the axisymmetric problem of uplift of a circular plate.

$$P_{max} = \gamma \pi b^2 \left[H \overline{F}_q - \frac{b}{3 \tan \alpha} \right] \tag{45}$$

If pullout capacity is separated into its two force components, soil weight and frictional shear, an artifact is revealed, namely that if the friction angle is sufficiently low, the shear component actually assists in the pullout of the anchor element. Figure 8-5(left) reveals that for a friction angle of 30°, pullout capacity is reduced at $H/2b$ ratios greater than 6, and Figure 8-5(right) provides further proof into the negative shear resistance that occurs in shallower cases and for soils with smaller friction angles.
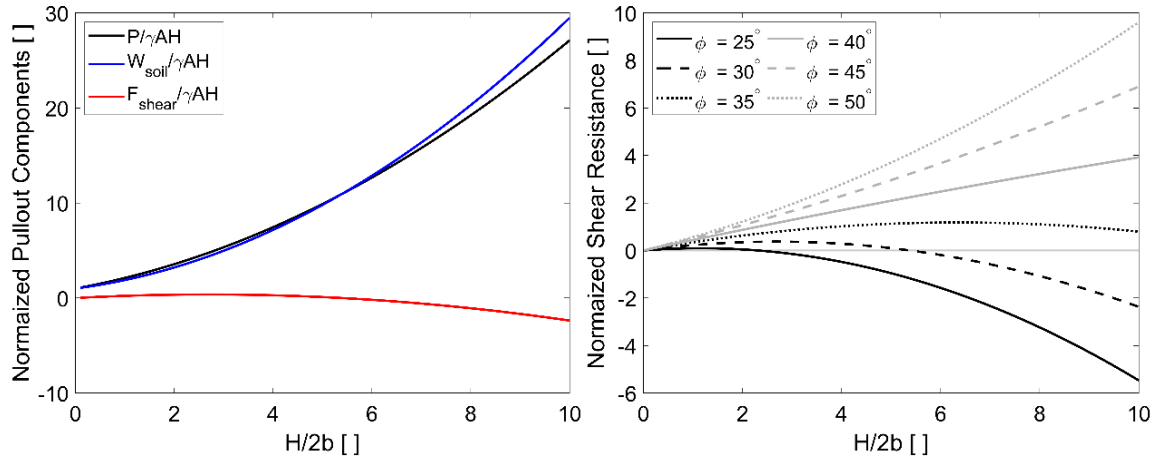
Figure 8-5. (left) Normalized pullout capacity components for $\phi = 30°$, (right) normalized shear resistance component for various friction angles. All components normalized by the weight of the cylindrical volume of soil directly above the anchor element.

8.4.5   *Logarithmic Spiral Failure Surface*

Similar to the circular failure surface, the logarithmic spiral failure surface, as shown in Figure 8-6, is generated when a specified logarithmic spiral, employed as a generatrix, is revolved around the vertical axis of the anchor element. In the geotechnical literature, logarithmic spirals in general are favored over a circular failure surface as the preferred assumed failure surface specifically because they allow for the soil to displace tangentially (Drucker and Prager 1952, Bolton 1986). The radius of the logarithmic spirals varies at a constant rate (except for $\psi = \pi/2$ case, when a circle is generated) because the angle, ψ, between the radius and the line tangent to the spiral remains constant. Consequently, if the complementary angle to ϕ is conceived as the dilation angle of the soil, a failure surface defined by a logarithmic spiral allows for physical separation of the discontinuous bodies, necessary in plasticity theory.
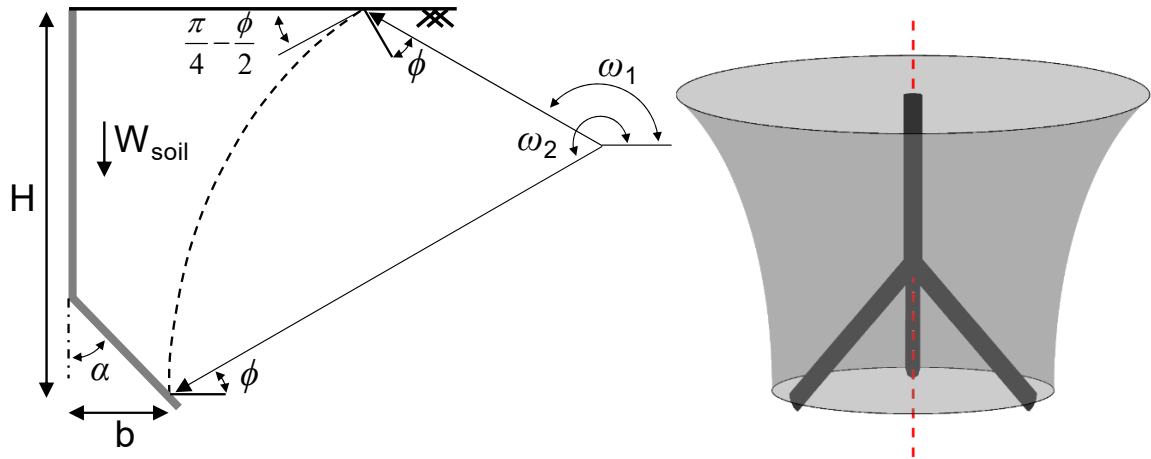
Figure 8-6. Free body diagram and three-dimensional schematic for a logarithmic spiral failure surface.

8.4.5.1 *Matsuo 1967* Pullout Capacity Model

This model uses a combination of a passive wedge at the surface that transitions into a logarithmic spiral at some distance below the soil surface. To determine the shear resistance on the failure surface, mean stress along the failure surface is first determined by solving a variant of Kotter's equation (alternate coordinate system) with the boundary condition of mean stress equal to zero at the soil surface, and then integrating the mean stress across the entire failure surface. Through the use of Kotter's equation, plane stress conditions are implemented in an axisymmetric problem; however, this approximation allows for the development of a rigorous solution to the differential equation.

8.4.5.2 *Meyerhof and Adams 1968* Pullout Capacity Model

As stated within *Meyerhof and Adams 1968*, the research does not provide a complete formulation but rather an approximate methodology (Equation 46). The shape of the failure surface is not explicitly defined (i.e. truncated pyramidal shaped), and as such, the calculation of the weight of soil is relegated to the user's discretion. For the purpose of

comparison, the weight of soil is determined from the volume generated by revolving a logarithmic spiral generatrix around the primary anchor axis. This is selected since the implemented coefficient of passive earth pressure and associated reduction factor is intrinsically based upon a logarithmic spiral failure, as derived by *Caquot and Kerisel 1949*.

$$P_{max} = W_{soil} + F_{shear}$$
$$F_{shear} = \gamma' \frac{\pi}{2} bH^2 s K_u \tan\phi$$
$$K_u = R(\delta, \varphi) \cdot K_p \cdot \frac{\tan\delta}{\tan\varphi} \tag{46}$$
$$s = 1 + \frac{m(\varphi)H}{2b}$$

8.5 Slip Line Analysis: Plate Anchor Application

Slip line analysis is a method within plasticity theory of determining failure loads. In geotechnical engineering, this method has been extensively utilized in the formulation of bearing capacity factors and the determination of lateral earth pressure (Larkin 1968, Bolton and Lau 1993). In this method, the material is assumed to be rigid below the yield stress and perfectly plastic when the yield stress is reached. For the calculation of failure load, plastic stress equilibrium is solved for assuming the material has reached yield stress at all locations, and then integrated along the slip lines, referred to as characteristic lines in mathematics or failure surfaces in traditional geotechnics.

For the derivation of pullout capacity of a root-inspired element, the effect of arching between branch axes is neglected and the failure surface is assumed to be symmetric around the axis of the root-inspired element. Consequently, the symmetry of problem allows for

an axisymmetric analysis to be performed, which was originally developed by *Cox et al. 1961*. Furthermore, the Mohr-Coulomb yield criterion with zero cohesion is adopted as the material model. In general, a field of slip lines is generated over the entire plastic domain and integrated over; however, for this analysis, a simplified approach is employed and the stress solely along a single failure surface is determined, which was originally devised by Kotter and applied to numerous problems including uplift of embedded objects (Balla 1961, Vesic et al. 1965, Matsuo 1967)

The problem is schematically described in Figure 8-7, where the shape of the failure surface is described by a logarithmic spiral that intersects the soil surface at a statically correct angle of $\pi/4-\phi/2$ to the horizontal and intersects the anchor element at angle of ϕ to the vertical. For this analysis, a few slight deviations from conventional slip line analysis derivations are adhered to, following *Matsuo 1967* and illustrated in Figure 8-8. Firstly, the stress components are written in terms of β, the angle between the slip line and the vertical, and secondly, the z-axis is positive upwards.
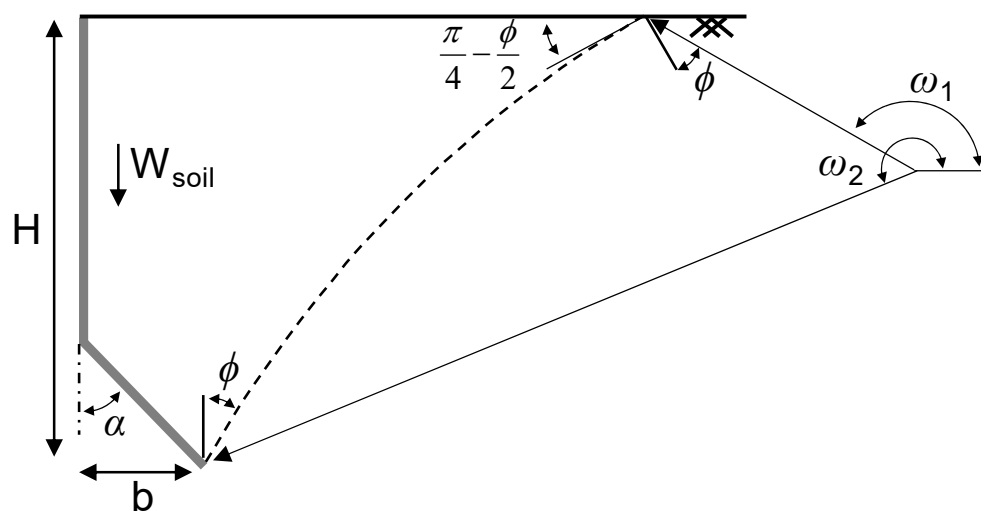
Figure 8-7. Schematic of relevant participating forces and failure surface description for Slip Line analysis.
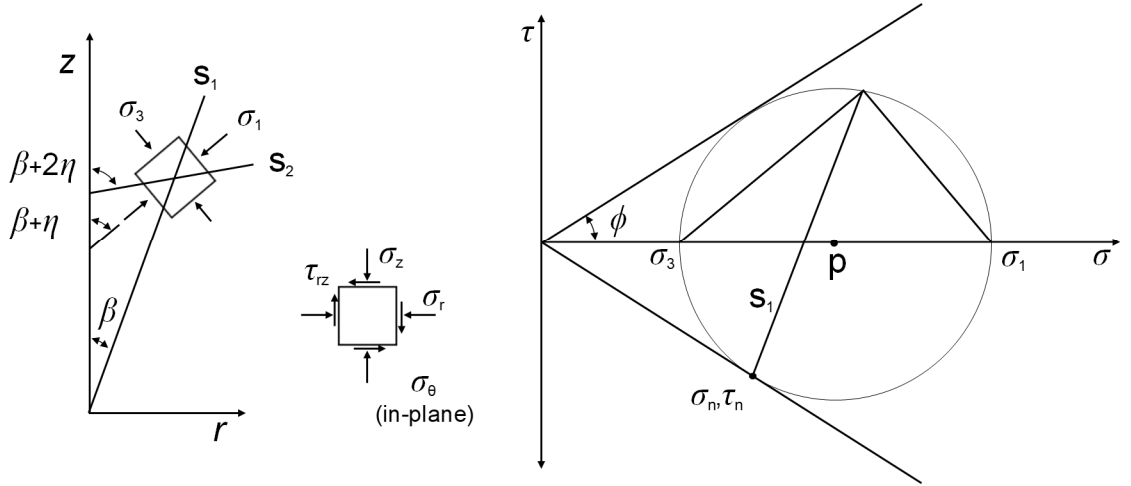
Figure 8-8. (left) Schematic detailing the definitions of β, s_1, and s_2, relative to the radial and height coordinates, (right) Mohr's circle with Coulomb failure criterion.

To begin the derivation, the Mohr-Coulomb failure criterion is defined in Equation 47.

$$\frac{\sigma_1 - \sigma_3}{2} = \frac{\sigma_1 + \sigma_3}{2} \sin\phi \tag{47}$$

Utilizing Mohr's circle, the stress components for an axisymmetric soil element at yield can be defined as follows, following the coordinate system described previously (Equation 48).

$$\begin{aligned}
\sigma_r &= p\left(1 - \sin\phi\cos 2\theta\right) = p\left[1 + \sin\phi\sin\left(2\beta - \phi\right)\right] \\
\sigma_z &= p\left(1 + \sin\phi\cos 2\theta\right) = p\left[1 - \sin\phi\sin\left(2\beta - \phi\right)\right] \\
\tau_{rz} &= p\sin\phi\sin 2\theta = p\sin\phi\cos\left(2\beta - \phi\right) \\
\sigma_\theta &= p\left(1 + K\sin\phi\right)
\end{aligned} \tag{48}$$

A coefficient, K, is utilized in the formulation of the hoop stress component to derive a more general equation, such that hoop stress is equal to major principal stress when $K = 1$ and the minor principal stress when $K = -1$. Furthermore, for an axisymmetric analysis,

262

debate on the validity of the *Haar and von Karman 1909* hypothesis, which states that the hoop stress must be equal to either the major or minor principal stress, abounds (Cox 1962, Bolton and Lau 1993). However, since no alternative assumption regarding hoop stress has been rigorously accepted, this hypothesis will be followed. Even more specifically, when the hoop strain is tensile, the hoop stress is equivalent to the minor principal stress (Houlsby 1982, Houlsby and Wroth 1982).

The common differential equations for plastic stress equilibrium for an axisymmetric element in the prescribed coordinate systems are defined in Equation 49.

$$
\frac{\partial \sigma_r}{\partial r} + \frac{\partial \tau_{rz}}{\partial z} + \frac{\sigma_r - \sigma_\theta}{r} = 0
$$
$$
\frac{\partial \tau_{rz}}{\partial r} + \frac{\partial \sigma_z}{\partial z} + \frac{\tau_{rz}}{r} + \gamma = 0
$$

(49)

By substituting into the equilibrium equations (Equation 49) the stress components (Equation 48), the general set of equations are produced (Equation 50).

$$
\left[1 + \sin\phi \sin(2\beta - \phi)\right]\frac{\partial p}{\partial r} + \sin\phi \cos(2\beta - \phi)\frac{\partial p}{\partial z}...
$$
$$
+ 2p\sin\phi\left[\cos(2\beta - \phi)\frac{\partial \beta}{\partial r} - \sin(2\beta - \phi)\frac{\partial \beta}{\partial z}\right]...
$$
$$
+ \frac{p\left[\sin\phi \sin(2\beta - \phi) - K\sin\phi\right]}{r} = 0
$$
$$
\sin\phi \cos(2\beta - \phi)\frac{\partial p}{\partial r} + \left[1 - \sin\phi \sin(2\beta - \phi)\right]\frac{\partial p}{\partial z}...
$$
$$
- 2p\sin\phi\left[\sin(2\beta - \phi)\frac{\partial \beta}{\partial r} + \cos(2\beta - \phi)\frac{\partial \beta}{\partial z}\right]...
$$
$$
+ \frac{p\sin\phi \cos(2\beta - \phi)}{r} + \gamma = 0
$$

(50)

The previous equations can be manipulated to yield partial differential equations in terms of the two differential slip lines lengths, s_1 and s_2, as shown in Equation 51.

$$\frac{\partial p}{\partial s_1} - 2p \tan\phi \frac{\partial \beta}{\partial s_1} + \frac{p \tan\phi \left[\cos\beta - K \sin(\beta - \phi) \right]}{r} + \gamma \frac{\cos(\beta - \phi)}{\cos\phi} = 0$$

$$\frac{\partial p}{\partial s_2} + 2p \tan\phi \frac{\partial \beta}{\partial s_2} + \frac{p \tan\phi \left[\sin(\beta - \phi) - K \cos\beta \right]}{r} - \gamma \frac{\cos(\beta - \phi)}{\cos\phi} = 0$$

(51)

If Equation 51(top) is rearranged in terms of the angle β differential, and the rate of change of the slip line in terms of the angle β (Equation 52) for a logarithmic spiral, Equation 53, a first-order differential equation, is produced.

$$\frac{ds}{d\beta} = \frac{\rho_0 e^{\tan\phi(\pi - \beta + \phi)}}{\cos\phi}$$

(52)

$$\frac{\partial p}{\partial \beta} - 2p \tan\phi + \left\{ \frac{p \tan\phi \left[\cos\beta - K \sin(\beta - \phi) \right]}{r} + \gamma \frac{\cos(\beta - \phi)}{\cos\phi} \right\} \frac{\rho_0 e^{\tan\phi(\pi - \beta + \phi)}}{\cos\phi} = 0$$

(53)

The mean stress along the surface constructed by a logarithmic spiral generatrix is solved for numerically by implementing the Forward Euler method, shown in Equation 54. This method is an explicit finite difference scheme commonly used to solve first-order differential equations.

$$p(\beta + \Delta\beta) = p(\beta)\left\{2\tan\phi\Delta\beta - \frac{\tan\phi\left[\cos\beta - K\sin(\beta - \phi)\right]}{r(\beta)}\chi(\beta)\Delta\beta + 1\right\}\ldots$$

$$+\gamma\frac{\cos(\beta - \phi)}{\cos\phi}\chi(\beta)\Delta\beta \tag{54}$$

$$\chi(\beta) = \frac{\rho_0 e^{\tan\phi(\pi - \beta + \phi)}}{\cos\phi}$$

Explicit schemes demand an initial starting point. Since the shear stress at the soil surface is zero, the algorithm proceeds down along the failure surface initiating at the soil surface.

Finally, the vertical shear force, F_{shear}, can be determined by integrating along the failure surface the shear and normal stress components (Equation 55).

$$dF_{shear} = \tau_n dA\cos\beta - \sigma_n dA\sin\beta$$

$$dA = 2\pi r(\theta)ds$$

$$ds = \frac{\kappa e^{\tan\phi\theta}}{\cos\phi}d\theta \tag{55}$$

$$F_{shear} = 2\pi\int_{\theta_1}^{\theta_2}(\tau_n\cos\beta - \sigma_n\sin\beta)r(\theta)\frac{\rho_0 e^{\tan\phi\theta}}{\cos\phi}d\theta$$

Pullout capacity is then determined by combining the vertical shear force along the failure surface with the uplifted weight of soil, described in the Appendix. Figure 8-9 provides a comparison in terms of the state of stress for three different cases, 1) $H/2b=2$, $\phi=30°$, 2) $H/2b=2$, $\phi=45°$, and 3) $H/2b=10$, $\phi=30°$, where for Figure 8-9(center) the normal stress is equivalent to the shear stress along the failure surface.
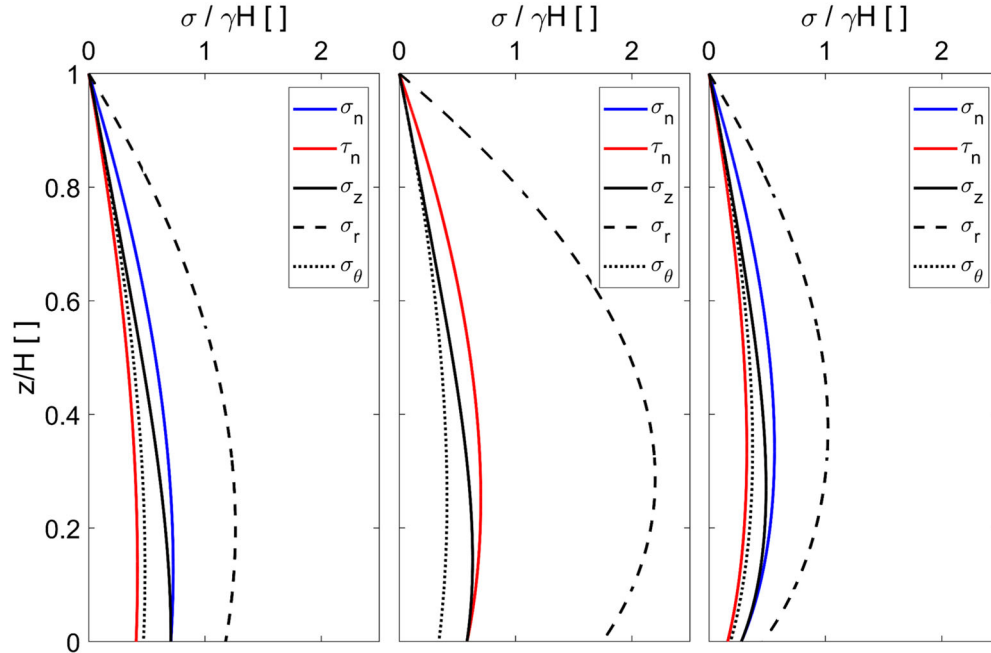
Figure 8-9. State of stress along failure surface with normalized depth for cases *H*/2*b*=2, *ϕ*=30° (left), *H*/2*b*=2, *ϕ*=45° (center), and *H*/2*b*=10, *ϕ*=30° (right).

8.5.1   Model Validation

To validate the Slip Line model, pullout factor values from selected pullout tests performed on circular anchor plates were compared to pullout factors computed using the Slip Line model (Figure 8-10). Numerous data sets were examined and largely the most accurate fits are presented. In general, the Slip Line method accurately or over predicted the pullout factor for a specified depth-to-width ratio. Furthermore, the Slip Line model is sensitive to the sole soil input parameter, peak friction angle, and the variance in pullout capacity with friction angle increases with the depth-to-width ratio (Figure 8-11). Utilization of the proper friction angle value is critical, particularly for 1g models due to the relatively high influence of dilatancy on peak strength at low stress conditions. For the model, the peak friction angle at the average stress value located at mid-embedment is recommended. Finally, the Slip Line model is a pullout capacity model for the breakout

failure mode and does not capture the failure mode change beyond the critical embedment ratio.
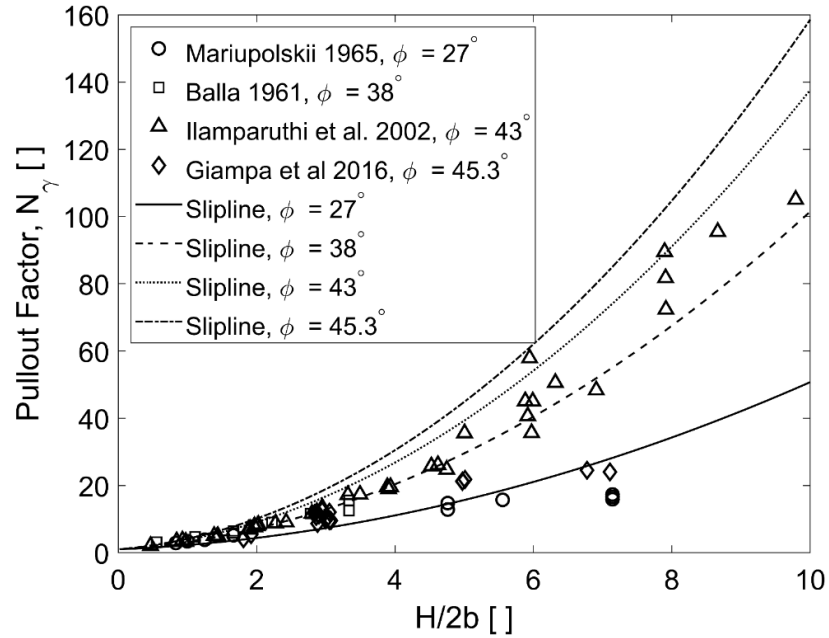
Figure 8-10. Comparison of experimental pullout factor data from the literature with pullout factor values computed with Slip Line analysis.
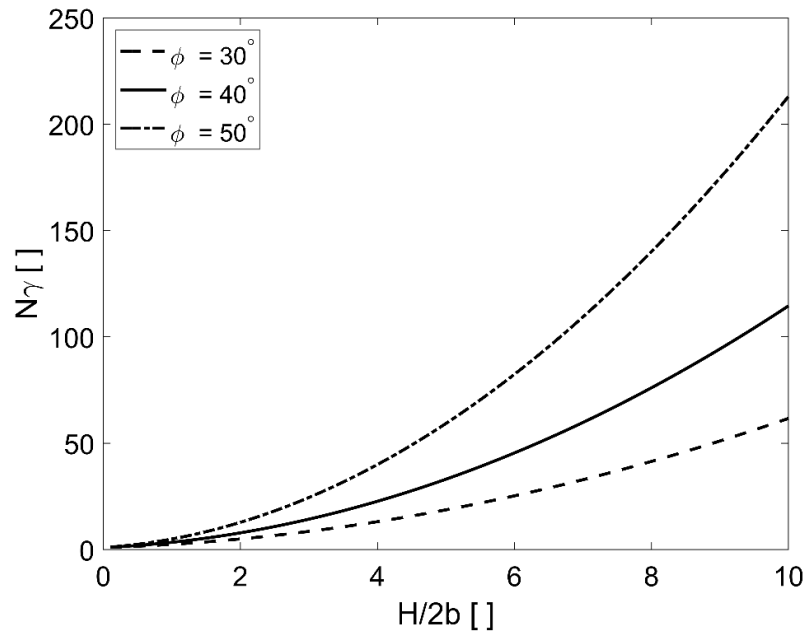
Figure 8-11. Variation in pullout factor with depth-to-width ratio for varying friction angle values.

8.5.2 Polynomial Approximation

As noted by *Baker and Konder 1966*, pullout capacity less than the critical embedment ratio is well approximated by a 2nd order polynomial. Correspondingly, to forgo further numerical approximation of Slip Line analysis equation for pullout capacity, a polynomial surface is fit to the pullout factor as a function of both geomaterial friction angle and the depth-to-width ratio (Equation 56).

$$N_\gamma = \left(A \tan^2 \phi + B \tan \phi \right) \left(\frac{H}{2b} \right)^2 + C \tan \phi \frac{H}{2b} + 1 \qquad (56)$$

A coefficient of determination of 1.0 is achieved with the following fitting coefficients, $A = 1.2081$, $B = 0.1709$, and $C = 1.7634$. Figure 8-12 is a contour plot of the best-fit polynomial surface shown in Equation 56.
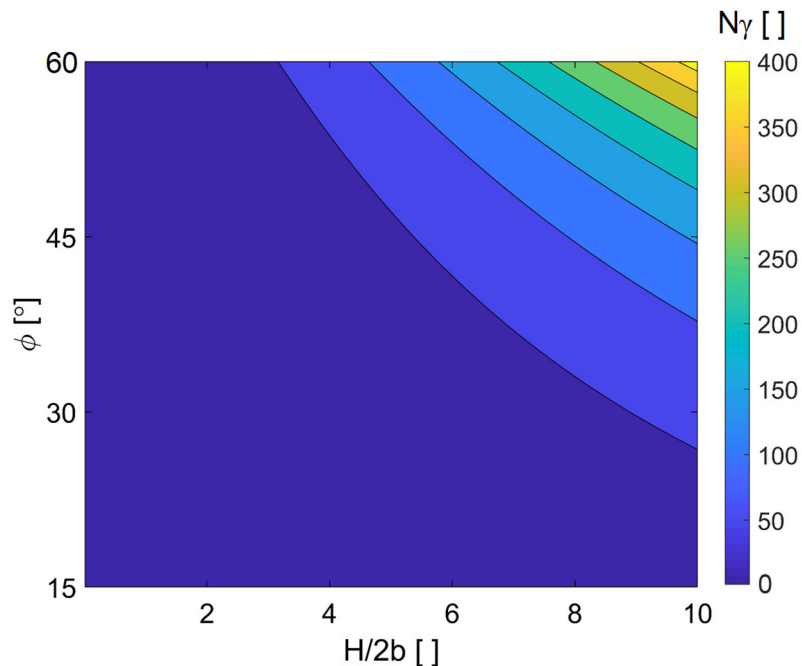
Figure 8-12. Polynomial surface approximation of Slip Line analysis pullout factor varying with depth-to-width ratio and friction angle.

8.6 Comparison of Pullout Capacity Models

Select plate anchor pullout capacity models are compared in terms of pullout factor with depth-to-width ratio for friction angle equal to 30° (Figure 8-13). The conical model ($\theta=\phi/2$) provides the lower bound while *Meyerhof and Adams 1968* provides the upper bound for the models selected.
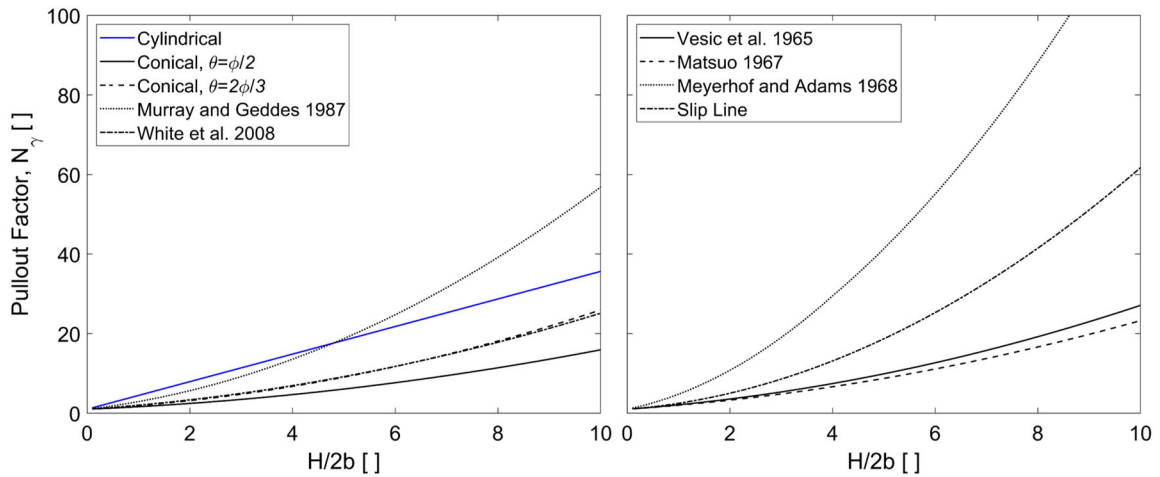
Figure 8-13. Comparison of pullout factor with depth-to-width ratio for cylindrical and conical failure surface models (left) and circular and logarithmic spiral failure surface models (right).

The accuracy of the documented pullout capacity models are evaluated with select plate anchor pullout capacity data in terms of the root mean square error, RMSE, an index of the goodness of fit (Figure 8-14). The root mean squared error is calculated from the residual error between the experimental pullout capacity data and the analytical models predicted capacity values, where Figure 8-15 demonstrates for a set of plate data, the relative accuracy of some of the models. Some of the literature pullout capacity data (e.g. *Saeedy 1971*, *Illamparuthi et al. 2002*) results in greater RMSE across all models. The cumulative root mean square error is documented in Figure 8-16 and indicates that the *Murray and*

Geddes 1987 model performed the best, followed by the Slip Line method and the adapted

White et al. 2008 model.
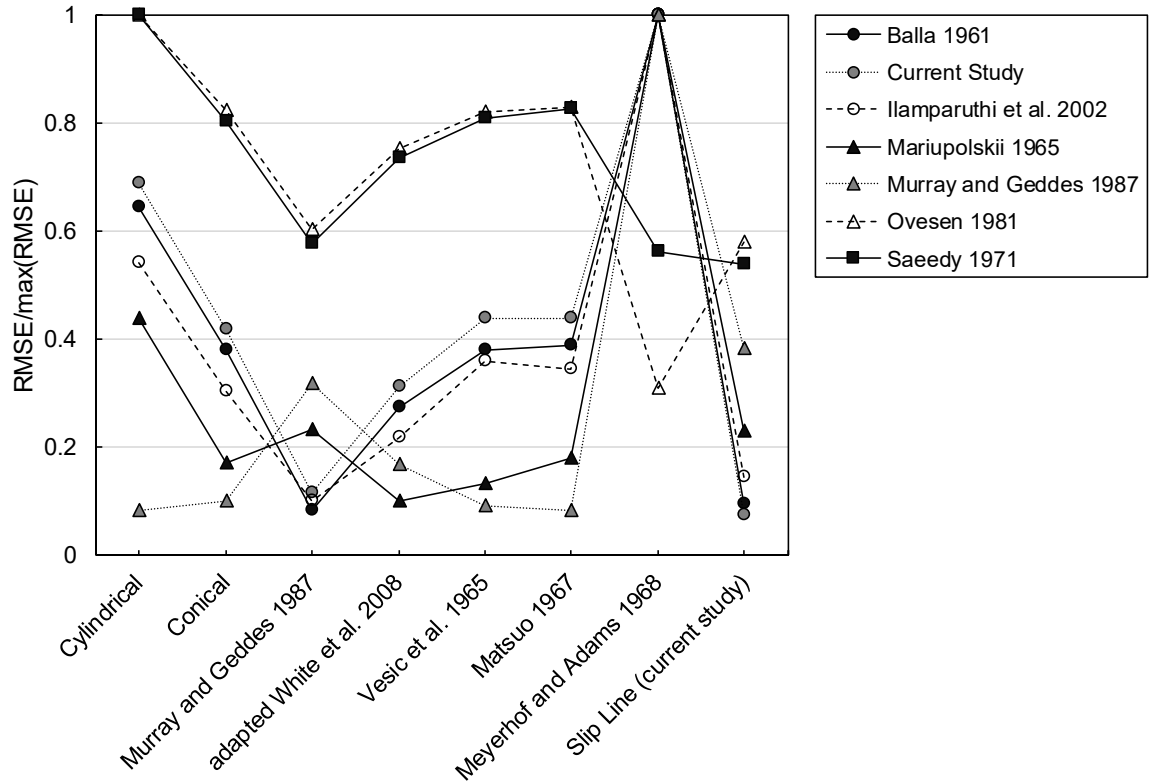
Figure 8-14. Comparison of pullout capacity models with literature plate anchor pullout data in terms of the normalized RMSE amongst all models.
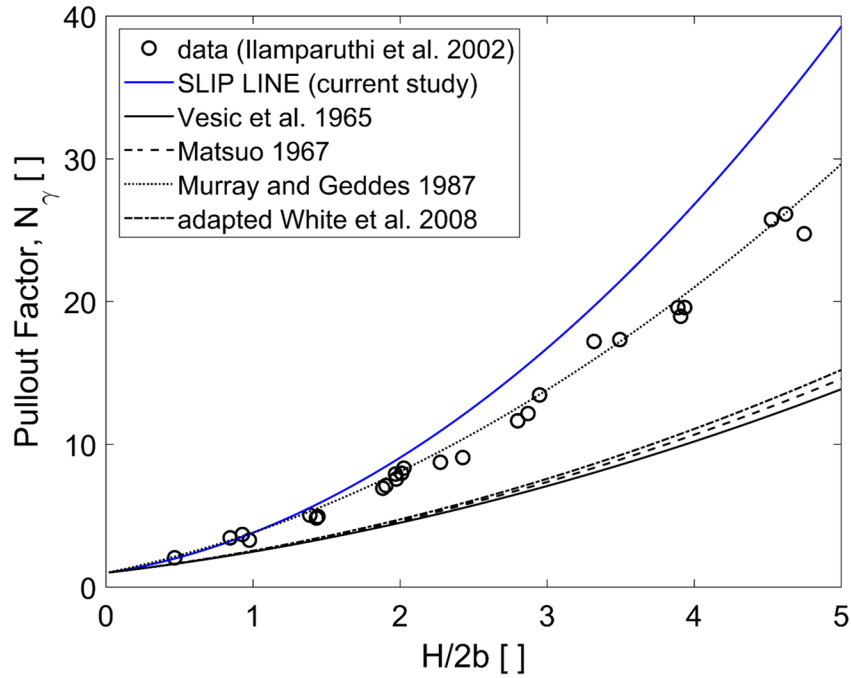
Figure 8-15. Pullout factor versus depth-to-width ratio with sample select pullout data (Ilamparuthi et al. 2002) and select pullout capacity prediction models.
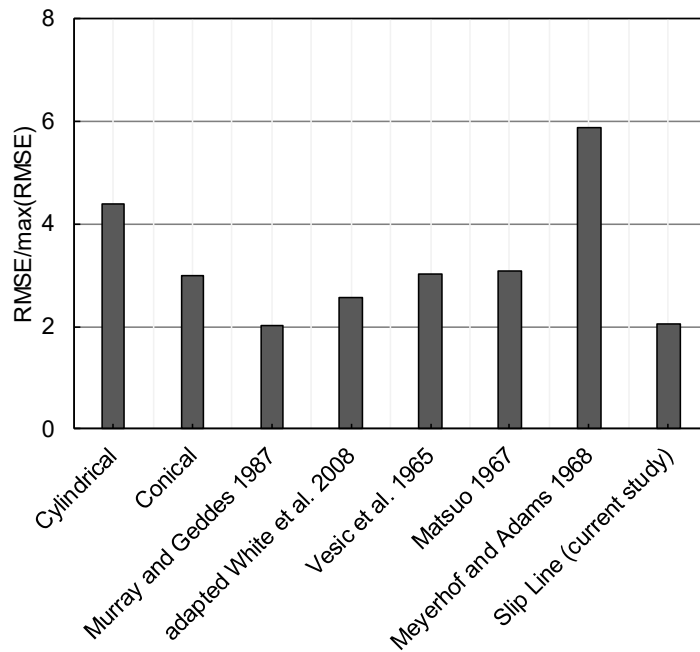
Figure 8-16. Cumulative performance of pullout capacity models with plate anchor pullout data from the literature.

8.7   Application of Slip Line Model to Root-Inspired Anchor Pullout Capacity

The following section details the reasoning and methodology for predicting root-inspired anchor pullout capacity with the Slip Line model. The underlying issue with the prediction of root-inspired anchor pullout capacity lies in the variation of the size of the breakout failure surface. As detailed in Chapter 7, the failure surface of a root-inspired anchor model in pullout initiates at some point along the length of model branch axes, termed the critical branch length, L_{cr}, and consequently, the relative volume of soil contained within the failure surface and the surface area of failure surface, which both influence pullout capacity, is severely dependent upon the critical failure surface intersection ratio, f. Therefore, given a means to predict the critical failure surface intersection ratio, the size of the failure surface can be defined and the Slip Line model can be applied.

The following methodology is observed for the prediction of f and corresponding utilization of the Slip Line model to predict pullout capacity:

1)   Calibrate the friction angle input values to Slip Line model for varying soil types using anchor plate pullout data, since for these models, f is assumed to equal 1

2)   Back-calculate f given the best-fit friction angle

3)   Utilize select f prediction based upon select failure mechanism hypothesis

8.7.1   Calibration

First, the friction angle input parameter for the Slip Line model is calibrated for all sand types using plate anchor pullout behavior data. Due to the difficulties in obtaining an accurate peak friction angle at the low stress levels of the 1g model tests (<0.5kPa) via

triaxial test, the optimal friction angle for each sand type at each tested relative density is back-calculated from plate anchor tests. Kinematically just and as proven with plate anchor failure surface visualization, the failure surface nucleates at the edge of the anchor plate and proceeds upwards to the soil surface (Balla 1961, Meyerhof and Adams 1968, Liu et al. 2012). For plate anchors, the critical failure surface intersection ratio is unity, and therefore, the anchor plate model tests serve as an upper limit for a root-inspired anchor model of the same depth-to-width ratio. An optimal friction angle was selected as the angle that minimizes the sum of squared residuals between experimental and predicted pullout capacity values. As an example, for the case of Ottawa F110 silica sand at a relative density of 80%, the best fit friction angle is equal to 39.3° as displayed in Figure 8-17.
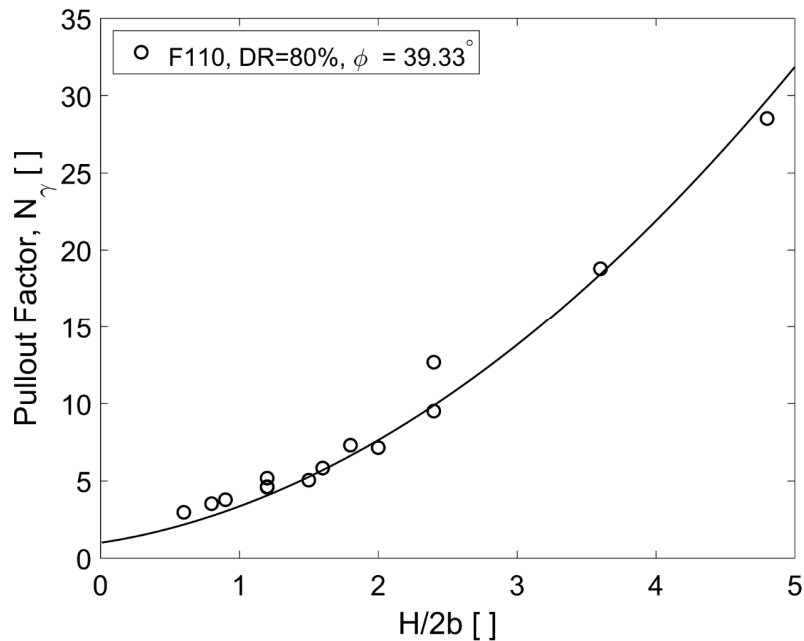
Figure 8-17. Pullout factor versus depth-to-width ratio for the optimal friction angle.

8.7.2   Back-Calculation of the Critical Failure Surface Intersection Ratio, f

With the calibrated friction angle parameter, the critical failure surface intersection ratio is determined for all root-inspired anchor model pullout tests, where the ratio that minimizes error in pullout capacity values between the predicted Slip Line value and the experimental value is selected. The trends in critical failure surface intersection ratio with various root-inspired anchor model geometric parameters and geomaterial conditions are displayed in Figure 8-18-Figure 8-20. In terms of the model geometric parameters, f increases towards unity as the number of branch axes and internal branching angle increases and while the depth-to-width ratio decreases. Geomaterial conditions and particle characteristics minimally affect the critical failure surface intersection ratio, since the variations in geomaterials are captured with the friction angle. In comparison with the effects of anchor morphology parameters on f, geomaterial type and conditions contribute negligibly.
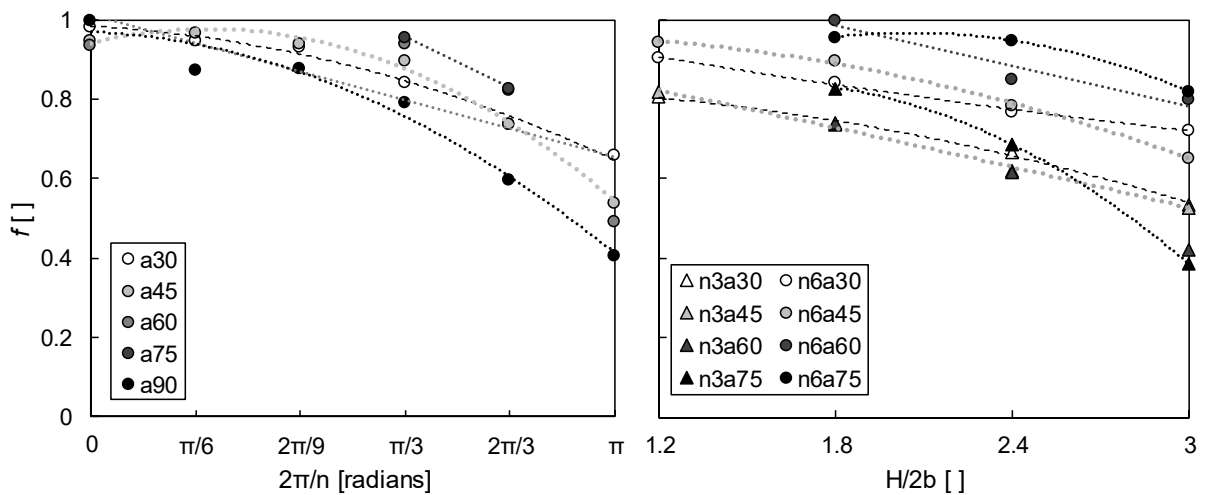
Figure 8-18. Effect of number of branch axes and depth-to-width ratio on f.
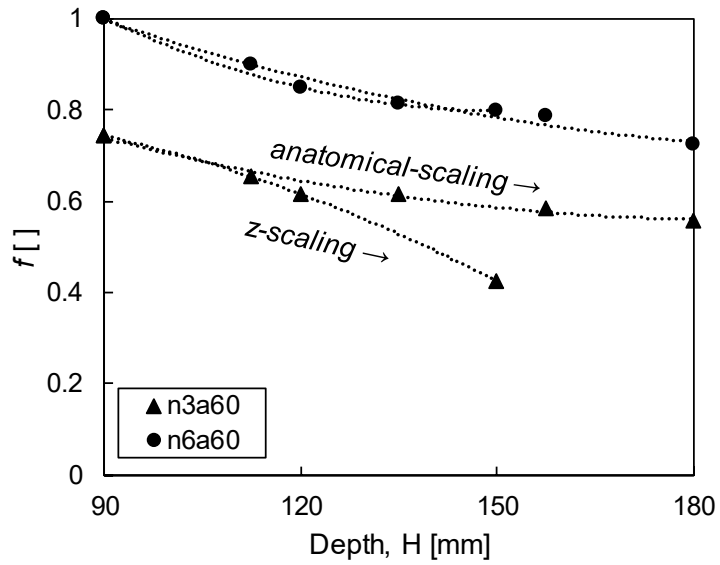
Figure 8-19. Effect of scaling type (anatomical versus z-scaling) on *f*.
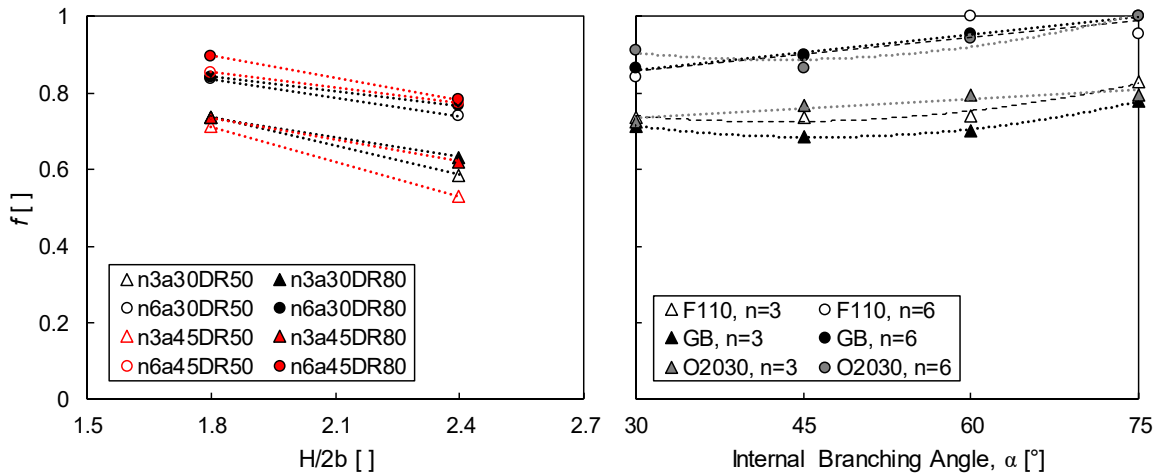
Figure 8-20. Effect of relative density and soil angularity and particle size on *f*.

8.7.3   Critical Failure Surface Intersection Ratio Prediction

8.7.3.1   Hypothesis 1: Branch Bending

Hypothesis 1 relates the relative kinematics of both particles and branching axes. Even in 1g benchscale pullout testing, the branching axes of root-inspired anchor models experience deflections during the pullout process. This hypothesis states that the failure

surface nucleates at a point along the branch axis length where significant branch axis deflection provides particles additional geometric freedoms, such that particles are no longer constrained to the upward movement of the branch axis.

8.7.3.1.1 Implementation Method: Deflection of a Cantilever Beam

For the deformation of root-inspired anchor model, a single branch axis is modeled as a cantilever beam (Figure 8-21), which is subjected to a distributed load, *q(x)* (Equation 57), due to the weight of soil above the model distributed to each branch axis, where *x* proceeds along the length of the branch axis.
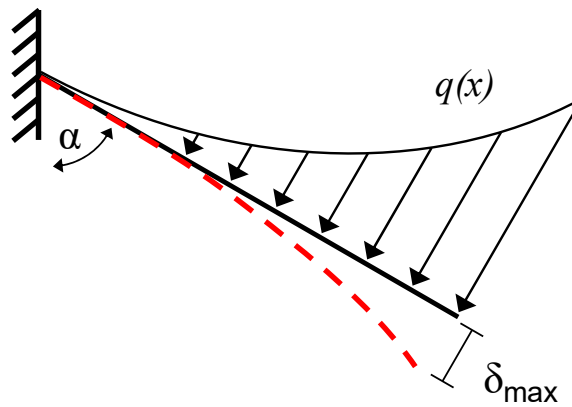
Figure 8-21. Schematic representation of the branch axis modeled as a cantilever beam subjected to a distributed load.

$$q(x) = \frac{2\pi\gamma'}{n} x \sin^2 \alpha \left(L_s + x \cos \alpha \right) \tag{57}$$

If Equation 57 is inputted into the standard differential equation for the deflection of a beam (Equation 58) and integrated assuming only one-dimensional deflection, the deflection of a beam is produced (Equation 59).

$$\frac{d^4v}{dx^4} = -\frac{q(x)}{EI} \tag{58}$$

$$v(x) = -\frac{\pi\gamma'}{180EIn} x^2 \sin^2 \alpha \left(\begin{array}{c} 45L^4 \cos\alpha - 20L^3 x \cos\alpha + \\ x^4 \cos\alpha + 60L^3 L_s - 30L^2 L_s x + 3L_s x^3 \end{array} \right) \tag{59}$$

If the deflection of the beam subject to the weight of soil above is related to the critical failure surface intersection ratio, following Equation 60, given fitting parameters, A=-0.31, B=0.09, a coefficient of determination of 0.56 is achieved (Figure 8-22).

$$f = A\log\left(\frac{\delta}{L}\right) + B \tag{60}$$
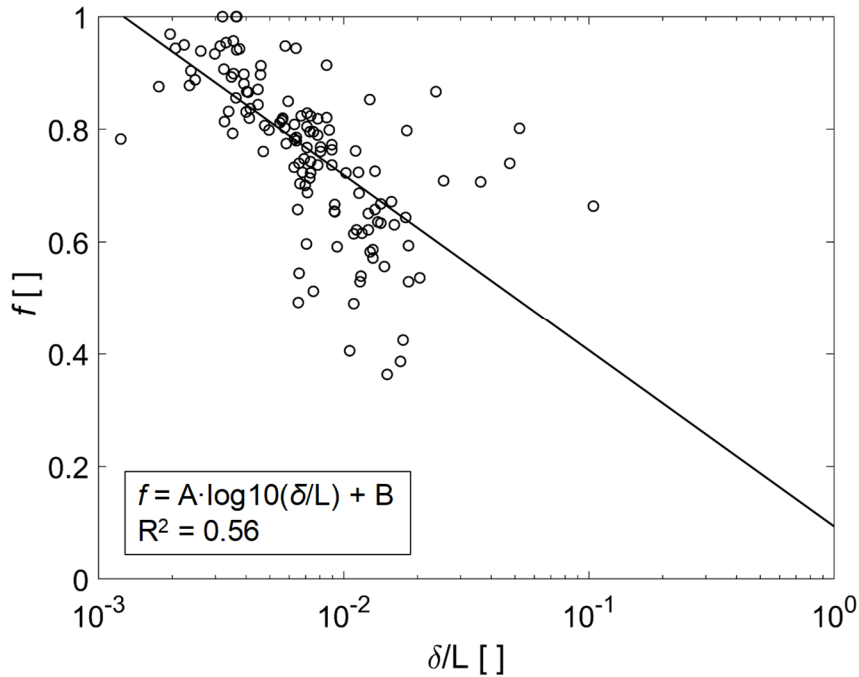
Figure 8-22. Relationship between beam deflection normalized by branch axis length and f.

8.7.3.2 Hypothesis 2: Soil Arching

The hypothesis underlying this method is that the critical failure surface intersection ratio is controlled by arching in soils. A specific depth-to-space ratio exists such that particle forces that arch across adjacent model branch axis are surpassed by the weight of the soil above and some frictional resistance. Several methods for determining the critical branch length based on this logic are attempted.

8.7.3.2.1   Implementation Method: Surface Area Ratio

For the most simplistic analysis, a simple area ratio is utilized and is defined as the surface area of the model projected onto the plane perpendicular to the stem axis over the area of the maximum inscribed circle of the projected model on the same place, where the area ratio is described in Chapter 5. A simple power law model (Equation 61) can be fitted to the data when constrained by known theoretical limits (i.e. model surface area ratio of 0 and 1 would produce critical failure surface intersection ratios of 0 and 1, respectively). For the power constant, *Cst*, equal to 0.2, the root-mean-square error is minimized, and a coefficient of determination of 0.53 is achieved (Figure 8-23). The simplistic logic behind this method suggests that soil arching is more likely to occur as the branching section of the model is increasingly filled in with branch axes, and therefore, the critical failure surface intersection ratio increases as primarily the number of branch axes and the diameter of the branch axes increases. However, this method of analysis is not physics based and fails to incorporate information regarding the embedment depth, which is a critical parameter for the development of arching in soils.

$$f = A_{ratio}{}^{Cst} \qquad\qquad (61)$$
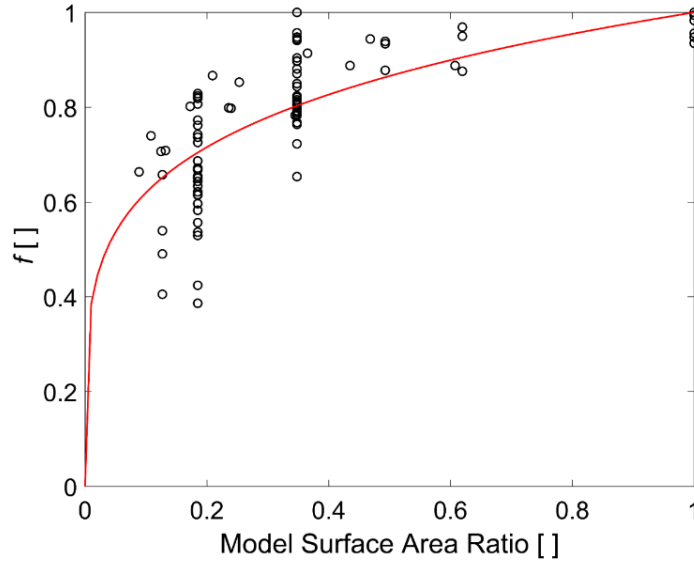
Figure 8-23. Relationship between model surface area ratio and *f*.

8.7.3.2.2   Implementation Method: Limits to Soil Arching

The depth-to-spacing ratio, along with the defined lateral earth pressure coefficient, K, are critical parameters to the stability of soil arching. The phenomenon of arching in soils suggests that the load transfer due to frictional resistance occurs as a body of soil is displaced relative to an adjacent, stationary soil body. The magnitude and transfer direction is dependent upon the direction of displacement and lateral earth pressure coefficient, and additionally, for the case of displaced body contained between two stationary bodies, the depth-to-space ratio is also critical, where a greater proportion of the original load on the displaced body is transferred to the surrounding bodies with increased depth-to-spacing ratio. From the literature, two-unique types of soil arching models (three total) were selected, 1) bin/silo theory-type models, where the force reduction is determined by solving the force balance on a sliding, differentiable wedge of soil given specific boundary conditions (Terzaghi 1943, Ladanyi and Hoyaux 1969), and 2) an upper bound solution provided by limit analysis, where the kinematically admissible velocity field is defined by

slip-lines inclined inward at an angle equivalent to soil friction angle, ϕ, to the vertical for active failure (i.e. downward movement). Both types of models perform two-dimensional analyses and assume that the in-plane stress and strain do not contribute. The depth-to-spacing ratio for the root-inspired anchor models can be defined in two-ways by the arc or chord length as shown in Figure 8-24 and detailed in Equation 62 and 63.

$$s_{max, arc} = \frac{2\pi}{n}b \tag{62}$$

$$s_{max, chord} = 2b\sin\left(\frac{\pi}{n}\right) \tag{63}$$
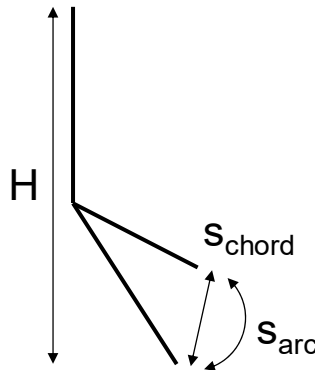
Figure 8-24. Schematic representation for the determination of the maximum depth-to-spacing ratio for a root-inspired anchor model.

For the bin/silo theory-type soil arching models the solutions of both *Ladanyi and Hoyaux 1969* and *Terzaghi 1943* were adopted for the analysis. The models are nearly identical except in the treatment of the lateral earth pressure coefficient, K, where K is equal to unity for *Terzaghi 1943* and is defined in Equation 64 for the *Ladanyi and Hoyaux 1969* model.

$$\frac{F}{\gamma s H} = \frac{1 - \exp(M)}{M}$$

$$M = 2 \tan \phi K \frac{H}{s} \tag{64}$$

$$K = \frac{1}{1 + 2 \tan^2 \phi}$$

An upper bound solution to the active wedge problem by limit analysis is derived by *Smith 1998* as a piecewise function (Equation 65). The three soil arching models are compared in terms of the proportion of the soil weight between the root-inspired anchor models that is transferred to the branch axes (Figure 8-25).

$$\frac{F}{\gamma s H} = \begin{cases} 1 - \dfrac{H}{s} \tan \phi, & \dfrac{H}{s} \leq \dfrac{1}{2 \tan \phi} \\[3mm] \dfrac{s}{4H \tan \phi}, & \dfrac{H}{s} > \dfrac{1}{2 \tan \phi} \end{cases} \tag{65}$$
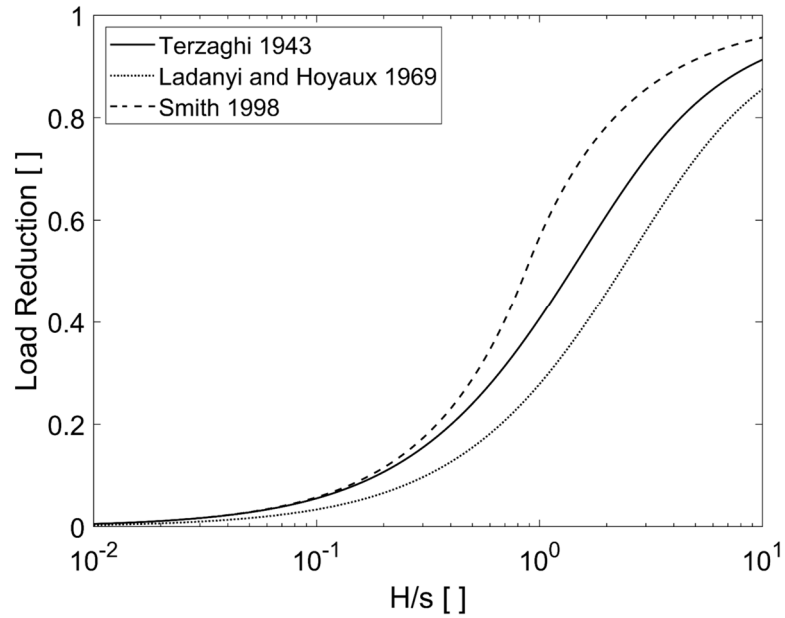
Figure 8-25. Load reduction curves of select soil arching models with the depth-to-spacing ratio assuming active soil failure.

281

No clear trend between the maximum depth-to-spacing ratio and critical failure surface intersection ratio was noticed. In further progression, based on the force still applied to the bottom of the body of soil between two branch axes, the height of an assumed half-ellipse of soil equivalent to remaining force was determined (Equation 66) and is shown schematically (Figure 8-26).

$$h = \frac{2F}{\gamma \pi s} \tag{66}$$
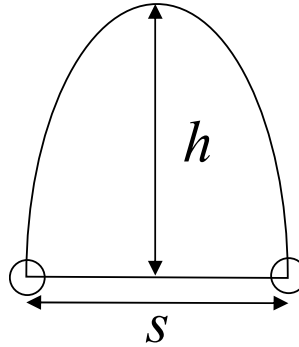
Figure 8-26. Schematic representation of the soil half-ellipse formed due to soil arching.

Furthermore, the relationship between the critical failure surface intersection ratio, f, and the half-ellipse height-to-model width ratio, h/b, is modeled with Equation 67 and is displayed in Figure 8-27 with fitting parameters, $A = 2.89$ and $B = 1.5$. With a linear least squares regression, a coefficient of determination of 0.67 is achieved.
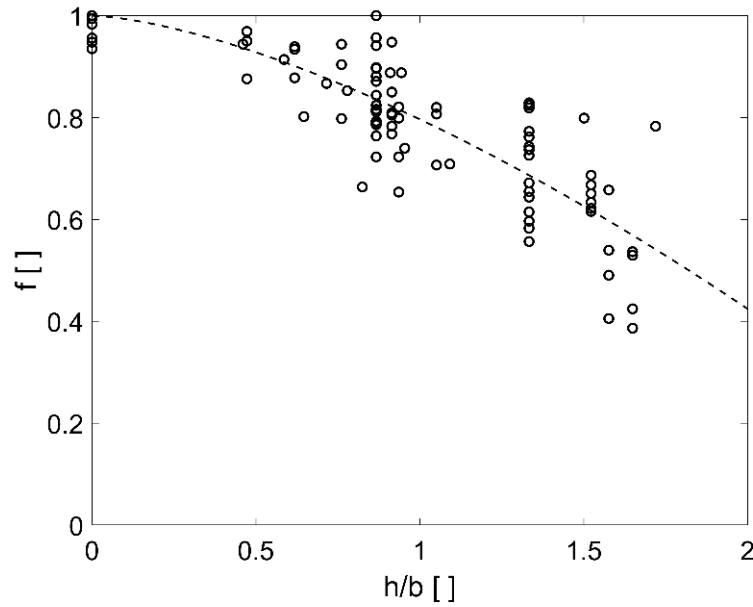
Figure 8-27. Relationship between the critical failure surface intersection ratio, f, and the half-ellipse height-to-model width ratio.

$$f = 1 - \left(\frac{h}{A \cdot b} \right)^{B}$$

(67)

8.7.3.2.3 Implementation Method: Feature Engineering

Feature engineering is a concept within machine learning for developing a predictive algorithm with select features based upon feature knowledge. In this case, select features were utilized in a simplistic linear regression model for the prediction of critical failure surface intersection ratio. The goal was to generate a predictive model that incorporated features of that root-inspired anchor model pullout system that describe the soil arching mechanism. The predictive model (Equation 68) utilizes four root-inspired anchor features, embedment depth, H, anchor model width, b, branch spacing, θ, and internal branching angle, α, and is displayed in Figure 8-28. With a linear least squares regression of Equation 68 with the input data, a coefficient of determination of 0.73 is achieved.

283
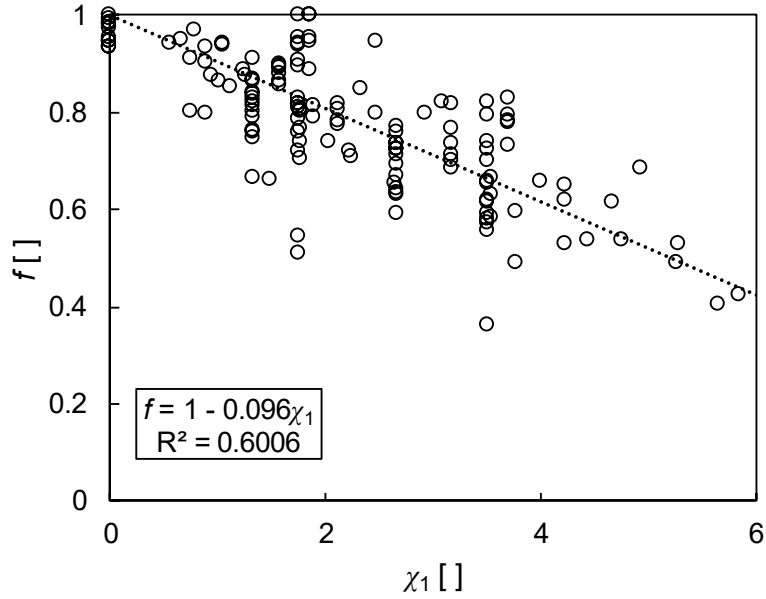
Figure 8-28. Relationship between the feature engineering index, χ_1, and the critical failure surface intersection ratio.

$$f = 1 - m\chi_1$$
$$\chi_1 = \frac{H}{2b}\frac{2\pi}{n}\sqrt{\sin\alpha} \tag{68}$$

8.7.3.3   Model Combination

The occurrence of a critical failure surface intersection ratio less than one is likely due to a combination of mechanisms; as such, the corresponding predictive model should incorporate the features of all involved mechanisms if the full behavior is to be captured. A second order polynomial surface, detailed in Equation 69, is utilized to combine two arbitrary models, X_1 and X_2. The statistical results of the combined models fitted with a polynomial surface is recorded in Table 8-1. The combination of feature engineering and soil arch height forms the best predictive model for f.

$$f = c_0 + c_1 X_1 + c_2 X_2 + c_3 X_1^2 + c_4 X_2^2 + c_5 X_1 X_2 \qquad (69)$$

Table 8-1. Results of combined methods for critical failure surface intersection ratio prediction.

	Combination	Fit Type	R^2	RMSE
1	Feature Engineering Beam Deflection	Polynomial Surface (χ_1, δ)	0.73	0.0745
2	Feature Engineering Soil Arch Height	Polynomial Surface (χ_1, h)	0.80	0.0654
3	Beam Deflection Soil Arch Height	Polynomial Surface ($\delta/L, h/b$)	0.68	0.0817

8.7.3.4   Comparison of Critical Failure Surface Intersection Ratio Predictive Models

The various critical failure surface intersection ratio models are analyzed in terms of their pullout capacity prediction, where the predicted f values are directly inputted into the Slip Line model and compared to the experimental pullout capacity values. Table 8-2 presents the results of the comparative analysis of the f models in terms of their pullout capacity predictive capabilities. The combinatorial f model that incorporates both feature engineering and soil arch height performs the best in terms of the highest coefficient of determination and lowest root mean square error, and the results are plotted in Figure 8-29, which additionally displays the upper and lower 90% confidence interval for each pullout capacity prediction based on the polynomial surface regression. As well, all f models are compared in Figure 8-30, which presents the percentage of predicted pullout capacity values that exists between increasing percent error bounds of the experimental data.

A perfectly predictive model is unachievable due to the level and propagation of uncertainty throughout the entire formation of the predictive model. Uncertainty exists in

both the experimental pullout capacity values (e.g. both plate and root-inspired anchor model data) and the assumptions and methodology used in the derivation of the Slip Line model (e.g. methodology (e.g. failure surface shape, average friction angle, soil state of failure along entire surface), which propagates in the prediction of the critical failure surface intersection ratio and the corresponding pullout capacity prediction.

Table 8-2. Error statistics in predicting pullout capacity, P_{max}, based on various f models.

f model	R^2	RMSE
Beam Deflection	0.9524	4.6525
Surface Area	0.9353	6.0456
Soil Arch Height	0.9362	6.0151
Feature Engineering	0.9232	6.7008
Combination(χ_1,δ)	0.9532	4.7989
Combination(χ_1,h)	0.9711	3.3905
Combination($\delta/L,h/b$)	0.9474	5.2374
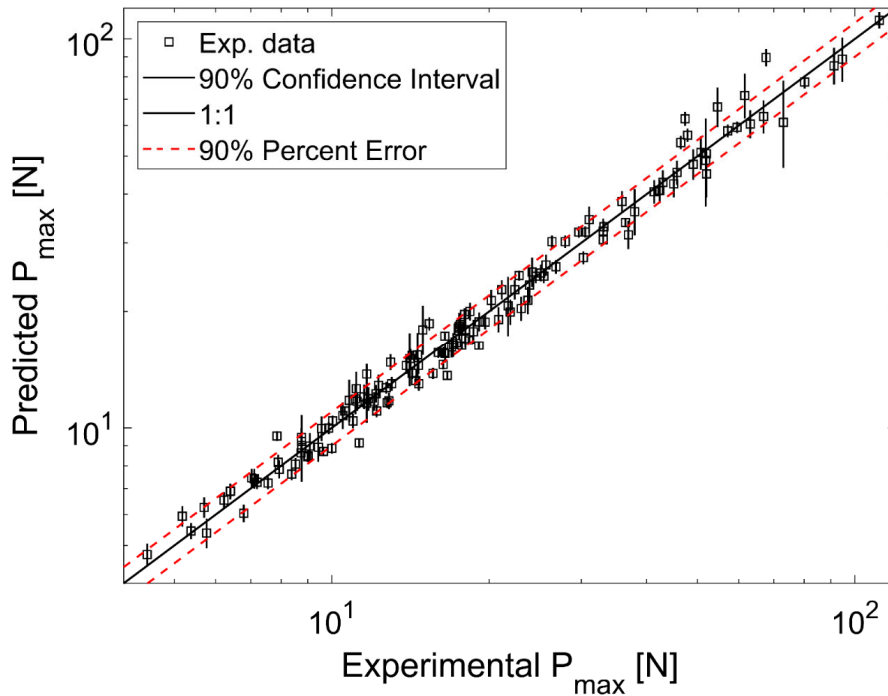
Figure 8-29. Predicted versus experimental pullout capacity for the Combination(χ_1,h) f model (line through data point signifies upper and lower 90% confidence interval based on the f regression model).
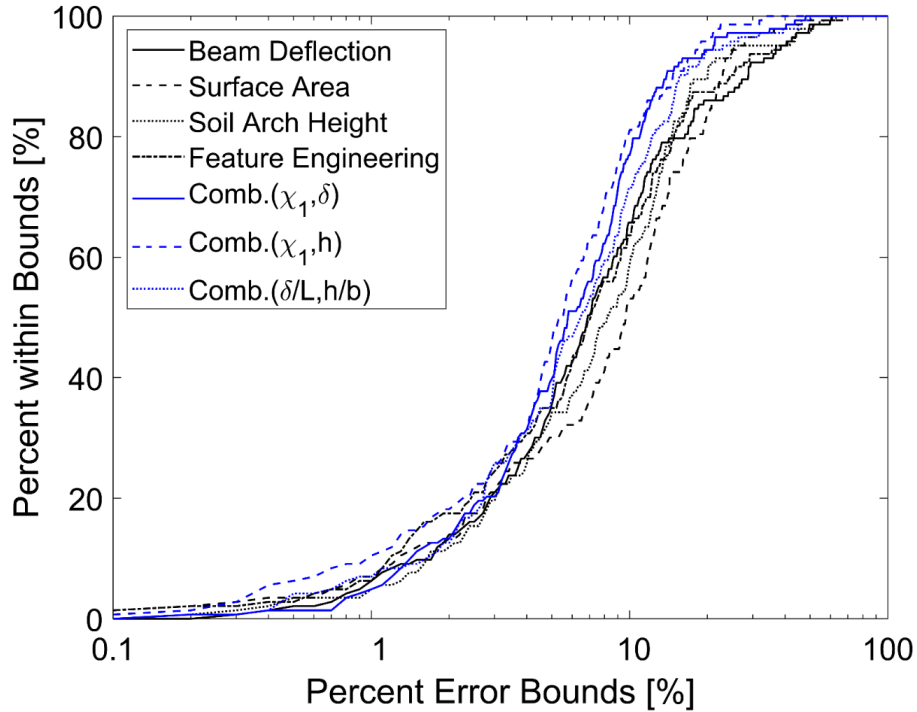
Figure 8-30. Percentage of pullout capacity data constrained within varying percent error bounds for different *f* models.

8.8 Conclusion

The conclusions from this chapter can be summarized in the following points:

- Pullout capacity models require many assumptions (e.g. failure surface, failure criterion, acting mechanisms stress state), which explains the multitude of models and no reached consensus.

- An axisymmetric Slip Line model is created to improve upon the work of the inherent plane strain assumptions within *Matsuo 1967* and *Vesic 1969,* while incorporating a geomechanically rigorous logarithmic spiral failure surface, and is shown to predict well anchor plate capacity data from both the literature and this study.

- The axisymmetric Slip Line model is adjusted to predict pullout capacity of a root-inspired anchor model by varying the critical failure surface intersection ratio, which naturally modifies the weight of uplifted soil and the frictional resistance along the failure surface.

- From various evaluated methods of predicting the critical failure surface intersection ratio, a combined method incorporating both the soil arching mechanism and feature engineering achieved best results in terms of the RMSE.

CHAPTER 9.   NUMERICAL PARAMETRIC STUDY OF THE FACTORS AFFECTING PULLOUT RESPONSE OF ROOT SYSTEM-INSPIRED ANCHORS

The purpose of this study is to extend the experimental campaign to investigate to a greater extent the behavior of the soil, the structure, and the soil-structure interaction. This parametric study further elucidates the role of soil properties (i.e. friction angle, dilation angle, soil stiffness), anchor properties (i.e. elastic modulus), and interface properties (i.e. interface friction) on pullout behavior.

9.1   Introduction

The numerical simulation of the pullout problem has been investigated through both FEM (Rowe and Davis 1982, Vermeer and Sutjiadi 1985, Tagaya et al. 1988, Koutsabeloulis and Griffiths 1989, Sakai and Tanaka 1998, Kumar and Kouzer 2008, Mokhbi et al. 2017) and DEM (Rui et al. 2016, Athani et al. 2017, Evans and Zhang 2019) methods. Some of the primary insights revealed from numerical simulations of plate anchor pullout include that dilatation angle and friction angle govern pullout capacity, the effect of initial stress state is slight except for at small dilation angles, the importance of axisymmetric conditions versus plane strain for circular and square plates, small anchor width-to-particle dimeter ratios significantly affect pullout factor particularly for anchors with smaller depth-to-width ratios, and that anchor interface friction/roughness contributes marginally to pullout capacity.

9.2   Numerical Modelling

FLAC3D (Fast Lagrangian Analysis of Continua in 3 Dimensions), a finite volume commercial software designed by Itasca Consulting Group, Incorporated, is utilized to simulate the pullout process for this study. This method employs an explicit, Lagrangian calculation scheme and a mixed-discretization method as opposed to an implicit scheme and reduced integration method common to finite elements, and for large-strain simulations, an explicit scheme is often faster due to due the calculation and memory demands for the inversion of the stiffness matrix in FEM. For simulations with large disparities in material properties or adjacent element sizes, the time step required to minimize numerical instability can effectively nullify the computational time advantage over FEM.

Simulation specifics including model geometry and boundary conditions, mesh generation and convergence, time step, and input parameters are documented in Chapter 4, as well as the results of model calibration with anchor plate pullout data.

9.2.1   *Material Property Selection*

Table 4-9 provides a list of the various input parameters, including material properties of the anchor, the soil, and the soil-anchor interface. The density of the soil was specified according the dry density of Ottawa F110 sand at a relative density of 80%. The initial stress state, dictated by the earth pressure coefficient, K, was selected as 1.0 due to the horizontal tamping of the soil box during the experimental sample preparation. For the soil the elastic modulus was varied significantly, yet a value of 15MPa was selected in calibration with pullout anchor tests. This value is in the typical range of soil moduli values and lower by an order of magnitude than the empirically predicted small strain modulus

(E_0~200MPa) (Cha et al. 2014). A selected Poisson's ratio, v, of 0.2 is a standard value for the modeling of drained, coarse-grained materials (Jefferies and Been 2016). A Mohr-Coulomb constitutive model was defined as the failure criterion for the soil, defined by the friction angle, ϕ, which is defined according to Equation 70 (Bolton 1986).

$$\phi = \phi_{CS} + \psi \tag{70}$$

A non-associative flow mechanism, $\psi=10°<\phi$ is specified following the results from Chapter 7 in the visualization of the soil kinematics relative to the failure surface. For the contact between soil and anchor elements, an interface friction angle dictates the strength of the interface shear response and is defined as a function of the critical state friction angle, where the value, $2/3\phi_{CS}$, was selected in accordance with the Ottawa sand-3D printed plastic shear response results detailed in Chapter 10. Within the contact model, the normal and shear stiffness were selected based on numerical stability and were shown to minimally affect the pullout response for the range of values tested. The elastic properties of the anchor were chosen according to Table 4-3.

9.2.2 Pullout Response

Characteristic pullout resistance-displacement trajectories for the pullout of a root-inspired anchor model are displayed in Figure 9-1. The curves are processed with a median filter to remove force spikes that occasionally occur in the plastic response, which prevents over prediction of pullout capacity.
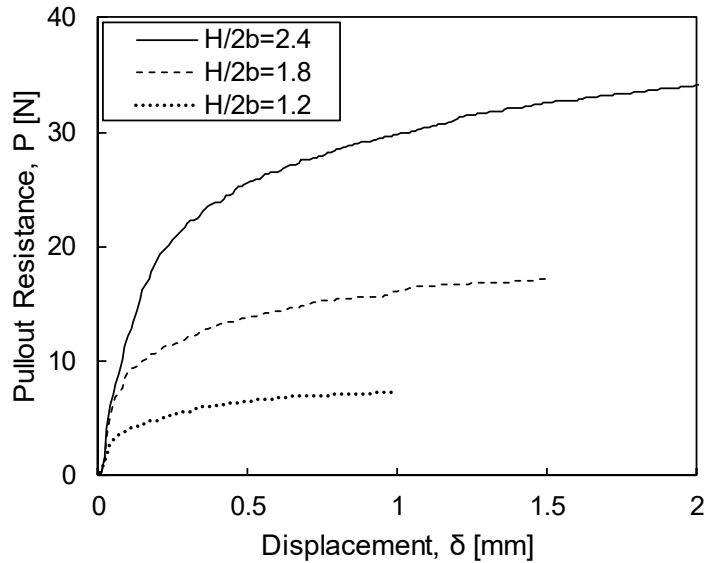
Figure 9-1. Characteristic load-displacement pullout response of model n3a45 of constant width, *b*=25mm, and at various embedment depths of 60, 90, and 120mm.

9.2.3   Interpreted Pullout Capacity

Common to the numerical simulation of the pullout problem with a Mohr-Coulomb constitutive model is the effect of contained plastic deformation that acts to enhance the pullout resistance past the expected failure displacement (Rowe and Davis 1982, Koutsabeloulis and Griffiths 1989) and is perfectly illustrated in Figure 9-1, where the relative rate of change in resistance with displacement intensifies with the depth-to-width ratio. As such, the determination of a pullout capacity value becomes subjective, just as in the case of interpreting a failure load from the load-displacement response of a pile in compression. Numerous methods of inferring a failure load have been detailed in the literature (Terzaghi 1943, van der Veen 1953, Chin 1970, Davisson 1970, Leonards and Lovell 1979, Fellenius 1980, Kulhawy 2004). Particular to the pullout problem, *Rowe and Davis 1982* define the failure resistance as the force that first exceeds four times the deformation present in the elastic response, whereas many other researchers neglect to

define pullout capacity. For this analysis, the exponential decay-type model (Equation 71) originally proposed by *van der Veen 1953* was fit to each load-displacement curve with a least squares regression, where P_{max} and ω, the arbitrary decay constant, are fitting parameters. This models removes much of the subjectivity present in other models. For example, in the *Terzaghi 1943* approach, which defines the interpreted failure load as the resistance at which the gradient of the curve plateaus to a constant, a user-defined threshold is required.

$$P = P_{\max}\left(1 - e^{-\omega\delta}\right)$$ (71)

9.2.4 Model Validation

The numerical model was calibrated with anchor plate pullout data due to the presumption that plate anchor data is less prone to variations in sample preparation and consequently in pullout response. Figure 9-2 documents the validation of the numerical model through a comparison in pullout capacity values between the FLAC3D simulation and experimental data of select root-inspired anchor models. With a 1:1 linear fit between numerical and experimental pullout capacity values, a coefficient of determination of 0.93 is achieved.
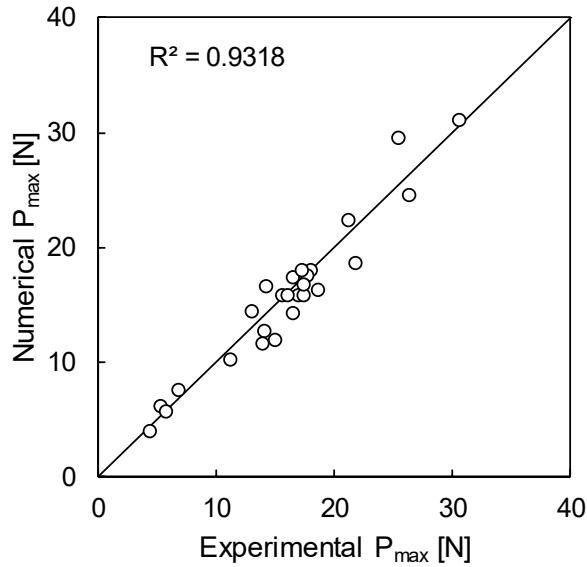
Figure 9-2. Validation of numerical model as evident by comparison of numerical and experimental pullout capacity values for 30 root-inspired anchor models.

9.2.4.1 Effect of Number of Branch Axes, n, and Depth-to-Width Ratio, $H/2b$

While the overall trends in pullout behavior with the number of branch axes (Figure 9-3) and depth-to-width ratio (Figure 9-4) exhibited in the numerical and experimental tests are similar, slight deviations are present. For example, pullout capacity has an asymptotic trend with increasing n in the experimental results, while the relationship appears cubic, bounded by $n=\infty$ and $n=3$, in the numerical results. As displayed in Figure 9-5, pullout resistance increases with the number of branch axes due to the relative increase in the volume and magnitude of soil mobilization. Additionally, for the case of varying depth-to-width ratio, the maximum tangent stiffness appears to quadratically increase with $H/2b$ in the experimental results while the stiffness appears to behave asymptotically from the numerical simulations. These discrepancies are likely the result of invalid model assumptions such as a uniform elastic modulus, friction angle, and dilation angle.
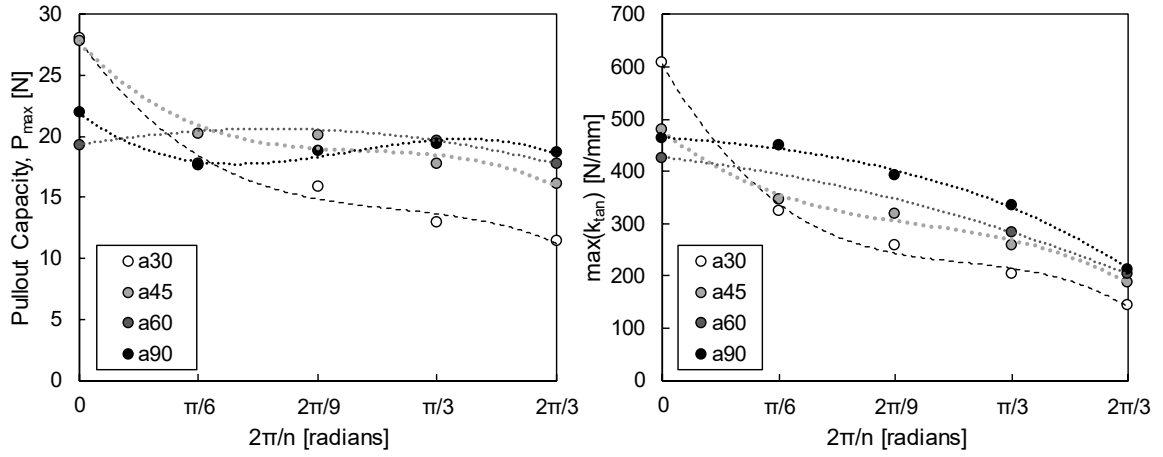
Figure 9-3. Effect of number of branch axes on pullout behavior for models of constant depth-to-width ratio, *H*/2*b*=1.8.
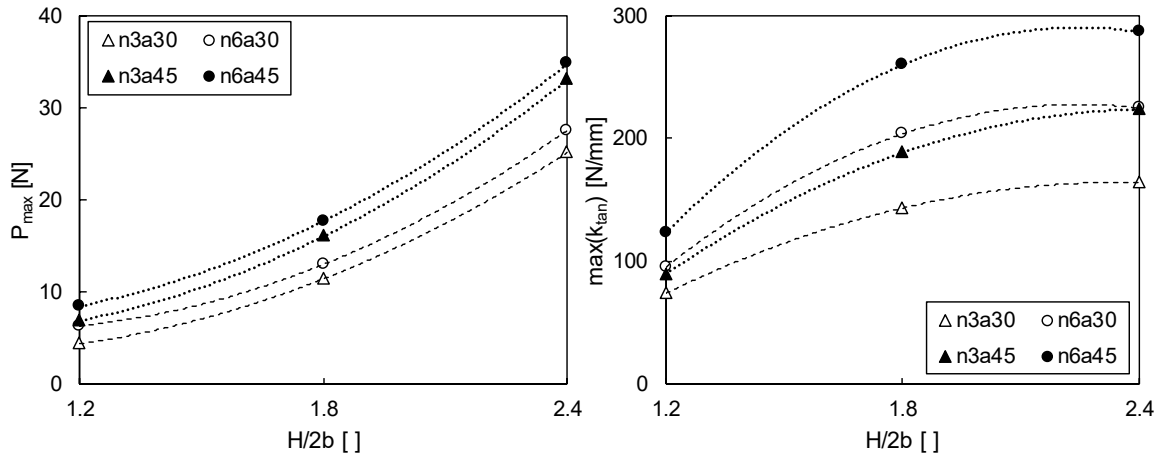
Figure 9-4. Effect of depth-to-width ratio on pullout behavior of models of constant width, *b* = 25mm.
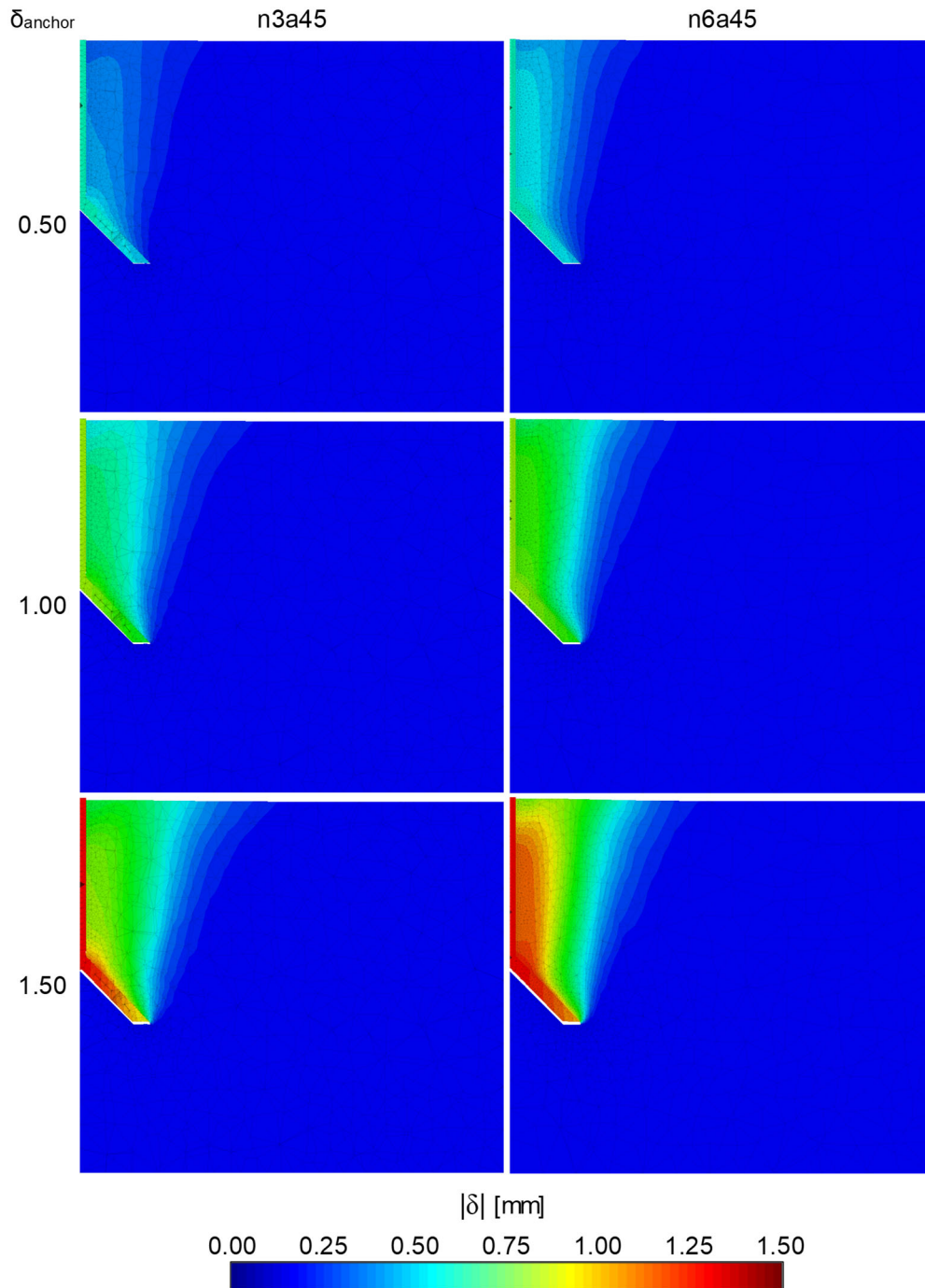
Figure 9-5. Comparison in the magnitude of displacement maps of root-inspired anchor models with 3 and 6 branching axes.

9.3   Parametric Study

After model validation, a parametric study into the effect of various soil, anchor, soil-anchor interface properties on the pullout capacity and stiffness was performed.

9.3.1 Effect of Friction Angle, ϕ

To investigate the role of internal friction angle, ϕ, on the pullout behavior of root-inspired anchors, the Mohr-Coulomb friction angle was varied between 31° and 51°, while dilation remained constant at 10°. As fully expected, an increase in the strength of the soil results in an increase in pullout capacity. Additionally, an increase in the strength of the soil through the specified friction angle manifests itself in an increase in maximum tangent stiffness, since an increase in pullout resistance is expected for the same anchor movement.
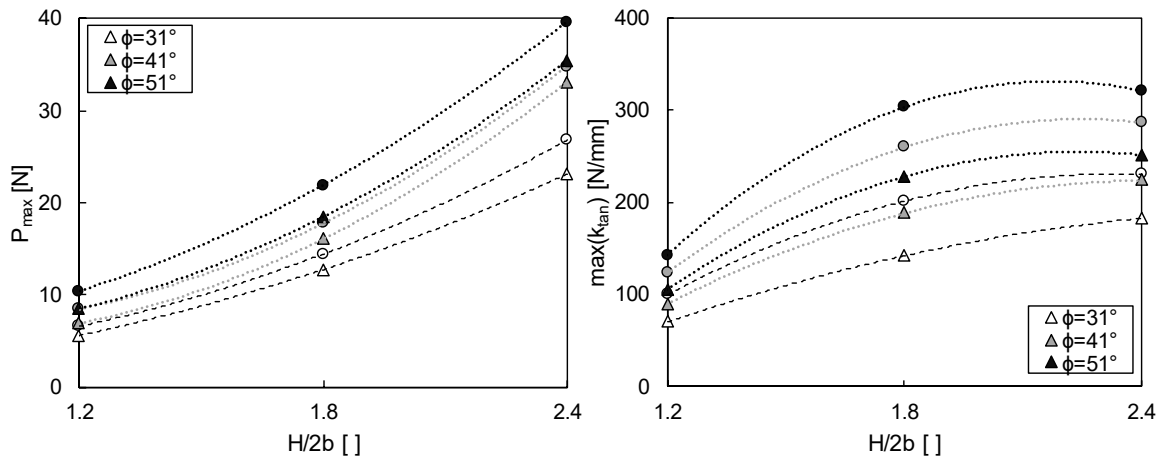
Figure 9-6. Effect of friction on pullout response of root-inspired anchors of constant width, *b*=25mm.

9.3.2 Effect of Dilation Angle, ψ

For this set of simulations, the friction angle was maintained at ϕ=41°, while the angle of dilation was varied between 0° and 41°. Results shown in Figure 9-7 reveal that both pullout capacity and maximum tangent stiffness increase with dilation angle and the

effect is magnified with increased depth. In the Mohr-Coulomb constitutive material model, dilation angle controls the orientation and magnitude of plastic flow, where a dilation angle of 0° corresponds to zero volume change past failure, which is unreasonable for the dense, dilative sand that is being modeled. Furthermore, a dilation angle equal to the mobilized friction angle, $\psi=\phi$, represents an associated flow rule, which is expected to increase the size of the failure surface.
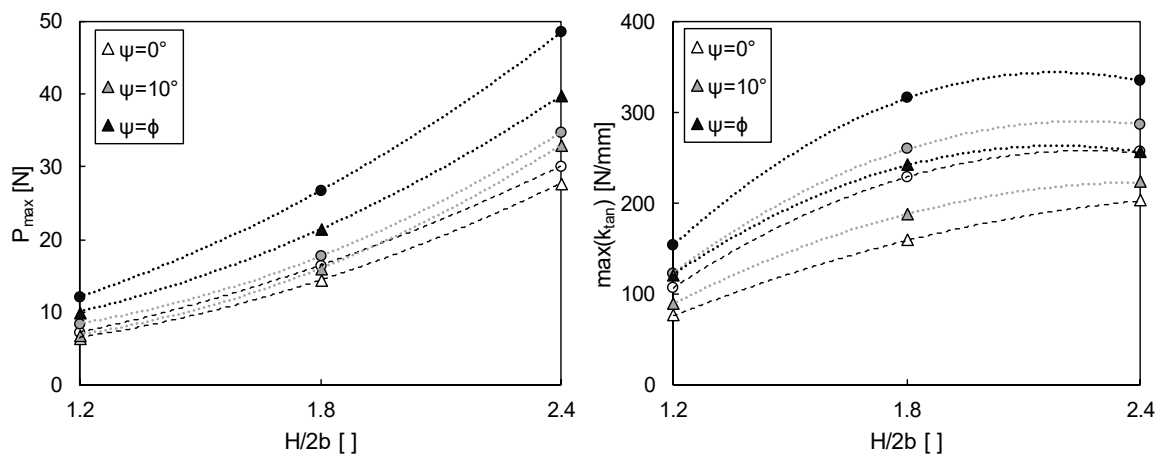
Figure 9-7. Effect of the angle of dilation on pullout capacity and maximum tangent stiffness for models of constant width.

9.3.3   Effect of Soil-to-Anchor Modulus Ratio

Figure 9-8 and Figure 9-9 demonstrate the effect of the anchor-to-soil elastic modulus ratio, E_a/E_s, on the pullout capacity and maximum tangent stiffness for simulations with constant soil modulus and anchor modulus, respectively, where the anchor and soil moduli are varied in orders of magnitude from the calibrated values. In both cases, both pullout capacity and stiffness increase as the relative magnitudes of either the anchor or the soil moduli are augmented (Figure 9-10). Pullout stiffness increases as the stiffness of the entire system is amplified, and solely the moduli ratio is not sufficient in determining

the elastic response. For the pullout of plate anchors, soil modulus was shown to have negligible impact on pullout capacity (Mokhbi et al. 2017); however, for root-inspired anchors, an increase in pullout capacity with both soil and anchor moduli is expected due to greater soil disturbance with a more rigid system, as demonstrated in Figure 9-11, which demonstrates the effect of anchor flexibility on soil displacement. To note, within the simulation, the soil is given a homogeneous elastic modulus, while in both the 1g pullout tests and in the field, the elastic modulus of the soil is expected to increase with depth.
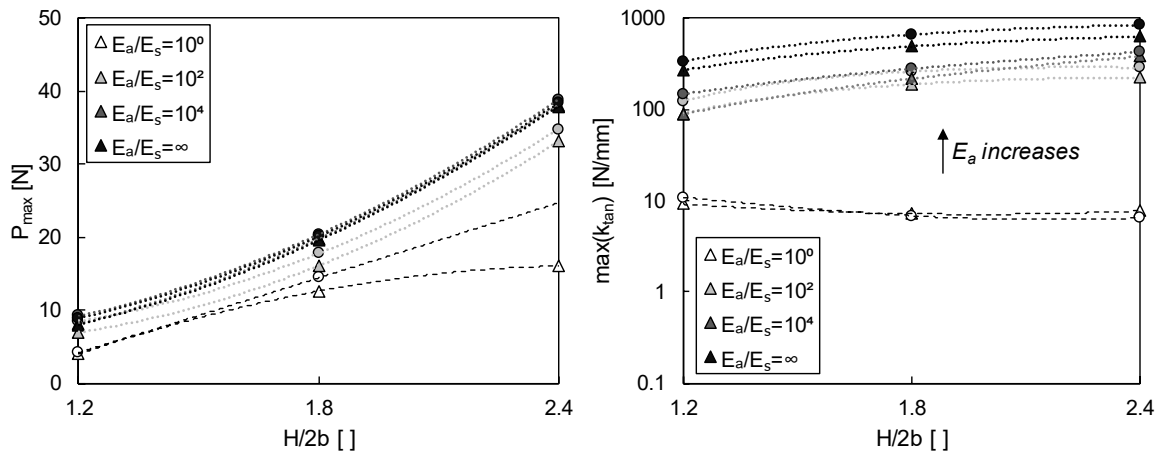
Figure 9-8. Effect of anchor-to-soil modulus ratio, E_a/E_s, on pullout behavior of root-inspired anchor of constant soil elastic modulus, (E_s=15MPa).
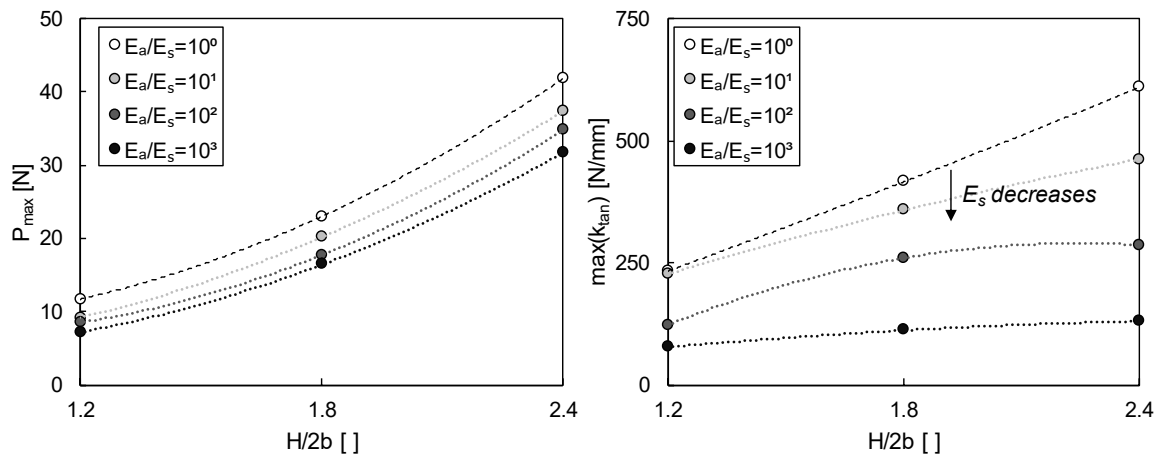
Figure 9-9. Effect of anchor-to-soil modulus ratio, E_a/E_s, on pullout behavior of root-inspired anchors with constant anchor elastic modulus, (E_a=1500MPa).
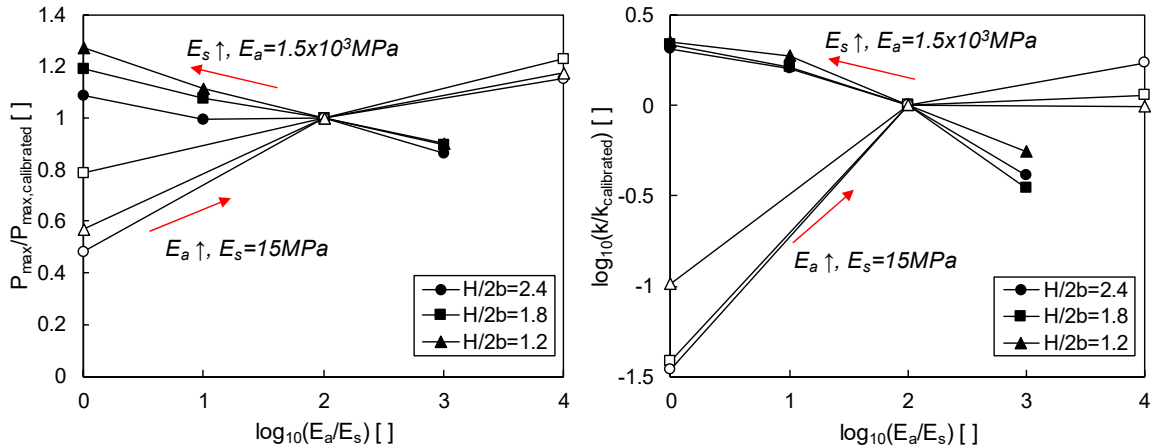
Figure 9-10. Additional illustration of the effect of both magnitude and ratio of the elastic moduli of the anchor and soil on pullout behavior, where pullout behavior indices are normalized by the values when E_a=1500MPa and E_s=15MPa.
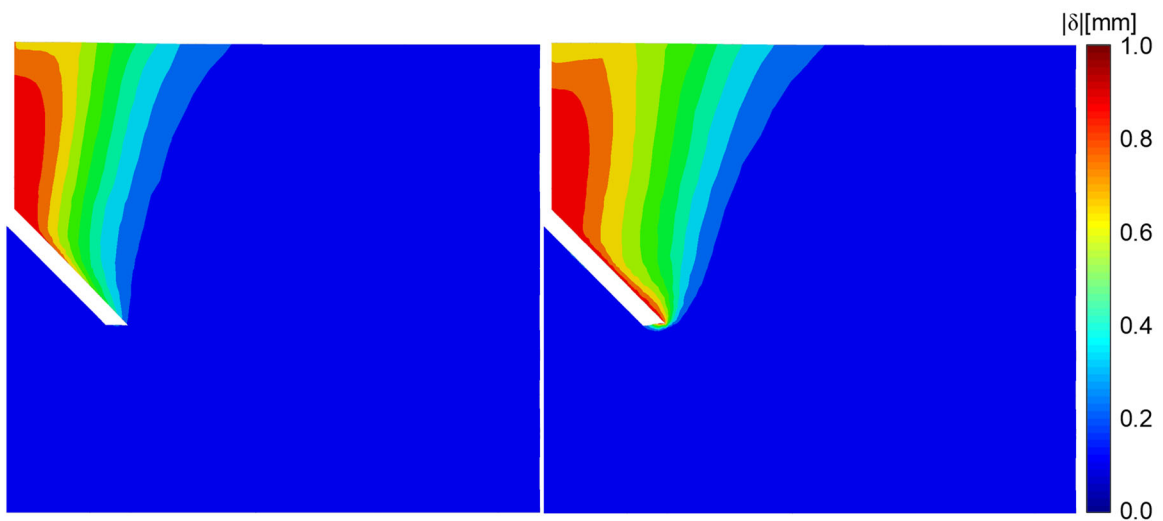
Figure 9-11. Magnitude of displacement field at 1mm of vertical displacement for a flexible, E_a=1500MPa, (left) and a rigid, E_a=∞, (right) anchor at a radial slice through soil and anchor.

9.3.4   Effect of Initial Lateral Earth Pressure Coefficient, K_0

The initial state of stress within the soil was varied between the upper and lower limits to the lateral earth pressure coefficient (i.e. $K_{passive}$ and K_{active}). No significant change in pullout capacity was achieved by varying the initial stress condition, as displayed in Figure 9-12 and previously documented in *Rowe and Davis 1982*. In addition, a greater

300

initial horizontal stress allows for a more immediate pullout response, resulting in a greater

maximum tangent stiffness with intial lateral earth pressure coefficient.
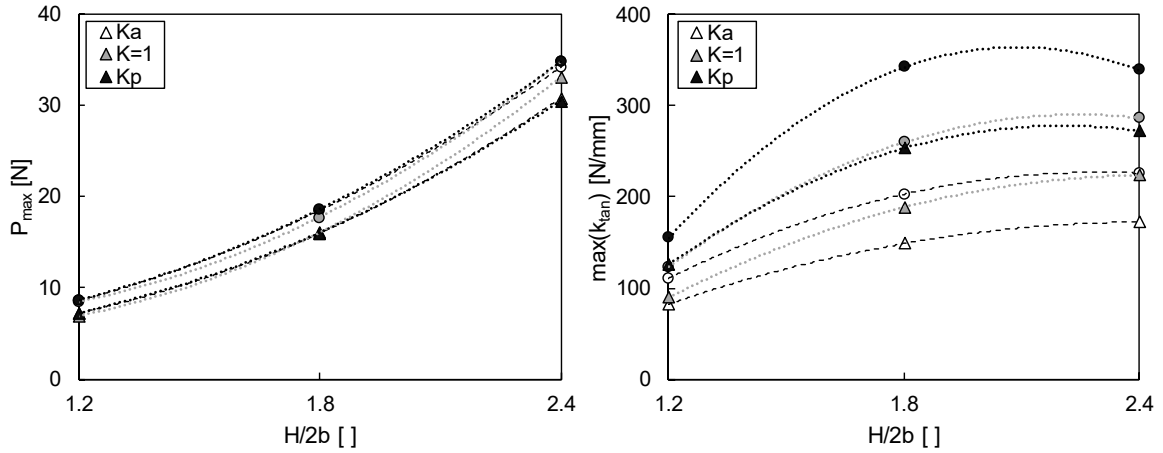
Figure 9-12. Effect of the initial stress state as defined by earth pressure coefficient on the pullout response of models of constant width, *b*=25mm.

9.3.5   Effect of Interface Friction Angle, δ

While the interface friction angle only marginally affects pullout capacity, a more

noticeable effect is observed for the case of maximum tangent stiffness (Figure 9-13). A

higher interface friction angle allows for a more immediate soil resistance response at the

soil-anchor interface causing a perceivable increase in pullout stiffness.
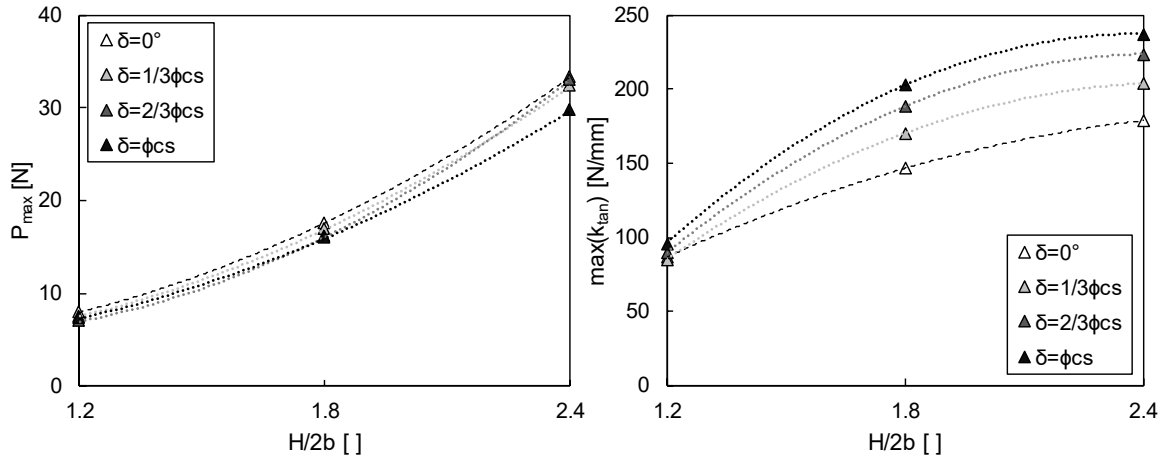
Figure 9-13. Effect of interface friction angle on the pullout response of models of constant width, *b*=25mm.

9.4   Conclusions

The numerical modeling of root-inspired anchor uplift provided the following conclusions:

- A plate anchor calibrated, finite volume, uplift model allowed for the validation of the trends in the experimental pullout response of root-inspired anchor models as well as for the insight into the effect of various properties of the soil-anchor system on pullout behavior.

- Pullout capacity, interpreted from a linear regression of the pullout resistance-displacement curve with an exponential decay model, is enhanced through the increase in both the friction and dilation angles, and a stiffening of the soil-anchor system, while the interface friction angle and initial stress state contributes negligibly.

- Dilation angle, a descriptor of the plastic volume change, controls the extent of the disturbed soil volume and as such, influences both the pullout capacity and maximum tangent stiffness.

- Anchor pullout stiffness, as represented by maximum tangent stiffness, is a system response, where the value is significantly dependent upon the elastic modulus of both the soil and anchor as well as the geometry of the anchor. Additionally, properties of the soil, including the friction and dilation angles, the initial lateral earth pressure coefficient, and the interface friction angle, all act to increase the maximum tangent stiffness.

Special Recognition: Professor Jean-Michel Pereira for his guidance and helpful discussions during my stay at École des Ponts ParisTech.

CHAPTER 10.   ADDITIONAL FACTORS INVOLVED IN THE

PULLOUT OF ROOT-INSPIRED ANCHOR MODELS

This chapter presents a collection of supplementary experimental studies that contribute in the comprehension of the mechanics of root-inspired anchor pullout behavior. In particular, the role of anchor model topology, surface roughness, and material stiffness on pullout response is evaluated. Following, a series of pullout tests were performed to explore the scalability of root-inspired anchor models in terms of their pullout behavior and associated pullout mechanisms.

10.1 Topological Order

Root system topology defines the connections between root system axes. The role of anchor model topology on pullout behavior is investigated by performing uplift tests on root-inspired anchor models of varying topological order. Generally, topological analyses of root systems are reserved to assess nutrient acquisition and transport efficiency (Fitter 1987, Bernston 1997); however, topology descriptors, including maximum pathlength and percentage of higher order axes, positively correlate with pullout capacity (Wu et al. 1988, Dupuy et al. 2005, Mickovski et al. 2007). As a preface, topology is an incomplete description of the geometry of a root-inspired anchor model, and the effects of topology on pullout response are therefore not exclusively due to topology. In this study, the effect of root-inspired anchor model topological order on pullout behavior is assed, where topological order, also known as generations, describes the degree to which an initial root axis bifurcates into root axis subsets, schematically represented in Figure 10-1.

Mathematically, topological order is determined as the average pathlength of the anchor model topology initiating at the soil surface node. For all models, the topological order is equivalent to the topological altitude, which is the maximum pathlength.
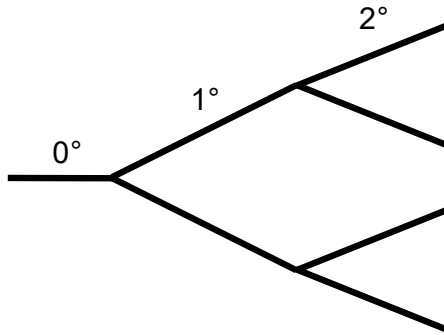
Figure 10-1. Schematic representation of topological order illustrating order 0°, 1°, and 2° branching.

10.1.1 Topology-Type Root-Inspired Anchor Models

Topological order is incorporated into two distinct root-inspired anchor models, 1) a wire model, and 2) a 3D printed model, shown in Figure 4-5 and fully described in Chapter 4. For the wire-type models, galvanized steel and LDPE wires are unraveled at varying levels of braiding, where order 0 branching corresponds to the unraveled wire rope, order 1 the outer strands are unraveled, and for order 2, all individual wires are unraveled. For the additive manufactured models, solely 1° and 2° models are fabricated, and the models retain a 3:1 bifurcation ratio for each increase in topological order, where the ratio refers to the number of daughter axes per parent axis.

10.1.2 Pullout Response of Wire Rope Anchor Models

Pullout behavior indices extracted from uplift tests performed on wire rope root-inspired anchor models are displayed in Figure 10-2, where "P" symbolizes the

polyethylene models, "S" the steel models, and "H" the embedment depth. Pullout capacity perceptibly increases with depth and topological order. The width of the root-inspired anchor model is inherently enlarged with the unraveling of the wire rope at progressive degrees of branching, which enhances pullout capacity due to the larger mobilized volume of soil. As well, a transition in the governing failure mechanism occurs between 0° and 2° topological models, where a failure surface occurs at the soil-model boundary for order 0 models and transitions to a full conical failure surface for order 2 models as evident by x-ray CT imaging. No variation in pullout capacity is distinguishable among the LDPE and steel wire models at the tested stress levels. For displacement at failure, a relative increase is observable for 1st order branching models. As an acting hypothesis, the relatively few model branch axes of 1° models compared with 2° models reduces particle confinement and allows for a greater mobilization of sand particles before a failure surface is formed. Additionally, the trends in the displacement compatibility indices, failure displacement and maximum tangent stiffness, remain constant or of negligible difference between the two material types, despite the significant difference in elastic moduli. The maximum tangent stiffness reflects the influence of increasing soil stiffness with depth, where generally stiffness increases with model embedment. Finally, due to constant model volume with topological order, material efficiency index increases with topological order by the same trend and reasoning at pullout capacity.
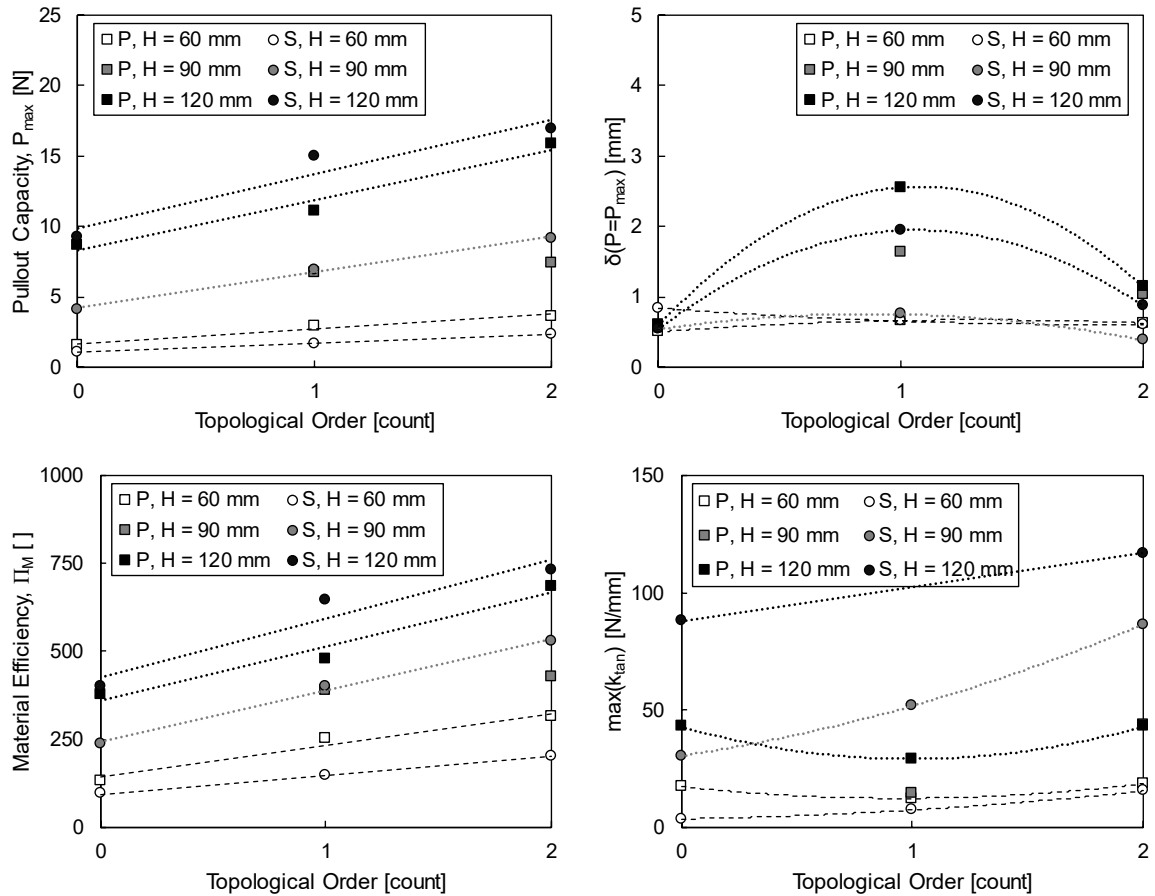
Figure 10-2. Pullout behavior with topological order of topology-type root-inspired anchor models.

10.1.3 Pullout Response of Additive Manufactured Topology-Type Anchor Models

The results of the pullout tests performed on the 3D printed topology-type anchor models are presented in the form of pullout behavior indices shown in Figure 10-3. The depth and width of the models is set at 90mm and 25mm for all models, respectively. Pullout capacity and pullout factor increase with topological order, which indicates that the size of the failure surface expands with an increase in topological order due perhaps to an increase in the critical failure surface intersection ratio, f, and/or a reduction in the spacing gap for soil arching. The trend however is reversed for the material efficiency index since a significant volume of material is added with additional branching orders. Models with

307

2nd order branching do attain higher maximum tangent stiffness values perhaps due to the higher initial load on the model during sample preparation. No clear trends in failure displacement are noticed.
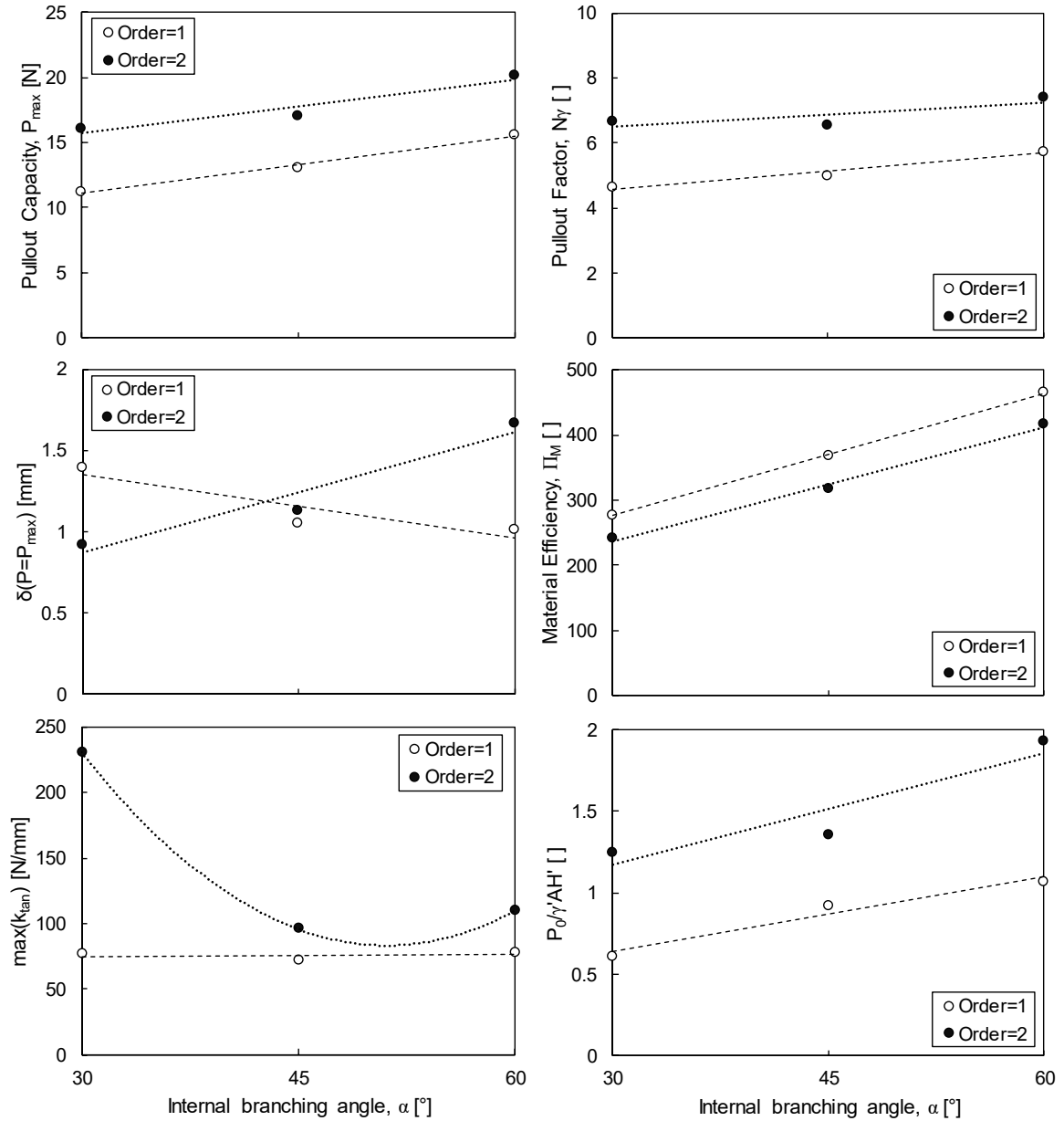
Figure 10-3. Pullout response of root-inspired anchor models with 1st and 2nd order branching.

10.2 Interface Shear Behavior of the Particle-3D Printed Plastic System

This section seeks to describe and investigate the interface shear response at the sand-additive manufactured polymer interface. The intent of this research is twofold, 1) to characterize the interface shear response between 3D printed polymer surfaces and coarse-grained soils from a broad context, and 2) to investigate the role of surface roughness and interface shear on the pullout of root-inspired anchors. The interface shear behavior between these two systems is assessed through two experimental methods, 1) interface direct shear tests between sand and 3D printed surfaces, and 2) pullout tests of root-inspired anchor models with varying surface roughness.

10.2.1 Shear Response of the Geomaterial-3D Printed Plastic Interface

10.2.1.1 Introduction

With the growing utilization of 3D printed materials in geotechnical engineering, characterization of the geomaterial-3D printed surface interface shear behavior, in particular the interface friction angle, is mandatory for mechanical analyses. This section investigates various factors affecting interface shear strength including additive manufacturing printing settings, object parameters, material properties, and geomaterial particle properties.

The assimilation of 3D printing technology into geotechnics has been rapid due to the ubiquity, economics, and utility of commercial 3D printers. Examples of the implementation include the additive manufacturing of geomaterials (Hanaor et al. 2016, Wang et al. 2017), geogrids (Fowmes et al. 2017, Stathas et al. 2017) and soil testing devices (Marks et al. 2016, Yuan et al. 2016, Chow and Wang 2017, Baker et al. 2018). Additive manufacturing allows the user to fabricate a three-dimensional, computer

generated object both quickly and economically. 3D printing is a rapidly advancing field that is currently comprised of various manufacturing methods, including fused filament fabrication (layers of melted filament), stereolithography (layered polymer cured by UV), and powder bed fusion (sintering of granules). For the purpose of this research, fused filament fabrication is the method of focus. The bulk mechanical properties of the resultant printed object are dependent not only on the filament material selection but also the machine settings and printing parameters, including extruder type, temperature settings, deposition speed, layer height, infill settings such as percent infill, orientation, and pattern, and shell settings such as shell thickness and orientation (Giordano et al. 1996, Ahn et al. 2002, Rankouhi et al. 2016, Dizon et al. 2017). In particular, the angle between the mechanical loading direction and the relative orientation of the filament layers can lead to substantial differences in the mechanical properties of the fabricated structure (Rodriguez et al. 2001, Letcher and Waytashek 2014, Rankouhi et al. 2016).

10.2.1.2 <u>Geomaterial Particle-Polymer Surface Interface Shear Behavior</u>

Interface shear response refers to the largely mechanical frictional response as two materials are displaced relative to each other with some applied contact force. Frictional behavior is governed by Amonton's laws of friction, which apply to dry, static cases and state that, 1) the shear force, F_{shear}, is directly proportional to the normal force, F_{normal}, through the proportionality constant, the coefficient of friction, μ, (Equation 72) and 2) the coefficient of friction is independent of the contact area.

$$F_{shear} = \mu F_{normal} \tag{72}$$

For dry materials, the shear force required to elicit relative interface displacement is due to adhesion in the form of intermolecular and surface forces as well as resistive forces due to physical geometric impedances (i.e. asperities), where the role of intermolecular and surface forces diminishes with increasing particle size. For the case of sliding at the geomaterial-polymer interface, the shear force additionally includes the resistance to form plastic deformations, known as plowing.

The shear response of the geomaterial-polymer interface is dependent upon the interplay between the characteristics of the geomaterial particles (e.g. particle shape, particle size, hardness, elastic modulus) and the polymer continuum (e.g. surface roughness, hardness, yield strength, elastic modulus). In general, larger interface friction angle values are expected with rougher surfaces up until the particles interlock with the surface, and the interface friction angle plateaus with increased roughness (Uesugi and Kishida 1986, Frost and DeJong 2005). The ability of the geomaterial to interlock with the polymer surface is dependent upon the shape and size of the particles relative to the surface morphology. In addition, the hardness ratio between the geomaterial and polymer surface is particularly important at higher normal stresses, where an increase in interface friction angle is expected due to plowing (O'Rourke et al. 1990, Frost et al. 2002). Once the concentrated particle normal stress exceeds the yield strength of the surface plastic damage begins, and the magnitude of surface damage and consequently the growth in interface friction angle is magnified in softer surfaces. More so, the resistance to plastic deformation increases exponentially with the polymer surface-to-particle hardness ratio (Stachowiak and Batchelor 2013). Furthermore, the interface shear response of geomaterials and various other infrastructure-related continuum surfaces (e.g. concrete, wood, polymer, steel) has

been shown to oppose Amonton's laws of friction, where the interface friction angle is stress and contact area dependent. Beyond the stress-dependency effects of plowing, most interface shear behavior involving particulate media encompasses a diminishing interface shear strength with increased normal stress (Archard 1957, Stark et al. 1996, Dove and Frost 1999). With increased normal stress, the number of contacts and the individual particle contact areas (i.e. Hertzian contact) increases, where the ratio of normal load to contact area is dependent upon the geometry and elastic moduli of the materials in contact. More so, the particle-polymer interface direct shear response is affected by both moisture (e.g. 3D printed polymers mechanical properties decline with moisture) and temperature (e.g. polymer hardness decreases with temperature) effects (Frost and Karademir 2016). Furthermore, conventional geotechnical interface direct shear testing is performed at low displacement rates ($\sim$0.1-5mm min^{-1}), and the resultant shear response is a product of the stick-slip mechanism, where both static and dynamic frictional processes occur. In general, larger shear forces are generated through static friction, where greater work is required to initiate movement.

10.2.1.3 Interface Direct Shear Tests

Approximately 80 interface direct shear tests were performed between 3D printed polymer surfaces and two Ottawa silica sand specimens (i.e. Ottawa F110 and Ottawa 20-30). The sand specimens were air pluviated to a relative density of 67% and 80% for the Ottawa F110 and 20-30 specimens, respectively. Normal stress was varied between 25 and 400kPa, and all tests were displacement rate controlled at a constant rate of 1mm min^{-1}. A small gap between the aluminum soil box and testing surface was applied during specimen preparation; however, the soil container was not rigidly fixed and was free to move in the

vertical direction, which aided to minimize post-peak shear force accumulation due to particle kinematic restraint. Due to the temperature-dependent shear response of polymers (Frost and Karademir 2016), tests were conducted at a relatively constant temperature between 21-23°C. The characteristic interface shear response between Ottawa 20-30 sand and smooth ABS for three different normal stresses is displayed in Figure 10-4, which is plotted in terms of the secant interface friction angle (Equation 73) and horizontal displacement. The complete experimental information is detailed in Chapter 4.

$$\delta_{\text{sec},i} = \tan\left(\frac{F_{shear,i}}{F_{normal,i}}\right) \tag{73}$$
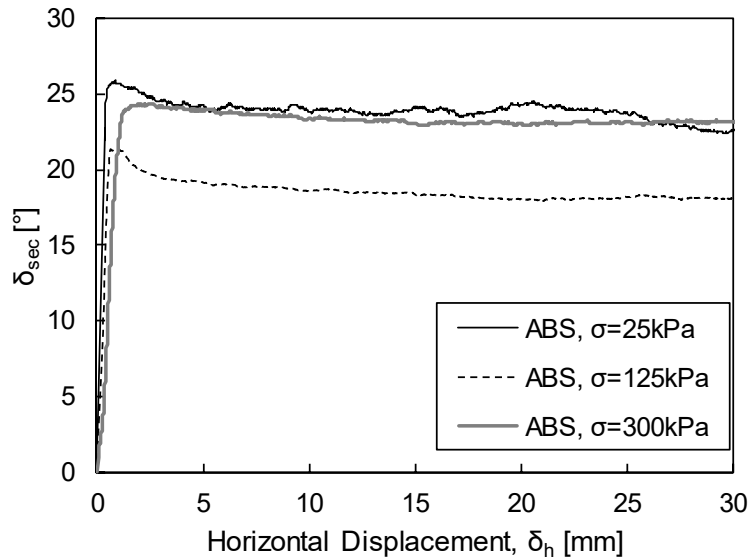
Figure 10-4. Secant Ottawa 20-30 sand-3D printed ABS interface friction angle with horizontal displacement for smooth 3D printed ABS surfaces with varying normal stress.

10.2.1.3.1 Effect of Surface Hardness

In the first set of tests, the interface shear response between Ottawa 20-30 silica sand and 3 surfaces, two smoothed additive manufactured polymer surfaces (i.e. HIPS and ABS) and one stainless steel plate. The peak shear stress is plotted versus normal stress from each test (Figure 10-5) and an interface friction angle is determined through a least squares regression of Equation 74. The best-fit interface friction angle for the current studies as well as previous studies is documented in Table 10-1 along with relevant Shore D Hardness (ASTM D2240) values and then plotted in Figure 10-6. For the 3D printed smoothed ABS and HIPS surfaces, the interface direct shear tests oppose the general interface friction angle-hardness trend; however, surface morphology measurements need to be gathered for a proper comparison, since surface roughness is assumed to be equivalent. To illustrate the stress- and contact area-dependency as well as the effects of plowing, peak secant interface friction angles are plotted with normal contact stress (Figure 10-7). Both ABS and HIPS surfaces demonstrate the initial reduction in peak secant friction angle with normal stress up until the plowing transition point, when plastic damage begins to substantially influence the shear behavior. Additionally, for the interface direct shear tests performed with steel surfaces, a "plowing-like" behavior is also observed with large normal stresses, which perhaps suggests additional mechanisms (e.g. soil container contact, repeated surface wear) are occurring since surface plowing is unlikely.

$$\tau_{peak} = \tan \delta_{peak} \sigma_n \qquad (74)$$
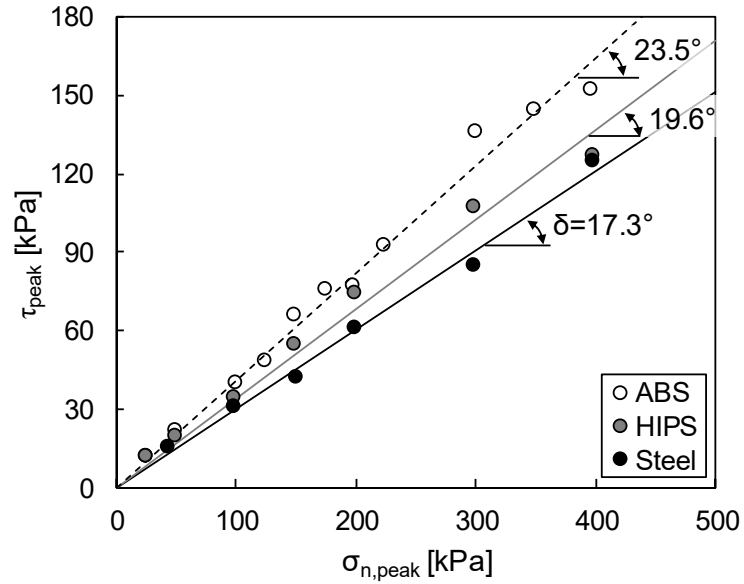
Figure 10-5. Peak shear stress versus normal stress for interface direct shear tests between Ottawa 20-30 silica sand and ABS, HIPS, and stainless steel.

Table 10-1. Tabulated Shore D Hardness values (mean and standard deviation) and average secant interface friction angles for various polymers with Ottawa 20-30 sand.

Material	Hardness (Shore D)		δ [°]
	μ	σ	
ABS	80.1	1.14	23.5
HIPS	75.7	1.17	19.6
HDPE	59.1[a]	0.73 [a]	22.2[a]
PVC	32.2[b]	0.58[b]	38.4[b]

a) Dove and Frost 1999, b) Frost and Karademir 2016
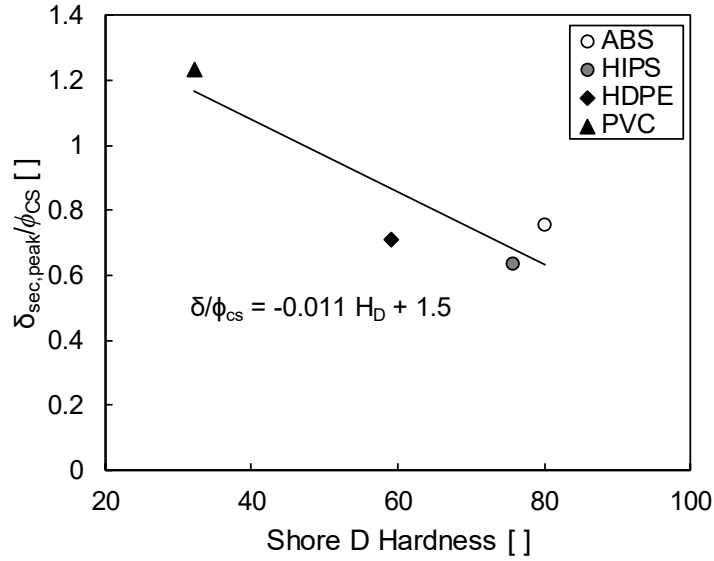
Figure 10-6. Geomaterial-polymer peak interface friction angle normalized by the geomaterial critical state friction angle versus polymer hardness (HDPE and PVC values from Dove and Frost 1999 and Frost and Karademir 2016, respectively).
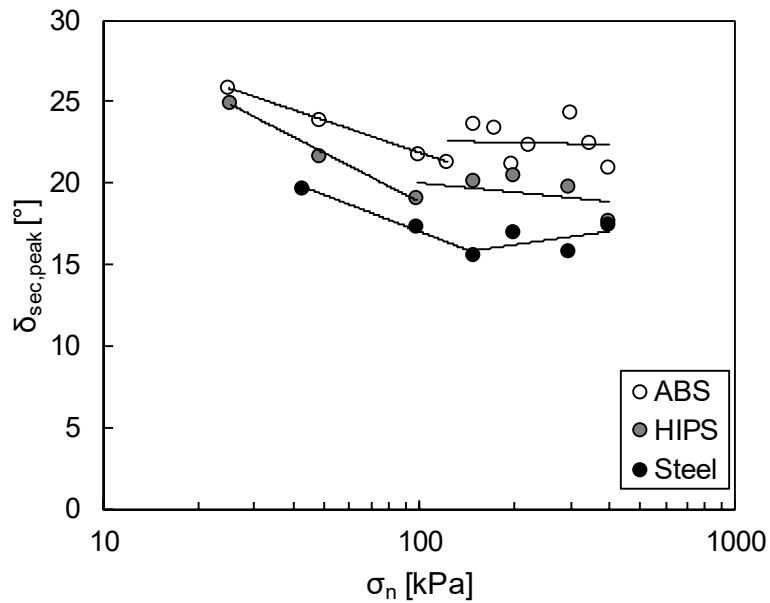
Figure 10-7. Peak secant interface friction angle between Ottawa 20-30 silica sand and ABS (3D printed), HIPS (3D printed), and stainless steel surfaces at various normal stresses.

10.2.1.3.2 Effect of Orientation - Filament Deposition and Shearing Directions

With fused filament fabrication, the orientation of deposited filament relative to the orientation of mechanical loading is critical to the mechanical behavior of the structure. The orientation of the deposited filament is dependent upon both the build orientation (i.e. the orientation of the 3D object on the build plate) and the raster angle (i.e. the angle in which a single polymer layer is deposited relative to the orientation of build plate). For this particular study, the filament-shearing orientation angle, θ, is varied by altering the raster angle of the outer deposited filament layers while the build orientation is kept constant (Figure 4-9). Unlike the previous study on the effect of surface hardness, all ABS surfaces utilized in this study are unaltered after printing.

Overall, the peak secant interface friction angle between 3D printed ABS surfaces and both Ottawa F110 and 20-30 silica sands increases as the relative angle between the deposited filament orientation and the direction of shearing is gradually varied in 15° increments from 0° to 90° (Figure 10-8). At an orientation of 0°, the deposited filament is parallel to the direction of shearing, and the sand particles experience a relatively smooth surface. Even though the particles trajectories are expected to be confined to the groves between adjacent filament deposits, the 0° case offers the least resistance to shearing. With a gradual increase in θ from filament deposits parallel to perpendicular to the direction of shearing, the increase in interface friction angle is explained by the gradual reduction in the gap between filament deposits (i.e. a greater percentage of particles are subjected to more immediate surface obstacles) and the particle kinematics are gradually constrained. Additionally, the largest changes in peak secant interface friction angle occur from 0° to

15° and from 75° to 90°, which emphasizes the importance of particle kinematic flexibility on interface shear response.
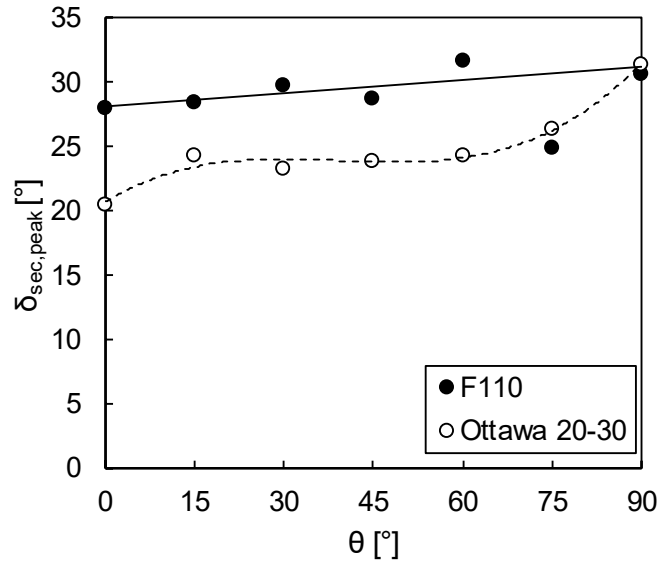
Figure 10-8. Peak secant interface friction angle with varying printing orientation relative to shearing direction for the ABS-Ottawa silica sand interface.

10.2.2 Effect of Surface Roughness on Pullout Behavior

This section seeks to clarify the role of surface roughness and associated interface shear behavior on the pullout behavior of root-inspired anchor models. More specifically, as hypothesized in Chapter 7, this section seeks to expose the effect of surface roughness on magnitude of the critical failure surface intersection ratio and whether surface roughness influences where the failure surface nucleates along the length of the model branching axes.

The effect of surface roughness on the pullout response of root-inspired anchor models is evaluated comparing the pullout behavior of three steel root-inspired anchor models with varying surface roughness (Figure 10-9). "Rough" is in reference to models with a single layer of Ottawa F110 sand particles glued to the model surface, whereas

"smooth" refers to an un-corroded steel surface. The interface friction angle for the rough surface approaches the friction angle of the sand, while the smooth interface is substantially lower, on the order of 21°. Despite the large discrepancy in peak interface friction values, the pullout capacity and corresponding pullout factor for both the smooth and rough cases demonstrate an almost imperceptible variance, where the percent change from the rough case is less than 1%. More so, all pullout behavior indices demonstrate minute changes with varying surface roughness with the notable exception of displacement at pullout capacity. A significant reduction in failure displacement, on the order of 1mm, is perceived for the rough surface, which implies that some degree of particle movement along the anchor model surface occurs before the particles are engaged in the surface.
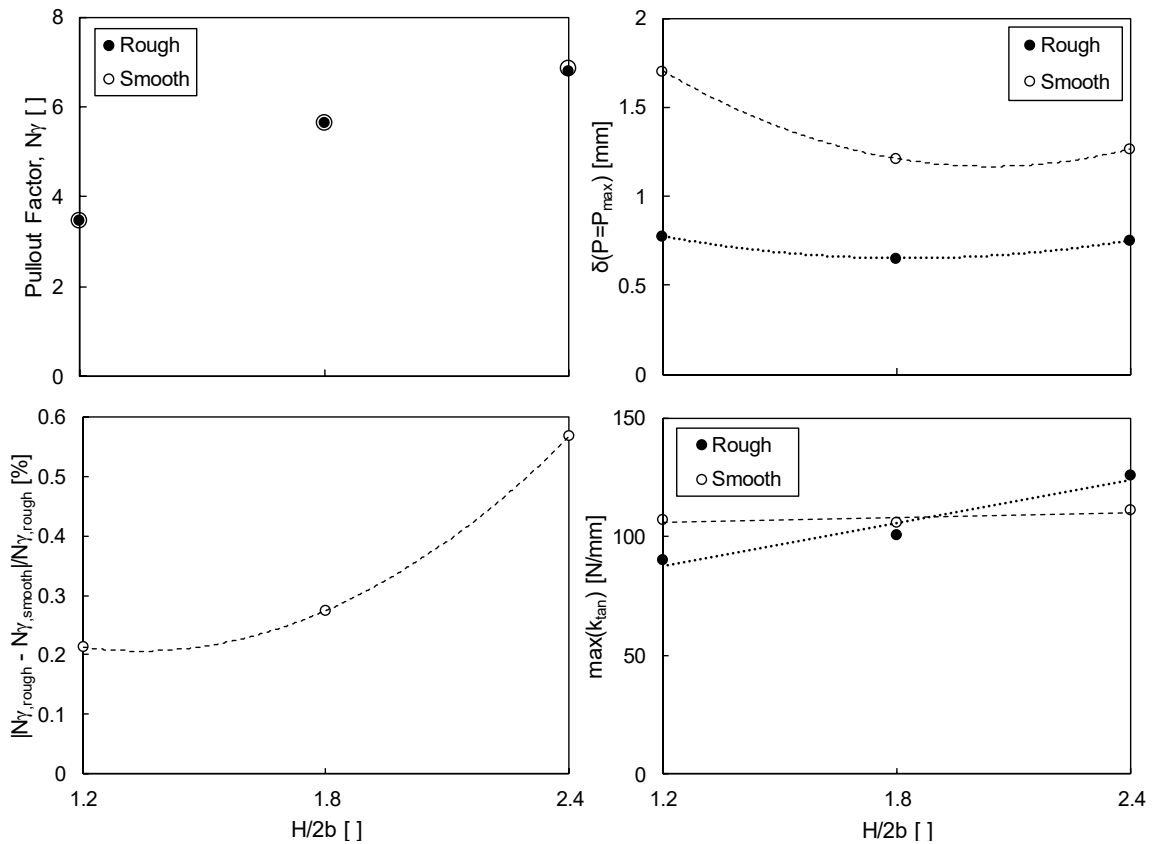
Figure 10-9. Effect of surface roughness on pullout behavior.

319

10.3 Material Stiffness

This series of tests exposes the role of model stiffness on pullout behavior. Three steel models with geometries similar to the 3D printed models were fabricated and tested. The model geometric features were selected to maximize model stiffness differences between models fabricated of ABS and steel (Table 10-2). In particular, only models with three branch axes were tested, while the depth-to-width ratio was altered. As well, a single layer of F110 particles were glued on the surface of steel models and tested to ensure that interface properties did not dominate the pullout response. Whereas additive manufacturing produces prototypes with 0.18mm of accuracy, the machined steel models though similar, were visibly irregular and distorted, particularly around the point of dichotomy. Consequently, differences in pullout capacity and pullout factor between the steel and ABS models are not strongly accepted (Figure 10-10). However, the variances in displacement at pullout capacity and maximum tangent stiffness among the two types of models are recognized, particularly due to the observed linear trends for the steel models. As revealed in Chapter 6, displacement at pullout capacity is strongly affected by model stiffness, where increased failure displacement values occurred for both models with longer branch axes and at deeper embedments. Consequently, the steel models highlight the importance of the model-to-soil stiffness ratio even more, since failure displacements remained relatively constant for all steel models. For both material types, maximum tangent stiffness increases with depth due most likely to the increased soil stiffness with depth; the rate at which pullout stiffness increases with depth is far greater for the ABS models.

Overall, the results from this set of experiments highlight the significance of the soil-to-model stiffness ratio on the global pullout behavior. Whereas displacement at pullout capacity was strongly dictated by model stiffness and maximum tangent stiffness by soil stiffness for ABS models, both displacement compatibility indices were dominated by the model stiffness for steel models. As such, the stiffness ratio must be considered in the scaling of root-inspired anchors, particularly in the selection of anchor material as well as the exponential increase in soil stiffness with depth.

Table 10-2. Geometric features of models tested to investigate the effect of model stiffness.

Model No.	n [count]	α [°]	H [mm]	L [mm]	$H/2b$ [ ]	Variable
1	3	30	90	50	1.8	--
2	3	30	90	75	1.2	Length
3	3	30	120	50	2.4	Depth
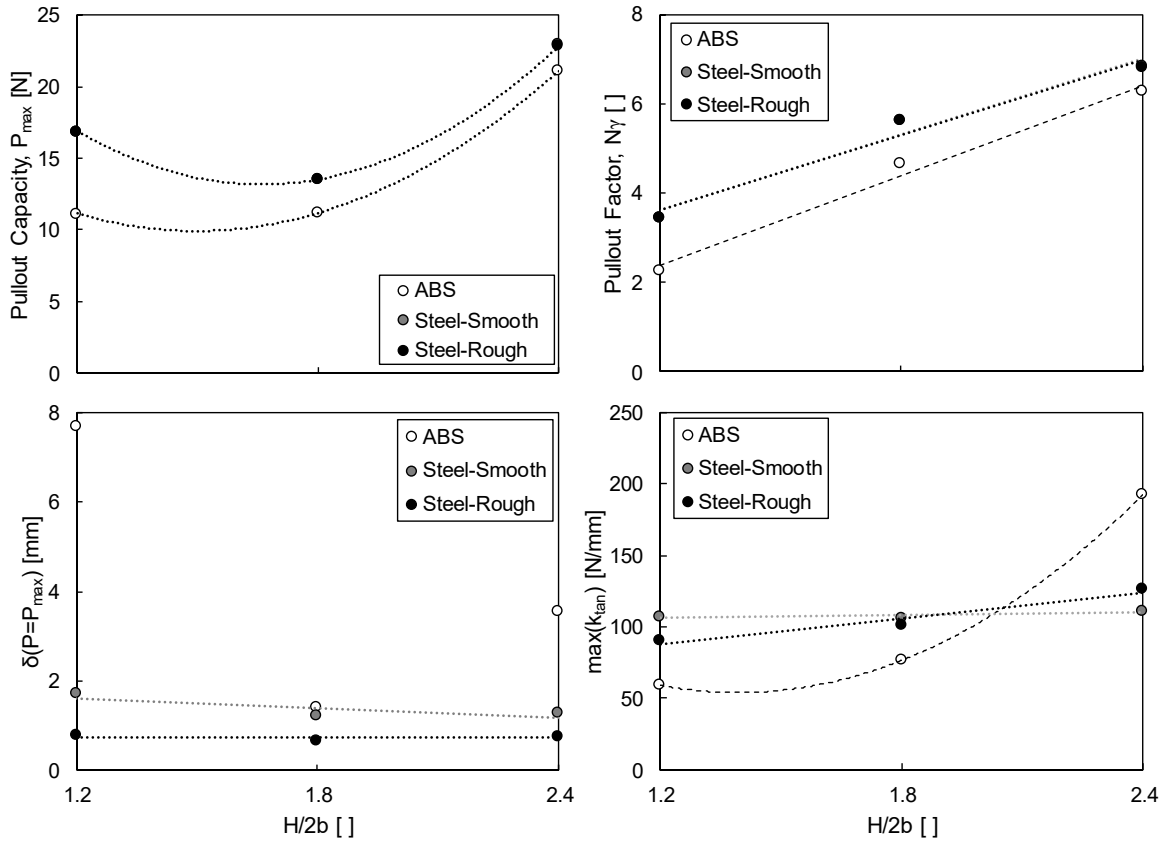
Figure 10-10. Pullout behavior indices with depth-to-width ratio for models of varying model material.

10.4 Geometric Scaling

The purpose of this section is to provide initial insights into the scaling of root-inspired anchor models, with particular interest in the scaling of the failure mechanism as represented by pullout behavior indices.

10.4.1 Scaling Models

For this section, both allometric (i.e. anisotropic, scaling that deviates from isometry) and isometric (i.e. uniform scaling) geometric scaled models (Figure 10-11) are evaluated in pullout. Table 10-3 documents the selected geometric scaled root-inspired anchor model features utilized in pullout testing. For the allometrically depth scaled models, the portion

of the root-inspired anchor model below the point of dichotomy remains the same, while the stem length is increased. The overall depth is scaled by 1, 1.33, and 1.67 times. Isometric scaling, the second type, refers to the equal scaling of all components in all directions, and with this scaling method, the model feature ratios remain constant. For this set of experiments, the depth-to-width ratio is fixed at 1.8, while the isometric scaling factor varies from 1 to 2 in increments of 0.25.
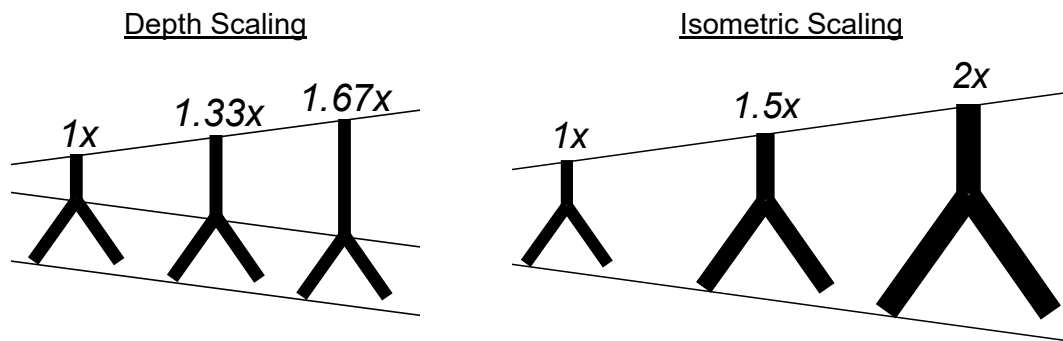
Figure 10-11. Schematic comparison of allometric depth scaling and isometric scaling.

Table 10-3. Geometric features of scaling models tested, including magnification scaling factors.

Scaling	n [count]	α [°]	H [mm]	$H/2b$ [ ]	Scaling [ ]
Depth	3/6	30/60	90/120/150	1.8/2.4/3.0	1/1.33/1.66
Isometric	3/6	30/60	90/112.5/135/157.5/180	1.8	1/1.25/1.5/1.75/2

10.4.2 Pullout Response

The resultant pullout behavior indices from scaled root-inspired anchor models are shown in Figure 10-12. For the models tested, a slight augmentation in pullout capacity values with depth is achieved for the isometrically scaled models, since the width of models is greater. Pullout factor with increasing isometric scaling factor reveals the stress-strain dependency of the strength of soils, where shallower models experience a greater rate of

dilation and corresponding peak shear behavior. Furthermore, depth scaling is preferential to isometric scaling in terms of pullout factor and material efficiency. As well, more obtuse internal branching angles are preferred in terms of both pullout factor and material efficiency. Additionally, the two scaling experiments illustrate the importance of model stiffness, in particular the stiffness of the branched section of the model, on displacement at pullout capacity.
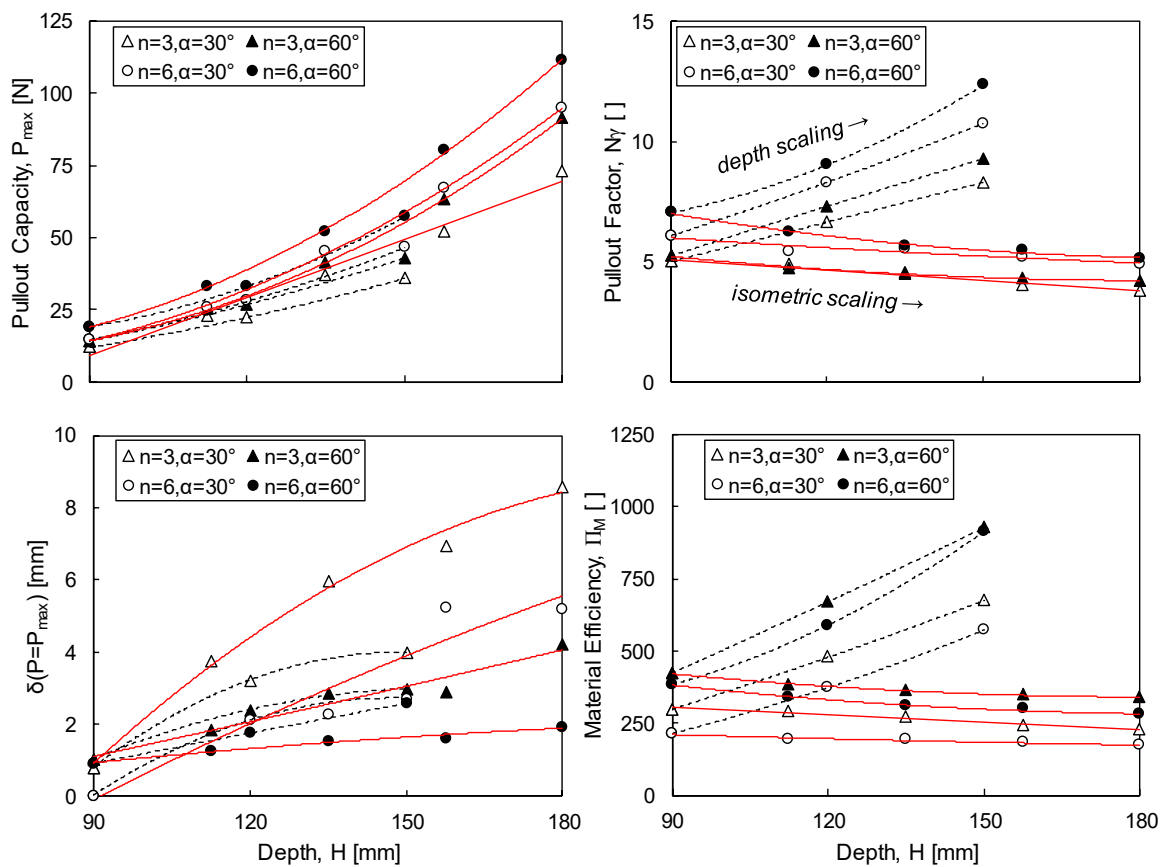
Figure 10-12. Pullout behavior indices with depth for two scaling methods (black dashed lines connect allometrically depth scaled models and red solid lines connect isometrically scaled models).

10.5 Conclusions

With greater design flexibility, comes increased outcome uncertainty and complexity. In comparison to conventional anchorage systems, root-inspired anchors offer a great deal of design freedom; yet as a byproduct, pullout behavior uncertainty increases exponentially due to both direct and combined feature effects. As a result, the purpose of this chapter is to confine to a greater degree the uncertainty in pullout behavior of root-inspired anchor models by investigating a small subset of the factors affecting pullout response (i.e. topological order, surface roughness, material stiffness, scalability). Analyses of pullout tests performed to realize the effects of topological order, interface friction, material stiffness, and geometric scalability on pullout behavior revealed the following seminal conclusions:

- Topological order, a measure of generational branching, enhances pullout capacity due to the development of a more complete conical failure surface and highlights the dependency of pullout factor and material efficiency indices on a geometric model description.

- The interface shear response, in terms of the secant interface friction angle with normal stress, was documented for between Ottawa silica sand and 3D printed surfaces.

- For the models and soil conditions tested (internal branching angles between 30-60°, $\delta_{sec,peak}/\phi_{CS} \geq 2/3$), model surface roughness had no perceptible effect on pullout capacity; however, models with smoother surfaces required greater vertical displacements to reach pullout capacity.

- The filament deposition layers orientation

- With greater depths, allometric depth scaling is more material efficient than isometrically scaled models.

- Geometric scaling of root-inspired anchor models in pullout tests highlights the significance of the stress- and strain-dependent strength characteristics of particulate media.

CHAPTER 11.   APPLICATION AND SCALE-UP CONSIDERATIONS FOR ROOT-INSPIRED ANCHORS

Within this chapter, preliminary thoughts are provided to address feasibility and constructability concerns neglected thus far within this body of work. While bench-scale experiments and numerical simulations implementing "wished-in-place" elements are reasonable for initial studies demonstrating a proof-of-concept or for providing an initial conceptualization of the governing mechanisms, as the study matures, clarification of the upscaling process is mandatory if the purpose of the research is to develop a functioning physical structure. While the method of fabrication and installation, which is still unknown, will undoubtedly affect the behavior of the root-inspired anchorage elements, the effects are purely conjectural and should not constrain the further development of root-inspired anchors. Furthermore, by discussing feasibility, the research is transported from the level of fundamental science to applied engineering, where the act of defining an application removes the cloak of abstractedness. Consequently, the transformation of root-inspired anchors from benchscale models to field scale ground anchors, capable of replacing conventional tieback and tiedown systems in specific site and soil conditions, is explored. The purpose of this chapter therefore is to distill the results of this entire body of research to provide preliminary guidelines for the design of a root-inspired ground anchor. Conventional ground anchorage systems will be described in terms of their purpose, design, installation, testing, and service, and following, various ideas will be presented on ways in which root-inspired anchorage elements might satisfy the demands imposed on conventional anchors.

11.1 Conventional Ground Anchors

A synopsis of tieback and tiedown design, installation, and testing is provided. As a preface, only the design of the ground anchor element is discussed, the design of the primary anchored infrastructure (e.g. retaining wall, dam, foundation), including acting forces, is neglected.

11.1.1 Description and Purpose

Ground anchors are linear, embedded, tensile elements that utilize the shear strength of the soil to provide a supplementary resistance to the primary structure, where the term ground anchor for this chapter will refer to both tiebacks and tiedowns. The anchored infrastructure (e.g. retaining wall, grade separation system, transmission tower, dams) are generally subjected to forces that cause an outwards displacement from the soil surface. The primary difference between tiebacks and tiedowns is the orientation, where tiebacks tend towards the horizontal while tiedowns are more vertically orientated, though both typically have some degree of tilt or inclination. A ground anchor is comprised of two main components, 1) a threaded bar or strand tendons, and 2) grout. As well, ground anchors generally are composed of a grouted bond and unbonded length, which is dependent upon the potential failure modes, such that bond length extends beyond the failure surface into competent soil.

11.1.2 Design

The principal objective of ground anchor design is to ensure the required factor of the safety of the primary structure by specifying an anchor of adequate bond length as to

provide the necessary supplemental resistance to failure. In the design of a ground anchor, both the failure of the anchor itself as well as the primary structure are considered. The primary modes of failure of the ground anchor include tensile failure of tendon/bar, shear failure of tendon/bar-grout interface, and shear failure of grout-soil interface. The failure modes of the primary structure is inherently infrastructure dependent, and a retaining wall, for example, is analyzed in terms of the wall failure (i.e. bending, rotation, and axial capacity) and global failure (i.e. sufficient passive rotation, overturning, and sliding).

11.1.2.1 Factors of Safety

The relevant Factors of Safety for ground anchor design include the Factor of Safety against shear failure at the soil/rock-grout interface (Equation 75) and the Factor of Safety against anchor tendon or bar tensile failure (Equation 76).

$$P_{design} \leq \frac{P_{max}}{FS} \tag{75}$$

$$\sigma_{ult} A_{cross} \geq FS \cdot P_{design} \tag{76}$$

The design Factor of Safety values are dependent upon the acceptable risk of both the owner and contractor, the permanence of the structure, and the specific site conditions. Conventional values for the Factor of Safety against shear failure of the soil-grout interface is 2 and 2 to 3 for the rock-grout interface, and for the tensile failure of the anchor strand or bar, a Factor of Safety of 1.67 is standard (PTI 2004).

11.1.2.2 Pullout Capacity and Bonded and Unbonded Lengths

The required resistance of an anchor is determined by the forces acting on the primary infrastructure. For a retaining wall, the design load of the ground anchor is the resultant of the passive and active forces acting on the wall with an assumed earth pressure distribution. The bond length is based upon the shear force capacity of the grout-soil interface. Commonly in design, the shear strength of the soil-grout interface is referenced from a look-up table of average shear strength values per anchor and soil type, where an average shear strength based upon an assumed stress state and soil-grout interface friction angle is marginalized. Simplistically, the general equation for the pullout capacity, P_{max}, of a linear ground anchor is a function of the surface area of the bonded soil-grout interface and the average ultimate shear strength along the bonded length, $\tau_{ult,avg}$. (Equation 77), where d is the drilled diameter of the hole and L_{bonded} is the grouted bond length.

$$P_{\max} = \pi d L_{bonded} \tau_{ult,avg} \tag{77}$$

The required anchor design resistance is provided by the length of bonded region (Equation 78).

$$L_{bonded} > \frac{P_{design}}{\pi d \tau_{ult}} \tag{78}$$

Generally, the bonded length is not greater than 12m (Sabatini et al. 1999) due to diminishing returns in the transfer of anchor tensile load to shear resistance along the soil-grout interface. As well, several constraints are placed on the unbonded length, such that 1) the unbonded length must extend past the potential failure surface by 1.5m or height of the wall divided by 5, whichever is less, due to uncertainity in the location of the predicted

failure surface, and 2) the unbonded length cannot be less than 4.5m for tendons and 3m for bars due common losses in shear resistance during initial tensioning (PTI 2004).

11.1.2.3 Anchor-Structure Displacement Compatibility

Additionally, primary structures are subjected to displacement requirements, which is transferred to the ground anchor design specifications, for if the ground anchor displaces under a design load, the primary structure either accrues a loss in required resistance or displaces with the anchor. To minimize ground anchor movement, the effective stiffness of the ground anchor can be improved through increasing the cross sectional area of the tendons or rod and to place the bonded length in a stiffer soil or rock strata. As specified in Section 11.1.5, each ground anchor must satisfy both elongation and creep standards if the anchor is to be considered competent.

11.1.3 Materials

The principal component of ground anchors are the steel tendons or bars that directly transfer the load from the primary structure to the soil. To provide the adequate resistance and displacement compliance requirements, high yield strength steel is utilized, where standard suppliers include Nucor Skyline Steel or Dywidag Systems International. To ensure a sufficient service life, the steel members must have some form of corrosion protection, even for temporary structures, and the protective measures vary depending on anchor region, where in the bonded or unbonded zones. Often the unbonded region is protected by a grease filled plastic sheath, while the bonded region should be completely surrounded by grout. Soil resistivity or pore fluid pH is used to indicate the level of corrosion protection required, where high ionic concentrations, low resistivity values, and

significant sulfide presence (i.e. grout degradation) demands more stringent protection. Additionally, ground anchors located near salt or brackish water, coal ash deposits, soils with high organic content, peat, or landfill waste typically require greater corrosion mitigation. In terms of the grout, conventionally cement grouts are utilized, where strict control of the water-to-cement ratio is critical to achieve the required compressive strength and to provide a sufficient tendon/bar-grout bond strength. In the insertion of the anchor within the drilled hole, plastic centralizers are utilized to center the tendons or bars to ensure the grout is equally encompasses the anchor. Trumpets, are used for permanent structures to provide corrosion resistance between the bearing plate and grouted unbonded length. The connection varies between the anchor and the primary structure depending on whether strand tendons or threaded bars are used. For strand anchors, each tendon is fitted with a conical wedge that grips the tendon and prevents slippage upon insertion into the wedge plate during tensioning (Figure 11-1). For threaded rod anchors, a nut is used to lock the rod in place during tensions. In both cases, the bearing plates act to transfer the load from the wedge plate or nut to the primary structure.
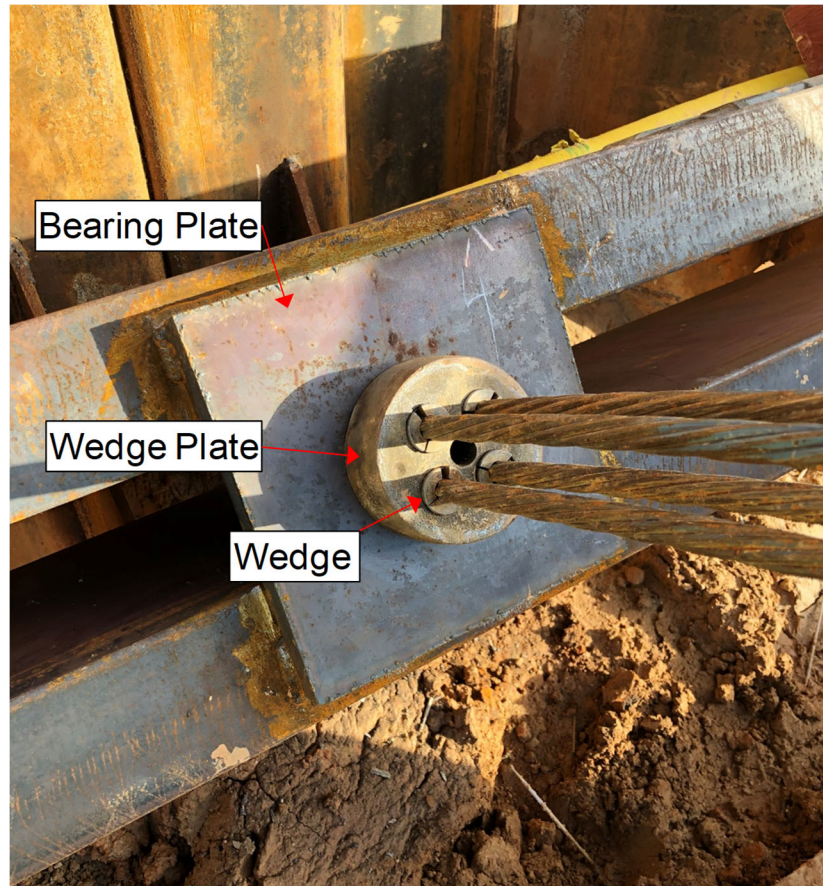
Figure 11-1. Labelled connection components of a strand ground anchor.

11.1.4 Installation

The installation procedure consists of 1) drilling the anchor shaft, 2) inserting the anchor strands or bars, 3) grouting, including set time, 4) primary structure-to-ground anchor connection, and 5) testing/tensioning. Drilling methods include rotary, percussion, combined rotary and percussion, and auger methods, and the method is selected based on the soil and site conditions. Shaft diameters are usually less than 0.3m in diameter, though in select special cases, holes up to 0.6m are performed for high capacity anchors (PTI 2004). Casing or drilling fluid is used for soils prone to collapse. More compact hydraulic

drill rigs, such as the Comacchio MC-28 pictured in Figure 11-2, are utilized that can accommodate all of the above mentioned drilling systems.

Figure 11-2. Comacchio MC 28 drill rig.

Before grouting, the hole must be cleaned to allow for the full attainment of the design strength. A tremie or grouting tube is typically inserted with the strands or rod into the drilled shaft, and either through gravity and pressure grouting, cement grout is pumped through the tube and the drill-hole is gradually filled from the bottom. After adequate set time, the anchor connection pieces are set in place, and anchor tensioning and testing can begin.

11.1.5 Tensioning and Testing

In the tensioning of ground anchors, proof or performance tests are performed to validate the load and displacement requirements of each anchor. A testing plan is dependent upon client needs but at minimum all anchors are subjected to a proof test, while a percentage of the anchors are subject to a more extensive performance test. In both cases, the anchor is gradually loaded and unloaded in cycles up to 133% of the design load. At each load, the displacement of the ground anchor is recorded such that the length of the bonded section can be backcalculated using an elastic analysis. For the performance test, a creep test is performed where the constant load (i.e. 133% of the design load) is applied for ten minutes, while the displacement is monitored, and if the anchor moves beyond the specified threshold (i.e. a percentage of the unbonded length), an extended creep test is conducted.

To tension the anchors, a hydraulic jack is placed around the anchor tendons or bars, and with a secondary set of wedges or locking nut, the anchor can be loaded to the desired load given a calibrated hydraulic jack load cell (Figure 11-3). To measure the displacement of the anchor during loading, two dial gauges are commonly used to measure the displacement of the primary structure and of the anchor itself. At the end of testing, the anchor is "locked-off," meaning that the strands or rod is stressed to the design load and the primary set of wedges or nut are inserted or tightened to the wedge plate or bearing plate, respectively. Upon depressurization of the hydraulic jack, the wedges or nuts prevent the anchor from relaxing and the design load is achieved. To note, often during "lock-off," the design load is marginally surpassed since some relaxation of the anchor occurs before the wedges or nut engage.

Figure 11-3. Tensioning of 4-strand tieback anchor with hydraulic jack.

11.2 Root-Inspired Anchors

This section provides initial suggestions and concepts regarding the design and implementation of a root-inspired anchor to replace conventional ground anchors in particular soil and site situations, where the basis for this knowledge draws upon insight from the previously documented experiments and analyses. To replace conventional systems, root-inspired anchor models must provide an obvious advantage over linear grouted ground anchors without providing a dramatic disadvantage.

11.2.1 Design

The design of a root-inspired anchor model includes the geometry, material properties, and an accurate means to predict the mechanical response.

11.2.1.1 Prediction of Capacity and Displacement

The Slip Line pullout capacity model modified with an empirical critical failure surface intersection ratio model developed in Chapter 8 can be utilized for the backcalculation of the embedment depth, H, and model width, b, given a required design load. As well, the ring pullout stiffness model can be utilized as a first order approximate for the displacement response of a root-inspired anchor model. Even more, the displacement response can be enhanced through the incorporation of a more realistic soil load-displacement model, as documented in Section 8.7.3.1, and of an additional spring component to account for the influence of the elastic modulus of the soil. However

11.2.1.2 Root-Inspired Anchor Geometry

The morphology-type root-inspired anchor model is selected for development due to a more rigorous testing program and associated insights as well as more coherent installation concepts. Selection of appropriate root-inspired anchor geometry properties is dependent upon both resistance and displacement specifications of the primary structure, and a general guideline for the selection of those features is displayed in Table 11-1, where insight is stimulated from the 1g pullout tests and the installation feasibility postulate that a simpler geometry is easier to construct.

Table 11-1. Preliminary guidelines for selection of root-inspired anchor morphological features.

Morphologic Feature	Design Guideline
Number of branch axes, n	Optimal range $3 \leq n \leq 6$
Embedment depth, H	Extend past potential failure surface
Width, b	Required capacity
Depth-to-width ratio, $H/2b$	ϕ dependent, $H/2b_{cr}(\phi=30°)<4$, $H/2b_{cr}(\phi=40°)<7$
Internal branching angle, α	Optimal range, $45°<\alpha<75°$
Branch axis length, L	Minimize based on displacement compatibility
Diameter, d	Anchor rod tensile strength, required stiffness

11.2.1.2.1 Number of Branch Axes, n

From Chapter 6, pullout capacity increases with the number of branch axes; yet, the increase in capacity diminishes with a decreased branching spacing, such that a significant capacity is achieved even for anchors with 3 branch axes. Additionally, for construction and installation considerations, root-inspired anchors with fewer branch axes are desirable.

11.2.1.2.2 Depth-to-Width Ratio, $H/2b$

The selection of embedment depth, H, and width, b, of a root-inspired anchor is analogous to the determination of the bonded length of a conventional anchor, where the capacity of a root-inspired anchor is heavily influenced by both parameters. For retaining wall or grade separation system design, the embedment depth must be sufficiently long to extend the anchor beyond the potential failure surface. As such, the width of the model can then be selected based on the required anchor resistance. Additionally, the depth-to-width ratio will be further constrained by the critical depth-to-width ratio, where the failure mode evolves from breakout to compression and flow beyond the specified ratio. Though experimentally, the critical embedment depth-to-width ratio was not identified for the root-

inspired anchor models, guidelines suggested by the literature (Meyerhof and Adams 1968, Vesic 1969) should be enacted and followed conservatively until it is clarified. As suggested by *Meyerhof and Adams 1698*, for a soil with an internal friction angle of 40°, a critical depth-to-width ratio, $H/2b$ of 7 (Meyerhof and Adams 1968). Contained within the selection of the depth to width ratio are the additional geometric parameters, internal branching angle, α, and branch axis length. From 1g pullout tests, an optimal range of $45°<\alpha<75°$ was revealed for pullout capacity. From ring pullout tests and 1g model tests, branch axis length was shown to critically affect the stiffness of the anchor model and the failure displacement. As such for a specified anchor width, selection of a greater internal branching angle allows to the branch axis length to be minimized.

11.2.1.2.3 Anchor Diameter, *d*

Pullout stiffness of a root-inspired anchor is dependent upon the diameter of the anchor, where smaller diameter anchors result in more compliant elements. As specified in Section 11.1.2.1, the anchor rod must satisfy the tensile failure factor of safety, which is dependent upon the ultimate strength of the steel and the cross-sectional area of the rod. Additional constraints on anchor diameter could include manufactured anchor rod limits.

11.2.2 Materials

The materials utilized in the fabrication of root-inspired anchors are not expected to differ substantially from those of conventional ground anchors, where corrosion protected (e.g. heat-shrink tubing or grease-filled sheaths) high strength steel rods, cement grout, trumpet, and connection components (e.g. bearing plate, nut) are all anticipated. However,

the biggest differentiator will be in the formation of the branching structure, which will be installation method dependent.

11.2.3 Installation Methods

In the development of this research, the most common criticism has been concerning the method of construction, where to the outside observer, the embedment of a branched structure in the subsurface seems infeasible, which is not surprising given that most geotechnical structures are linear. However, this section provides preliminary conceptualizations of root-inspired anchor system installation methods with aims to illustrate the viability of root-inspired anchor construction and to generate further ideation.

11.2.3.1 Wedge Method

The premise behind this concept is that a manufactured wedge structure will be utilized to direct the integrated insertion and bending of the anchor rods into the surrounding soil (Figure 11-4). The wedge would consist of troughs for the guided insertion of the individual rods. As well, high strength steel casing would be required to prevent rod buckling during the compressive loading of the rods.

Figure 11-4. Schematic of wedge method for installation of root-inspired anchor.

11.2.3.2 Guided Insertion

With this method, a prefabricated pile structure with guided tubes would first be inserted into a predilled shaft, and correspondingly, the individual anchor rods would be inserted and directed through individual guided tubes (Figure 11-5). The prefabricated pile structure could be fabricated from concrete with steel tubes at the point of bending.

Figure 11-5. Schematic of guided insertion method, pre (top) and post (bottom) anchor rod insertion.

11.2.3.3 Additional Methods

This section discusses the utilization of individual or a combination of existing technologies for the fabrication of a branched ground anchor. One idea includes the utilization of directional drilling or trenchless technologies to drill shafts at varying angles and curvatures from the soil surface, which would be followed by the insertion of strand anchors and grouting. Next, a Franki Pile-inspired ground anchor could be formed by the utilization of a reaming drill. Additionally, an "Expander Body"-inspired anchor could be installed by inflating steel bladder (Broms 1985). As well, numerous former or current U.S. patents detail multiple apparatuses for the insertion of components at some degree of inclination from the axis of the drilled shaft, and a few select patents are detailed in Figure 11-6. As well, a multitude of patents detail the design of helical pile-type anchorage system with subtle distinctions to illustrate uniqueness. Furthermore, anchor creations from other

fields beyond geotechnics can be exploited, such as drywall-type anchors, marine anchors, and barbed-structures. In addition, most of these installation methods can utilize pressure grouting to augment the soil-grout bond.
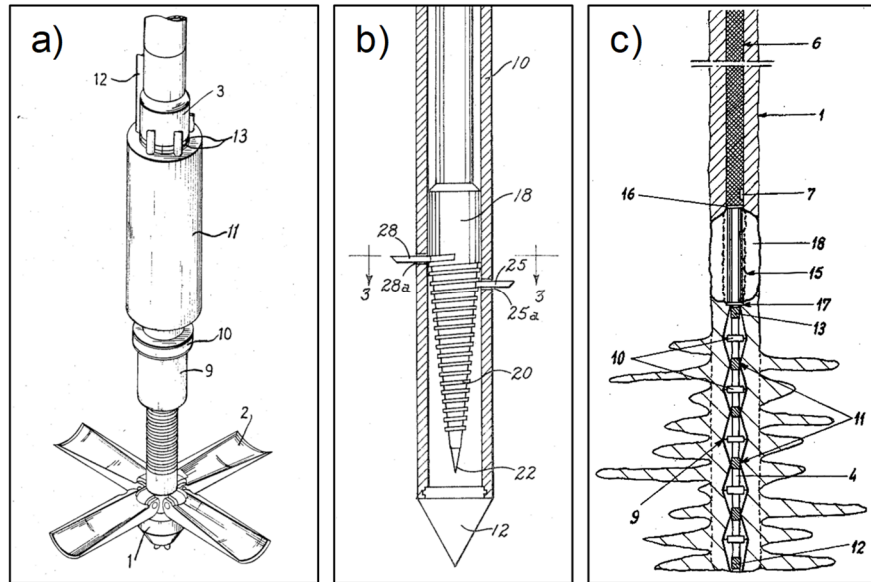
Figure 11-6. a) US Patent 4592178 detailing a ground anchor with extendable sleeves (H. Lu 1985), b) US Patent 3628337 detailing a ground anchor with lateral extending elements via a screw mechanism (F. Stepanich and T. Adams 1969), c) US Patent 3494134 detailing a ground anchor with supplemental jet grouting (G. Jorge 1970).

11.2.4 Uncertainty in Upscaling

Additional concerns in the scaling of 1g model tests to quarter-, half-, or full-field scale anchors are provided including potential scale effects and their influence on the salient experimental conclusions.

11.2.4.1 Scale Effects Involved in 1g Model Tests

The scaling of root-inspired anchor models from the benchscale (i.e. length scale of 10^{-1}m) to ¼-½ prototypes (i.e. 10^{0}m length scale) to full-field scale (i.e. 10^{1}m) requires precise scrutiny of the results at every stage. A rigorous model requires similitude across

all features, and therefore, scale effects refers to any influence in the behavior of the reduced-scale model due to dissimilitude. A model complying with this standard is difficult to achieve in geotechnics due to nature of the primary constituent, soil, where the behavior of the material is dependent upon numerous factors, such as stress state, particle properties, and pore fluid characteristics. Additionally, simply presenting data in a dimensionless form though a necessary step in the analysis of a scaled model, by no means ensures scalability. If the 1g benchscale pullout tests are to be considered as models to prototype or field scale anchors, complete knowledge, consideration, and treatment of the scale effects is mandatory, where preliminary thoughts were provided in Section 6.1.2. In the case of the vertical uplift of an embedded object, particle size and stress state are two factors that are alleged to violate similitude and thus affect the pullout response.

11.2.4.1.1 Stress State Effect

Inherent to 1g model tests is the dissimilitude in stress state between the model and the application. Due to the stress and strain dependent behavior of granular material, an equivalent stress state to the application should be modeled in the reduced scale test, and correspondingly, when the stress state is not replicated, the effects of the dissimilitude is manifested in the entirety of the process. Figure 11-7 illustrates, in the conventional plate anchor form, the effect of stress state on pullout factor for models of constant depth-to-width ratio, such that a degradation in pullout factor occurs in models of increasing width.
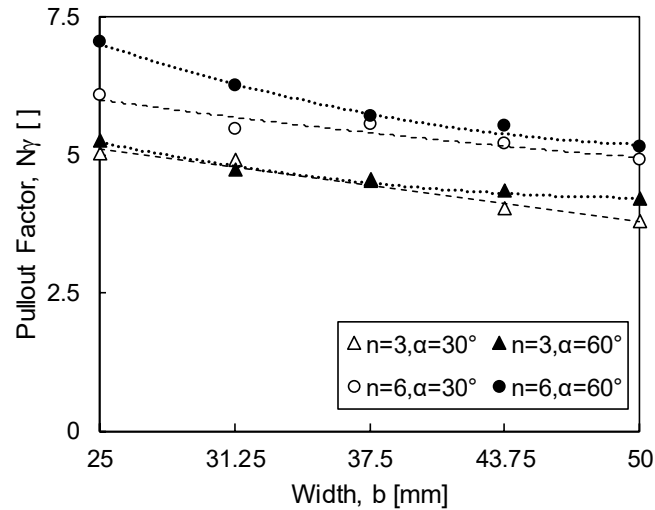
Figure 11-7. Evidence of the effect of stress state on pullout behavior for models of constant depth-to-width ratio (*H*/2*b*=1.8).

1g model tests allow for greater dilation angles due to lower confining stresses compared to field scale applications. As such, not only is it theorized that the size of the failure surface expands with decreased confinement and increased dilation angle, as evident from both experimental and numerical indications, but also the shearing resistance is expected to increase due a greater mobilized friction angle. To compensate for this mismatch, it is proposed that a stress-dependent model be used to predict pullout capacity, where both the shape of the failure surface and friction angle along the surface are dependent upon the stress state at that depth.

The stress state manifests itself in the displacement compatibility indices as well. Both failure displacement and pullout stiffness, proxied by maximum tangent stiffness, are dependent upon the elastic and plastic properties of the soil, the initial lateral earth pressure coefficient, and the morphology of the anchor, where the first two are directly related to the state of stress in the soil. In particular, failure displacement is by definition dependent upon the length of the soil mobilized to reach the ultimate load, and therefore proportional

to the length of the failure surface, which is again affected by stress state. To note, for a logarithmic spiral surface, the length of the spiral surface as viewed from the plane of constant azimuthal angle, has a linear relationship with the embedment depth and as such, can serve as a means to normalize failure displacement and demonstrate deviations with various influences (Figure 11-8). In all, due to the dependency of both displacement compatibility indices on the properties of the soil and anchor, accurate prediction of the displacement response requires a model that incorporates the governing properties of both soil and anchor properties, including elastic moduli and anchor geometry.
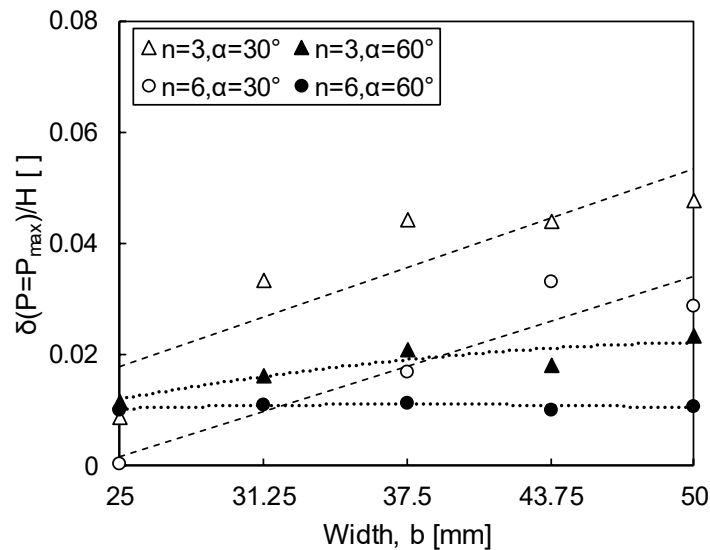
Figure 11-8. Normalized failure displacement with width for models of constant depth-to-width ratio (*H*/2*b*=1.8).

11.2.4.1.2 Particle Size Effects

The effect of particle size on pullout behavior is difficult to assess experimentally due to the combined effect of stress state; yet even in centrifuge modeling, particle size is not scaled properly, where the mean particle size should be reduced by the scaling factor. As shown by *Ovesen 1981*, plate anchor models sufficiently wider than the mean particle

size, $2b/d_{50}$>48, experience no perceivable effect on pullout capacity. Numerical studies suggest that pullout factor has a linear relationship with mean particle diameter-to-model width ratio, $d_{50}/2b$, (Sakai and Tanaka 1998, Athani et al. 2017), where the percent change in pullout factor decreases with the depth-to-width ratio. All root-inspired anchor models complied with above criteria, though some plate and pile anchor tests did not, which only further supports the credibility of root-inspired anchors. Furthermore, the mechanics of the uplifted root-inspired anchor problem is subject to another particle size affected phenomenon, which is in the extent of soil arching models. Related to the mechanism of soil arching, *Chambon and Corte. 1994* states that for tunnel stability, particle size effect is negligible at ratios of s/d_{50}>175; therefore, all root-inspired anchors, regardless of size experience some increase in stability near the point of dichotomy, yet for even the benchscale models, the effect vanishes relatively quickly along the length of the branch axis for models susceptible to arching limitations (i.e. models with few branch axes). Additionally, particle size is critical in the scaling of interface shear interactions, specifically when the shear response is dependent upon the particle size-to-characteristic interface feature ratio. The interface shear strength diminishes as the particle size surpasses the characteristic roughness length.

11.2.4.2 <u>Soil-to-Anchor Stiffness Ratio</u>

From both numerical and experimental results, the soil-to-anchor stiffness ratio contributes significantly to the pullout response. Through the utilization of a more compliant 3D printed plastic anchors instead of more rigid steel members, the contrast in stiffness ratio between the 1g models and an assumed full scale root-inspired anchor is minimized.

11.3 Conclusions

A brief synopsis of the primary conclusions of Chapter 11 are presented.

- The overall design and specifications of conventional ground anchors are reviewed to highlight and document the requirements of a field scale root-inspired anchor to replace tiebacks and tiedowns in specific situations.

- Guidelines to the design of a root-inspired anchor system are presented based upon the results of the numerous experimental and numerical tests performed within this dissertation.

- The Slip Line capacity formulation with incorporated critical failure surface intersection ratio model serves as an initiation point for the prediction of root-inspired anchor pullout, where a model that incorporates the stress and strain dependent nature of soil is desirable.

- Numerous installation concepts are provided to initiate the conceptualization of a constructing a root-inspired anchor within the soil.

Special Recognition: Hayward Baker, Inc. Redd Schoening, Michael Morello, Jonathan Reece, Avery Lunsford, and Matt Barr

CHAPTER 12.   CONCLUSIONS AND RECOMMENDATIONS

12.1 Salient Conclusions and Contributions

This dissertation serves as a source of inspiration for the progression of root-inspired geotechnics, whether that stimulates further advancement in the design of root-inspired anchorage systems or the development of new root-inspired geotechnical solutions. In particular, this body of research provides a preliminary knowledge base for the design of root-inspired anchorage systems. Particular focus was placed on understanding the mechanical behavior of both the geomaterial and the root-inspired anchor during anchor uplift and the associated influence of soil and anchor properties on the pullout process.

12.1.1 Pullout Behavior of Root-Inspired Anchors

12.1.1.1 Global Pullout Response

- Pullout capacity, P_{max}, is mandatory for anchor design and for root-inspired anchors, pullout capacity increases with depth-to-width ratio, the number of branch axes (though a loss in increased capacity occurs with additional branch axes and a substantial capacity is achieved with even 3 branch axes), and is optimized at an internal branching angle of $45°<\alpha<75°$. In terms of soil properties and conditions, P_{max} is augmented by an increase in relative density, particle angularity, friction and dilation angles, initial lateral earth pressure coefficient, and both soil and anchor elastic moduli.

- Pullout factor, $N\gamma$, provides an effective means to normalize pullout capacity for comparative analyses amongst various anchor morphologies, where an optimal

internal branching angle range of 60°<α<90° is revealed due to the subtraction of the weight of conical volume of soil below the anchor. For other variations in anchor and soil properties, similar general trends as for pullout capacity occur.

- Failure displacement, $\delta(P=P_{max})$ and pullout stiffness, proxied in this dissertation by maximum tangent stiffness, $\max(k_{tan})$, are mandatory for anchorage system design particularly for anchor-infrastructure displacement compatibility as well as performance and proof testing of anchors and are both dependent upon the stiffness of the soil-anchor system. Failure displacement maintains a direct relationship with the branch axis spacing, depth-to-width ratio, and particle size. Pullout stiffness increases with anchor features (e.g. number of branch axes, depth-to-width ratio, internal branching angle, anchor elastic modulus), soil properties (e.g. relative density, mobilized friction and dilation angles, soil elastic modulus) and conditions (e.g. initial lateral earth pressure coefficient), and the interface shear strength. In general, displacement at pullout capacity is more sensitive to variations in anchor morphology than maximum tangent stiffness.

- Material efficiency, Π_M, defined as pullout capacity normalized by the weight of the anchor model provides an initial measure of the sustainability of a design and increases with the depth-to-width ratio, branch axis spacing, θ, is optimized for an internal branching angle of 60°<α<90°, and with all soil properties that act to enhance pullout capacity.

- The shear strength of the sand-3D printed plastic interface is dependent upon the properties of the sand (e.g. angularity), the 3D printed material properties (e.g. hardness) and printing parameters (e.g. filament deposition orientation), and the

contrast in particle-to-surface properties (e.g. particle size-to-characteristic roughness length). Interface friction angle has no appreciable effect on the pullout capacity of root-inspired anchor models, though displacement compatibility indices are influenced, where failure displacement decreases and pullout stiffness increases with increase interface friction angle.

12.1.1.2 <u>Evolution of Soil Kinematics during Anchor Pullout</u>

- Visualization of the localization of shear strain into mature rupture surfaces was achieved with 2D DIC and 3D DVC analyses of x-ray CT images of the soil-anchor system during the pullout process.

- The interpreted weight of the uplifted soil in the DVC-generated failure surface revealed that the weight of soil alone is not sufficient in predicting pullout resistance, where shearing resistance along the failure surface and at the soil-anchor interface below the failure surface are expected.

- A logarithmic spiral generatrix, which is mechanically rigorous for a Mohr-Coulomb material (e.g. kinematically admissible failure surface) can well define the shape of the failure surface when viewed from the constant azimuth plane of a cylindrical soil volume.

- Visualization of the soil displacement trajectories with shear strain localization reveals that geomaterials tested do not comply with the normality condition and that the angle between adjacent soil movement and the failure surface varies significantly depending on soil properties and to a lesser extent, anchor features.

- Evidence of soil arching in the region circa the branching portion of the root-inspired anchors was identified and provides a mechanism for the production of a breakout-type failure surface for anchors with solely 3 branch axes. The failure surface appears as a petaloid shape (i.e. bottom of plastic soda bottle) in the zone surrounding the point of dichotomy of a root-inspired anchor, where an apparent arc spanning the individual branch axes differentiates the uplifted and pseudo-stationary soil regions.

12.1.1.3 Prediction of Pullout Response

- In general, pullout capacity models require many assumptions (e.g. failure surface, failure criterion, acting mechanisms stress state), which explains the multitude of uplift capacity models in the literature with no defined consensus

- An axisymmetric, logarithmic spiral failure surface-type Slip Line model was formulated to predict pullout capacity of a root-inspired anchor system, where the models improves upon the inherent plane strain assumptions within *Matsuo 1967* and *Vesic 1969.* The model well predicts anchor plate capacity data from both the literature and this current study.

- The axisymmetric Slip Line model is adjusted to predict pullout capacity of a root-inspired anchor model by varying the critical failure surface intersection ratio, which naturally modifies the weight of uplifted soil and the frictional resistance along the failure surface.

- From various evaluated methods of predicting the critical failure surface intersection ratio, a combined method incorporating both the soil arching mechanism and feature engineering provided the best prediction in terms of the RMSE.

12.1.2 Promotion of Existing Technologies in Bio-Geotechnics

In the development of this research numerous existing technologies and concepts were exploited. This dissertation documents and provides explicit reasoning for the further utilization of these technologies in the development of bio-geotechnics.

12.1.2.1 Application of X-ray Computed Tomography

- This dissertation promotes the utilization of x-radiation radiography and computed tomography for bio-mediated or bio-inspired of the internal processes of soil in conjunction with technologies.

- The design and development of an in-house, geotechnics laboratory x-ray CT scanner at 10-20% the price of a commercial scanner is described. Details of a geotechnics x-ray CT scanner, including equipment specification explanations, geometry layout and correction, design tradeoffs, and reconstruction and image processing techniques, are provided for future design.

- The utilization of x-ray CT to visualize the geomaterial kinematics, deformation, and failure behavior during uplift of root-inspired anchor models is achieved.

12.1.2.2 Application of Additive Manufacturing

- A Lulzbot TAZ 6 fused filament fabrication printer was utilized in the manufacturing of the majority of the anchor models utilized in the experimental

program and allowed for the rapid and economic manufacturing of computer designed models with relative high accuracy.

- The interface shear response between additive manufacturing thermoplastic surfaces and coarse-grained particulate materials at varying stress levels and with various printing properties was evaluated, where the interface shear strength is notably dependent upon filament orientation, hardness, and print resolution.

- Additive manufacturing allowed for rapid and ease-in-fabrication production of multiple experimental implements for experimental apparatuses (e.g. specimen holder for x-ray CT scanner, centering device for reaction frame)

12.1.2.3 <u>Application of Bio-Inspired Design</u>

The application of bio-inspired design to geotechnics offers a novel perspective for the reconsideration of traditional geotechnical engineering. Bio-inspired design is a transformational concept whereby the evolved principles of biological organisms are translated into human designed solutions. Humans can exploit the refined properties of nature instead of reinventing the wheel and can approach problems from an alternative and creative view point. In this dissertation, the bio-inspired process was applied to the development of a novel ground anchorage system, and the progression of the design of a root-inspired anchor is documented. The selection of biological principles for incorporation into a root-inspired anchor featured a gradual refinement process, where 1) plant root systems were selected for their multifunctionality, adaptability, and material efficiency attributes, 2) fibrous root systems were selected due to their enhanced ability to resist uplift forces, and 3) specific architectural features of fibrous root systems (e.g. number of root axes, root system breadth, root system length, topological pathlength) were

chosen from their positive relations with pullout behavior. The features were incorporated into morphology- and topology-type root-inspired anchor models. As well, the principal designer purports that the design features many limitations due to the intrinsic bias of the user (e.g. mechanics focused, neglection of critical root systems properties, fabrication constraints) and proposes that the design of a root-inspired ground anchor is incomplete and could benefit from an additional design cycle including the re-visitation of root system properties, the incorporation process, and the performance evaluation.

12.2 Recommendations for Future Work

This research provides a thorough yet incomplete foundation for the development and evaluation of a root-inspired anchor element. While significant progress concerning the conceptualization of the pullout process of was achieved, naturally gaps are still present. Recommendations for additional development include topics in both the fundamental and upscaling levels, where insights can be pursued in tandem with the proper research methodology. The following topics are suggested:

- Develop and evaluate a suite of root-inspired anchor installation methods, with an emphasis on ease of implementation.

- Explore the evolution in the pullout mechanics of anchors at greater embedment depth-to-width ratios, with a particular focus on identification of the critical depth-to-width and influence of anchor and soil properties on that limit

- Evaluate the mechanical behavior of the root-inspired anchor-soil system at varying orientations of the primary axis of the anchor in relation to the soil surface with particular aims of providing more guided insight for the development of tieback

versus tiedown anchors, where *Rowe and Davis 1982* and *Ovesen 1981* document an increase in capacity with rotation of the pullout orientation from vertical to horizontal. As well, investigate the evolution of the failure surface as both the soil surface normal and anchor primary axis are rotated 90°.

- Investigate the mechanical behavior of the soil-anchor system in compression, subjected to lateral forces, with surcharge, and with cyclic loading, all of which are mandatory for the field scale development (e.g. transmission tower, wind turbines).

- In terms of numerical modelling, incorporate a critical state-based constitutive model such as Nor Sand instead of Mohr-Coulomb, such that effects of contained plastic flow are minimized and that stress- and strain-dependency of soil is added.

- For the analytical investigation, develop a stress-dependent pullout capacity model where both the curvature of the failure surface and the shearing resistance along the surface at depth is dependent upon the dilation angle.

APPENDIX A. SUPPLEMENTAL RESOURCES

A.1   Strength Tests of Living Roots and Root System Analogs from the Literature

A summary of select compression, pullout, and pullover tests performed on both living roots and root analogs are displayed in the subsequent sections.

Table A1. Compilation and summaries of strength tests performed on living root systems.

Test	Conclusion	Species	Root System Architecture	Reference
Compression	- Roots buckled due to low confining pressure - load-displacement curves - max load increased with diameter - results analyzed versus Toakley 1965 and Whitman and Luscher 1962	Hemlock (*Tsuga sieboldii*)	Unknown, root buckled before root branched, root was tortuous	Wu et al. 1988
Pullout	- mentions friction - root hairs were involved in pullout resistance - stiffness comparison between root and soil	Sunflower (*Helianthus annus*) seedlings	Rigid taproot with laterals (tap and root ball)	Ennos 1989
Pullout	- Pullout capacity increases with root depth and soil strength - critical length: the length the root will break instead of continuing to transfer tension to soil via shear	Leek (*Allium porrum*) seedlings	Fibrous roots without root hairs	Ennos 1990
Pullout	- Assess role of branching, laterals, and root hairs on anchorage - root hairs have no effect on pullout resistance	Onion (*Allium cepa*) Thale cress mutants (*Arabidopsis thaliana*)	Onion: unbranched adventitious roots without root hair Cress: taproot, mutant with root hair deficient, and mutant	Bailey et al. 2002

	- branching increases pullout resistance		with reduced lateral roots	
Pullout	- Segments cut to resemble model roots made of rubber and wood - max pullout: dichotomous > herringbone > taproot - Max pullout increased with depth of laterals - pay attention to interface properties	Willow segments (*Salix viminalis*)	- Taproot, herringbone, dichotomous	Mickovski et al. 2007
Pullout	- Interface friction not determined due to unknown tortuosity/curvature effects - pullout resistance of real root > model root	Willow (*Salix viminalis*)	Single roots	Mickovski et al 2010
██				
Static winch pullover	- Observed bearing capacity type failure (my own observation)	Sitka Spruce (*Picea sitchensis*)	- Asymmetric root plate (longer radius on windward side) - plate + shallow laterals + sinkers close to stem base Shallow due to waterlogging	Coutts 1983
Static pullover	- Anchorage dominated by adventitious roots that act as props and guy lines	Maize (*Zea mays*)	Adventitious + fibrous (adventitious coronal root)	Ennos et al. 1993

	- Peripheral lignification of basal area - only 6.5% of dry mass is dedicated for root system - increase anchorage of root system by using thicker, more rigid roots - failure primarily due to buckling of roots			
Static winch Pullover	- Root spread and root/shoot ratio - shallower plates had longer laterals (more spread) - shallower plates had more mass dedicated to roots versus the stem - more biomass was located on leeward side proposed because of restricted depth and resistance to bending suggests that taproot is important	Sitka spruce (*Picea sitchensis*)	Plate root Root depth restricted by waterlogging	Nicoll and Ray 1996
Static winch pullover	- Leeward roots provide 25% of anchorage, while 75% comes from taproot, windward laterals and sinkers - Sinkers improve efficiency of anchorage system	Hybrid larch (*larix europea x japonica*)	Taproot + shallow laterals with sinkers	Crook and Ennos 1996
Static winch pullover	- Larger trunks (9cm diameter) actively failed soil, taproot did not pullout	King tropical tree (*Mallotus wrayi*)	Taproot	Crook and Ennos 1998

	- Smaller trees (>7cm) either broke in the trunk or bent at the trunk and then returned to position - tap root diameter and length do not scale isometrically with trunk diameter - only smaller trees can rely solely on taproot to resist overturning - anchorage strength scaled with the 2nd power of trunk diameter			
Static winch pullover	- Taproot critical to anchorage for the Pinus genus - anchorage resistance scaled with the 3rd power of trunk diameter - trees are weaker in compression than tension - Younger tree typically fail more in trunk and older trees in roots	Maritime pine (*Pinus pinaster*)	Taproot + laterals	Stokes 1999
Static winch pullover	- Scots pine > birch > Norway spruce - Frozen ground required higher pullover forces and all pines broke in stem - trees with deeper plates more resistive but trees with	Scots pine (*Pinus sylvestris*), Norway spruce (*Picea abies*), birch (*Betula* spp.)	Plate roots	Peltola et al. 2000

	wider plates did not correlate with maximum pullover moment			
Static winch pullover	- Beech>oak>fir>spruce- - root biomass, root system asymmetry, and root strength all critical to anchorage strength	European beech (*Fagus sylvatica*), English oak (*Quercus robur*), Douglas fir (*Pseudotsuga mexziesii*), Norway spruce (*Picea abies*)	Beech – heart; fir – heart; oak – tap; spruce - sinker	Stokes et al. 2000
Static pullover	- Plants with thicker and longer taproots resisted larger moments - Implication: long/thin > short/thick for same volume of material	Oilseed Rape (*Brassica napus*)	taproot	Goodman, Crook, Ennos 2001
Static winch pullover	- Contains CSA and DBH, eccentricity and aspect ratio - root asymmetric - rotation point below ground surface - failure: leeward roots pushed into ground, and windward roots pulled in tension and came out of ground - As DBH increased, Max Moment increased - most dry mass located in lateral roots (avg. 6)	Macedonia pine (*Pinus peuce*)	Deep taproot+Laterals+few sinker	Mickovski and Ennos 2003

	- more laterals located parallel to wind force vs. perpendicular			
Static winch pullover	- Eccentricity, CSA, dry mass - Mechanical properties: bending modulus, rigidity, bending strength, yield strength - trees flexed while growing and then pulled over - CSA increased in flexed trees, especially in lateral roots parallel to flex direction - # of lateral roots increased in flexed (8 vs 5) - Dry mass changed little between flexed and control trees, and no real change in root:shoot ratio	Scots pine (*Pinus sylvestris),* seedlings	- Taproot+laterals	Mickovski and Ennos 2003
Static winch pullover	- taproot critical for younger trees but as tree matures, taproot does not isometrically scale and consequently contributes less to moment resistance - edge trees had more mass dedicated to roots than crown than inner stand trees - edge tree more resistant to pullover	Maritime pine (*Pinus pinaster*)	Plate root 25% with taproot	Cucchi et al. 2004

Table A2. Compilation and summaries of strength tests performed on root system analogs.

Test	Conclusion	Root System Architecture	Reference
Pullout	- Max pullout resistance tap < herringbone < dichotomous - max pullout: wood > rubber and at smaller displacements (interface strength mobilize along whole root instantly for wood) - max pullout: wet sand > dry sand - rigid > flexible because rigid moves soil where as flexible flows in path - conclusion that saturation increases suction and therefore effective stress	1) Taproot, 2) Herringbone, 3) Dichotomous Wood and rubber models	Mickovski et al. 2007
Pullout	- factors affecting pullout resistance: branching angle, branch length, surface area, # of branches - herringbone > dichotomous but there was no good way to normalize data	1) Taproot + laterals, 2) Dichotomous (random) 3) herringbone Copper coated steel wire (3mm taproot, 1.5mm laterals),	Stokes et al. 1996
Lateral/Pullout at angles	- Bearing capacity term N_c calculated (6-11), typically in range of 5-7 using cavity expansion, Reese et al. 1971 up to 50	Dichotomous (flexible wire cable EI=1350 N cm^2)	Wu et al. 1988
Pullout	- Medium: silica sand (D_{50}=0.12mm) - Provides values of interface friction (δ_w=21°, δ_r=27°)	Taproot Wood (E=1264MPa) and rubber (E=29MPa) analogs	Mickovski et al. 2010

A.2   Derivation of *White et al. 2008* Pullout Capacity Model Adapted to Plate Anchors

A derivation for plate pullout capacity is formed by adapting the model of *White et al. 2008* for a 2D problem to the case of an axisymmetric problem. In the adaptation the assumptions regarding the constant normal stress, use of K_0, and an inclined failure surface defined by an angle, θ, are maintained. For ease of calculation, the failure surface is projected onto a radial circular section of the identical proportions.
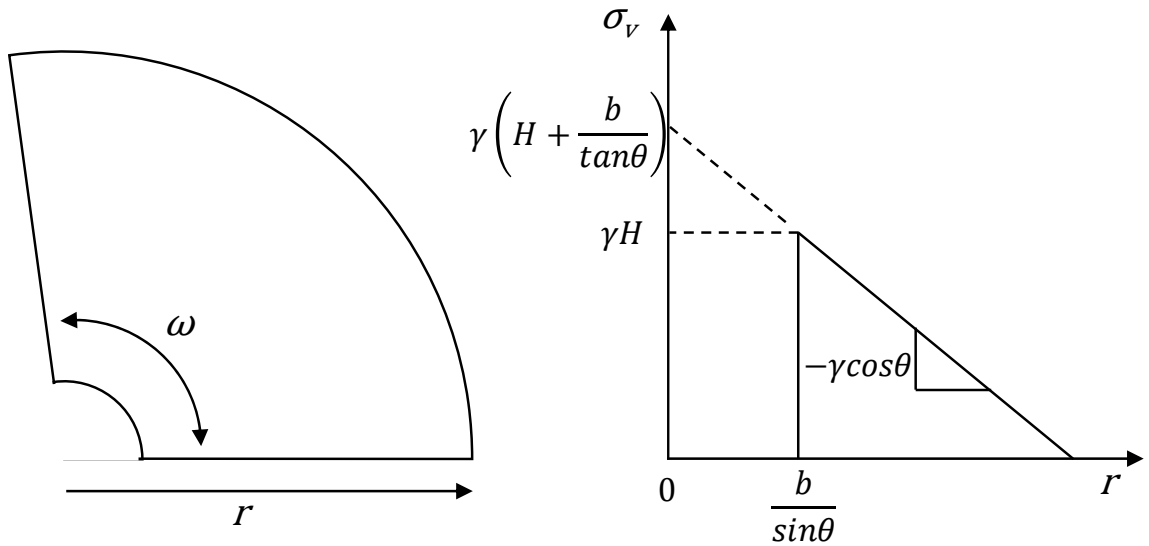
Figure A1. Schematic of the unwrapped area of conical failure surface with vertical stress along failure surface.

The normal and shear stress at depth along the failure surface are defined in Equation A1.

$$\sigma_n = \sigma_v \left[\frac{1+K_0}{2} + \frac{K_0-1}{2} \cos 2\theta \right]$$
$$\tau_f = \sigma_n \tan \phi_P$$

(A1)

Subsequently, the normal force on the conical failure surface can be determined in Equation A2.

$$F_{normal} = \omega \int_{\frac{b}{\sin\theta}}^{\frac{H}{\cos\theta}+\frac{b}{\sin\theta}} \sigma_n r \, dr$$

$$F_{normal} = \int_0^{2\pi\sin\theta} \int_{\frac{b}{\sin\theta}}^{\frac{H}{\cos\theta}+\frac{b}{\sin\theta}} \gamma' \left[-r^2\cos\theta + r\left(H + \frac{b}{\tan\theta}\right)\right]\left[\frac{1+K_0}{2} + \frac{K_0-1}{2}\cos 2\theta\right] dr \, d\omega \qquad \text{(A2)}$$

$$F_{normal} = \pi\gamma' \frac{H^2}{3} \frac{1}{\cos\theta}\left[\frac{1+K_0}{2} - \frac{1-K_0}{2}\cos 2\theta\right](3b + H\tan\theta)$$

A balance of forces including the weight of soil within the failure surface, the shear and normal forces along the failure surface, pullout capacity, P_{max}, is determined as shown in Equation A3.

$$\sum F_y = 0$$

$$P_{max} = \gamma'\frac{\pi}{3}\left[\tan^2\theta\left(\frac{b}{\tan\theta} + H\right)^3 - b^3\left(\frac{1}{\tan\theta} + \frac{1}{\tan\alpha}\right)\right] + F_{shear}\cos\theta - F_{normal}\sin\theta \qquad \text{(A3)}$$

Through substitution of the shear and normal force into equation A3, the final solution to pullout capacity for a plate anchor (Equation A4) using the methodology described in *White et al. 2008* is revealed.

$$P_{max} = \gamma' \frac{\pi}{3} \left[\begin{array}{l} \tan^2 \theta \left(\dfrac{b}{\tan \theta} + H \right)^3 - \dfrac{b^3}{\tan \theta} \cdots \\ + H^2 \left(\tan \varphi_P - \tan \theta \right) \left(\dfrac{1 + K_0}{2} - \dfrac{1 - K_0}{2} \cos 2\theta \right) \left(3b + H \tan \theta \right) \end{array} \right] \qquad \text{(A4)}$$

A.3   Volume Contained within Logarithmic Spiral Failure Surface

The volume contained within the surface generated by a logarithmic spiral generatrix is schematically illustrated in Figure A2 and the equation to describe the volume is shown in Equation A5.
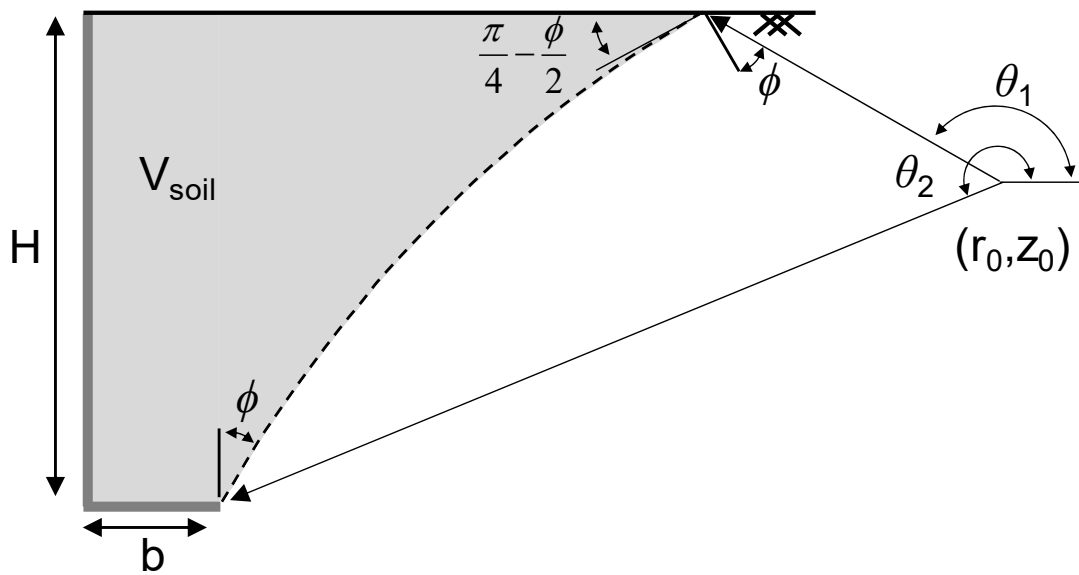
Figure A2. Schematic for the determination of the volume of soil contained within the surface generated by logarithmic spiral generatrix (shaded area).

$$V = \frac{\pi \rho_0}{12(9\kappa^3 + \kappa)} \left\{ \begin{array}{l} e^{\kappa\theta_1} \begin{bmatrix} 24\rho_0{}^2\kappa^2 e^{2\kappa\theta_1}\cos\theta_1 + \ldots \\ 3\kappa\left[3\rho_0{}^2\left(1+\kappa^2\right)e^{2\kappa\theta_1} + 4\left(1+9\kappa^2\right)\left(r_0+b\right)^2\right]\sin\theta_1 + \ldots \\ \rho_0\left(1+9\kappa^2\right)e^{\kappa\theta_1}\ldots \\ \left[6\left(r_0+b\right)+6\kappa\left(r_0+b\right)\sin 2\theta_1 + \rho_0\kappa e^{\kappa\theta_1}\sin 3\theta_1\right] \end{bmatrix} - \\[2em] e^{\kappa\theta_2} \begin{bmatrix} 24\rho_0{}^2\kappa^2 e^{2\kappa\theta_2}\cos\theta_2 + \ldots \\ 3\kappa\left[3\rho_0{}^2\left(1+\kappa^2\right)e^{2\kappa\theta_2} + 4\left(1+9\kappa^2\right)\left(r_0+b\right)^2\right]\sin\theta_2 + \ldots \\ \rho_0\left(1+9\kappa^2\right)e^{\kappa\theta_2}\ldots \\ \left[6\left(r_0+b\right)+6\kappa\left(r_0+b\right)\sin 2\theta_2 + \rho_0\kappa e^{\kappa\theta_2}\sin 3\theta_2\right] \end{bmatrix} \end{array} \right\} \quad \text{(A5)}$$

$$\theta_1 = \frac{3\pi}{4} + \frac{\phi}{2}$$

$$\theta_2 = \pi$$

$$r_0 = -\rho_0 e^{\kappa\theta_2}\cos\theta_2 = -H\frac{e^{\kappa\theta_2}\cos\theta_2}{e^{\kappa\theta_1}\sin\theta_1 - e^{\kappa\theta_2}\sin\theta_2}$$

REFERENCES

Abe, K. and Ziemer, R.R., 1991. Effect of tree roots on a shear zone: modeling reinforced shear stress. *Canadian Journal of Forest Research*, *21*(7), pp.1012-1019.

Abernathy, B. and Rutherford, I.D., 2001. The effects of riparian tree roots in relation to riverbank stability. *Earth Surface Processes and Landforms*, *25*, pp.921-938.

Abramento, M. and Whittle, A.J., 1995. Experimental evaluation of pullout analyses for planar reinforcements. *Journal of Geotechnical Engineering*, *121*(6), pp.486-492.

Ahn, S.H., Montero, M., Odell, D., Roundy, S. and Wright, P.K., 2002. Anisotropic material properties of fused deposition modeling ABS. *Rapid Prototyping Journal*, *8*(4), pp.248-257.

Alsaleh, M.I., Alshibli, K.A. and Voyiadjis, G.Z., 2006. Influence of micromaterial heterogeneity on strain localization in granular materials. *International Journal of Geomechanics*, *6*(4), pp.248-259.

Alshibli, K.A. and Sture, S., 2000. Shear band formation in plane strain experiments of sand. *Journal of Geotechnical and Geoenvironmental Engineering*, *126*(6), pp.495-503.

Altaee, A. and Fellenius, B.H., 1994. Physical modeling in sand. *Canadian Geotechnical Journal*, *31*(3), pp.420-431.

Altman, W. and Young, D.H., 1968. Stresses in thin conical shells. *International Association for Bridge and Structural Engineering*, *28*(1), pp.1-16.

Anderson, C.J., Coutts, M.P., Ritchie, R.M. and Campbell, D.J., 1989. Root extraction force measurements for Sitka spruce. *Forestry: An International Journal of Forest Research*, *62*(2), pp.127-137.

Andò, E., 2013. *Experimental investigation of microstructural changes in deforming granular media using x-ray tomography,* Doctoral dissertation, Université de Grenoble, France.

Andò, E., Hall, S.A., Viggiani, G., Desrues, J. and Bésuelle, P., 2012. Grain-scale experimental investigation of localised deformation in sand: a discrete particle tracking approach. *Acta Geotechnica*, *7*(1), pp.1-13.

Anselmucci, F., Andó, E., Sibille, L., Lenoir, N., Peyroux, R., Arson, C., Viggiani, G. and Bengough, A.G., 2019. Root-reinforced sand: kinematic response of the soil. In *E3S Web of Conferences* (Vol. 92, p. 12011). EDP Sciences.

Archard, J.F., 1957. Elastic deformation and the laws of friction. *Proceedings of the Royal Society of London. Series A. Mathematical and Physical Sciences*, *243*(1233), pp.190-205.

Arthur, J.R.F. and Menzies, B., 1972. Inherent anisotropy in a sand. *Géotechnique*, *22*(1), pp.115-128.

Arthur, J.R.F., Dunstan, T., Al-Ani, Q.A.J.L. and Assadi, A., 1977. Plastic deformation and failure in granular media. *Geotechnique*, *27*(1), pp.53-74.

Ashby, M.F. and Medalist, R.M., 1983. The mechanical properties of cellular solids. *Metallurgical Transactions A*, *14*(9), pp.1755-1769.

Athani, S., Kharel, P., Airey, D. and Rognon, P., 2017. Grain-size effect on uplift capacity of plate anchors in coarse granular soils. *Géotechnique Letters*, *7*(2), pp.167-173.

Bailey, P.H., Currey, J.D. and Fitter, A.H., 2002. The role of root system architecture and root hairs in promoting anchorage against uprooting forces in *Allium cepa* and root mutants of *Arabidopsis thaliana*. *Journal of Experimental Botany*, *53*(367), pp.333-340.

Baker, J., Guillard, F., Marks, B. and Einav, I., 2018. X-ray rheography uncovers planar granular flows despite non-planar walls. *Nature Communications*, *9*(1), p.5119.

Baker, S.R. and Friedman, G.M., 1969. A non-destructive core analysis technique using X-rays. *Journal of Sedimentary Research*, *39*(4), pp.1371-1383.

Baker, W.H. and Konder, R.L., 1966. Pullout load capacity of a circular earth anchor buried in sand. *Highway Research Record*, 108, pp.1-10.

Bałachowski, L., 2007. Size effect in centrifuge cone penetration tests. *Archives of Hydro-Engineering and Environmental Mechanics*, *54*(3), pp.161-181.

Balla, A., 1961. The resistance to breaking-out of mushroom foundations for pylons. In *Proceedings of the 5th International Conference on Soil Mechanics and Foundation Engineering, Paris* 1, (pp. 569-576), Dunod, Paris.

Barthélémy, D. and Caraglio, Y., 2007. Plant architecture: a dynamic, multilevel and comprehensive approach to plant form, structure and ontogeny. *Annals of Botany*, *99*(3), pp.375-407.

Bay, B.K., 2008. Methods and applications of digital volume correlation. *The Journal of Strain Analysis for Engineering Design*, *43*(8), pp.745-760.

Bengough, A.G. and McKenzie, B.M., 1997. Sloughing of root cap cells decreases the frictional resistance to maize (*Zea mays L.*) root growth. *Journal of Experimental Botany*, *48*(4), pp.885-893.

Bengough, A.G. and Mullins, C.E., 1990. Mechanical impedance to root growth: a review of experimental techniques and root growth responses. *Journal of Soil Science*, *41*(3), pp.341-358.

Bengough, A.G. and Mullins, C.E., 1991. Penetrometer resistance, root penetration resistance and root elongation rate in two sandy loam soils. *Plant and Soil*, *131*(1), pp.59-66.

Berger, M., 2010. XCOM: Photon cross sections database. *http://www.nist.gov/pml/data/xcom/index.cfm*.

Bernstein, L., 1975. Effects of salinity and sodicity on plant growth. *Annual Review of Phytopathology*, *13*(1), pp.295-312.

Berntson, G.M., 1995. The characterization of topology: a comparison of four topological indices for rooted binary trees. *Journal of Theoretical Biology, 177*, pp. 271-281.

Berntson, G.M., 1997. Topological scaling and plant root system architecture: developmental and functional hierarchies. *The New Phytologist*, *135*(4), pp.621-634.

Berntson, G.M., Lynch, J. and Snapp, S., 1998. Fractal geometry and the description of plant root systems: current perspectives and future applications. In *Fractals in Soil Science*, (pp.113-152). CRC Press, Boca Raton.

Bisshopp, K.E. and Drucker, D.C., 1945. Large deflection of cantilever beams. *Quarterly of Applied Mathematics*, 3(3), pp.272-275.

Blackwell, P.G., Rennolls, K. and Coutts, M.P., 1990. A root anchorage model for shallowly rooted Sitka spruce. *Forestry: An International Journal of Forest Research*, *63*(1), pp.73-91.

Bolton, M.D. and Lau, C.K., 1993. Vertical bearing capacity factors for circular and strip footings on Mohr–Coulomb soil. *Canadian Geotechnical Journal*, *30*(6), pp.1024-1033.

Bolton, M.D., 1986. Strength and dilatancy of sands. *Géotechnique*, *36*(1), pp.65-78.

Bornert, M., Brémand, F., Doumalin, P., Dupré, J.C., Fazzini, M., Grédiac, M., Hild, F., Mistou, S., Molimard, J., Orteu, J.J. and Robert, L., 2009. Assessment of digital image correlation measurement errors: methodology and results. *Experimental Mechanics*, *49*(3), pp.353-370.

Bouma, A.H., 1964. Notes on X-ray interpretation of marine sediments. *Marine Geology*, *2*(4), pp.278-309.

Bradshaw, A.D., 1965. Evolutionary significance of phenotypic plasticity in plants. In *Advances in Genetics*, 13, (pp. 115-155), Academic Press, Cambridge, MA

Bradshaw, A.S., Giampa, J.R., Gerkus, H., Jalilvand, S., Fanning, J., Nanda, S., Gilbert, R., Gavin, K. and Sivakumar, V., 2016. Scaling considerations for 1-g model horizontal plate anchor tests in sand. *Geotechnical Testing Journal*, *39*(6), pp.1006-1014.

Bransby, P.L., 1968. *Stress and strain in sand caused by rotation of a model wall,* Doctoral dissertation, University of Cambridge, UK.

Broms, B.B., 1985. Expander Bodies–A new concept for underpinning of structures. In *Proceedings of the 11th International Conference on Soil Mechanics and Foundation Engineering, San Francisco*, 3, (pp.1531-1534). Balkema, Rotterdam.

Brouwer, R., 1963. Some aspects of the equilibrium between overground and underground plant parts. *Jaarboek van het Instituut voor Biologisch en Scheikundig onderzoek aan Landbouwgewassen*, pp.31-39.

Brusseau, M.L., Peng, S., Schnaar, G. and Costanza-Robinson, M.S., 2006. Relationships among air-water interfacial area, capillary pressure, and water saturation for a sandy porous medium. *Water Resources Research*, *42*(3).

Buckingham, E., 1914. On physically similar systems: illustrations of the use of dimensional equations. *Physical Review*, *4*(4), p.345.

Burholt, D.R. and Hof, J.V.T., 1971. Quantitative thermal-induced changes in growth and cell population kinetics of Helianthus roots. *American Journal of Botany*, *58*(5), pp.386-393.

Butterfield, R., 1999. Dimensional analysis for geotechnical engineers. *Géotechnique*, *49*(3), pp.357-366.

Calvert, S.E. and Veevers, J.J., 1962. Minor structures of unconsolidated marine sediments revealed by x-radiography 1. *Sedimentology*, *1*(4), pp.287-295.

Camp III, W.M. and Parmar, H.S., 1999. Characterization of pile capacity with time in the Cooper Marl: study of applicability of a past approach to predict long-term pile capacity. *Transportation Research Record*, *1663*(1), pp.16-24.

Canadell, J., Jackson, R.B., Ehleringer, J.B., Mooney, H.A., Sala, O.E. and Schulze, E.D., 1996. Maximum rooting depth of vegetation types at the global scale. *Oecologia*, *108*(4), pp.583-595.

Cannon, W.A., 1949. A tentative classification of root systems. *Ecology*, *30*(4), pp.542-548.

Casimiro, I., Marchant, A., Bhalerao, R.P., Beeckman, T., Dhooge, S., Swarup, R., Graham, N., Inzé, D., Sandberg, G., Casero, P.J. and Bennett, M., 2001. Auxin transport promotes Arabidopsis lateral root initiation. *The Plant Cell*, *13*(4), pp.843-852.

Cassel, D.K., Brown, J.M. and Johnson, G.A., 1990. Computer tomographic analysis of water distribution and flow in porous media. *Theoretical and Applied Climatology*, *42*(4), pp.223-228.

Cha, M., Santamarina, J.C., Kim, H.S. and Cho, G.C., 2014. Small-strain stiffness, shear-wave velocity, and soil compressibility. *Journal of Geotechnical and Geoenvironmental Engineering*, *140*(10), p.06014011.

Chakrabarti, A., Sarkar, P., Leelavathamma, B. and Nataraju, B.S., 2005. A functional representation for aiding biomimetic and artificial inspiration of new ideas. *Ai Edam*, *19*(2), pp.113-132.

Chambon, P. and Corte, J.F., 1994. Shallow tunnels in cohesionless soil: stability of tunnel face. *Journal of Geotechnical Engineering*, *120*(7), pp.1148-1165.

Cheng, M.Y., Cao, M.T. and Tran, D.H., 2014. A hybrid fuzzy inference model based on RBFNN and artificial bee colony for predicting the uplift capacity of suction caissons. *Automation in Construction*, *41*, pp.60-69.

Cheuk, C.Y., White, D.J. and Bolton, M.D., 2008. Uplift mechanisms of pipes buried in sand. *Journal of Geotechnical and Geoenvironmental Engineering*, *134*(2), pp.154-163.

Chin, F.K., 1970. Estimation of the ultimate load of piles from tests not carried to failure. In *Proceedings of the 2nd Southeast Asian Conference on Soil Engineering, Singapore, 1970.* (pp.81-92). Southeast Asian Society of Soil Engineering, Singapore.

Cho, G.C., 2001. *Unsaturated soil stiffness and post-liquefaction shear strength,* Doctoral dissertation, Georgia Institute of Technology, USA.

Chow, J.K. and Wang, Y.H., 2017. Preparation of High-Quality Load-Preserved Fabric Clay Samples for Microstructural Characterizations: A Pragmatic Guide Featuring a 3-D–Printed Oedometer. *Geotechnical Testing Journal*, *40*(5), pp.891-905.

Coppin, N.J., Richards, I.G., Barker, D.H., Morgan, R.P.C., Rickson, R.J., 1990. *Use of vegetation in civil engineering*. Construction Industry Research and Information Association, London.

Cortes, D.D., Martin, A.I., Yun, T.S., Francisca, F.M., Santamarina, J.C. and Ruppel, C., 2009. Thermal conductivity of hydrate-bearing sediments. *Journal of Geophysical Research: Solid Earth*, *114*(11).

Coutts, M.P., 1983. Root architecture and tree stability. In *Tree Root Systems and their Mycorrhizas*, pp. 171-188, Dordrecht.

Coutts, M.P., 1986. Components of tree stability in Sitka spruce on peaty gley soil. *Forestry: An International Journal of Forest Research*, *59*(2), pp.173-197.

Coutts, M.P., Nielsen, C.C.N. and Nicoll, B.C., 1999. The development of symmetry, rigidity and anchorage in the structural root system of conifers. *Plant and Soil*, *217*(1-2), pp.1-15.

Cox, A.D., 1962. Axially-symmetric plastic deformation in soils—II. Indentation of ponderable soils. *International Journal of Mechanical Sciences*, *4*(5), pp.371-380.

Cox, A.D., Eason, G. and Hopkins, H.G., 1961. Axially symmetric plastic deformations in soils. *Philosophical Transactions of the Royal Society of London. Series A, Mathematical and Physical Sciences*, *254*(1036), pp.1-45.

Crook, M.J. and Ennos, A.R., 1996. Mechanical differences between free-standing and supported wheat plants, *Triticum aestivum L. Annals of Botany*, *77*(3), pp.197-202.

Crook, M.J. and Ennos, A.R., 1998. The increase in anchorage with tree size of the tropical tap rooted tree *Mallotus wrayi*, King (*Euphorbiaceae*). *Annals of Botany*, *82*(3), pp.291-296.

Crook, M.J., Ennos, A.R. and Banks, J.R., 1997. The function of buttress roots: a comparative study of the anchorage systems of buttressed (*Aglaia and Nephelium ramboutan* species) and non-buttressed (*Mallotus wrayi*) tropical trees. *Journal of Experimental Botany*, *48*(9), pp.1703-1716.

Cubrinovski, M. and Ishihara, K., 2002. Maximum and minimum void ratio characteristics of sands. *Soils and Foundations*, *42*(6), pp.65-78.

Cucchi, V. and Bert, D., 2003. Wind-firmness in *Pinus pinaster Ait.* stands in Southwest France: influence of stand density, fertilisation and breeding in two experimental stands damaged during the 1999 storm. *Annals of Forest Science*, *60*(3), pp.209-226.

Cucchi, V., Meredieu, C., Stokes, A., Berthier, S., Bert, D., Najar, M., Denis, A. and Lastennet, R., 2004. Root anchorage of inner and edge trees in stands of Maritime pine (*Pinus pinaster Ait.*) growing in different podzolic soil conditions. *Trees*, *18*(4), pp.460-466.

Czarnes, S., Hallett, P.D., Bengough, A.G. and Young, I.M., 2000. Root-and microbial-derived mucilages affect soil structure and water transport. *European Journal of Soil Science*, *51*(3), pp.435-443.

Czarnes, S., Hiller, S., Dexter, A.R., Hallett, P.D. and Bartoli, F., 1999. Root: soil adhesion in the maize rhizosphere: the rheological approach. *Plant and Soil*, *211*(1), pp.69-86.

Danjon, F., Caplan, J.S., Fortin, M. and Meredieu, C., 2013. Descendant root volume varies as a function of root type: estimation of root biomass lost during uprooting in *Pinus pinaster*. *Frontiers in Plant Science*, *4*, p.402.

Danjon, F., Fourcaud, T. and Bert, D., 2005. Root architecture and wind-firmness of mature *Pinus pinaster*. *New Phytologist*, *168*(2), pp.387-400.

Danjon, F., Stokes, A. and Bakker, M.R., 2013. Root systems of woody plants. In *Plant Roots* ed. Eshel and Beeckman, (pp.1-26). CRC Press, Boca Raton.

Das, B.M. and Seeley, G.R., 1975. Uplift capacity of buried model piles in sand. *Journal of Geotechnical and Geoenvironmental Engineering*, *101*(10), pp.1091-1094.

Davie, J.R., 1973. *Behaviour of cohesive soils under uplift forces,* Doctoral dissertation, University of Glasgow, UK.

Deans, J.D. and Ford, E.D., 1983. Modelling root structure and stability. In *Tree Root Systems and Their Mycorrhizas* (pp. 189-195). Springer, Dordrecht.

Deldin, J.M. and Schuknecht, M., 2014. The AskNature database: enabling solutions in biomimetic design. In *Biologically Inspired Design* (pp. 17-27). Springer, London.

Delhaize, E. and Ryan, P.R., 1995. Aluminum toxicity and tolerance in plants. *Plant Physiology*, *107*(2), p.315.

Desrues, J., Lanier, J. and Stutz, P., 1985. Localization of the deformation in tests on sand sample. *Engineering Fracture Mechanics*, *21*(4), pp.909-921.

Dexter, A.R., 1987. Compression of soil around roots. *Plant and Soil*, *97*(3), pp.401-406.

Díaz-Rodríguez, J.A., Cruz, R.L.S., Dávila-Alcocer, V.M., Vallejo, E. and Girón, P., 1998. Physical, chemical, and mineralogical properties of Mexico City sediments: a geotechnical perspective. *Canadian Geotechnical Journal*, *35*(4), pp.600-610.

Dickin, E.A. and Leung, C.F., 1990. Performance of piles with enlarged bases subject to uplift forces. *Canadian Geotechnical Journal*, *27*(5), pp.546-556.

Dickin, E.A. and Leung, C.F., 1992. The influence of foundation geometry on the uplift behaviour of piles with enlarged bases. *Canadian Geotechnical Journal*, *29*(3), pp.498-505.

Dickin, E.A., 1988. Uplift behavior of horizontal anchor plates in sand. *Journal of Geotechnical Engineering*, *114*(11), pp.1300-1317.

Dizon, J.R.C., Espera Jr, A.H., Chen, Q. and Advincula, R.C., 2018. Mechanical characterization of 3D-printed polymers. *Additive Manufacturing*, *20*(1), pp.44-67.

Donald, R.G., Kay, B.D. and Miller, M.H., 1987. The effect of soil aggregate size on early shoot and root growth of maize (*Zea mays L.*). *Plant and Soil*, *103*(2), pp.251-259.

Doreau-Malioche, J., Combe, G., Viggiani, G. and Toni, J.B., 2018. Shaft friction changes for cyclically loaded displacement piles: an X-ray investigation. *Géotechnique Letters*, *8*(1), pp.66-72.

Dorioz, J.M., Robert, M. and Chenu, C., 1993. The role of roots, fungi and bacteria on clay particle organization. An experimental approach. In *Soil Structure/Soil Biota Interrelationships,* (pp. 179-194). Elsevier, Amsterdam.

Dove, J.E. and Frost, J.D., 1999. Peak friction behavior of smooth geomembrane-particle interfaces. *Journal of Geotechnical and Geoenvironmental Engineering*, *125*(7), pp.544-555.

Dove, J.E., 1996. *Particle-geomembrane interface strength behavior as influenced by surface topography*, Doctoral dissertation, Georgia Institute of Technology, USA.

Drennan, P.M. and Nobel, P.S., 1998. Root growth dependence on soil temperature for *Opuntia ficus-indica*: influences of air temperature and a doubled CO_2 concentration. *Functional Ecology*, *12*(6), pp.959-964.

Drew, M.C., 1975. Comparison of the effects of a localised supply of phosphate, nitrate, ammonium and potassium on the growth of the seminal root system, and the shoot, in barley. *New Phytologist*, *75*(3), pp.479-490.

Drucker, D.C. and Prager, W., 1952. Soil mechanics and plastic analysis or limit design. *Quarterly of Applied Mathematics*, *10*(2), pp.157-165.

Dumlao, M.R., Ramananarivo, S., Goyal, V., DeJong, J.T., Waller, J. and Silk, W.K., 2015. The role of root development of Avena fatua in conferring soil strength. *American Journal of Botany*, *102*(7), pp.1050-1060.

Dupuy, L., Fourcaud, T. and Stokes, A., 2005. A numerical investigation into factors affecting the anchorage of roots in tension. *European Journal of Soil Science*, *56*(3), pp.319-327.

Dupuy, L., Fourcaud, T. and Stokes, A., 2007. A numerical investigation into the influence of soil type and root architecture on tree anchorage. In *Eco-and ground bio-engineering: The use of vegetation to improve slope stability,* (pp. 175-189). Springer, Dordrecht.

Dyson, A.S. and Rognon, P.G., 2014. Pull-out capacity of tree root inspired anchors in shallow granular soils. *Géotechnique Letters*, *4*(4), pp.301-305.

Eapen, D., Barroso, M.L., Ponce, G., Campos, M.E. and Cassab, G.I., 2005. Hydrotropism: root growth responses to water. *Trends in Plant Science*, *10*(1), pp.44-50.

Edmaier, K., Crouzy, B., Ennos, R., Burlando, P. and Perona, P., 2014. Influence of root characteristics and soil variables on the uprooting mechanics of *Avena sativa* and *Medicago sativa* seedlings. *Earth Surface Processes and Landforms*, *39*(10), pp.1354-1364.

Ennos, A.R. and Fitter, A.H., 1992. Comparative functional morphology of the anchorage systems of annual dicots. *Functional Ecology*, pp.71-78.

Ennos, A.R., 1989. The mechanics of anchorage in seedlings of sunflower, *Helianthus annuus L. New Phytologist*, *113*(2), pp.185-192.

Ennos, A.R., 1990. The anchorage of leek seedlings: the effect of root length and soil strength. *Annals of Botany*, *65*(4), pp.409-416.

Ennos, A.R., 1993. The scaling of root anchorage. *Journal of Theoretical Biology*, *161*(1), pp.61-75.

Ennos, A.R., 2000. The mechanics of root anchorage. *Advances in Botanical Research,* 33, pp. 133-157.

Ennos, A.R., Crook, M.J. and Grimshaw, C., 1993. The anchorage mechanics of maize, *Zea mays*. *Journal of Experimental Botany*, *44*(1), pp.147-153.

Esposito, M., 2017. Photon-Counting Detectors for X-ray Imaging. *Handbook of X-ray imaging: Physics and Technology*. CRC Press, Boca Raton.

Evans, T.M. and Zhang, N., 2019. Three-Dimensional Simulations of Plate Anchor Pullout in Granular Materials. *International Journal of Geomechanics*, *19*(4):04019004, pp.1-14.

Evans, T.M., 2005. *Microscale physical and numerical investigations of shear banding in granular soils*, Doctoral dissertation, Georgia Institute of Technology, USA.

Farouki, O.T., 1981. The thermal properties of soils in cold regions. *Cold Regions Science and Technology*, *5*(1), pp.67-75.

Feldkamp, L.A., Davis, L.C. and Kress, J.W., 1984. Practical cone-beam algorithm. *Journal of the Optical Society of America A*, 1(6), pp.612-619.

Fellenius, B.H., 1980. The analysis of results from routine pile load tests. *Ground Engineering*, *13*(6), pp.19-31.

Ferrucci, M., Leach, R.K., Giusca, C., Carmignato, S. and Dewulf, W., 2015. Towards geometrical calibration of x-ray computed tomography systems—a review. *Measurement Science and Technology*, *26*(9):092003.

Fitter, A.H. and Ennos, A.R., 1989. Architectural constraints to root system function. *Aspects of Applied Biology*, *22*(1), pp. 15-22.

Fitter, A.H. and Stickland, T.R., 1991. Architectural analysis of plant root systems 2. Influence of nutrient supply on architecture in contrasting plant species. *New Phytologist*, *118*(3), pp.383-389.

Fitter, A.H., 1987. An architectural approach to the comparative ecology of plant root systems. *New Phytologist*, *106*, pp.61-77.

Fitter, A.H., Stickland, T.R., Harvey, M.L. and Wilson, G.W., 1991. Architectural analysis of plant root systems 1. Architectural correlates of exploitation efficiency. *New Phytologist*, *118*(3), pp.375-382.

Flannery, B.P., Deckman, H.W., Roberge, W.G. and D'Amico, K.L., 1987. Three-dimensional X-ray microtomography. *Science*, *237*(4821), pp.1439-1444.

Fourcaud, T., Blaise, F., Lac, P., Castéra, P. and De Reffye, P., 2003. Numerical modelling of shape regulation and growth stresses in trees. *Trees*, *17*(1), pp.31-39.

Fourcaud, T., Ji, J.N., Zhang, Z.Q. and Stokes, A., 2007. Understanding the impact of root morphology on overturning mechanisms: a modelling approach. *Annals of Botany*, *101*(8), pp.1267-1280.

Fowmes, G.J., Dixon, N., Fu, L. and Zaharescu, C.A., 2017. Rapid prototyping of geosynthetic interfaces: Investigation of peak strength using direct shear tests. *Geotextiles and Geomembranes*, *45*(6), pp.674-687.

Friml, J., 2003. Auxin transport—shaping the plant. *Current Opinion in Plant Biology*, *6*(1), pp.7-12.

Frost, J.D. and DeJong, J.T., 2005. In situ assessment of role of surface roughness on interface response. *Journal of Geotechnical and Geoenvironmental Engineering*, *131*(4), pp.498-511.

Frost, J.D. and Karademir, T., 2016. Shear-induced changes in smooth geomembrane surface topography at different ambient temperatures. *Geosynthetics International*, *23*(2), pp.113-128.

Frost, J.D., DeJong, J.T. and Recalde, M., 2002. Shear failure behavior of granular–continuum interfaces. *Engineering Fracture Mechanics*, *69*(17), pp.2029-2048.

Fu, K., Moreno, D., Yang, M. and Wood, K.L., 2014. Bio-inspired design: an overview investigating open questions from the broader field of design-by-analogy. *Journal of Mechanical Design*, *136*(11):111102.

Gardiner, B., Peltola, H. and Kellomäki, S., 2000. Comparison of two models for predicting the critical wind speeds required to damage coniferous trees. *Ecological Modelling*, *129*(1), pp.1-23.

Garnier, J. and Konig, D., 1998. Scale effects in piles and nails loading tests in sand. In *Proceedings of the International Conference Centrifuge 98*, *Tokyo, Japan*, (pp. 205-210). Balkema, Rotterdam.

Garnier, J., Gaudin, C., Springman, S.M., Culligan, P.J., Goodings, D., Konig, D., Kutter, B., Phillips, R., Randolph, M.F. and Thorel, L., 2007. Catalogue of scaling laws and similitude questions in geotechnical centrifuge modelling. *International Journal of Physical Modelling in Geotechnics*, *7*(3), pp.1-23.

Geddes, J.D., and Murray, E.J., 1991. Passive inclined anchorages in sand. *Journal of Geotechnical Engineering*, *117*(5), pp. 810-814.

Genet, M., Stokes, A., Salin, F., Mickovski, S.B., Fourcaud, T., Dumail, J.F. and Van Beek, R., 2005. The influence of cellulose content on tensile strength in tree roots. *Plant and Soil*, *278*(1-2), pp.1-9.

Geuzaine, C. and Remacle, J.F., 2009. Gmsh: A 3-D finite element mesh generator with built-in pre-and post-processing facilities. *International Journal for Numerical Methods in Engineering*, *79*(11), pp.1309-1331.

Ghaly, A., Hanna, A. and Hanna, M., 1991. Uplift behavior of screw anchors in sand. I: dry sand. *Journal of Geotechnical Engineering*, *117*(5), pp.773-793.

Giampa, J.R., Bradshaw, A.S. and Schneider, J.A., 2016. Influence of dilation angle on drained shallow circular anchor uplift capacity. *International Journal of Geomechanics*, *17*(2), p.04016056.

Giordano, R.A., Wu, B.M., Borland, S.W., Cima, L.G., Sachs, E.M. and Cima, M.J., 1997. Mechanical properties of dense polylactic acid structures fabricated by three dimensional printing. *Journal of Biomaterials Science, Polymer Edition*, *8*(1), pp.63-75.

Goodman, A.M. and Ennos, A.R., 1996. A comparative study of the response of the roots and shoots of sunflower and maize to mechanical stimulation. *Journal of Experimental Botany*, *47*(10), pp.1499-1507.

Goodman, A.M. and Ennos, A.R., 1999. The effects of soil bulk density on the morphology and anchorage mechanics of the root systems of sunflower and maize. *Annals of Botany*, *83*(3), pp.293-302.

Goodman, A.M., Crook, M.J. and Ennos, A.R., 2001. Anchorage mechanics of the tap root system of winter-sown oilseed rape (*Brassica napus L.*). *Annals of Botany*, *87*(3), pp.397-404.

Gray, D.H. and Barker, D., 2004. Root-soil mechanics and interactions. *Riparian Vegetation and Fluvial Geomorphology*, *8*, pp.113-123.

Gray, D.H. and Ohashi, H., 1983. Mechanics of fiber reinforcement in sand. *Journal of Geotechnical Engineering*, *109*(3), pp.335-353.

Gray, D.H. and Sotir, R.B., 1995. Biotechnical stabilization of steepened slopes. *Transportation Research Record*, 1474, pp.23-23.

Gregory, P. J. 2006. Plant roots: growth, activity and interactions with the soil. Blackwell Publishing, London.

Gregory, P.J., 1986. Response to temperature in a stand of pearl millet (*Pennisetum typhoides S. & H.*) VIII. Root growth. *Journal of Experimental Botany*, *37*(3), pp.379-388.

Grime, J.P. and Mackey, J.M.L., 2002. The role of plasticity in resource capture by plants. *Evolutionary Ecology*, 1*6*(3), pp.299-307.

Grime, J.P., 1977. Evidence for the existence of three primary strategies in plants and its relevance to ecological and evolutionary theory. *The American Naturalist*, *111*(982), pp.1169-1194.

Hall, S.A., Bornert, M., Desrues, J., Pannier, Y., Lenoir, N., Viggiani, G. and Bésuelle, P., 2010. Discrete and continuum analysis of localised deformation in sand using X-ray micro CT and volumetric digital image correlation. *Géotechnique*, *60*(5), p.315.

Hall, S.A., Wright, J., Pirling, T., Andò, E., Hughes, D.J. and Viggiani, G., 2011. Can intergranular force transmission be identified in sand? *Granular Matter*, *13*(3), pp.251-254.

Hamza, O., Bengough, A.G., Bransby, M.F., Davies, M.C.R., Halpin, C. and Hallett, P.D., 2007. Novel biomechanical analysis of plant roots. In *Eco-and Ground Bio-*

Engineering: The Use of Vegetation to Improve Slope Stability (pp. 13-20). Springer, Dordrecht.

Hanaor, D.A.H., Gan, Y., Revay, M., Airey, D.W. and Einav, I., 2016. 3D printable geomaterials. G*éotechnique*, *66*(4), pp.323-332.

Handy, R.L., 1985. The arch in soil arching. *Journal of Geotechnical Engineering*, *111*(3), pp.302-318.

Helms, M., Vattam, S.S. and Goel, A.K., 2009. Biologically inspired design: process and products. *Design Studies*, *30*(5), pp.606-622.

Helms, M.E., Vattam, S.S., Goel, A.K., Yen, J. and Weissburg, M., 2008. Problem-driven and solution-based design: twin processes of biologically inspired design. In *Proceeding of the 28th Annual Conference of ACADIA, Minneapolis*

Hewlett, W.J. and Randolph, M.F., 1988. Analysis of piled embankments. In *International Journal of Rock Mechanics and Mining Sciences and Geomechanics Abstracts*, *25*(6) (pp. 297-298). Elsevier Science, Amsterdam.

Hillel, D., 2000. *Fundamentals of Soil Physics*. Academic Press, Cambridge.

Hinsinger, P., Bengough, A.G., Vetterlein, D. and Young, I.M., 2009. Rhizosphere: biophysics, biogeochemistry and ecological relevance. *Plant and soil*, *321*(1-2), pp.117-152.

Ho, T.K., 1995. Random decision forests. In *Proceedings of 3rd International Conference on Document Analysis and Recognition. 1*, (pp. 278-282). IEEE, Piscataway.

Hodge, A., Berta, G., Doussan, C., Merchan, F. and Crespi, M., 2009. Plant root growth, architecture and function. *Plant and Soil*, *321*(1-2), pp.153-187.

Houlsby, G.T. and Wroth, C.P., 1982. Direct solution of plasticity problems in soils by the method of characteristics. *NASA STI/Recon Technical Report No*, *83*, pp. 1-24.

Houlsby, G.T., 1982. Theoretical analysis of the fall cone test. *Géotechnique*, *32*(2), pp.111-118.

Ilamparuthi, K. and Muthukrishnaiah, K., 1999. Anchors in sand bed: delineation of rupture surface. *Ocean Engineering*, *26*(12), pp.1249-1273.

Ilamparuthi, K., Dickin, E.A. and Muthukrisnaiah, K., 2002. Experimental investigation of the uplift behaviour of circular plate anchors embedded in sand. *Canadian Geotechnical Journal*, *39*(3), pp.648-664.

Imseeh, W.H., Druckrey, A.M. and Alshibli, K.A., 2018. 3D experimental quantification of fabric and fabric evolution of sheared granular materials using synchrotron micro-computed tomography. *Granular Matter*, *20*(2), p.24.

Jackson, R.B., Canadell, J., Ehleringer, J.R., Mooney, H.A., Sala, O.E. and Schulze, E.D., 1996. A global analysis of root distributions for terrestrial biomes. *Oecologia*, *108*(3), pp.389-411.

Jaffe, M.J., 1973. Thigmomorphogenesis: the response of plant growth and development to mechanical stimulation. *Planta, 114*, pp. 143-157.

Jaffe, M.J., 1976. Thigmomorphogenesis: a detailed characterization of the response of beans *(Phaseolus vulgaris L.*) to mechanical stimulation. *Zeitschrift für Pflanzenphysiologie*, *77*(5), pp.437-453.

Jefferies, M. and Been, K., 2016. *Soil liquefaction: a critical state approach*. CRC press, Boca Raton.

Jewell, R.A. and Wroth, C.P., 1987. Direct shear tests on reinforced sand. *Géotechnique*, *37*(1), pp.53-68.

Jewell, R.A., Milligan, G.W.E. and Dubois, D., 1985. Interaction between soil and geogrids. In *Polymer grid reinforcement* (pp. 18-30). Thomas Telford Publishing, London.

Johnson, N.C., Graham, J.H. and Smith, F.A., 1997. Functioning of mycorrhizal associations along the mutualism–parasitism continuum. *The New Phytologist*, *135*(4), pp.575-585.

Kabir, M., Kasap, S. and Rowlands, J., 2007. Photoconductors for x-ray image detectors. *Springer Handbook of Electronic and Photonic Materials*, pp.1121-1137.

Kananyan, A.S., 1966. Experimental investigation of the stability of bases of anchor foundations. *Soil Mechanics and Foundation Engineering*, *3*(6), pp.387-392.

Karrenberg, S., Blaser, S., Kollmann, J., Speck, T. and Edwards, P.J., 2003. Root anchorage of saplings and cuttings of woody pioneer species in a riparian environment. *Functional Ecology*, *17*(2), pp.170-177.

Kaspar, T.C. and Bland, W.L., 1992. Soil temperature and root growth. *Soil Science*, *154*(4), pp.290-299.

Kawamoto, R., Andò, E., Viggiani, G. and Andrade, J.E., 2016. Level set discrete element method for three-dimensional computations with triaxial case study. *Journal of the Mechanics and Physics of Solids*, *91*, pp.1-13.

Khuder, H., Stokes, A., Danjon, F., Gouskou, K. and Lagane, F., 2007. Is it possible to manipulate root anchorage in young trees? *Plant and Soil*, *294*(1-2), pp.87-102.

Kim, J., Zhang, Y., Seol, Y. and Dai, S., 2019. Particle crushing in hydrate-bearing sands. *Geomechanics for Energy and the Environment*, (in press).

Koutsabeloulis, N.C. and Griffiths, D.V., 1989. Numerical modelling of the trap door problem. *Géotechnique*, *39*(1), pp.77-89.

Kulhawy, F.H., 2004. On the axial behavior of drilled foundations. In *GeoSupport 2004: Drilled Shafts, Micropiling, Deep Mixing, Remedial Methods, and Specialty Foundation Systems* ed. Turner and Mayne, *Orlando, USA,* (pp. 34-51), ASCE Press, Reston.

Kumar, J. and Kouzer, K.M., 2008. Vertical uplift capacity of horizontal anchors using upper bound limit analysis and finite elements. *Canadian Geotechnical Journal*, *45*(5), pp.698-704.

Ladanyi, B. and Hoyaux, B.J.C.G.J., 1969. A study of the trap-door problem in a granular mass. *Canadian Geotechnical Journal*, *6*(1), pp.1-14.

Lade, P.V., Cole Jr, D.A. and Cummings, D., 1984. Multiple failure surfaces over dip-slip faults. *Journal of Geotechnical Engineering*, *110*(5), pp.616-627.

Lade, P.V., Liggio Jr, C.D. and Nam, J., 2009. Strain rate, creep, and stress drop-creep experiments on crushed coral sand. *Journal of Geotechnical and Geoenvironmental Engineering*, *135*(7), pp.941-953.

Larkin, L.A., 1968. Theoretical bearing capacity of very shallow footings. *Journal of the Soil Mechanics and Foundations Division*, *94*(6), pp.1347-1360.

Lary, D.J., Alavi, A.H., Gandomi, A.H. and Walker, A.L., 2016. Machine learning in geosciences and remote sensing. *Geoscience Frontiers*, *7*(1), pp.3-10.

Lenoir, N., Bornert, M., Desrues, J., Bésuelle, P. and Viggiani, G., 2007. Volumetric digital image correlation applied to X-ray microtomography images from triaxial compression tests on argillaceous rock. *Strain*, *43*(3), pp.193-205.

Leonards, G.A. and Lovell, D., 1979. Interpretation of load tests on high-capacity driven piles. In *Behavior of Deep Foundations*. (pp.388-415), ASTM International, West Conshohocken.

Letcher, T. and Waytashek, M., 2015, March. Material property testing of 3D-printed specimen in PLA on an entry-level 3D printer. In *ASME 2014 International Mechanical Engineering Congress and Exposition, Montreal, Canada,* (pp.1-8), American Society of Mechanical Engineers Digital Collection, New York.

Lide, D.R. ed., 2009. *CRC Handbook of Chemistry and Physics* (Vol. 89). CRC press, Boca Raton.

Liu, J., Liu, M. and Zhu, Z., 2011. Sand deformation around an uplift plate anchor. *Journal of Geotechnical and Geoenvironmental Engineering*, *138*(6), pp.728-737.

Lizzi, F., 1993. 'Pali radice'structures. In *Underpinning and Retention* (pp. 84-156). Springer, Boston.

Lucarotti, C., Totaro, M., Sadeghi, A., Mazzolai, B. and Beccai, L., 2015. Revealing bending and force in a soft body through a plant root inspired approach. *Scientific Reports*, *5*, 8788.

Lunne, T., Knudsen, S., Blaker, Ø., Vestgården, T., Powell, J.J.M., Wallace, C.F., Krogh, L., Thomsen, N.V., Yetginer, G. and Ghanekar, R.K., 2019. Methods used to determine maximum and minimum dry unit weights of sand: Is there a need for a new standard? *Canadian Geotechnical Journal*, *56*(4), pp.536-553.

Lynch, J., 1995. Root architecture and plant productivity. *Plant Physiology*, *109*(1), pp.1-13.

MacFall, J.S., Johnson, G.A. and Kramer, P.J., 1991. Comparative water uptake by roots of different ages in seedlings of loblolly pine (*Pinus taeda L.*). *New Phytologist*, *119*(4), pp.551-560.

Malamy, J.E., 2005. Intrinsic and environmental response pathways that regulate root system architecture. *Plant, Cell & Environment*, *28*(1), pp.67-77.

Mallett, S.D., Matsumura, S. and Frost, D.J., 2018. Additive manufacturing and computed tomography of bio-inspired anchorage systems. *Géotechnique Letters*, *8*(3), pp.219-225.

Mariupol'skii, L.G., 1965. The bearing capacity of anchor foundations. *Soil Mechanics and Foundation Engineering*, *2*(1), pp.26-32.

Marks, B., Guillard, F. and Einav, I., 2016. High speed X-ray imaging of particulate flows. In *12th International Conference on Bulk Materials Storage, Handling and Transportation, Darwin, Australia,* (pp. 274-278). Engineers Australia, Barton.

Mason, E.G., 1985. Causes of juvenile instability of *Pinus radiata* in New Zealand. *New Zealand Journal of Forestry Science*, *15*(3), pp.263-280.

Matsuo, M., 1967. Study on the uplift resistance of footing I. *Soils and Foundations*, *7*(4), pp.1-37.

Mattheck, C.M. and Mattheck, C., 1998. *Design in nature: learning from trees*. Springer Science & Business Media, Berlin.

Mattheck, G.C., 1991. *Trees: The Mechanical Design*. Springer Science & Business Media, Berlin.

Mazzolai, B., Corradi, P., Mondini, A., Mattoli, V., Laschi, C., Mancuso, S., Mugnai, S. and Dario, P., 2008. Inspiration from plant roots: a robotic root apex for soil exploration. *Proceedings of Biological Approaches for Engineering, University of Southampton*, pp.50-3.

McCully, M.E., 1999. Roots in soil: unearthing the complexities of roots and their rhizospheres. *Annual Review of Plant Biology*, *50*(1), pp.695-718.

Menon, C., Vincent, J.F.V., Lan, N., Bilhaut, L., Ellery, A., Gao, Y., Zangani, D., Carosio, S., Manning, C., Jaddou, M. and Eckersley, S., 2008, August. Bio-inspired micro-drills for future planetary exploration. In *CANEUS 2006: MNT for Aerospace Applications, Toulouse, France,* (pp. 117-128). American Society of Mechanical Engineers Digital Collection, New York.

Merifield, R.S. and Sloan, S.W., 2006. The ultimate pullout capacity of anchors in frictional soils. *Canadian Geotechnical Journal*, *43*(8), pp.852-868.

Meyerhof, G.G. and Adams, J.I., 1968. The ultimate uplift capacity of foundations. *Canadian Geotechnical Journal*, *5*(4), pp.225-244.

Mickovski, S.B. and Ennos, A.R., 2003. Anchorage and asymmetry in the root system of *Pinus peuce*. *Silva Fennica*, *37*(2), pp.161-173.

Mickovski, S.B. and Ennos, A.R., 2003. The effect of unidirectional stem flexing on shoot and root morphology and architecture in young *Pinus sylvestris* trees. *Canadian Journal of Forest Research*, *33*(11), pp.2202-2209.

Mickovski, S.B., Bengough, A.G., Bransby, M.F., Davies, M.C.R., Hallett, P.D. and Sonnenberg, R., 2007. Material stiffness, branching pattern and soil matric potential affect the pullout resistance of model root systems. *European Journal of Soil Science*, *58*(6), pp.1471-1481.

Mickovski, S.B., Bransby, M.F., Bengough, A.G., Davies, M.C.R. and Hallett, P.D., 2010. Resistance of simple plant root systems to uplift loads. *Canadian Geotechnical Journal*, *47*(1), pp.78-95.

Mickovski, S.B., Hallett, P.D., Bransby, M.F., Davies, M.C., Sonnenberg, R. and Bengough, A.G., 2009. Mechanical reinforcement of soil by willow roots: impacts of root properties and root failure mechanism. *Soil Science Society of America Journal*, *73*(4), pp.1276-1285.

Mickovski, S.B., van Beek, L.H. and Salin, F., 2005. Uprooting resistance of vetiver grass (*Vetiveria zizanioides*). *Plant and Soil*, *278*(1-2), pp.33-41.

Mitchell, J.K. and Santamarina, J.C., 2005. Biological considerations in geotechnical engineering. *Journal of Geotechnical and Geoenvironmental Engineering*, *131*(10), pp.1222-1233.

Moayedi, H. and Rezaei, A., 2019. An artificial neural network approach for under-reamed piles subjected to uplift forces in dry sand. *Neural Computing and Applications*, *31*(2), pp.327-336.

Mokhbi, H., Mellas, M., Mabrouki, A. and Pereira, J.M., 2018. Three-dimensional numerical and analytical study of horizontal group of square anchor plates in sand. *Acta Geotechnica*, *13*(1), pp.159-174.

Monaenkova, D., Gravish, N., Rodriguez, G., Kutner, R., Goodisman, M.A. and Goldman, D.I., 2015. Behavioral and mechanical determinants of collective subsurface nest excavation. *Journal of Experimental Biology*, *218*(9), pp.1295-1305.

Morita, K., Otani, J., Mukunoki, T., Hironaka, J. and Pham, K.D., 2007. Evaluation of vertical and lateral bearing capacity mechanisms of pile foundations using X-ray CT. In *Proceedings of international workshop on recent advances of deep foundations, Yokosuka, Japan,* (pp. 217-223). Taylor & Francis, London.

Muduli, P.K., Das, M.R., Samui, P. and Kumar Das, S., 2013. Uplift capacity of suction caisson in clay using artificial intelligence techniques. *Marine Georesources & Geotechnology*, *31*(4), pp.375-390.

Mühlhaus, H.B. and Vardoulakis, I., 1987. The thickness of shear bands in granular materials. *Géotechnique*, *37*(3), pp.271-283.

Munns, R., 2002. Comparative physiology of salt and water stress. *Plant, Cell & Environment*, *25*(2), pp.239-250.

Murray, E.J. and Geddes, J.D., 1987. Uplift of anchor plates in sand. *Journal of Geotechnical Engineering*, *113*(3), pp.202-215.

Nagel, K.A., Kastenholz, B., Jahnke, S., Van Dusschoten, D., Aach, T., Mühlich, M., Truhn, D., Scharr, H., Terjung, S., Walter, A. and Schurr, U., 2009. Temperature responses of roots: impact on growth, root system architecture and implications for phenotyping. *Functional Plant Biology*, *36*(11), pp.947-959.

Nakrani, S. and Tovey, C., 2004. On honey bees and dynamic server allocation in internet hosting centers. *Adaptive Behavior*, *12*(3-4), pp.223-240.

Nicoll, B.C. and Ray, D., 1996. Adaptive growth of tree root systems in response to wind action and site conditions. *Tree Physiology*, *16*(11-12), pp.891-898.

Nicoll, B.C., Berthier, S., Achim, A., Gouskou, K., Danjon, F. and Van Beek, L.P.H., 2006. The architecture of *Picea sitchensis* structural root systems on horizontal and sloping terrain. *Trees*, *20*(6), pp.701-712.

Nielsen, K.L., Lynch, J.P. and Weiss, H.N., 1997. Fractal geometry of bean root systems: correlations between spatial and fractal dimension. *American Journal of Botany*, *84*(1), pp.26-33.

Nikl, M., 2006. Scintillation detectors for x-rays. *Measurement Science and Technology*, *17*(4), pp.37-54.

Niklas, K.J., 1989. Mechanical behavior of plant tissues as inferred from the theory of pressurized cellular solids. *American Journal of Botany*, *76*(6), pp.929-937.

Niklas, K.J., 1992. *Plant biomechanics: an engineering approach to plant form and function*. University of Chicago Press, Chicago, USA.

Niklas, K.J., Molina-Freaner, F., Tinoco-Ojanguren, C. and Paolillo Jr, D.J., 2002. The biomechanics of *Pachycereus pringlei* root systems. *American Journal of Botany*, *89*(1), pp.12-21.

Nilaweera, N.S. and Nutalaya, P., 1999. Role of tree roots in slope stabilisation. *Bulletin of Engineering Geology and the Environment*, *57*(4), pp.337-342.

Noo, F., Clackdoyle, R., Mennessier, C., White, T.A. and Roney, T.J., 2000. Analytic method based on identification of ellipse parameters for scanner calibration in cone-beam tomography. *Physics in Medicine & Biology*, *45*(11), p.3489.

Nye, P.H. and Tinker, P.B., 1977. *Solute movement in the soil-root system*, 4. University of California Press, Berkley, USA.

Oades, J.M., 1978. Mucilages at the root surface. *Journal of Soil Science*, *29*(1), pp.1-16.

Ochiai, H., Otani, J., Hayashic, S. and Hirai, T., 1996. The pull-out resistance of geogrids in reinforced soil. *Geotextiles and Geomembranes*, *14*(1), pp.19-42.

Oda, M. and Kazama, H., 1998. Microstructure of shear bands and its relation to the mechanisms of dilatancy and failure of dense granular soils. *Géotechnique*, *48*(4), pp.465-481.

Operstein, V. and Frydman, S., 2000. The influence of vegetation on soil strength. *Proceedings of the Institution of Civil Engineers: Ground Improvement*, *4*(2), pp.81-89.

Oppelt, A.L., Kurth, W. and Godbold, D.L., 2001. Topology, scaling relations and Leonardo's rule in root systems from African tree species. *Tree Physiology*, *21*(2-3), pp.117-128.

O'Rourke, T.D., Druschel, S.J. and Netravali, A.N., 1990. Shear strength characteristics of sand-polymer interfaces. *Journal of Geotechnical Engineering*, *116*(3), pp.451-469.

Otani, J., Mukunoki, T. and Obara, Y., 2000. Application of X-ray CT method for characterization of failure in soils. *Soils and Foundations*, *40*(2), pp.111-118.

Otani, J., Pham, K.D. and Sano, J., 2006. Investigation of failure patterns in sand due to laterally loaded pile using X-ray CT. *Soils and Foundations*, *46*(4), pp.529-535.

Ovesen, N.K., 1981. Centrifuge tests of uplift capacity of anchors. In *Proceedings of the 10th International Conference on Soil Mechanics and Foundation Engineering, Stockholm, Sweden,* (pp. 717-722), Balkema, Rotterdam.

Pagès, L., 1999. Root system architecture: from its representation to the study of its elaboration. *Agronomie, 19*(3-4), pp.295-304.

Palmeria, E.M. and Milligan, G.W.E., 1989. Scale and other factors affecting the results of pull-out tests of grids buried in sand. *Géotechnique*, *39*(3), pp.511-542.

Passioura, J.B., 1983. Roots and drought resistance. In *Developments in Agricultural and Managed Forest Ecology*, (pp.265-280), Elsevier, Amsterdam.

Passioura, J.B., 2002. Soil conditions and plant growth. *Plant, Cell & Environment*, *25*(2), pp.311-318.

Peltola, H. and Kellomäki, S., 1993. A mechanistic model for calculating windthrow and stem breakage of Scots pines at stand age. *Silva Fennica, 27*(2), pp.99-111.

Peltola, H., Kellomäki, S., Hassinen, A. and Granander, M., 2000. Mechanical stability of Scots pine, Norway spruce and birch: an analysis of tree-pulling experiments in Finland. *Forest Ecology and Management*, *135*(1-3), pp.143-153.

Peltola, H., Kellomäki, S., Väisänen, H. and Ikonen, V.P., 1999. A mechanistic model for assessing the risk of wind and snow damage to single trees and stands of Scots pine, Norway spruce, and birch. *Canadian Journal of Forest Research*, *29*(6), pp.647-661.

Peng, S., Hu, Q., Dultz, S. and Zhang, M., 2012. Using X-ray computed tomography in pore structure characterization for a Berea sandstone: Resolution effect. *Journal of Hydrology*, *472*, pp.254-261.

Petrášek, J. and Friml, J., 2009. Auxin transport routes in plant development. *Development*, *136*(16), pp.2675-2688.

Pitts, R.J., Cernac, A. and Estelle, M., 1998. Auxin and ethylene promote root hair elongation in Arabidopsis. *The Plant Journal*, *16*(5), pp.553-560.

Pollen, N. and Simon, A., 2005. Estimating the mechanical effects of riparian vegetation on stream bank stability using a fiber bundle model. *Water Resources Research*, *41*(7):W07025

Post-Tensioning Institute, 2004. *Recommendations for prestressed rock and soil anchors*. Post-Tensioning Institute, Pheonix, USA.

Potyondy, J.G., 1961. Skin friction between various soils and construction materials. *Géotechnique*, *11*(4), pp.339-353.

Pregitzer, K.S., King, J.S., Burton, A.J. and Brown, S.E., 2000. Responses of tree fine roots to temperature. *The New Phytologist*, *147*(1), pp.105-115.

Pyrak-Nolte, L.J., Montemagno, C.D. and Nolte, D.D., 1997. Volumetric imaging of aperture distributions in connected fracture networks. *Geophysical Research Letters*, *24*(18), pp.2343-2346.

Rankouhi, B., Javadpour, S., Delfanian, F. and Letcher, T., 2016. Failure analysis and mechanical characterization of 3D printed ABS with respect to layer thickness and orientation. *Journal of Failure Analysis and Prevention*, *16*(3), pp.467-481.

Rao, K.S.S. and Kumar, J., 1994. Vertical uplift capacity of horizontal anchors. *Journal of Geotechnical Engineering*, *120*(7), pp.1134-1147.

Raven, J.A. and Edwards, D., 2001. Roots: evolutionary origins and biogeochemical significance. *Journal of Experimental Botany*, *52*(1), pp.381-401.

Ray, D. and Nicoll, B.C., 1998. The effect of soil water-table depth on root-plate development and stability of Sitka spruce. *Forestry: An International Journal of Forest Research*, *71*(2), pp.169-182.

Read, D.B. and Gregory, P.J., 1997. Surface tension and viscosity of axenic maize and lupin root mucilages. *The New Phytologist*, *137*(4), pp.623-628.

Read, D.B., Gregory, P.J. and Bell, A.E., 1999. Physical properties of axenic maize root mucilage. *Plant and Soil*, *211*(1), pp.87-91.

Reubens, B., Poesen, J., Danjon, F., Geudens, G. and Muys, B., 2007. The role of fine and coarse roots in shallow slope stability and soil erosion control with a focus on root system architecture: a review. *Trees*, *21*(4), pp.385-402.

Revil, A., 2000. Thermal conductivity of unconsolidated sediments with geophysical applications. *Journal of Geophysical Research: Solid Earth*, *105*(B7), pp.16749-16768.

Robinson, D., 1994. The responses of plants to non-uniform supplies of nutrients. *New Phytologist*, *127*(4), pp.635-674.

Rocha, M. 1957. The possibility of solving soil mechanics problems by the use of models. In *Proceedings of the 4th International Conference on Soil Mechanics and Foundation Engineering, London, England*. (pp. 183-188). Butterworths, London.

Rodríguez, J.F., Thomas, J.P. and Renaud, J.E., 2001. Mechanical behavior of acrylonitrile butadiene styrene (ABS) fused deposition materials: Experimental investigation. *Rapid Prototyping Journal*, *7*(3), pp.148-158.

Roscoe, K.H., 1970. The influence of strains in soil mechanics. *Géotechnique*, *20*(2), pp.129-170.

Rowe, R.K. and Davis, E.H., 1982. The behaviour of anchor plates in sand. G*éotechnique*, *32*(1), pp.25-41.

Rui, R., van Tol, F., Xia, X.L., van Eekelen, S., Hu, G. and Xia, Y.Y., 2016. Evolution of soil arching: 2D DEM simulations. *Computers and Geotechnics*, *73*, pp.199-209.

Russo, P., 2017. *Handbook of X-ray imaging: physics and technology*. CRC Press, Boca Raton.

Ryan, P.R., Shaff, J.E. and Kochian, L.V., 1992. Aluminum toxicity in roots: correlation among ionic currents, ion fluxes, and root elongation in aluminum-sensitive and aluminum-tolerant wheat cultivars. *Plant Physiology*, *99*(3), pp.1193-1200.

Sabatini, P.J., Pass, D.G. and Bachus, R.C., 1999. *Ground anchors and anchored systems* (No. FHWA-IF-99-015). United States Federal Highway Administration. Office of Bridge Technology.

Saeedy, H.S., 1971. *Analytical and experimental stability of earth anchors*, Doctoral dissertation, Oklahoma State University, USA.

Sakai, T. and Tanaka, T., 1998. Scale effect of a shallow circular anchor in dense sand. *Soils and Foundations*, *38*(2), pp.93-99.

Santamarina, J.C. and Cho, G.C., 2001. Determination of critical state parameters in sandy soils—simple procedure. *Geotechnical Testing Journal*, *24*(2), pp.185-192.

Santamarina, J.C., Klein, A. and Fam, M.A., 2001. Soils and waves: Particulate materials behavior, characterization and process monitoring. *John Wiley & Sons, Inc,* New York.

Schenk, H.J. and Jackson, R.B., 2002. Rooting depths, lateral root spreads and below-ground/above-ground allometries of plants in water-limited ecosystems. *Journal of Ecology*, *90*(3), pp.480-494.

Schwarz, M., Cohen, D. and Or, D., 2010. Root-soil mechanical interactions during pullout and failure of root bundles. *Journal of Geophysical Research: Earth Surface*, *115,*F4025.

Shin, H. and Santamarina, J.C., 2011. Open-mode discontinuities in soils. *Géotechnique Letters*, *1*(4), pp.95-99.

Smith, C.C., 1998. Limit loads for an anchor/trapdoor embedded in an associative Coulomb soil. *International Journal for Numerical and Analytical Methods in Geomechanics*, *22*(11), pp.855-865.

Stachowiak, G. and Batchelor, A.W., 2013. *Engineering tribology*. Butterworth-Heinemann, Oxford, UK.

Stark, T.D., Williamson, T.A. and Eid, H.T., 1996. HDPE geomembrane/geotextile interface shear strength. *Journal of Geotechnical Engineering*, *122*(3), pp.197-203.

Stathas, D., Wang, J.P. and Ling, H.I., 2017. Model geogrids and 3D printing. *Geotextiles and Geomembranes*, *45*(6), pp.688-696.

Steinhagen, H.P., 1977. Thermal conductive properties of wood, green or dry, from-40 to+ 100 C: a literature review. *Gen. Tech. Rep. FPL-09. Madison, WI: US Department of Agriculture, Forest Service, Forest Products Laboratory. 10*, pp.9.

Stern, K.R., Bidlack, J.E., Jansky, S. and Uno, G., 2006. *Introductory Plant Biology with contributions by James E. Bidlack, Shelley H. Jansky, Gordon E. Uno*, McGraw-Hill Higher Education, Boston.

Stirzaker, R.J., Passioura, J.B. and Wilms, Y., 1996. Soil structure and plant growth: impact of bulk density and biopores. *Plant and Soil*, *185*(1), pp.151-162.

Stokes, A., 1994. *Responses of young trees to wind: effects on root architecture and anchorage strength*, Doctoral dissertation, University of York, UK.

Stokes, A., 1999. Strain distribution during anchorage failure of *Pinus pinaster Ait.* at different ages and tree growth response to wind-induced root movement. *Plant and Soil*, *217*(1-2), pp.17-27.

Stokes, A., Atger, C., Bengough, A.G., Fourcaud, T. and Sidle, R.C., 2009. Desirable plant root traits for protecting natural and engineered slopes against landslides. *Plant and Soil*, *324*(1-2), pp.1-30.

Stokes, A., Drexhage, M. and Guitard, D., 2000. A method for predicting the possible site of failure in trees during mechanical loading. In *The Supporting Roots of Trees and Woody Plants: Form, Function and Physiology,* (pp. 279-285). Springer, Dordrecht.

Stokes, A., Nicoll, B.C., Coutts, M.P. and Fitter, A.H., 1997. Responses of young Sitka spruce clones to mechanical perturbation and nutrition: effects on biomass allocation, root development, and resistance to bending. *Canadian Journal of Forest Research*, *27*(7), pp.1049-1057.

Stone, K.J. and Wood, D.M., 1992. Effects of dilatancy and particle size observed in model tests on sand. *Soils and Foundations*, *32*(4), pp.43-57.

Sutherland, H.B., 1988. Uplift resistance of soils. *Géotechnique*, *38*(4), pp.493-516.

Sutton, M.A., Orteu, J.J. and Schreier, H., 2009. *Image correlation for shape, motion and deformation measurements: basic concepts, theory and applications*. Springer Science & Business Media, Berlin.

Tagaya, K., Scott, R.F. and Aboshi, H., 1988. Pullout resistance of buried anchor in sand. *Soils and Foundations*, *28*(3), pp.114-130.

Tagliaferri, F., Waller, J., Andò, E., Hall, S.A., Viggiani, G., Bésuelle, P. and DeJong, J.T., 2011. Observing strain localisation processes in bio-cemented sand using x-ray imaging. *Granular Matter*, *13*(3), pp.247-250.

Takahashi, H., 1997. Hydrotropism: the current state of our knowledge. *Journal of Plant Research*, *110*(2), p.163-169.

Takano, M., Takahashi, H., Hirasawa, T. and Suge, H., 1995. Hydrotropism in roots: sensing of a gradient in water potential by the root cap. *Planta*, *197*(2), pp.410-413.

Tanaka, T. and Sakai, T., 1993. Progressive failure and scale effect of trap-door problems with granular materials. *Soils and Foundations*, *33*(1), pp.11-22.

Tatsuoka, F., Ishihara, M., Di Benedetto, H. and Kuwano, R., 2002. Time-dependent shear deformation characteristics of geomaterials and their simulation. *Soils and Foundations*, *42*(2), pp.103-129.

Tavares, S.A., 1996. Thin conical shells with constant thickness and under axisymmetric load. *Computers & Structures*, *60*(6), pp.895-921.

Tavenas, F. and Rochelle, P.L., 1972. Accuracy of relative density measurements. *Géotechnique*, *22*(4), pp.549-562.

Taylor, Z.J., Gurka, R., Kopp, G.A. and Liberzon, A., 2010. Long-duration time-resolved PIV to study unsteady aerodynamics. *IEEE Transactions on Instrumentation and Measurement*, *59*(12), pp.3262-3269.

Teixeira, S.H., Bueno, B.S. and Zornberg, J.G., 2007. Pullout resistance of individual longitudinal and transverse geogrid ribs. *Journal of Geotechnical and Geoenvironmental Engineering*, *133*(1), pp.37-50.

Terzaghi, K. 1943. Theoretical Soil Mechanics. *John Wiley & Sons, Inc,* New York.

Terzaghi, K., Peck, R.B. and Mesri, G., 1996. Soil mechanics. *John Wiley & Sons,* New York.

Tymrak, B.M., Kreiger, M. and Pearce, J.M., 2014. Mechanical properties of components fabricated with open-source 3-D printers under realistic environmental conditions. *Materials & Design*, *58*, pp.242-246.

Uesugi, M. and Kishida, H., 1986. Influential factors of friction between steel and dry sands. *Soils and Foundations*, *26*(2), pp.33-46.

Valdes, J.R. and Santamarina, J.C., 2003. Bio-inspired particulate filters. In *Proceedings of the 16th ASCE Engineering Mechanics Conference, Seattle,* p.4, ASCE Press, Reston.

van der Veen, C., 1953. The bearing capacity of pile. In *Proceedings of the 3rd International Conference on Soil Mechanics and Foundation Engineering, Zurich, Switzerland*, 2, (pp.84-90). Zurich.

Van Eyndhoven, G. and Sijbers, J., 2017. Iterative Reconstruction Methods in X-ray CT. In *Handbook of X-ray imaging: physics and technology, 18,* (pp. 693-712), CRC Press, Boca Raton

Van Noordwijk, M. and De Willigen, P., 1987. Agricultural concepts of roots: from morphogenetic to functional equilibrium between root and shoot growth. *Netherlands Journal of Agricultural Science, 35*, pp.487-496.

Vangla, P., Roy, N. and Gali, M.L., 2018. Image based shape characterization of granular materials and its effect on kinematics of particle motion. *Granular Matter*, *20*(1), p.6.

Vermeer, P.A., 1990. The orientation of shear bands in biaxial tests. *Géotechnique*, *40*(2), pp.223-236.

Vermeer, P.A., and Sutjiadi, W. 1985. The uplift resistance of shallow embedded anchors. In *Proceedings of the 11th International Conference on Soil Mechanics and Foundation Engineering*, *San Francisco, USA* (pp.1635-1938), CRC Press, Boca Raton.

Vesic, A.S., 1969. *Breakout resistance of objects embedded in ocean bottom*. Duke University Press, Durham, USA.

Vesic, A.S., Wilson, W.E., Clough, G.W., and Tai, T.L., 1967. *Theoretical studies of cratering mechanisms affecting the stability of cratered slopes (Technical Report No. 3-699)*. United States Army Corps of Engineers, Vicksburg, Mississippi, USA.

Viggiani, G., Lenoir, N., Bésuelle, P., Di Michiel, M., Marello, S., Desrues, J. and Kretzschmer, M., 2004. X-ray microtomography for studying localized deformation in fine-grained geomaterials under triaxial compression. *Comptes Rendus Mécanique*, *332*(10), pp.819-826.

Vincent, J.F. and Mann, D.L., 2002. Systematic technology transfer from biology to engineering. *Philosophical Transactions of the Royal Society of London. Series A: Mathematical, Physical and Engineering Sciences*, *360*(1791), pp.159-173.

Vincent, J.F., Bogatyreva, O.A., Bogatyrev, N.R., Bowyer, A. and Pahl, A.K., 2006. Biomimetics: its practice and theory. *Journal of the Royal Society Interface*, *3*(9), pp.471-482.

Wadell, H., 1932. Volume, shape, and roundness of rock particles. *The Journal of Geology*, *40*(5), pp.443-451.

Waldron, L.J. and Dakessian, S., 1981. Soil reinforcement by roots: calculation of increased soil shear resistance from root properties. *Soil Science*, *132*(6), pp.427-435.

Waldron, L.J., 1977. The shear resistance of root-permeated homogeneous and stratified soil. *Soil Science Society of America Journal*, *41*(5), pp.843-849.

Wang, L., Gong, W., Yin, Y. and Tong, X., 2014. Field Experimental Study on Vertical Bearing Capacity of Root-Caisson Foundation. In *Advances in Soil Dynamics and Foundation Engineering, Shanghai, China,* (pp. 274-283). ASCE Press, Reston.

Wang, L.B., Frost, J.D. and Lai, J.S., 2004. Three-dimensional digital representation of granular material microstructure from X-ray tomography imaging. *Journal of Computing in Civil Engineering*, *18*(1), pp.28-35.

Watanabe, Y., Lenoir, N., Otani, J. and Nakai, T., 2012. Displacement in sand under triaxial compression by tracking soil particles on X-ray CT data. *Soils and Foundations*, *52*(2), pp.312-320.

Watt, M., McCully, M.E. and Jeffree, C.E., 1993. Plant and bacterial mucilages of the maize rhizosphere: comparison of their soil binding properties and histochemistry in a model system. *Plant and Soil*, *151*(2), pp.151-165.

Weaver, J.E., 1958. Classification of root systems of forbs of grassland and a consideration of their significance. *Ecology, 39*(3), pp.394-401.

Went, F.W., 1974. Reflections and speculations. *Annual Review of Plant Physiology*, *25*(1), pp.1-27.

White, D.J., Cheuk, C.Y. and Bolton, M.D., 2008. The uplift resistance of pipes and plate anchors buried in sand. *Géotechnique*, *58*(10), pp.771-779.

White, D.J., Take, W.A. and Bolton, M.D., 2003. Soil deformation measurement using particle image velocimetry (PIV) and photogrammetry. *Géotechnique*, *53*(7), pp.619-631.

Wildenschild, D., Vaz, C.M.P., Rivers, M.L., Rikard, D. and Christensen, B.S.B., 2002. Using X-ray computed tomography in hydrology: systems, resolutions, and limitations. *Journal of Hydrology*, *267*(3-4), pp.285-297.

Willemink, M.J., Persson, M., Pourmorteza, A., Pelc, N.J. and Fleischmann, D., 2018. Photon-counting CT: technical principles and clinical prospects. *Radiology*, *289*(2), pp.293-312.

Winter, A.G. and Hosoi, A.E., 2011. Identification and evaluation of the Atlantic razor clam (*Ensis directus*) for biologically inspired subsea burrowing systems. *Integrative and Comparative Biology, 51*(1), pp.151-157

Wu, T.H., Beal, P.E. and Lan, C., 1988. In-situ shear test of soil-root systems. *Journal of Geotechnical Engineering*, *114*(12), pp.1376-1394.

Wu, T.H., McKinnell III, W.P. and Swanston, D.N., 1979. Strength of tree roots and landslides on Prince of Wales Island, Alaska. *Canadian Geotechnical Journal*, *16*(1), pp.19-33.

Wu, T.H., McOmber, R.M., Erb, R.T. and Beal, P.E., 1988. Study of soil-root interaction. *Journal of Geotechnical Engineering*, *114*(12), pp.1351-1375.

Yamamuro, J.A. and Lade, P.V., 1993. Effects of strain rate on instability of granular soils. *Geotechnical Testing Journal*, *16*(3), pp.304-313.

Yu, Z., Leng, S., Jorgensen, S.M., Li, Z., Gutjahr, R., Chen, B., Halaweish, A.F., Kappler, S., Yu, L., Ritman, E.L. and McCollough, C.H., 2016. Evaluation of conventional imaging performance in a research whole-body CT system with a photon-counting detector array. *Physics in Medicine & Biology*, *61*(4), pp.1572-1595.

Yuan, Q., Wang, Y.H., Tam, P.O., Li, X. and Gao, Y., 2016. Making a biaxial testing system with the aid of 3D printing technique to examine the kinetic behavior of particulate media. *Geotechnical Testing Journal*, *39*(2), pp.264-281.

Zettler, T.E., 1999. *Operational induced changes in geomembrane surface topography*. Master's Thesis, Georgia Institute of Technology, USA.